5-4-2011 12:00 AM

Experimental and Numerical Development of Anchor-Jointed Precast Structural Wall System and Optimum Design of Prestressed Slabs

Mohamed El Semelawy, *The University of Western Ontario*

Supervisor: A. A. El Damatty, *The University of Western Ontario*

A thesis submitted in partial fulfillment of the requirements for the Doctor of Philosophy degree in Civil and Environmental Engineering

Recommended Citation

El Semelawy, Mohamed, "Experimental and Numerical Development of Anchor-Jointed Precast Structural Wall System and Optimum Design of Prestressed Slabs" (2011). *Electronic Thesis and Dissertation Repository*. 171.
https://ir.lib.uwo.ca/etd/171

EXPERIMENTAL AND NUMERICAL DEVELOPMENT OF ANCHOR-JOINTED PRECAST STRUCTURAL WALL SYSTEM
AND
OPTIMUM DESIGN OF PRESTRESSED SLABS

(Spine title: Anchor-jointed Precast Structural Wall System / Optimum Design of prestressed slabs)

(Thesis Format: Monograph)

By

Mohamed El Semelawy

Graduate Program in Engineering Science
Department of Civil and Environmental Engineering

A thesis submitted in partial fulfillment
of the requirements for the degree of
Doctor of Philosophy

School of Graduate and Postdoctoral Studies
The University of Western Ontario
London, Ontario, Canada
June, 2011

The University of Western Ontario

School of Graduate and Postdoctoral Studies

CERTIFICATE OF EXAMINATION

Supervisors	Examiners
______________________________	______________________________
Dr. El Damatty A.A.	Dr. F. M. Bartlett
______________________________	______________________________
Supervisory Committee	Dr. W. W. El Dakhakhni
______________________________	______________________________
Dr. Maged A. Youssef	Dr. M. H. El Naggar
______________________________	______________________________
	Dr. R. E. Khayat

The thesis by

Mohamed El Semelawy

entitled:

Experimental and Numerical Development of Anchor-Jointed Precast Structural Wall System and Optimum Design of Prestressed Slabs

is accepted in partial fulfillment of the
for the requirements of the degree of
Doctor of Philosophy

Date______________________________

____
Chair of the Thesis Examination Board

ABSTRACT

Precast concrete shear walls are used to resist lateral loads in low- to medium-rise buildings. An innovative joining technique is proposed to accelerate construction process and to reduce concrete damage possibility and capital loss during an earthquake event. Panels are jointed using steel anchor bolts, therefore, the system is designated "anchor-jointed precast structural wall system". In this system, anchors are utilized as a structural fuse. Damaged anchors are easily replaced after an earthquake, thus minimizing repair costs and serviceability disruptions. In the first part of this thesis, conceptual development of the system is carried out. A research program of combined analytical and experimental studies is initiated to characterize the system.

Four specimens are tested under monotonic horizontal load. Each specimen consists of a precast concrete wall panel and a base jointed through a horizontal joint. Joints tested in the current program are designed so that different failure modes could be investigated. A non-linear finite element model is developed. Through a model development process, model parameters are examined and rationally estimated to accurately replicate the behaviour. The model is then utilized to study the effect of selected parameters. The study reveals that anchor-jointed precast structural wall system has shown excellent structural behaviour with regards to their lateral capacity and ductility and may be used efficiently as a lateral-load-resisting system. However, further experimental and analytical studies are needed before that system can be adopted by relevant codes. Based on the analyses presented, it is concluded that applied gravity loads can greatly enhance the lateral capacity of the system. Also, varying the anchor bar length is an efficient parameter that may be used to reach a target performance level of ductility

In the first part of the thesis, a system for resisting later load has been developed. To augment the design of a building, the prestressed flat slab system is chosen as the main flooring system and its design is optimized. A robust numerical tool that integrates design, analysis, and optimization techniques is developed. Although the objective function, Cost, is simple and monotonic, the optimization problem is quiet challenging. Direct search methods and heuristic optimization techniques are considered. Results suggest that search should be conducted along a constraint boundary using multi-objective evolutionary algorithm.

KEYWORDS: shear walls, nonlinear, finite element, LS-DYNA, anchor bolts, precast concrete, shear, joints, design, prestressed flat-slab, optimization, heuristic, multi-objective, genetic algorithm.

ACKNOWLEDGEMENT

I would like to express my sincere gratitude to Professor Ashraf El Damatty for his support throughout my study at The University of Western Ontario. I would also like to thank Professors Ashraf Nassef and Maged Youssef for providing valuable help and insight.

A huge thank-you goes out to Ahmed Soliman, Ph.D. candidate, for his help and technical advice through the experimental part of this project. My test set-up would not have been possible without his valuable input. In addition, I would like to thank Mr. Wilbert Logan, UWO laboratory supervisor, for his enthusiasm and technical support for my experiments. Also, I would like to thank Dr. Mohamed Attia for his assistance in getting me started with the LS-DYNA.

Part of the steel anchors used in this testing program was donated by Williams Form Engineering Corporation, London, Canada. This in-kind support is kindly appreciated. Also financial support from The University of Western Ontario and NSERC is greatly acknowledged.

Last but not least, I would like to thank my family for their support; to my parents, wife, and son Omar.

TABLE OF CONTENTS

LIST OF TABLES

LIST OF FIGURES

CHAPTER 1

Introduction

The work presented in this thesis attempts to develop an economic system to be used for concrete buildings. First, a new innovative system for precast concrete shear walls is introduced. Precast shear walls are mainly used to resist lateral loads. The new system is titled as "Anchor-jointed precast structural wall system". Secondly, in Chapter 5, a robust numerical tool to aid in designing prestressed flat slabs under gravity loads for minimum cost.

1.1 Anchor-jointed precast concrete structural wall system

Shear walls are often used to resist earthquake and wind loads. They also can be utilized to transmit gravity loads. Their inherently high strength and stiffness offer a great advantage in resisting lateral loads. Precast shear walls consist of reinforced concrete panels that are cast in a concrete plant, transported, and erected and connected together onsite. Precast construction is getting more and more popular among construction methods implemented in North America. The system advantage lies in its rapid cost-effective construction and durability due to greater quality control over the material and workmanship of the plant-produced panels. Precast construction is quick, efficient, and economic. Moreover, precast concrete walls can be constructed with an insulation layer to provide better energy efficiency.

The performance of precast concrete shear walls serving as the main lateral force resisting system during the 1988 Armenia earthquake was superior to all other structural systems (Wylie and Filson 1989). For buildings with such a system, only minor cracking at some panels and joints was observed. On the other hand, buildings with other systems suffered severe damages and partial to complete collapses. Generally, precast concrete shear wall behaviour is highly dependent on the response of the base panel-to-foundation joint. Precast structural shear wall systems will be more accepted as a primary lateral-load-resisting system for low-to-medium rise buildings if they are efficiently jointed. Properly connected precast elements will survive a seismic event and would experience less damage compared to cast-in-place construction (Soudki et al. 1995, Schultz and Magana 1996, and Priestley et al. 1999).

In general, precast shear wall can be categorized according to their design philosophy into two main categories: either emulative or nonemulative (jointed) detailing. Emulative detailing involves designing a connection that is intended to respond to lateral displacement in the same manner as cast-in-place monolithic wall. On the other hand, for nonemulative (jointed) detailing, the connection is expected to be weaker than the adjacent precast panels and a gap opening at the panel-to-panel interface is anticipated. Structural behaviour of the two categories is different in stiffness, strength, energy-absorption, and ductility characteristics. The non-emulative joints are included in the ACI-318-08 code, whereas it was not permitted by previous versions.

For the jointed detailing, the panel-to-panel and base panel-to-foundation joints are considered planes of weakness due to their reduced strength and stiffness. Highly localized inelastic deformations occur in the base panel-to-foundation joint region due to rocking and sliding of the joint, and thus, the overall behaviour of the wall is governed by the response at this joint. Different typologies of jointing techniques were studied. In general, tested joints utilized ductile vertical continuity reinforcement (bonded or unbonded). Continuity across the joints was achieved through grouting sleeves, welding or bolting to a steel section, or using prestressing tendons (Soudki et al., 1995 and Schultz and Magana 1996, Holden et al. 2003, Kurama et al. 1999 and Hutchinson 1991). A slotted-bolted friction joint was utilized by Bora et al. (2007) to avoid brittle wall or anchorage failure in thin hollow-core precast panels.

In this study, a new innovative jointing technique is proposed to accelerate construction process and to minimize damage and capital loss in the aftermath of a seismic event. Panels are jointed using steel anchor bolts and nuts. Inspired by the jointing technique, the system is designated "anchor-jointed precast structural wall system". In this regard, steel anchors can be used as a structural fuse. The structural fuse concept introduces a sacrificable structural element that provides adequate structural ductility and strength during an earthquake event. During an earthquake, energy dissipation is provided by yielding of the steel anchor. Cracking and damage in concrete panels is significantly minimized. Damaged anchors could be easily replaced, after an earthquake, minimizing repair costs and serviceability disruptions. In the proposed system, grouting or welding is not required, thus simplifying the construction process and reducing its time. A brief introduction to the system is presented in the following sections.

1.1.1 Geometry and joints details of the prototype system

The overall dimensions of the panel are 6,096×2,438 mm. The cross section consists of a 76-mm thick concrete web; stiffened by four vertical stiffeners (152 × 254 mm). Fifty mm diameter holes are located every 610 mm to accommodate anchor bolts used to connect a panel to the adjoining panels. Typical elevation and cross section of prototype panel and the location of the holes for the anchor bolts are depicted in Figure 1.1. Adjoining panels are connected through horizontal and/or vertical joints as illustrated in Figure 1.2. The suggested configuration could be used to construct simple or coupled shear walls. Walls are considered to be coupled if the vertical joints are designed to transfer the shear flow generated by the coupling action. It should be noted that vertical and horizontal panel-to-panel joints, in addition to base-panel-to-foundation joints, are fairly identical as shown in Figure 1.2. Figure 1.3 illustrates a possible practical erectoin sequence for the proposed joint. Erection process involves placing of the panels in their proper positions within the structure (stabilizing it with temporary bracing), sliding anchor bolts through the prefabricated holes, and then securing with two nuts. The behaviour of the proposed joint can be superior to other joints in the aspect of energy dissipation and damage prevention, as shall be explained in the following sections.

For the proposed joint, the inelastic demand is lumped at the base panel-to-foundation interface through opening of a single crack. The joint may be designed to soften and undergo large nonlinear lateral drift with little damage. The anchors do not transfer considerable tensile stresses into concrete due to lack of bond, and therefore, seismically induced structural damage is concentrated in yielding and damage, in tension, of the anchor bolts. This allows the precast panel to remain elastic. Following a damaging earthquake event, only damaged anchor bolts would need to be replaced. Therefore, anchors may act as structural fuses.

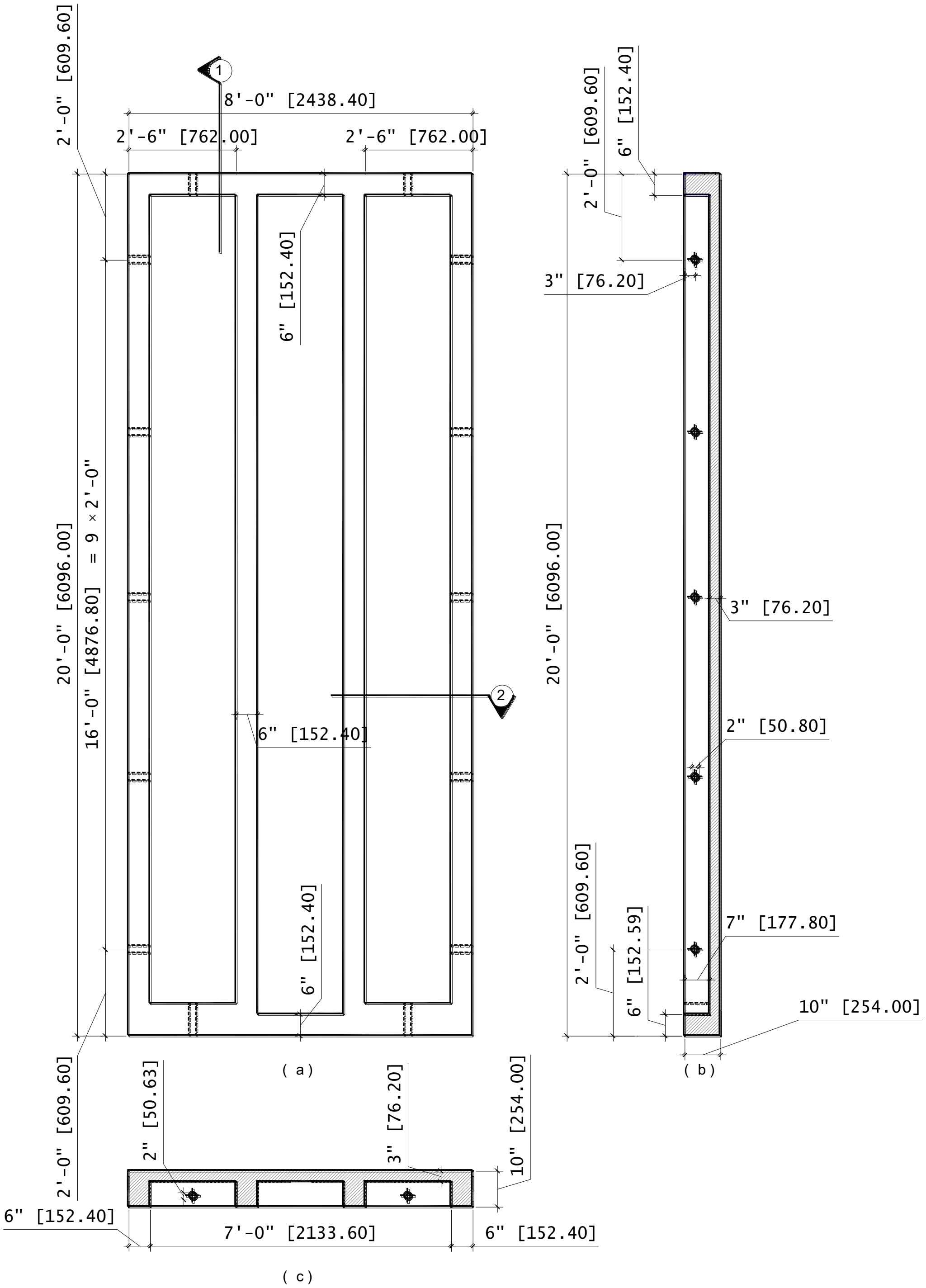

Figure 1.1: Typical concrete dimension of the prototype panel (a) Elevation (b) Section 1 (c) Section 2

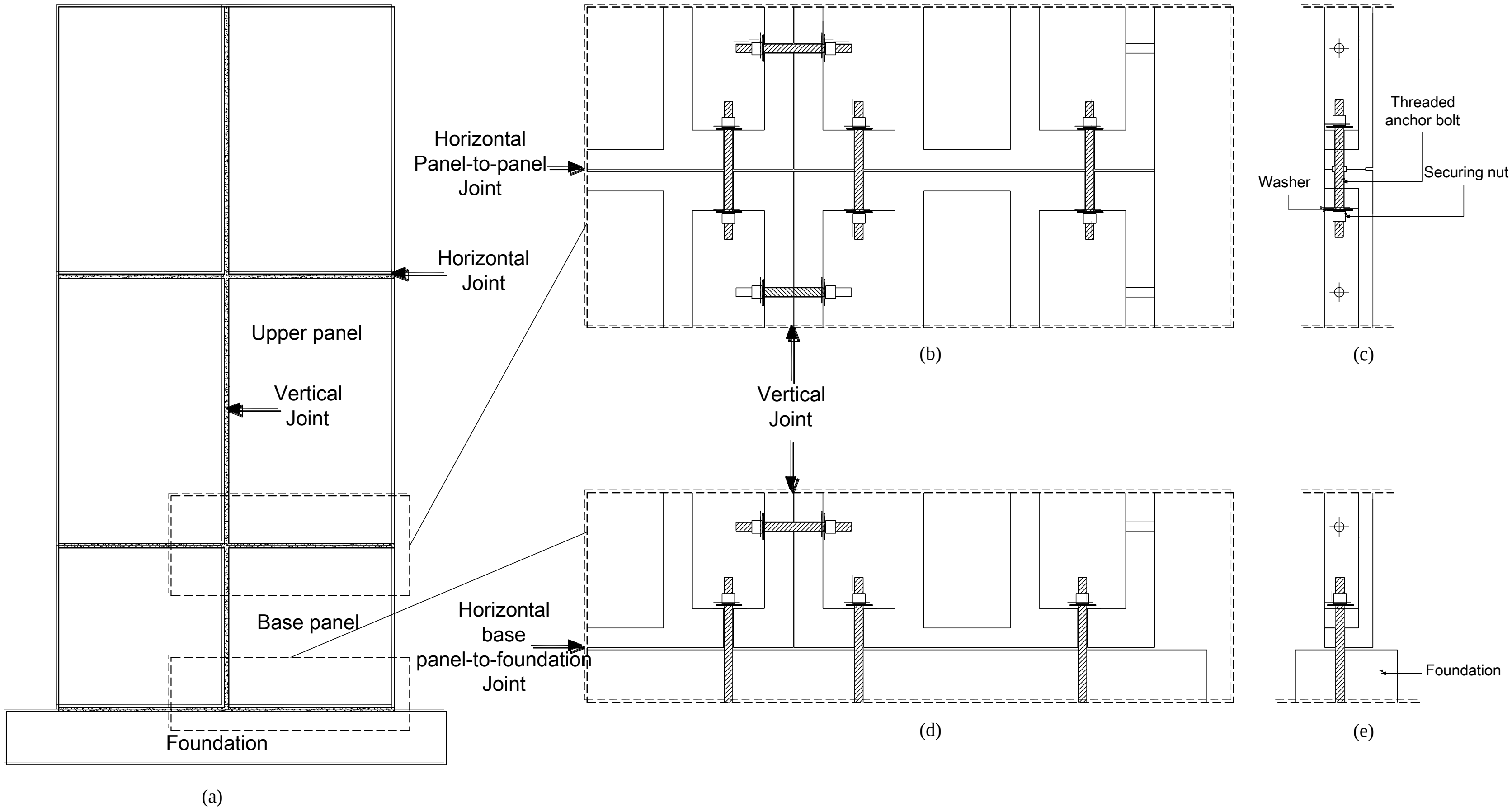

Figure 1.2: Precast shear wall details (a) wall (b)panel-to-panel joint (enlarged) (c) panel-to-panel joint cross-sectional side view (enlarged) (d) base panel-to-foundation joint (enlarged) (e) base panel-to-foundation cross-sectional side view (enlarged)

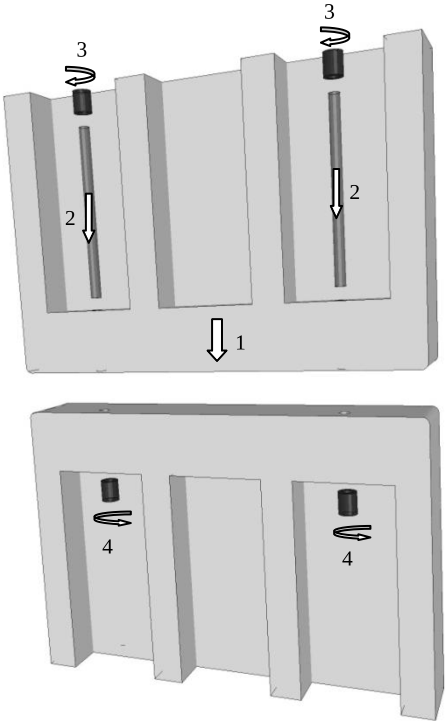

Figure 1.3: anchor-jointed precast structural wall system assembly

1.1.2 Objective and scope

A research program of combined analytical and experimental studies is initiated at the University of Western Ontario to develop, assess, and validate design procedure for the proposed jointing technique. An experimental program is designed focusing on conceptual development and creation of basic information on strength and associated failure modes of the anchor-jointed precast structural wall system for design purposes. Experimental study is followed by an analytical investigation to develop and validate a numerical model capable of simulating the proposed joint response to shear and bending loads.

Both studies are carried out in an effort to allow for code adaption of the anchor-jointed precast structural wall system. Codification process, as required by ITG-5.1-07 (ACI 2008), involves three stages: (1) behaviour characterization through experimental and analytical analyses, (2) developing design/analysis procedures for a generic form of the system, and (3) validation testing of specimens designed according to the developed design procedures. Other nonemulative walls, namely the unbonded post-tensioned precast structural wall system, is already recognized and accepted by the ACI-318-08 code (Refer to clause 21.10.3). The system design requirements are found in ITG-5.2-09 (ACI 2009).

1.2 Optimum design of prestressed slabs

1.2.1 Introduction

In the first part of the thesis, a system for resisting later load has been developed. To augment the design of a building, the prestressed flat slab system is chosen as the main flooring system and its design is optimized. Prestressed concrete flat slab system is widely used for residential and office buildings, hotels, hospitals and parking garages in North America. The system has proven its structural efficiency and economy. The use of post-tensioning allows for material savings due to reduced slab thickness. Post-tensioning also reduces the cracking and deflection of the slab under service loads. The design process of the post-tensioned flat-slab system to resist gravity loads is well defined in international codes. Considering the numerous feasible designs, this study attempts to find the optimum combination of design variables to achieve minimum construction cost.

Modern heuristic search algorithms are powerful tools used in optimization problems in different fields. However, structural design is the selection of design variables subject to behavioural and strength constraints; a process for which heuristic optimization techniques are very much suitable. Heuristic optimization techniques such as Genetic Algorithm and Simulated Annealing were successfully used in design optimization of concrete structures (Coello et al. 1997; Payá et al. 2008; Atabay and Gulay 2009;Martí and González-Vidosa 2010). In spite of the huge capabilities of modern heuristics, they are rarely utilized by practicing engineers. In the current engineering practice, choice of an economical design is based on the designer experience together with a number of rules of thumb. Nevertheless, design optimization is gaining more significance due to potential savings in cost and fierce international competition.

Structural design optimization has gained more popularity with the rapid development in optimization techniques together with the availability of powerful computers. In general, more studies were concerned with optimization of steel rather than concrete structures (Cohn and Dinovitzer 1994). Numerous studies were published addressing the design optimization of concrete structures and concrete structural elements (e.g., Templeman 1983; Choi and Kwak 1990; Coello 1997; Balling and Yao 1997; Kousmousis and Arsenis 1998; Sahab et al. 2005 (a&b); Payá et al. 2008; Atabay and Gulay 2009). Nevertheless, few studies were concerned with the design of prestressed concrete slab. One of the first attempts to consider the optimum design of prestressed concrete slabs was carried out by Rozvani and Hampson (1963). MacRae and Cohn (1987) used nonlinear programming for optimization and conjugate direction method coupled with equivalent load method for analysis. They minimized areas of prestressing and passive steel for a given section and reinforcement arrangement. Kuyucular (1991) considered several predefined cable profiles for a given section to minimize the prestressing cables weight. He carried out structural analysis by coupling finite element and equivalent load method. The method involved a time consuming procedure of calculating several factors for each cable profile, hampering the automation of optimization process. In both studies, optimization was carried out for a given slab thickness. Excluding one of the main design variables would weaken the applicability of the design tool to engineering practice. Lounis and Cohn (1993) considered minimization of two objective functions (Cost and Initial camber) by using one as the objective function and the other as a constraint using the ε-constraint approach. They used Projected Lagrangian algorithm for optimization and sectional stress analysis and force-in-tendon method for analysis. Although all design variables were considered in optimization, their analysis method limits the application of their method to simple structures. The current study attempts to take the optimization of prestressed concrete flat slab a step further by considering all the design variables in the optimization process. This is possible considering the great advancement in the modern optimization heuristics.

1.2.2 Objective

The main objective of this part is to utilize the huge capabilities of modern heuristic search algorithms for structural design optimization of pre-stressed concrete slabs in order to develop a general, flexible, and relatively easy to use tool for practicing engineers. A robust numerical tool integrating design, analysis, and optimization techniques is developed for this purpose. The tool utilizes the Finite Element method for the structural analysis of the system. Optimum values for the slab thickness, number and size of tendons, and tendon profile are sought subject to design constraints imposed by the relevant code of practice. The objective function incorporates the cost of both concrete and prestressing tendons.

1.3 Thesis layout

In Chapter 2, the conceptual development of the anchor-jointed structural wall system is carried out. An experimental program is carried out to evaluate the performance of the new jointing technique. The details of the testing program and results are demonstrated. The tests results are used to characterize the behaviour of the system; primarily determining lateral strength and possible associated modes of failure.

In Chapter 3, a non-linear finite element numerical model is developed to capture the effects of the new joining technique on precast concrete shear walls behaviour and possible associated failure modes. Through a model development process, material properties, material model parameters, element size, mesh layout, and contact definitions are examined and fine-tuned to accurately capture the behaviour. Structural response and associated failure modes of the system to bending and shearing loads are studied thoroughly, including breakout of concrete cone, rupture of steel anchor, dowel action and shear friction. Sub-assemblies and similar tested joints available in the literature are modeled. Correlative studies between analytical model and experimental data are presented.

In Chapter 4, information and insight gained from conducted simulations are utilized to develop a reliable model for the anchor-jointed precast structural wall system. The model is then verified against the tests presented in Chapter 3. The developed model is extended beyond the test data to study the effect of selected parameters on the structural response of the tested specimens. These parameters are: (1) gravity loads, (2) anchor length, and (3) anchor pretension force.

In Chapter 5, a numerical tool capable of finding the optimum design of a prestressed concrete flat slab system using modern heuristic search algorithms is developed. The introduced tool employs finite element analysis for structural analysis with prestressing modelled explicitly using tendon elements. As a demonstration problem, the optimum design of a square prestressed flat slab supported on four columns at the corners and spanning 5.0 m is investigated. The Canadian code CSA A23.3 is chosen as the design code. Direct search methods, heuristic optimization techniques such as Genetic Algorithms, and multi-objective optimization techniques are considered. Results of different optimization procedures are presented and discussed. Recommendation for effective optimization technique is given.

CHAPTER 2

Lateral Resistance of Anchor-Jointed Precast Structural Wall System: Conceptual Development and Experimental Investigation

2.1 Introduction

A new innovative jointing technique is proposed to connect precast concrete panels forming a structural shear wall. The basic concept of the system and main practical consideration is developed herein. In this system, panels are connected using steel anchor bolts. That can be utilised as structural fuses. The structural fuse concept introduces a sacrificable structural element that provides adequate structural ductility and strength during an earthquake event. This element, during an earthquake, will be damaged (sacrificed) while preserving all other structural elements. However, the integrity of the gravity load path is maintained. Only the structural fuse is replaced in the aftermath of an event and thus minimizing capital loss and service disruption. Another advantage of the newly proposed system is that it is easier to construct. Connection is established just by tightening the nuts. Grouting or welding is not needed.

Structural shear walls are massive. Due to their inherently high lateral strength, high levels of lateral forces are needed to perform testing. A full size test may be infeasible with respect to cost considering the amount and size of equipment necessary for testing. A total of four reduced scale specimens are tested under the effect of a monotonically increasing horizontal displacement applied at the top. The monotonic response is construed as a practical tool for evaluation of the seismic response as it approximates the experimental resistance envelope under cyclic or dynamic action. Each specimen has been studied thoroughly before conducting the next test. Utilizing information and insight gained from each test, modifications were suggested and implemented in the next test to further improve the structural behaviour.

Details of the conducted experimental program are presented. First a description of the test specimens and material properties are given, followed by a description of the test set-up and procedure. Then, experimental observations and discussion of each test are presented. After that, the overall behaviour including failure modes, gap/contact behaviour, force transfer mechanism, and the effect of studied parameters are discussed. Finally, the basis of developing analytical procedures for system response prediction is explained.

2.2 Test specimen

Test specimens are sized to simulate the behaviour of a horizontal connection near the base of a typical pre-cast shear wall where the behaviour under bending moments governs. Bearing in mind the limitation imposed by the testing facility and the complexities associated with the joint behaviour needed to be captured by the test specimen, a scale of 1:2.5 is chosen. The size of the reduced scale specimens is the maximum size that could be tested in the testing facility. However, cross-sectional dimensions are slightly modified due to practical consideration regarding minimum reinforcement spacing and cover and minimum feasible thickness. These slight modifications are deemed insignificant as the joint behaviour is mainly dependent on the joint details rather than the panel cross-section. Each specimen consists of two parts; a precast concrete wall panel and a base block. The two parts are joined by a horizontal joint, as depicted in Figure 2.1.

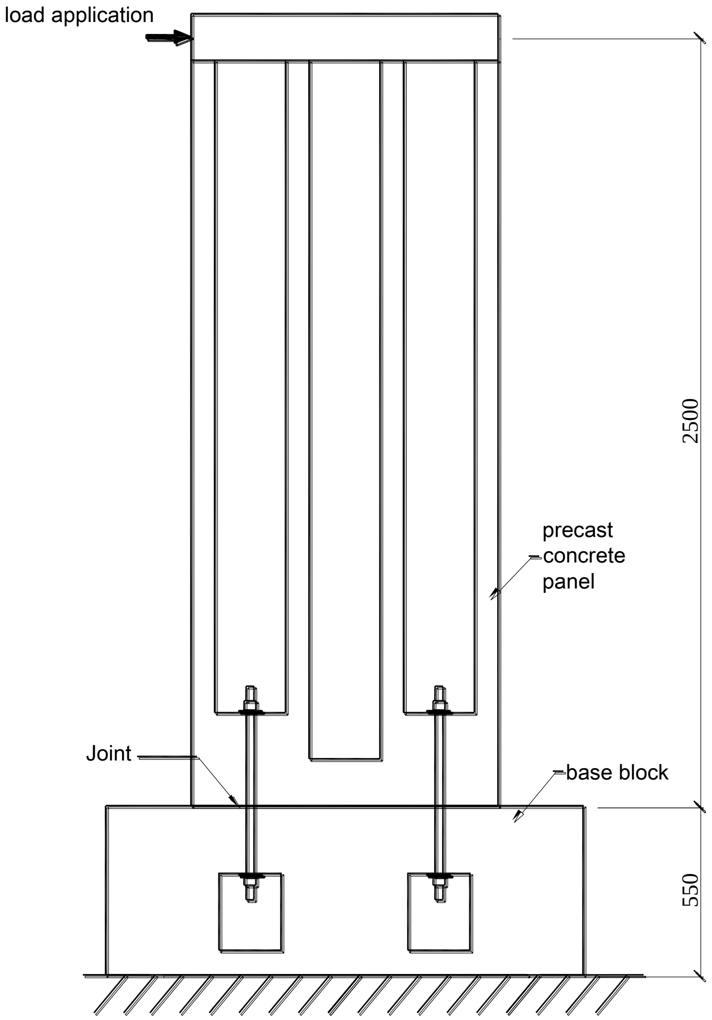

Figure 2.1: Specimen configuration

2.2.1 Precast concrete panel

The test panels are proportioned to reflect the characteristics of the prototype panel described in Figure 1.1. The test panels are dimensioned assuming the same material properties and the same shear-span-to-wall-length ratio of 2.5. A distributed reinforcement layout similar to the prototype panel is used preserving the reinforcement ratio, $\rho = A_s/A_c$, where A_s is the reinforcement area and A_c is the cross-sectional area of the concrete section.

To correlate the test results to the expected prototype behaviour, similitude or scaling laws are applied (ACI Committee 444, 1979). Using the Buckingham's Pi theorem (Murphy, 1960), two independent dimensionless ratios representing the behaviour are set to be equal in both the reduced scale test and the full scale. Scaling of the base shear is determined by forming the dimensionless ration P/EL^2, where P is the load, E is the modulus of elasticity and L is the length.

$$\left[\frac{P}{EL^2}\right]_{\text{reduced scale}} = \left[\frac{P}{EL^2}\right]_{\text{full scale}}$$

$$\text{same material properties assumed i.e. } \frac{E_{\text{full scale}}}{E_{\text{reduced scale}}} = 1 \qquad (2.1)$$

$$\frac{P_{\text{full scale}}}{P_{\text{reduced scale}}} = \frac{L_{\text{full scale}}}{L_{\text{reduced scale}}} = 2.5^2 = 6.25$$

On the other hand, the displacement is presented as the ratio of the wall lateral displacement to the wall height. As such the full scale (i.e. if the prototype panel is tested) is expected to achieve the same drift angle.

The overall dimensions of the test panel are 2,575×990 mm, corresponding to a height-to-length ratio (h_w/ℓ_w) of 2.6, while the shear-span-to-wall-length ratio is 2.5 as mentioned earlier. This relatively high ratio ensures that the behaviour is governed by flexural (e.g. gap opening) rather than shear (e.g. sliding). The cross section consists of a 70-mm thick concrete web stiffened by vertical stiffeners. Vertical stiffeners are 75-mm wide × 70-mm thick. Two holes, 610-mm apart, located midway between two vertical stiffeners to accommodate anchor bolts are used to connect a panel to the base block. Resistance to breakout failure is provided by anchor blocks at panel corners. The generic dimensions and reinforcement details of the precast concrete panel are depicted in Figure 2.2 and 2.3. All reinforcement has nominal yield strength of 400 MPa. Upper loading beam dimensions are chosen as 280×150 mm to facilitate loading.

Joints tested in the current program are sized up so that different failure modes could be investigated. A total of four joints are tested. Variations of the anchor block size and reinforcement details, in addition to steel anchor type are studied. An overview of the tested panels is given in Table 2.1.

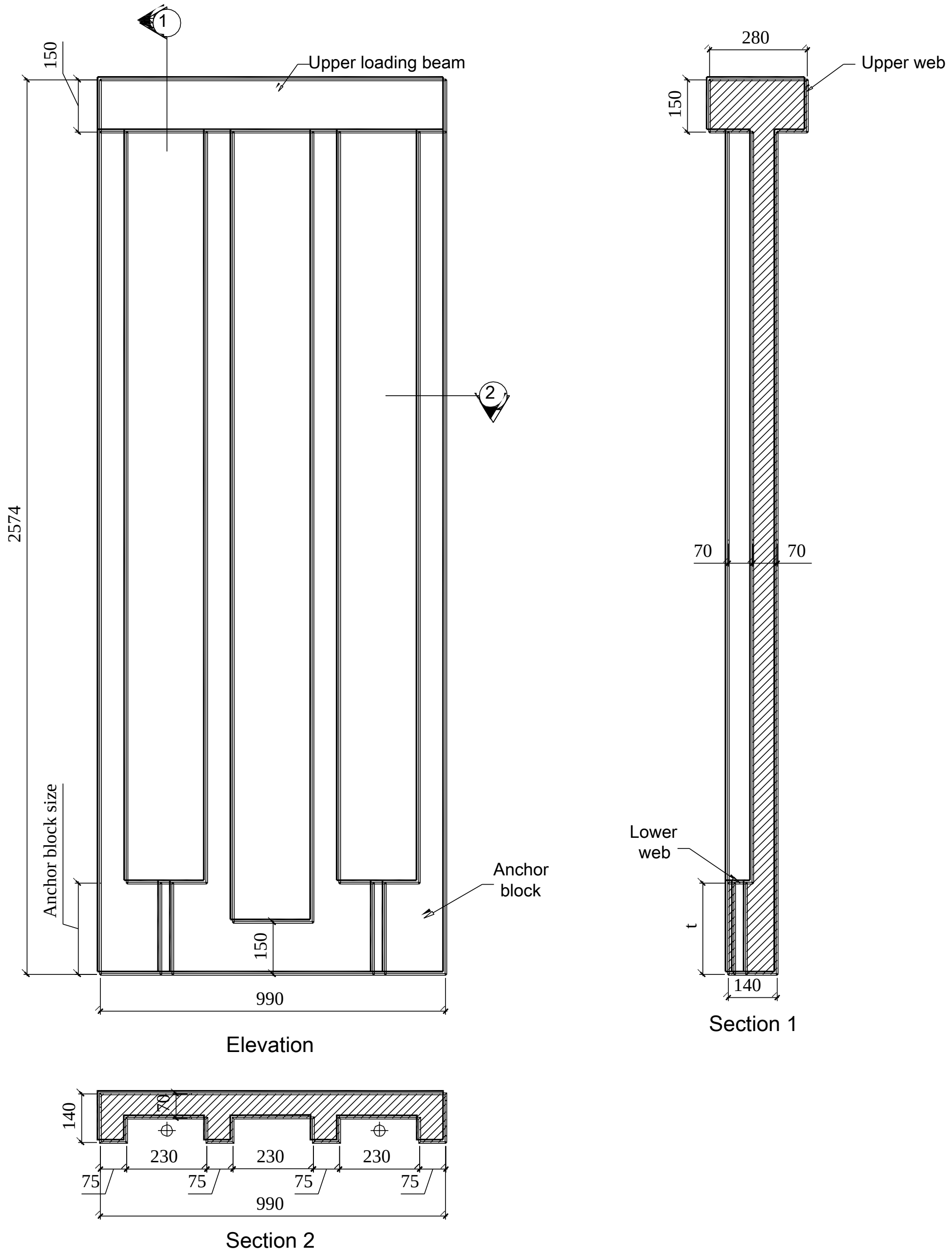

Figure 2.2: Generic dimensions of the precast concrete panel

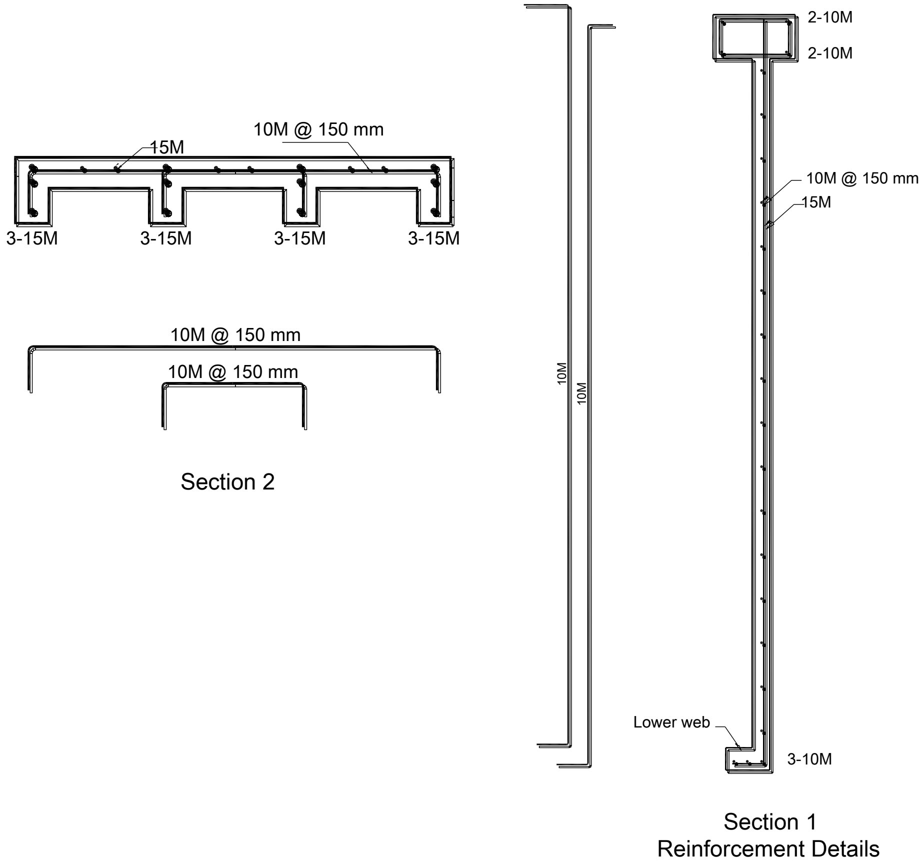

Figure 2.3: Reinforcement details of the precast concrete panels

Table 2.1: Overview of the experimental results

Test	anchor block size [mm]	steel anchor type	Anchor area [mm^2]	ultimate strength [MPa]
Test 1	150	Grade 75	510	742.4
Test 2	330	Threaded anchor – Type I	391	367.6
Test 3	550	Threaded anchor – Type I	391	367.6
Test 4	605	Threaded anchor – Type II	391	805.2

2.2.2 Concrete base block

Concrete base block is sized and detailed to sustain maximum anticipated internal forces due to testing (see Appendix VI). The overall dimensions of the base block are 480×550×1540 mm. Two 200×200 mm voids are embedded to facilitate tightening of the steel anchors nuts during specimen erection. A horizontal groove along the top surface is used to pass and protect the wires of the strain gauges attached to the steel anchors. Details of the base block are depicted in Figure 2.4.

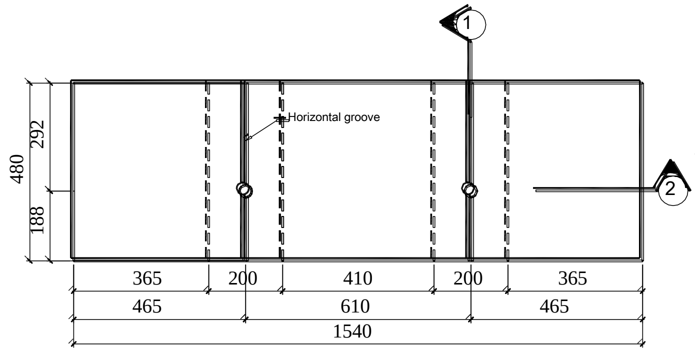

plan

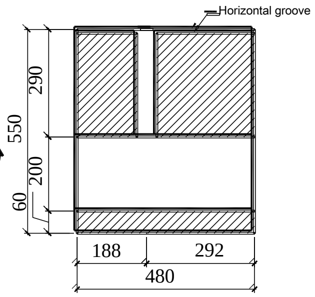

Section 1 - Concrete Dimensions

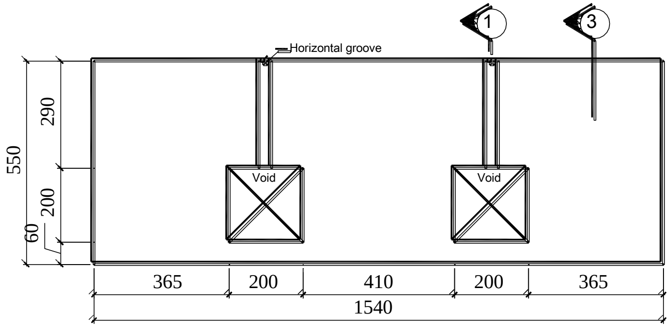

Section 2 - Concrete Dimensions

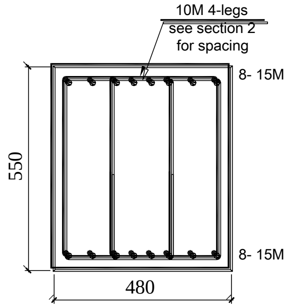

Section 3 - Reinforcement Details

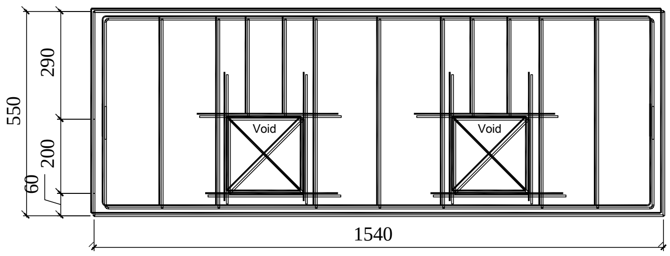

Section 2 - Stirrups Reinforcement Details
10M - 4 legs

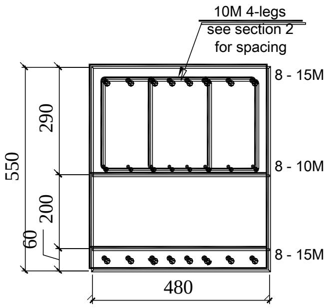

Section 1 - Reinforcement Details

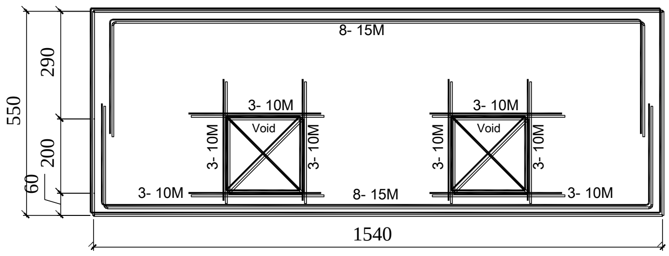

Section 2 - Reinforcement Details

Figure 2.4: Details of base block

2.3 Material properties

2.3.1 Concrete

The concrete for the precast panel and base block is supplied by a ready-mix concrete company. Self-compacting concrete (SCC) with maximum aggregate size of 10 mm is used to facilitate concrete placing. Concrete mix design properties are listed in Table 2.2. The water/binding-material ratio of the mix is 0.354. The workability is measured using slump flow test (ASTM C1611). SCC flow reaches 500 mm diameter in 1.98 seconds and the slump flow is 640 mm. Visual inspection of the concrete indicates that concrete segregation resistance is acceptable. Standard cylinders (4" in diameter and 8" in height) are cast. Six cylinders are moist cured and tested for the 28-day compressive (ASTM C39) and splitting (ASTM C496) strength. The 28-day compressive strength is 70.8 MPa, while splitting strength is 6.0 MPa. The other cylinders are kept alongside the panels where their curing conditions are kept as close as possible to those of the panels. For these cylinders the compressive strength is slightly higher, 71.5 MPa. Detailed cylinder tests results are presented in Appendix III.

Table 2.2: Concrete mix design properties

	Dry weight [kg/m^3]
Cement	375
Slag	125
Stone	890
Sand	910
water	177

Admixtures

	mL/m^3
High range water reducer	2125
Normal range retarding water reducers	1000
Viscosity modifier	500

2.3.2 Steel anchors

Three types of anchors are utilized. One sample of each type is tested under direct tensile load. The obtained stress-strain curve is depicted in Figure 2.5. Relevant properties are summarized in Table 2.3.

Table 2.3: Steel anchor properties

Type	Thread Root Diameter [mm]	Net area [mm^2]	Elastic Modulus [GPa]	Ultimate Stress [MPa]	Ultimate Strain	Proof/yield Stress [MPa]
Grade 75 All-thread rebar	25.48	510	160.9	742.4	0.0696	492.0
1" Threaded Bar – Type I	21.48	391	166.6	367.6	0.0922	308.0
1" Threaded Bar – Type II	21.48	391	173.2	805.2	0.0450	650.0

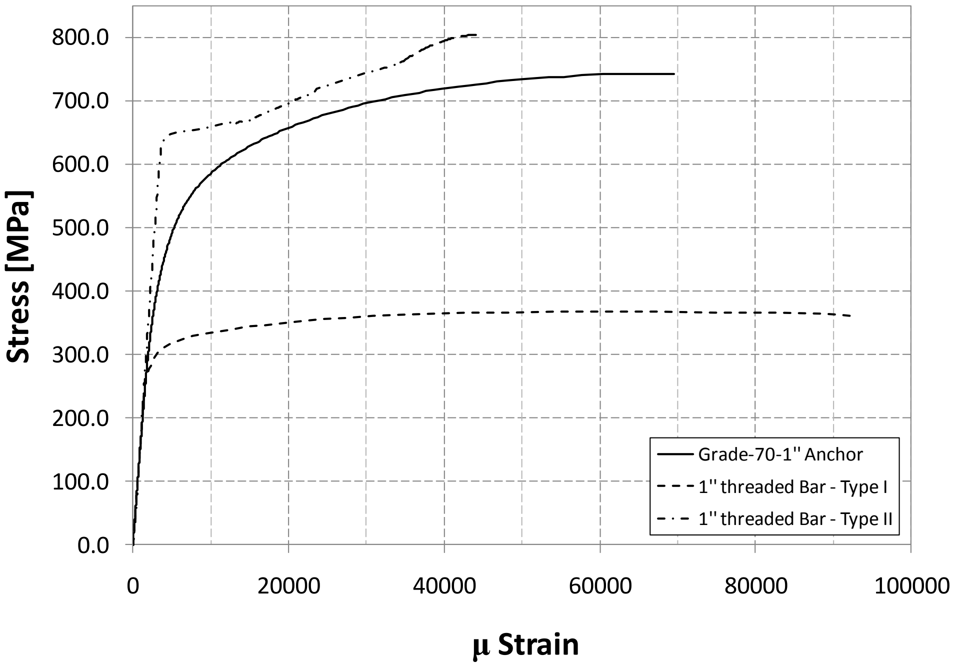

Figure 2.5: Stress-strain curve for tested anchor bolts

2.4 Test set-up

2.4.1 Loading and support system

The base block is fixed to the strong laboratory floor using four strong anchor bolts and four steel beams as shown in Figures 2.6 through 2.8. Anchors are slid through their designated holes, protruding out of the concrete base block. Using the laboratory overhead crane, the precast panel is lowered down to its proper position, and then the anchors are secured by nuts. The precast concrete panel is supported laterally to ensure out-of-plane stability using a bracing rod. A pin connection located at the end of the bracing is oriented to allow the wall to move freely in the in-plane direction. As such, the bracing system has no contribution to the in-plane lateral resistance of the joint. The loading system consists of a 250-kN loading actuator and a reaction frame. Load is applied at 2.50 m above the joint level, resulting in a base moment to shear ratio of $M_b/V_b=2.52\ell_w$, where ℓ_w is the panel width. Prior to loading, the steel anchors are tightened up and the corresponding strains are recorded. Following that, a small horizontal load is applied to the specimen and all the LVDTs are zeroed then the load is applied at a rate of ~1.5 mm/min.

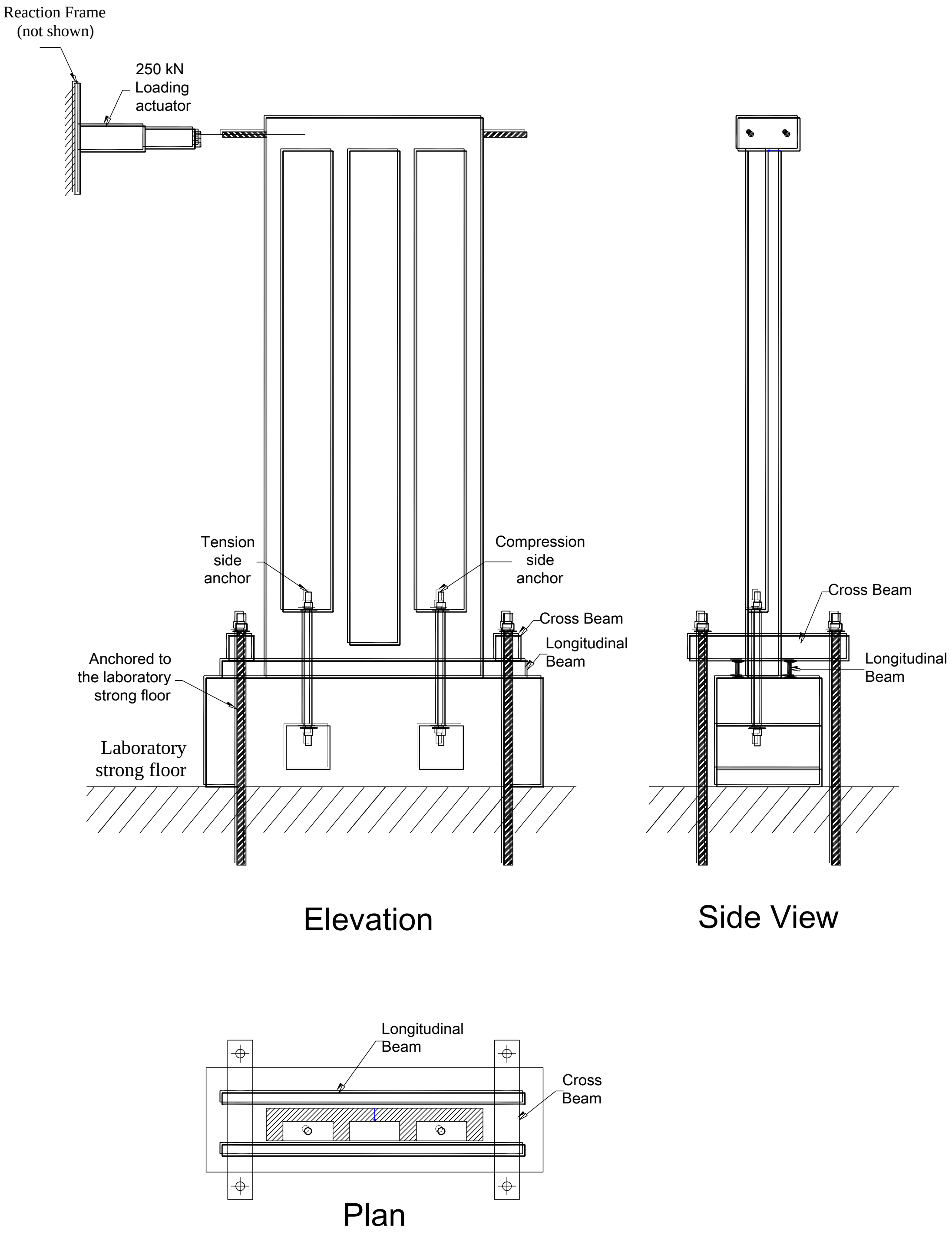

Figure 2.6: Schematic of test set-up

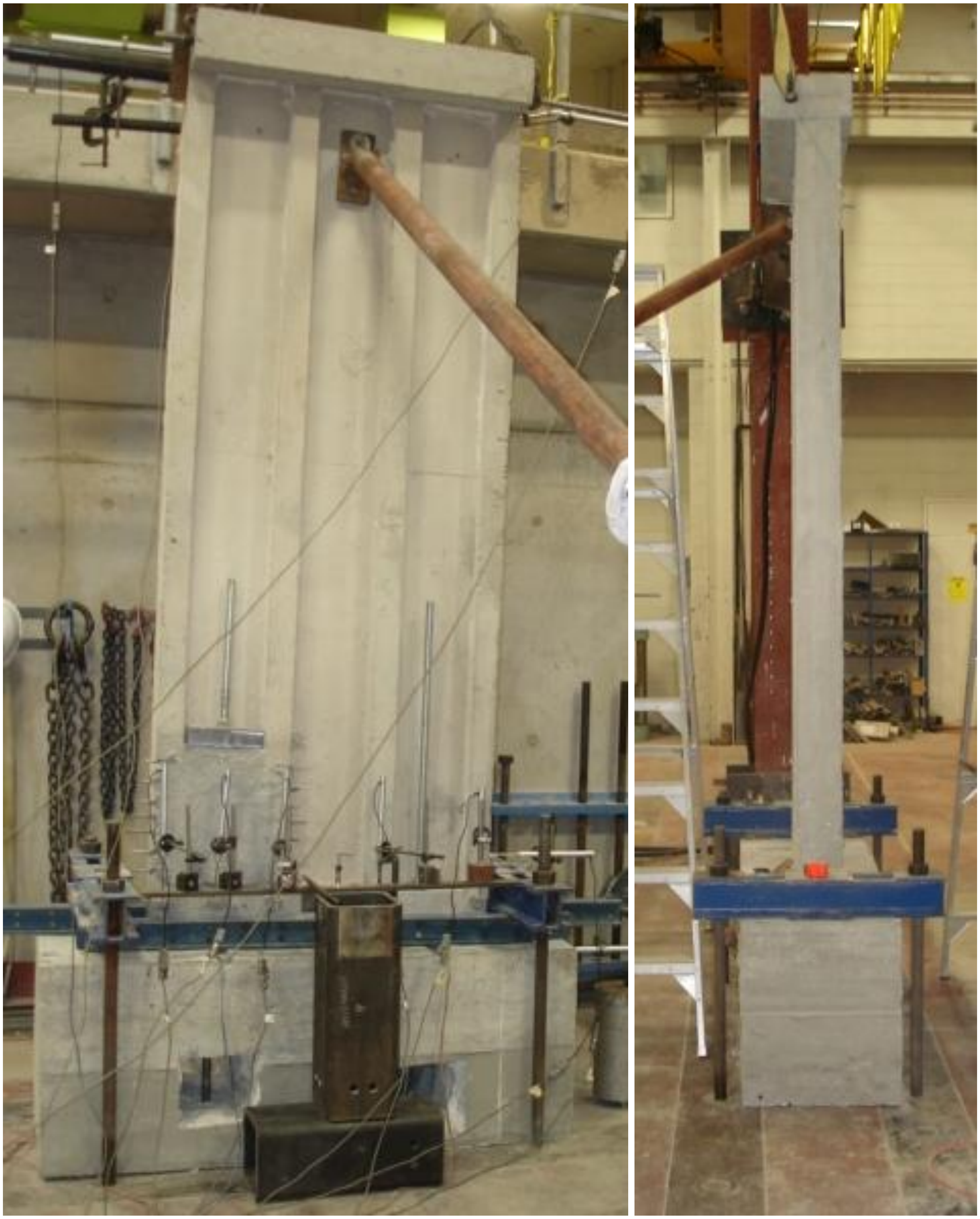

(a) (b)

Figure 2.7: Test set-up

Figure 2.8: Test set-up (concrete base block)

2.4.2 Instrumentation

A computer-controlled data acquisition system is used to record all electronic test data from LVDTs, strain gauges, and actuator load.

2.4.2.1 Linear Variable Differential Transducers (LVDT's)

Eleven Linear Variable Differential Transducers (LVDTs) are used to record in-plane displacement of the wall panel and the concrete base block, gap/contact behaviour and sliding at the joint interface. Layout of the used LVDTs is shown in Figure 2.9. Two LVDTs are mounted horizontally on the top of the specimen to monitor the horizontal deformation. Five LVDTs are aligned vertically at the joint to monitor the joint deformation and the gap/contact behavior. Another two LVDT's are positioned in vertical alignment at the top of the specimen to monitor the panel displacements. The last two are installed horizontally just above and below the joint to record the joint sliding.

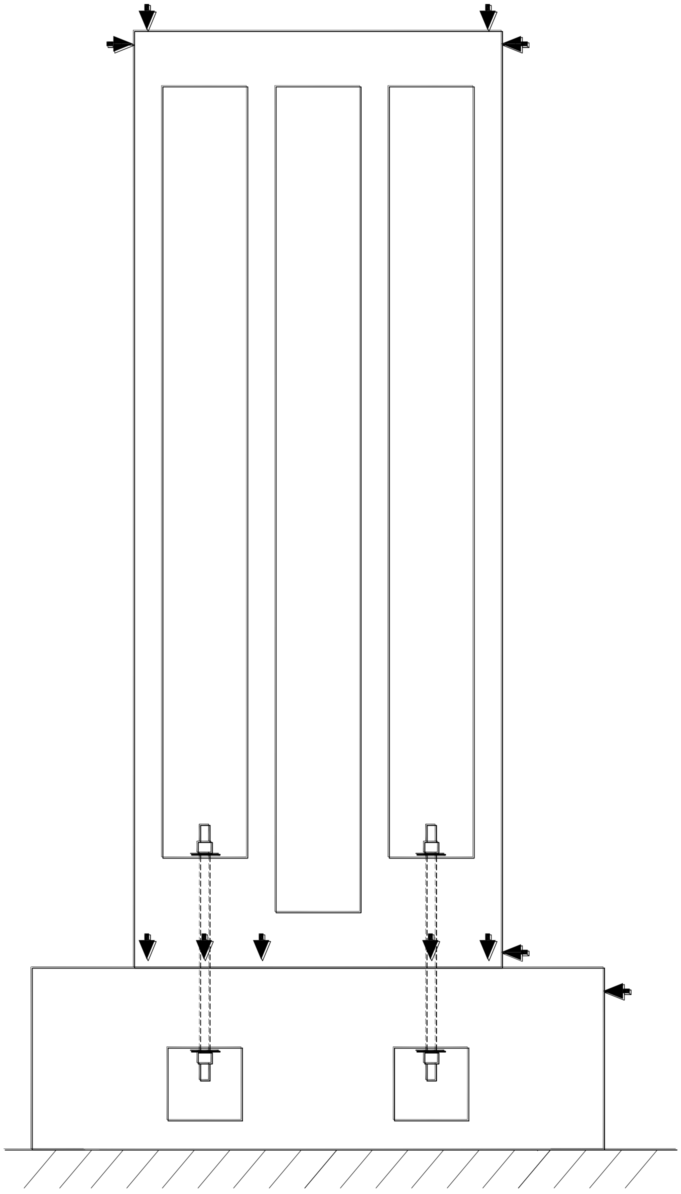

➡ LVDT location

Figure 2.9: Layout and designations for LVDT's

2.4.2.2 Strain Gauges

Four electrical strain gauges, with ¼–inch gauge lengths, are applied to each anchor bolt to monitor the anchor strain during testing (see Figure 2.10). The strain measurements are correlated to the anchor forces using the stress-strain relationship obtained from the sample testing. Strain gauges readings of the anchor bars are recorded during tightening of anchors prior to testing and during testing. The strain gauges are installed on opposite surfaces to eliminate any bending effects that may occur. Four strain gauges are used to reduce the possibility of measurement errors by averaging the four readings. To provide appropriate contact area between the bar and the strain, a minimal surface of the threads is smoothed and sanded to a buffed finish with varying grits of emery sanding paper and cleaned with a solvent to remove any contaminants.

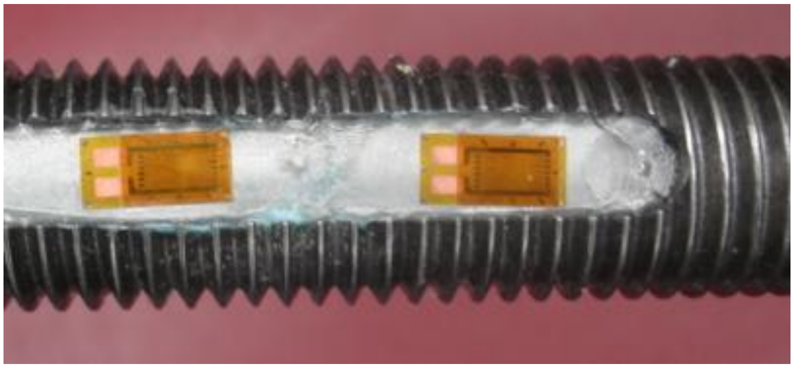

Figure 2.10: Strain gauge

2.5 Experimental Results and discussion

Results of the experimental program are presented in the following section. The wall drift is defined as the ratio of the wall lateral displacement to the shear span length, defined as the distance from the joint level to the load application level (2.5 m). The lateral displacement is obtained after correcting the displacement readings to account for rigid body displacements, i.e. slip. The lateral displacement is taken as the average of the readings of the top horizontal LVDT's minus the displacement at the base of the wall (see Figure 2.11). For the gap/contact behaviour, the last contact point is considered as an equivalent neutral axis, which is the location where vertical displacements of LVDTs mounted along the joint change sign. The bar forces are obtained from the recorded axial strains (refer to Figure 2.5).

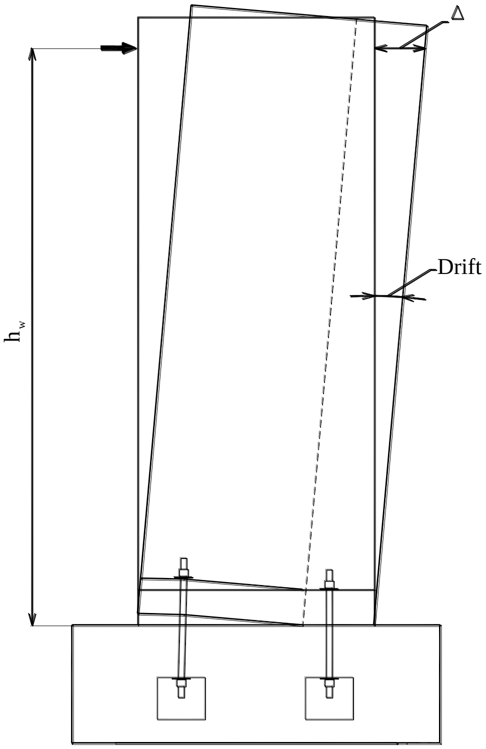

Figure 2.11: Definition of wall drift

2.5.1 Test 1

Prior to testing, forces of 61.3 and 66.8 kN are recorded at the end of tightening process for the tension and compression side anchors, respectively. At the beginning of the horizontal displacement application, these forces are reduced to 57.2 and 58.9 kN due to elastic shortening of the surrounding concrete.

Figure 2.12 describes the base shear-drift response. As load is applied, bending moment accumulates at the joint level causing the force in the tension side anchor to increase and the force in the compression side anchor to be released as shown in Figure 2.13. At a drift of ~0.09 %, corresponding to 14.2 kN of base shear, the lateral stiffness is reduced from ~6.00 kN/m to

~0.80 kN/m, implying gap initiation as the applied load overcomes the initial compressive stresses resulting from anchor tightening. Due to gap formation, the contact length decreases and consequently the developed compressive bearing stresses is expected to increase.

The first visible crack is observed at drift of ~0.43 %, which corresponds to 20.6 kN of base shear; this crack is located in the anchor block immediate to the anchor bolt on the front face of the specimen and is inclined at ~43 degrees (see Figure 2.14). The sound of the concrete cracking is clearly heard. This first crack is accompanied by further reduction of the tangent stiffness to ~0.35 kN/m. As a result, the increasing rate of the tensile force in the tension side anchor and the reduction rate in the compression force in the compression side anchor is decreased approximately by 51% and 70%, respectively (see Figure 2.13).

At a drift of ~0.85%, a maximum load of 24.5 kN is attained leading to the formation of a breakout cone-like failure surface around the tension anchor as depicted in Figure 2.15. As the test progresses (draft > 0.85 %), no further increase in the load carrying capacity is observed, however, extensive damage in the concrete around the tensile anchor occurs, as shown in Figure 2.16. As a result, the axial load in the tension side anchor is considerably reduced. At maximum load, the gap opening measured at the outermost stiffener on the tension side is ~3.71 mm. At this stage, the joint behaviour is clearly governed by the concrete breakout at the tension side anchor.

Cracking at the back face of the tension side and minor spalling of the concrete cover at the compression side of the joint are observed as seen in Figures 2.17 and 2.18. Figure 2.19 shows the tension side of the panel after removing damaged concrete. There are virtually no other parts of the panel that are cracked or damaged.

Recognizing the inherent weakness of the original panel to breakout failure, which prevents the system from resisting higher levels of lateral loads, modification to the panel geometry and reinforcement detailing to provide an alternative load path is proposed and tested as illustrated in the next section.

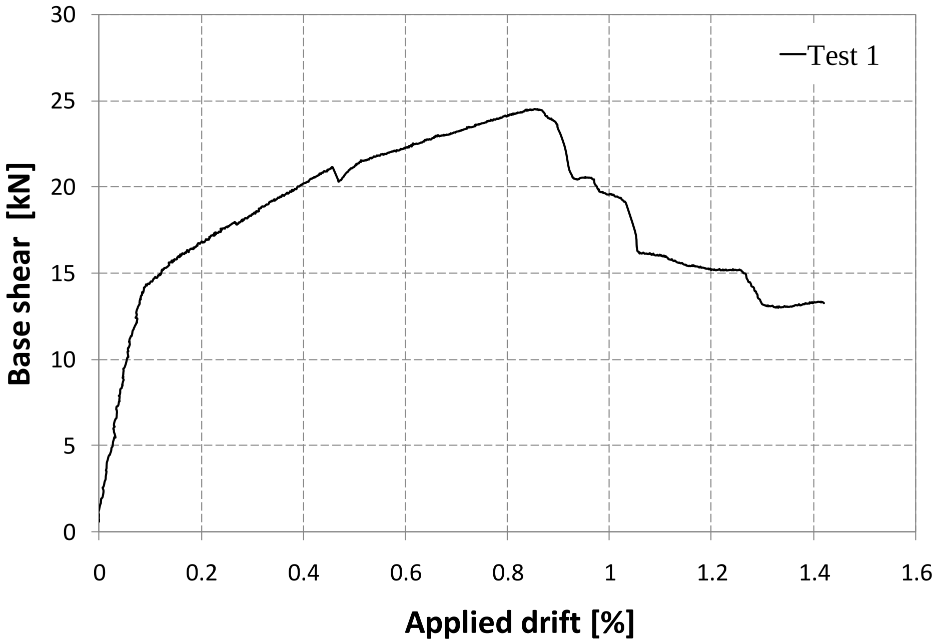

Figure 2.12: Base shear-drift response of Test 1

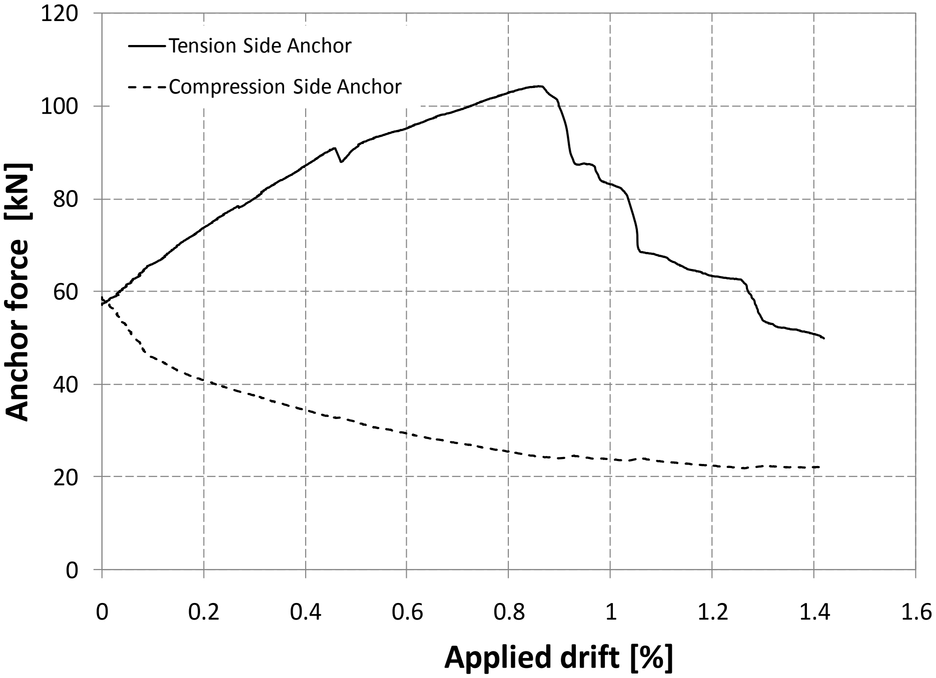

Figure 2.13: Anchor load variation during Test 1

Figure 2.14: First visible crack

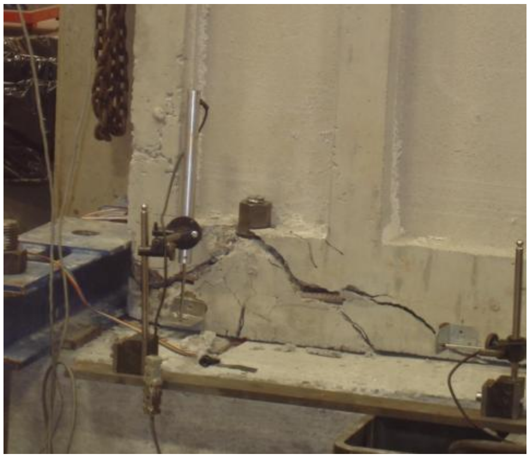

Figure 2.15: Damage at maximum load

Figure 2.16: Extensive damage in the concrete surrounding the tension anchor (post-peak)

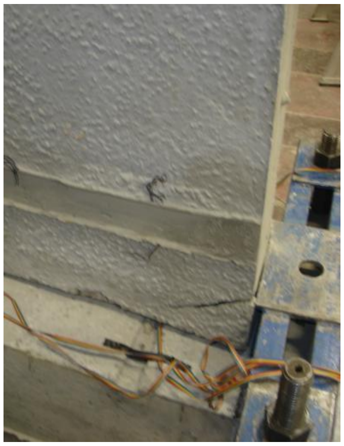

Figure 2.17: Crack developed at the back face on the tension side of the joint

Figure 2.18: Minor cover spalling at the compression side of the joint

Figure 2.19: Tension anchor side of the joint at the end of the test: front face (left) back face (right)

2.5.2 Test 2

2.5.2.1 Strengthening

The concrete panel is strengthened to avoid breakout failure observed in Test1 by providing an alternative load path. In this modification, the anchor force is intended to be resisted by panel reinforcement rather than concrete only. Eight 3/8" threaded bars are arranged to transfer the anchor load to the adjacent vertical stiffeners and the 70-mm thick concrete web as depicted in Figure 2.20 and 2.22 (a). The threaded bars are designed to transfer the entire anchor load through shearing across two planes along the interface between old and new concrete. All other possible existing transfer mechanisms are ignored for design simplicity. Figure 2.21 illustrates the proposed new load path through existing reinforcement in the concrete panel. New concrete is poured to increase the anchor block size to 330 mm to fit the added threaded rebars with reasonable spacing (~40 mm). The strength of the added concrete is approximately equal to the original concrete strength. In addition, a 2"-thick steel plate is added to ensure that anchor load is distributed over the largest possible area. Since this test applies only a monotonic load, these modifications are only applied to the tension side anchor block as shown in Figure 2.22.

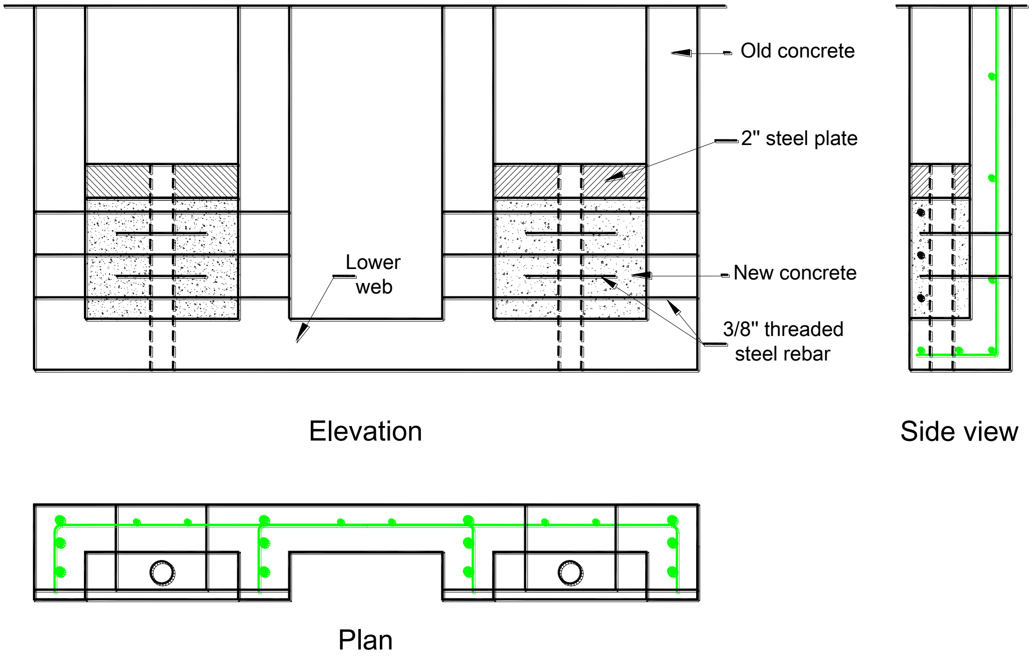

Figure 2.20: strengthening of concrete panel against concrete breakout

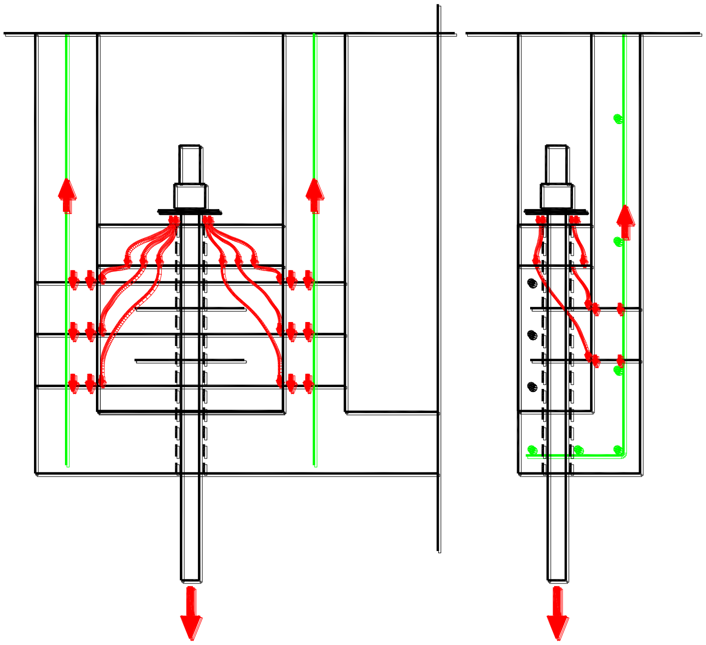

Figure 2.21: force transfer to the web and stiffeners reinforcement

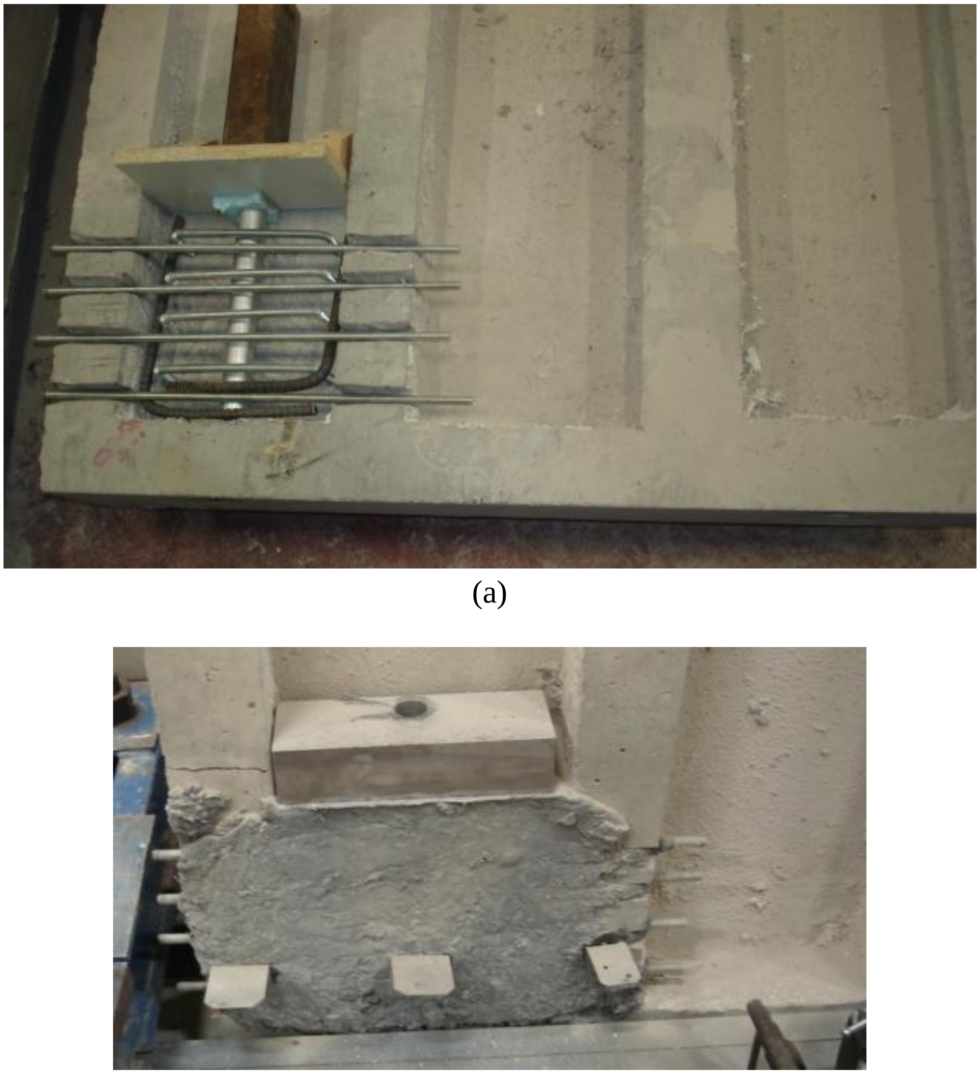

(a)

(b)

Figure 2.22: Strengthening of the tension side anchor block (a) Reinforcement (b) after casting

2.5.2.2 Test

At the beginning of the test, the forces in the tension and compression anchors are 34.8 and 30.0 kN, respectively. As load is applied, gap opening is initiated at a drift of ~0.07 %, corresponding to 9.0 kN of base shear. As a result, the initial joint lateral stiffness is reduced from ~4.05 kN/m to ~3.02 kN/m. as illustrated in Figure 2.23. Gap opening is confirmed by the increase in the

LVDT reading monitoring joint deformations. Similar to Test 1, the gap formation results in a shorter contact length, as seen in Figure 2.26, and consequently higher compressive bearing stresses. Figure 2.25 shows snap shots of the sectional deformation at different applied drifts.

As horizontal displacement is applied, the anchor forces are increased. The tension steel anchor reaches its proof stress, 308.0 MPa, at a drift of ~0.62 %, corresponding to 42.8 kN of base shear as depicted in Figure 2.24. Beyond this point, the base shear is increased until reaching a plateau at a load of 50.8 kN.

Initially, horizontal cracks are formed in the outermost vertical stiffeners on the tension side immediately above the anchor block. As load increases, new cracks are formed and spread upward in the stiffener, and its opposite back face. Thereafter, cracks are formed in the second and third stiffeners as shown in Figure 2.27. Cracks also initiate at the bottom of the mentioned stiffeners and spread upward. Vertical stiffeners cracks are more or less evenly spaced. Moreover, no cracks or any signs of distress are observed within the anchor block area. These observations confirm that the majority of the anchor load is transferred through the proposed load path.

At this stage, the joint behaviour is clearly governed by the anchor elongation rather than concrete breakout as in Test 1 (see Section 2.5.1). Moreover, using the proposed reinforcement scheme and a longer anchor block shifted the failure mode to yielding and rupture of steel anchors. As the test progresses, the steel anchor continues to yield and the load dropped gradually until failure is attained by rupture of the tension anchor at drift of ~3.27 %. At this drift, the gap opening measured at the outermost stiffener on the tension side is ~30.0 mm (see Figure 2.25). Other than the cracks in the vertical stiffeners, the precast panel remains intact. The panel exhibits minor cracking and spalling of the concrete at the compression side of the joint as seen in Figure 2.28. All damage and yielding is concentrated in the steel anchor with minimum damage to the panel, steel anchors can work as a structural fuse.

An unexpected deformation of the base block is observed, accompanied by a formation of a diagonal crack originating from the corner of the 200×200 mm void on the tension side of the base block. This deformation will cause an error in the horizontal LVDT's readings due to rigid body rotation of the base. Support conditions of the base are enhanced with additional supporting members to avoid this source of error in the remaining tests.

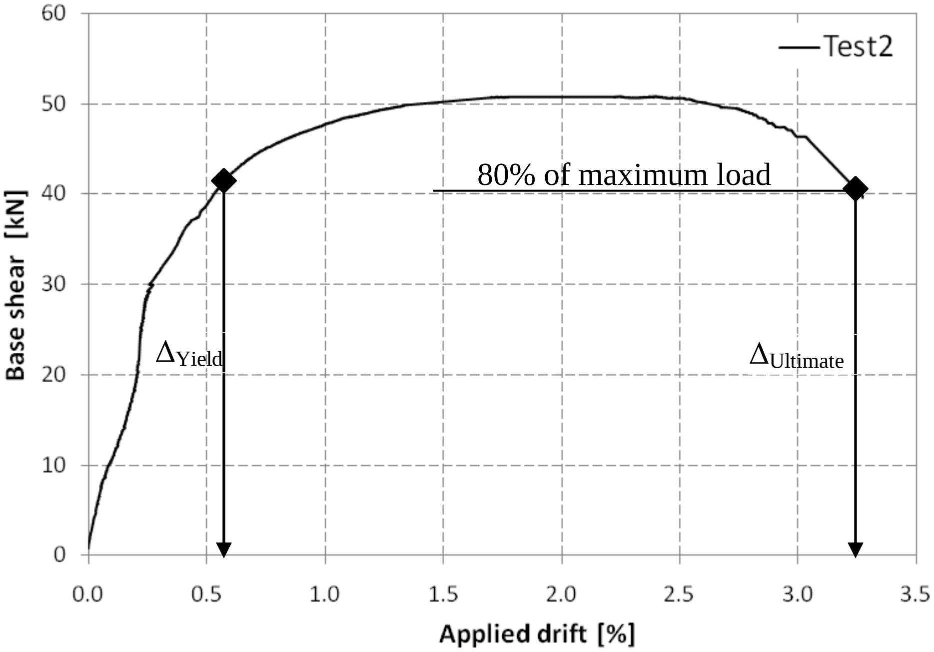

Figure 2.23: Base shear-drift response of Test 2

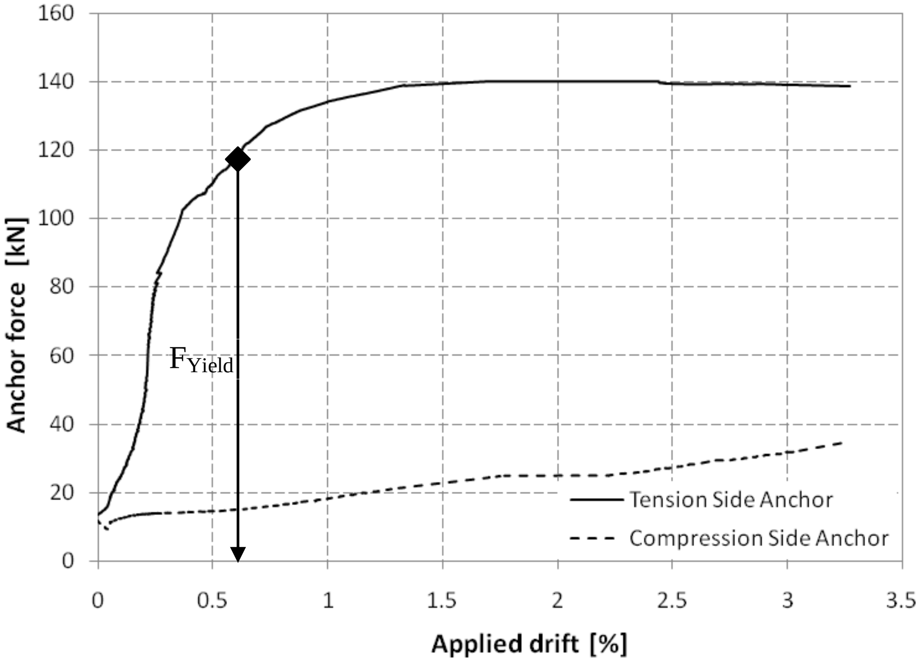

Figure 2.24: Anchor load variation during Tes2

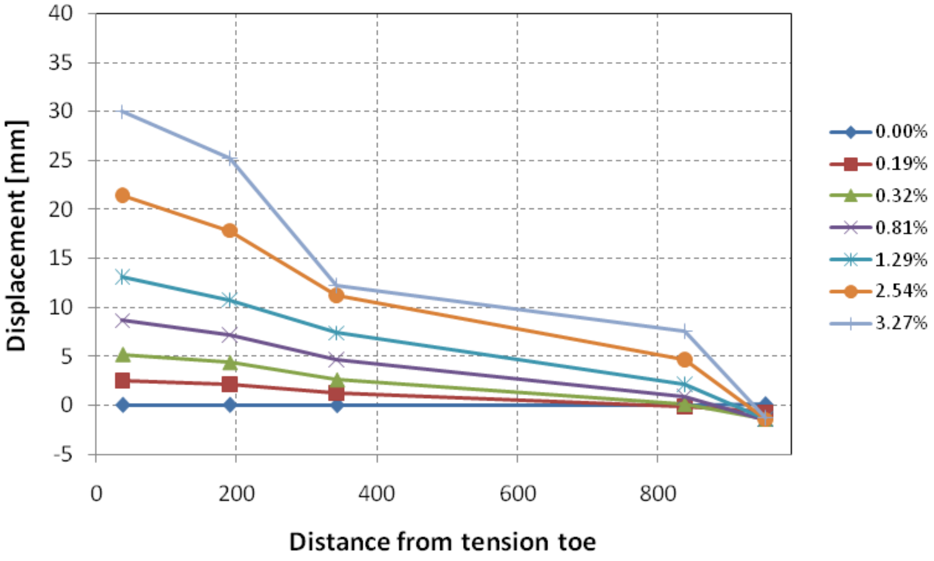

Figure 2.25: X-Sectional deformation at joint interface (Test 2)

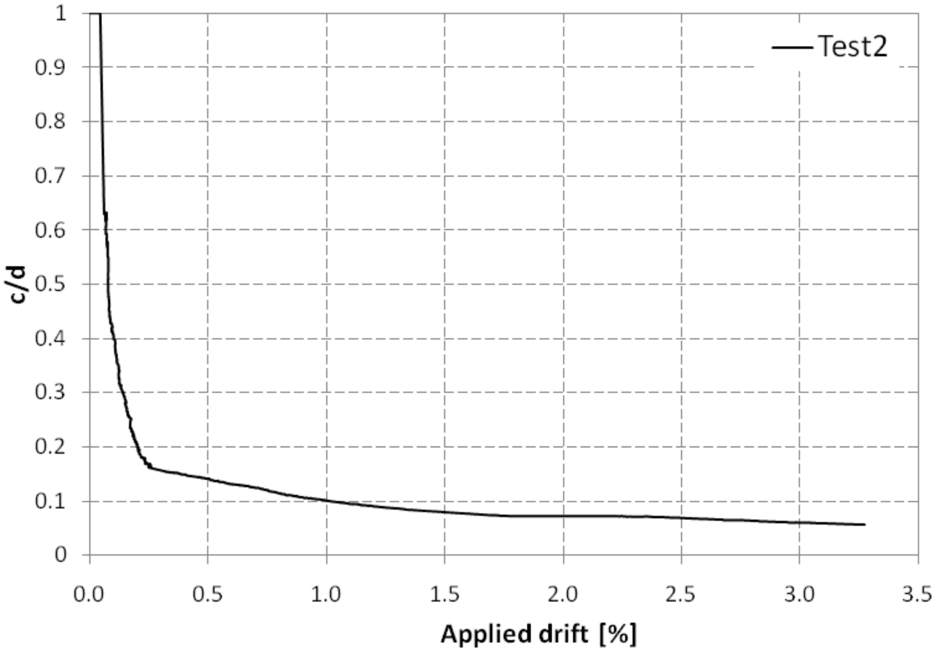

Figure 2.26: contact length versus wall drift (Test 2)

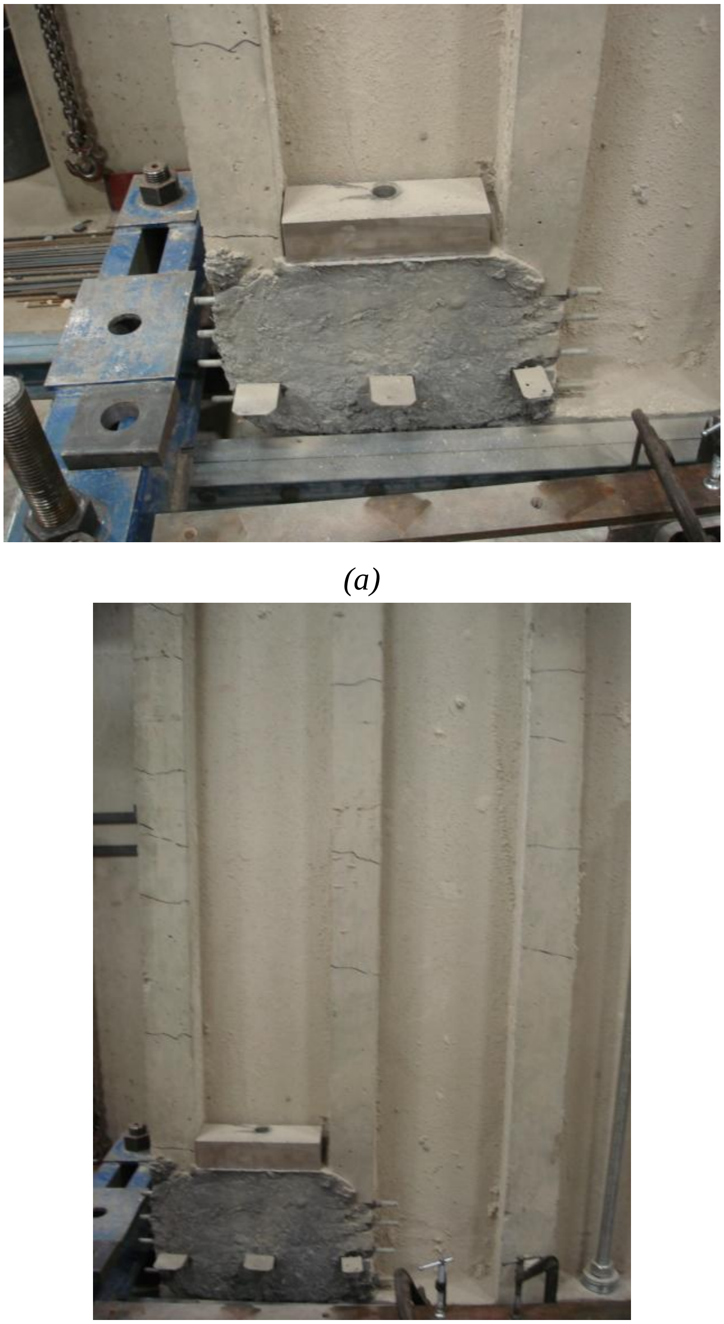

(a)

(b)

Figure 2.27: (a) Cracks initiated at the tension side stiffener just above the anchor block (b) cracks spreads upwards and new cracks are formed in the second and third stiffeners

Figure 2.28: Cracking and spalling of concrete at the compression toe

2.5.3 Test 3

In order to investigate the anchor block size on the joint behaviour, an identical specimen to that of Test 2 is used but with increased anchor block size (330 mm in Test 2 specimen versus 610 mm in Test 3 specimen). Prior to loading, the forces in the tension and compression anchors are 12.5 and 1.8 kN, respectively. Figure 2.30 depicts the variation of the force in the tension and compression side anchors versus the applied lateral drift. Unfortunately, all strain gauges of the tension side anchor have been damaged after the bar has reached its proof stress.

Figure 2.29 describes the base shear-drift response. Similar to previous tests, at a drift of ~0.05 %, corresponding to 8.5 kN of base shear, the initial lateral stiffness of the joint is reduced from ~3.80 kN/m to ~2.50 kN/m due to gap initiation. Cross-sectional deformation at the joint interface is shown in Figure 2.31 and contact length (as a ratio of the reinforcement depth, c/d) versus wall drift is depicted in Figure 2.32. Figure 2.34 shows a side view of the tension and compression toes, showing gap opening at the tension side and complete bearing at the compression side. The base shear-drift response remains approximately linear up to the steel anchor reaching its proof stress, 308.0 MPa (as shown in Figure 2.30), at a drift of ~0.69 %, corresponding to 43.2 kN of base shear. Crack formation is identical to Test 2. Beyond this point, the base shear is increased until reaching a plateau at a load of 51.5 kN. Cracking and minor spalling of the concrete cover at the compression side of the joint is observed as seen in Figure 2.33. As the steel anchor continues to yield, the load drops gradually until failure is attained by rupture of the tension anchor at drift of ~3.50%. Similar to Test 2, the fuse concept is manifested as no cracks in the panel other than the cracks in the vertical stiffeners; all damage is concentrated in the yielding and rupture of the anchor. At maximum drift (~3.50%), the gap opening measured at the outermost stiffener on the tension side is ~36.3 mm (see Figure 2.31). At this stage, the joint behaviour is clearly governed by the anchor elongation. Comparison between the behavoiur of specimen in Test 2 and 3 is given in Section 2.6.6.2.

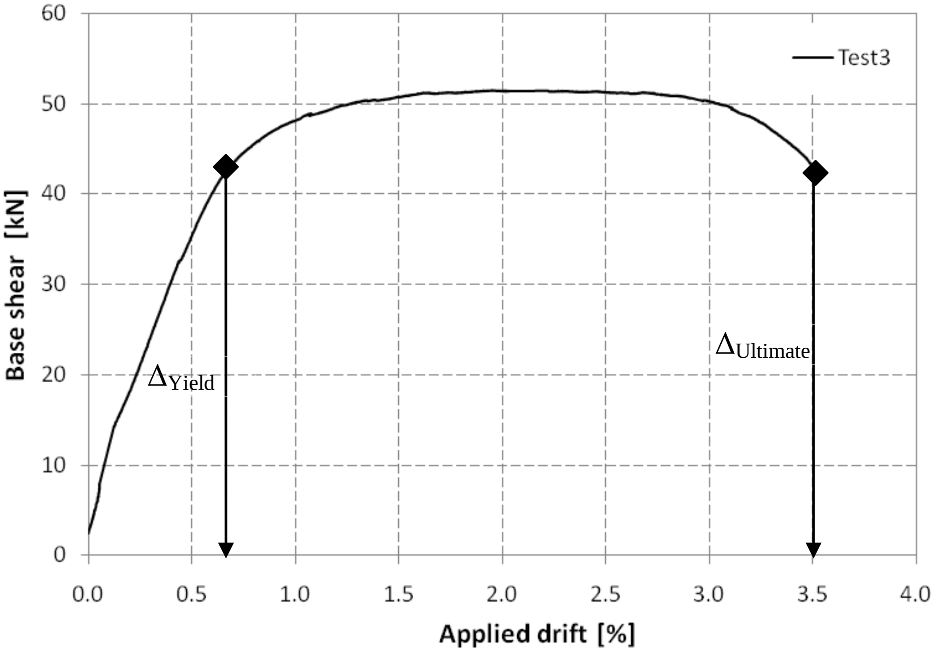

Figure 2.29: Base shear-drift response of Test 3

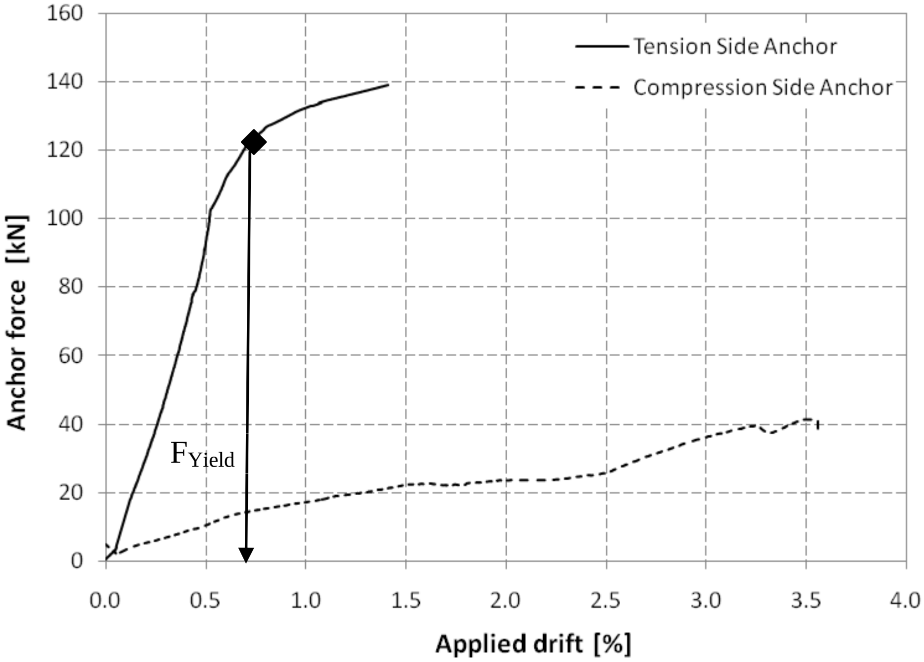

Figure 2.30: Anchor load variation during Test 3

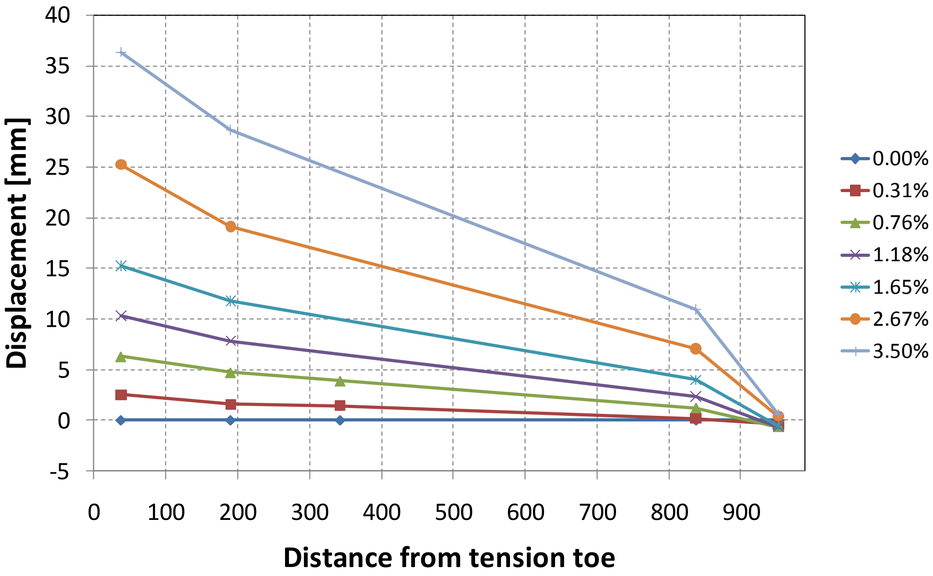

Figure 2.31: X-Sectional deformation at joint interface (Test 3)

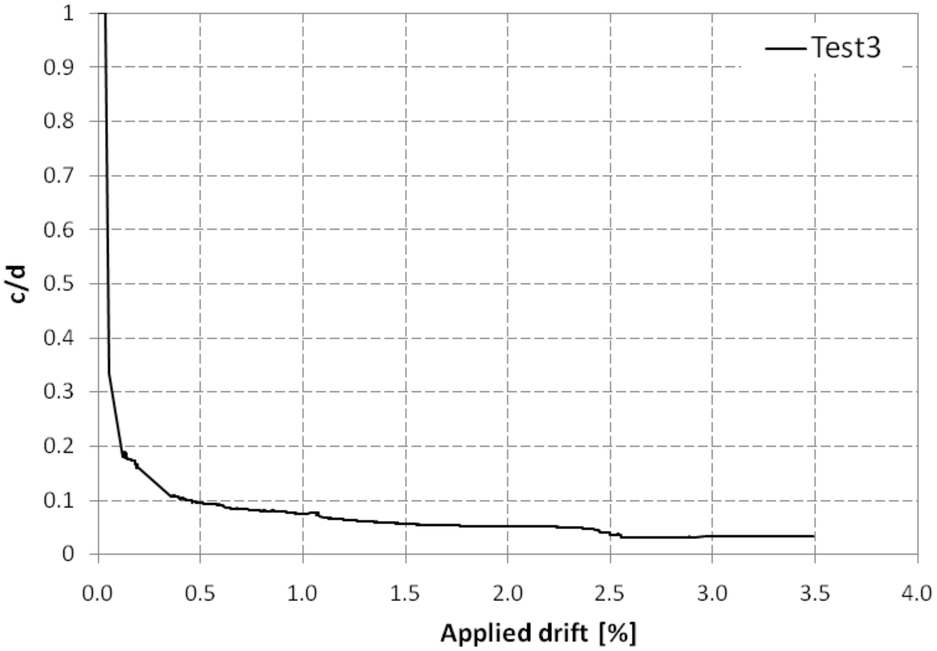

Figure 2.32: contact length versus wall drift (Test 3)

Figure 2.33: Cracking and spalling of concrete at the compression toe (Test 3)

(a) (b)

Figure 2.34: Deformation at gap opening of ~30.0, measured at the outermost stiffener on the tension side (a) Gap opening at the tension side toe (b) contact between panel and base block at the compression side toe

2.5.4 Test 4

Aiming to study the compression failure mode, an identical specimen to Test 3 is Specimen used in Test 4 is identical to that of Test 3 is used bur with stronger anchor steel type (f_{ult} = 367.6 MPa for Test 3 versus 805.2 MPa for Test 4). Moreover, the 2″ steel plate used in Test 2 and Test 3 to distribute anchor load is eliminated (refer to Figure 2.20) and regular washers are used. The use of such steel plate may increase the overall system cost. At the beginning of the horizontal load application, the forces in the tension and compression anchors are 17.8 and 3.1 kN, respectively.

At a drift of ~0.15 %, corresponding to 11.6 kN of base shear, the initial joint lateral stiffness is reduced due to initiation of gap opening. The base shear-drift response remains approximately linear afterwards (Figure 2.35). Details of the cross-sectional deformation and contact length during gap opening are shown in Figure 2.37 and Figure 2.38.

Initially, horizontal cracks are formed in the tension side vertical stiffeners immediately above the anchor block. As load increases, cracks are formed and spread upward in the tension side stiffener. In the same time, anchor forces are increased as seen in Figure 2.36. Thereafter, cracks are formed in the second stiffeners as shown in Figure 2.39. A few cracks are observed in the anchor block immediately under the anchor washers as seen in Figure 2.40. No significant damage is observed in the anchor block area, indicating that removing the steel thick plate had minor effects on the behaviour. Brittle compression failure in occurs suddenly at 66.5 kN of load corresponding to ~1.40% of drift, as seen in Figure 2.41. In addition, several diagonal cracks are formed marking the compression field within the panel. At maximum drift (~1.40%), the gap opening measured at the outermost stiffener on the tension side is ~18.8 mm (see Figure 2.37). The gap opening is governed by anchor elongation; however, the failure is governed by concrete compressive strength. Comparison between the behavoiur of specimen in Test 3 and 4 is given in Section 2.6.6.3.

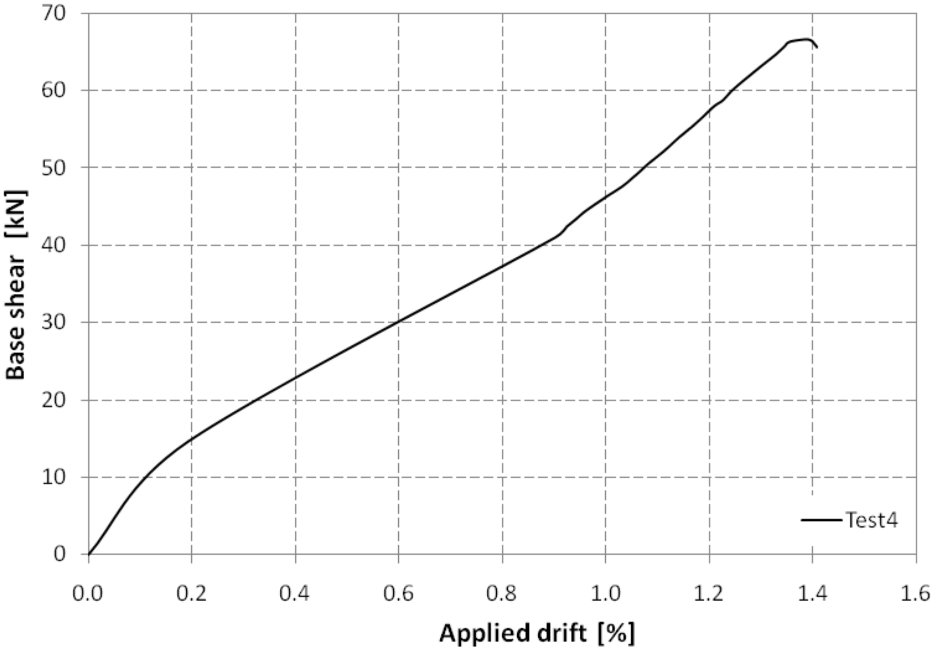

Figure 2.35: Base shear-drift response of Test 4

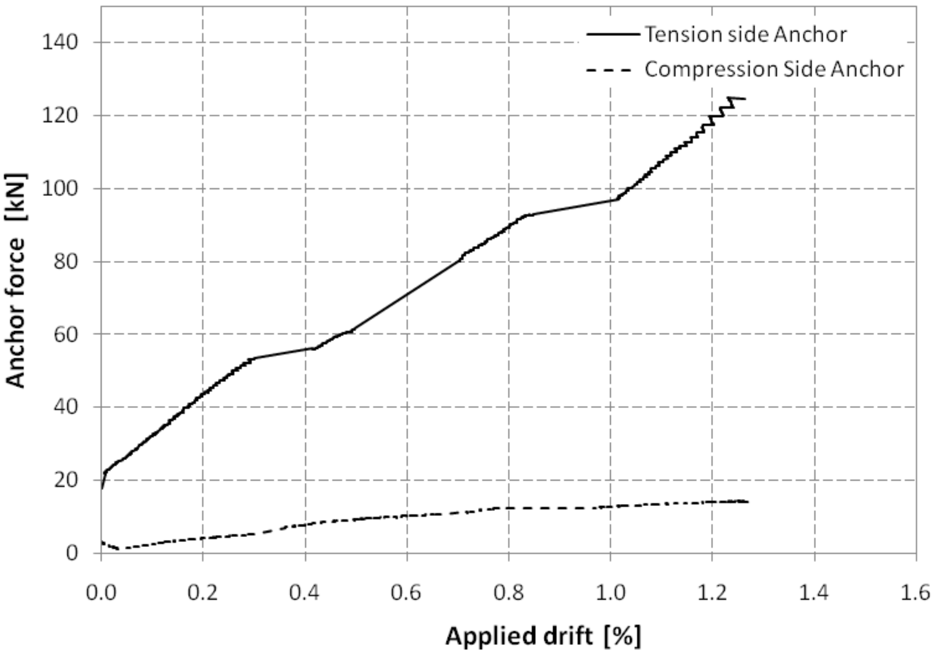

Figure 2.36: Anchor load variation during Test 4

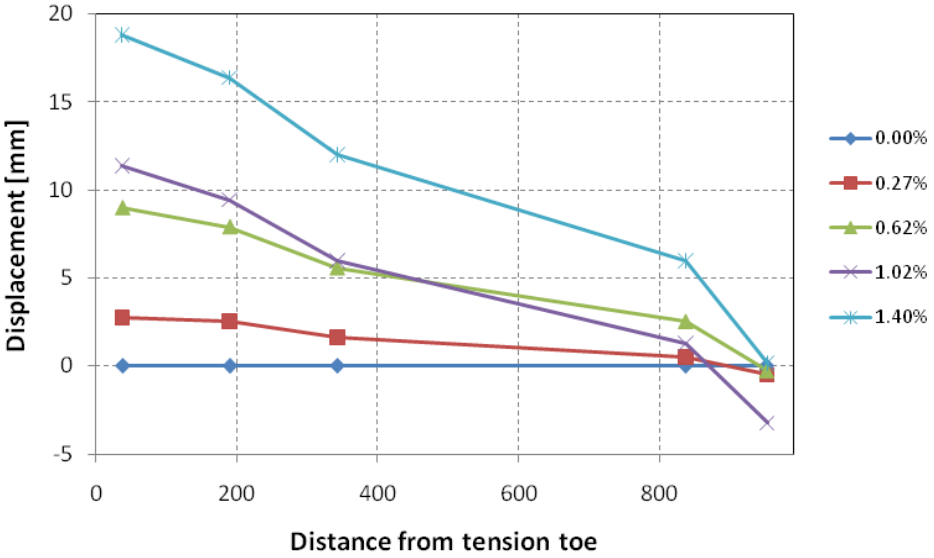

Figure 2.37: X-Sectional deformation at joint interface (Test 4)

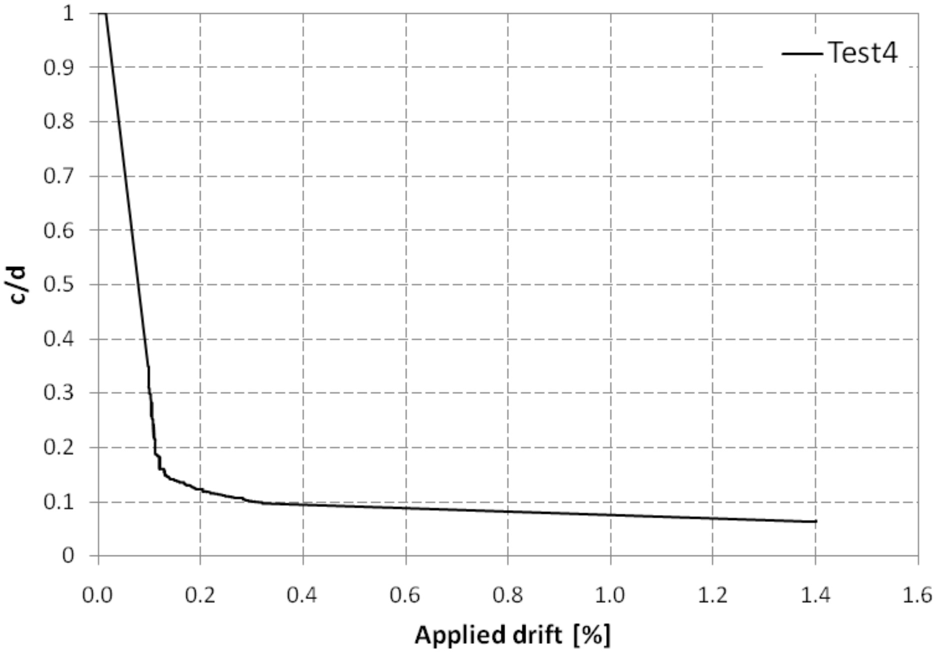

Figure 2.38: contact length versus wall drift (Test 4)

Figure 2.39: Cracks formed in the concrete panel

Figure 2.40: Cracks in the anchor block area

Figure 2.41: Concrete compression failure

2.6 General Discussion of Test Results

2.6.1 Failure modes

Based on the testing program conducted, the ultimate capacity of the joint is attained upon one of the following:

1. Ductile failure: Anchors yielding and rupturing, i.e. $\varepsilon_s = \varepsilon_{rupture}$.
2. Brittle failure: Concrete compression failure under bearing stresses.
3. Brittle failure: Concrete cone breakout of the anchor block.

Figure 2.42 illustrates the expected failure modes. A successful design should avoid brittle failures. Significant yielding of steel anchor should occur before concrete crushes or breaks out, i.e. under-reinforced behaviour is desired.

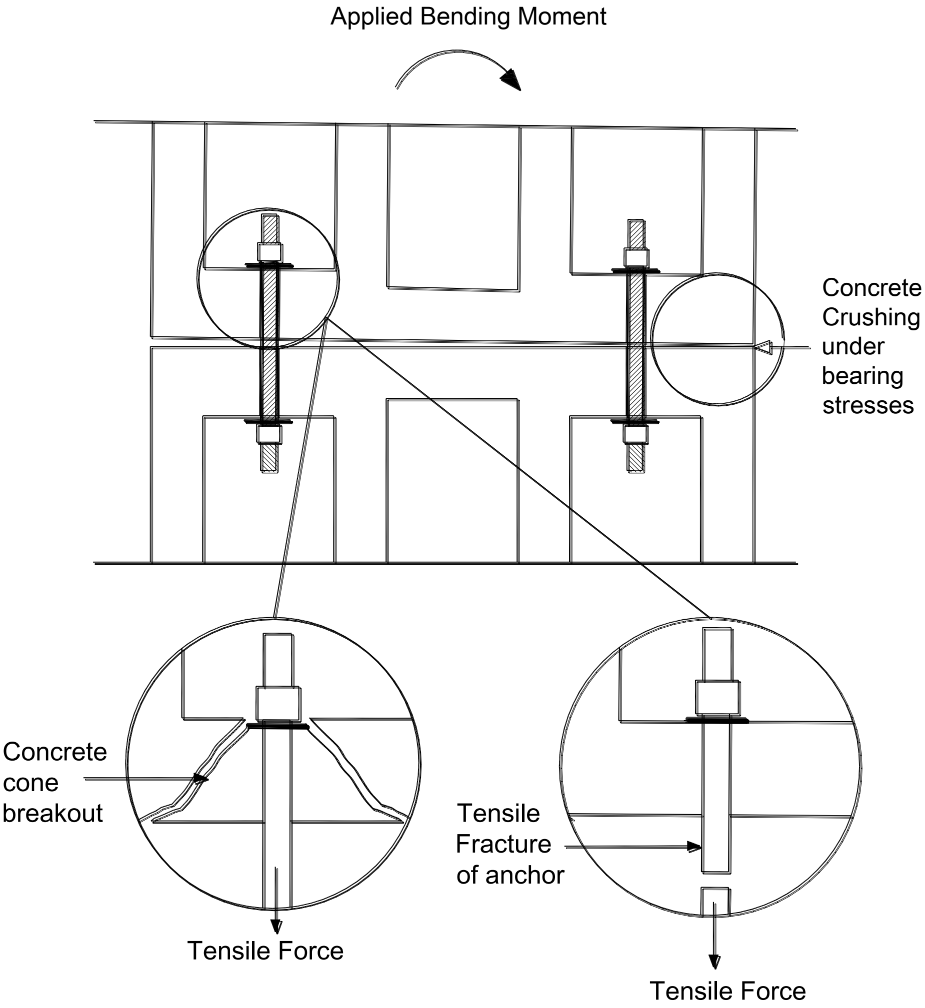

Figure 2.42: Observed modes of failure

2.6.2 General behaviour of the test specimens

The wall behaviour is mainly governed by gap opening at the horizontal joint. The lateral load-lateral displacement response of the joints governed by ductile failure, i.e. steel anchor yielding and rupture, can be idealized as illustrated in Figure 2.43. At the beginning of the test, the concrete panel and the base block are in full contact. Moreover, the joint is under compressive stresses due to panel own weight and anchor pretension, if any. The joint behaves in a linear elastic manner up to the initiation of gap opening (i.e. decrease in the contact area). At this stage, stiffness of the joint is dependent on the dimensions of the contact area and the pretensioning forces, rather than the steel anchor area or position. Gap opening occurs at the extreme tension corner at the joint interface as the applied load overcomes the initial compressive stresses. Nonlinear behaviour starts with gap opening. However, at small gap openings, nonlinearity is not significant. Stiffness reduction is attributed to the increased gap opening and at later stages to nonlinear behaviour of steel anchor in tension. As lateral displacement is further increased, steel anchors yield due to increased stresses originating from bending moments and dowel action forces. Yielding causes the lateral load to increase slowly up till maximum load is reached. Failure is attained by rupture of steel anchor. Excellent displacement capacity can be achieved. Points of particular interest are:

Point I: initiation of gap opening.
Point II: tension side steel anchor reaching its yield/proof stress.
Point III: tension side steel anchor reaching its maximum stress
Point IV: crushing of concrete cover on the compression side toe.
Point V: failure due to rupture of tension side steel anchor.

Joints governed by brittle failure, i.e. concrete compression or breakout failure, are not able to develop reasonable displacement capacity and fails prematurely in a sudden way before reaching point II.

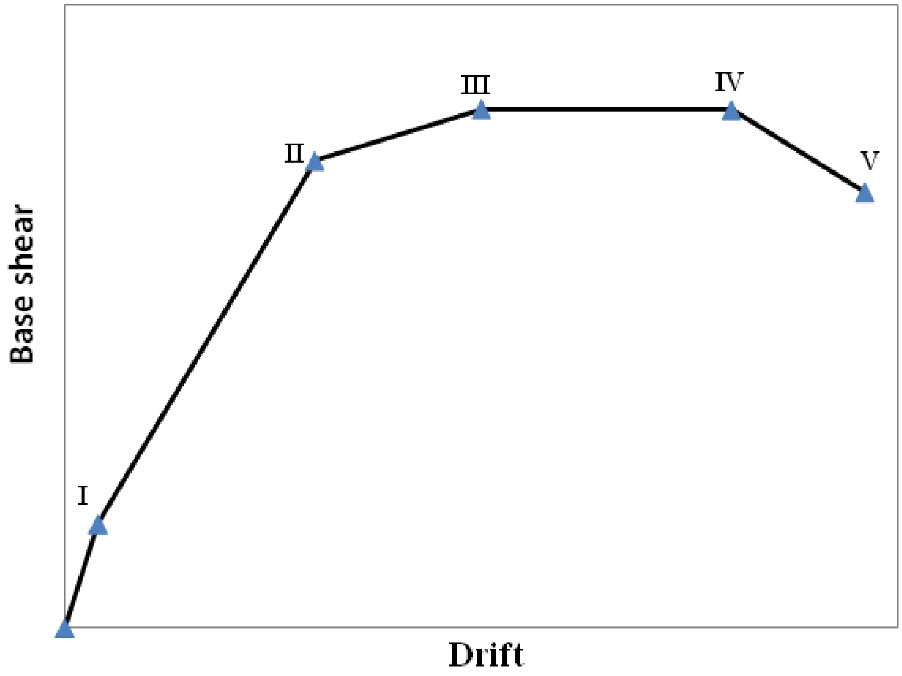

Figure 2.43: General base shear-drift response of the tested specimens

2.6.3 Gap/Contact behaviour

Gap opening is a key source of nonlinear behaviour of the anchor-jointed precast structural wall system. Since nonlinear behaviour is concentrated at the base panel-to-foundation section, damage to the concrete panel is minimized. The main source of nonlinearity in cast-in-place monolithic walls is the steel rebar and concrete plastic damage in the plastic hinge zone. Hence, significant damage including large non-recoverable deformations and strains with wide residual cracks is expected in monolithic walls. Typical contact length versus wall drift observed in the experimental program is illustrated in Figure 2.44. The last contact point is considered as an equivalent neutral axis after the gap opens, which is the location where vertical displacements of LVDTs mounted along the joint change sign. For more accurate determination of the contact length, a more sophisticated method should be used in future tests. A more accurate determination of the contact length is needed for development of accurate analysis procedures.

At first, the full length of the panel is in contact with the foundation, i.e. contact length is equal to the panel length, c/d = 1.0. Contact length decreases rapidly initially, reduces gradually, and then maintains a certain value with increasing drift. Figure 2.45 illustrates the deformed shape at the bottom panel-to-foundation joint based on recorded date during tests. It is evident that plane sections do not remain plain after bending. Deformed shape can be idealized by four straight lines EF, FG, GH and HI, where F is at the end of the contact length, G is at centre line of the vertical stiffener, and H is the centre line of the tension anchor bolt.

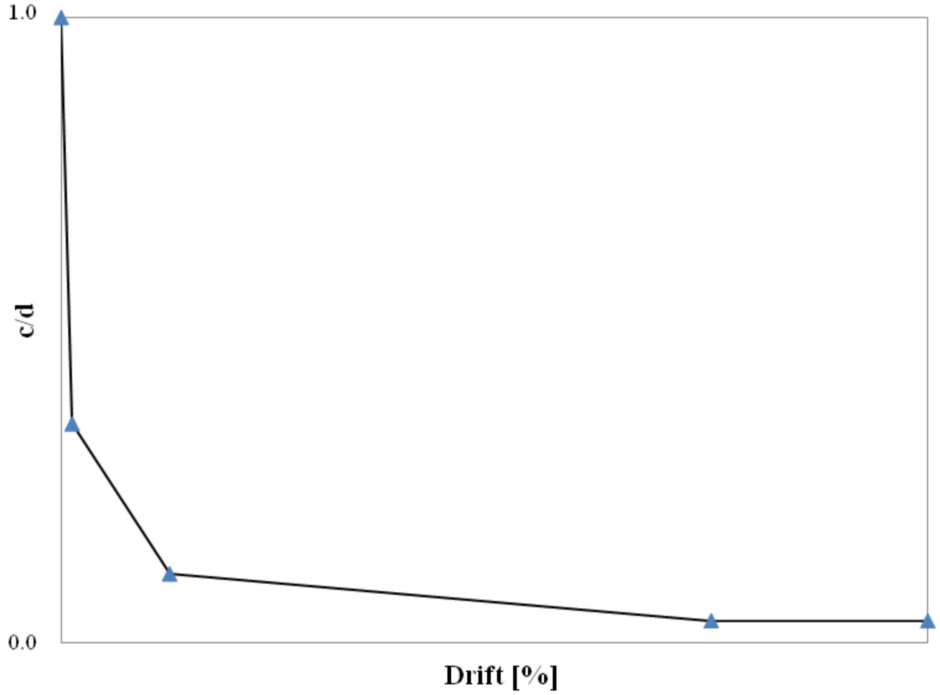

Figure 2.44: Typical contact length versus wall drift response

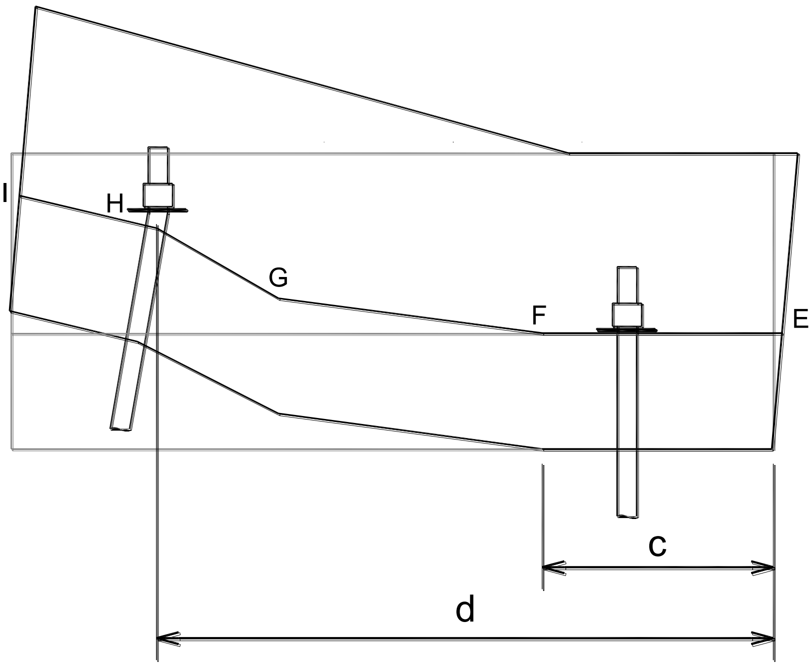

Figure 2.45: deformed shape at the bottom panel-to-foundation joint (deformation exaggerated for visualization)

2.6.4 Shear force transfer across Joint

Figure 2.46 shows the mechanism of shear force transfer from the wall panel to foundation. Initially, shear force is transferred through shear friction along the contact area. As lateral drift increases, the contact area decreases while the resultant compressive force increases, finally causing the shear friction force to decrease. Once the applied shear force exceeds the shear friction force, slip across the joint is initiated. Relative displacement between the panel and the foundation causes the steel anchors to deform. The resistance to deformation is attributed to dowel action mechanism. Tensile and shear stresses due to dowel forces add to the tensile stresses already in the anchor due to bending. Based on experimental observation, it is concluded that tension side anchor is more engaged in transferring the applied shear force as: (1) only minor increase in axial strains in the compression side anchor during testing is recorded, (2) after the test, the tension side anchor is kinked, whereas compression side anchor remains straight. Dowel forces are attributed to one of three modes: shear, flexural, and kinking (Paulay et al. 1974 – see Figure 2.47). The deformed shape of the tension side anchor infers that it is resisting shear in the kinking mode. Lateral behaviour of the tested precast walls is governed by flexural behaviour rather than shear sliding. Observed slip is in the order of 5.0 – 9.0 mm (see Appendix VII). ITG 5-1 (ACI 2008) requires the joint slip to be less than 0.06 inch – 1.5 mm. Sliding could be reduced if gravity loads is considered as it increases significantly the shear friction resistance.

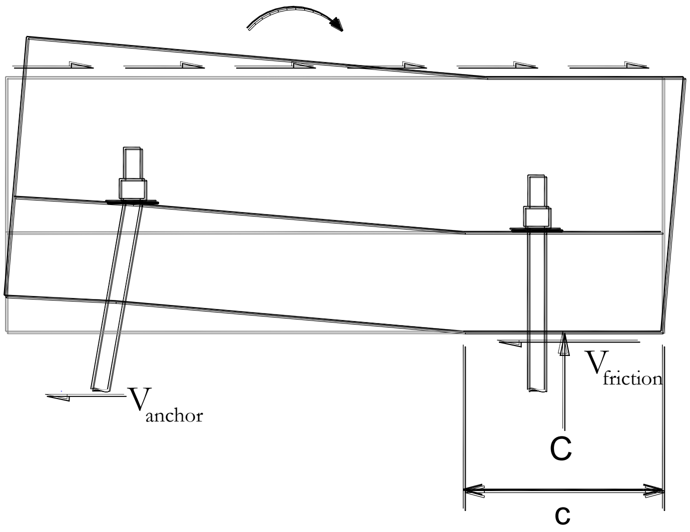

Figure 2.46: Shear force transfer across joint

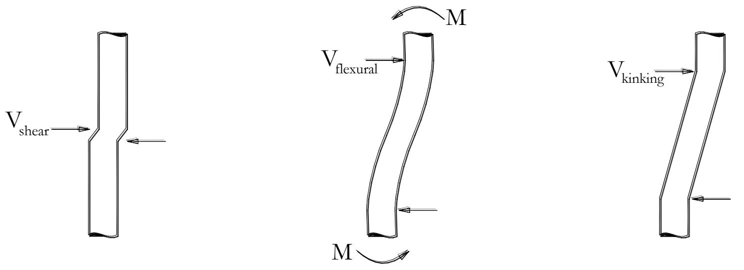

Shear mode Flexural mode Kinking mode

Figure 2.47: Dowel action mode (after Paulay et al. 1974)

2.6.5 What governs the joint behaviour?

Based on the testing program conducted together with critical analysis of the anchor-jointed precast structural wall system, main parameters governing the joint behaviour can be identified as following:

1- Geometry of the joint: dimensions of the contact area $(b\times \ell_w)$, distance from extreme compression fibre to the centroid of the steel anchor, d, and area and length of steel anchor, A_a, L_a.

2- Material properties: steel and concrete characteristic stress-strain relationship.

3- Loading: applied gravity loads, and pretension force in anchors.

4- Geometry and reinforcement of the concrete panel: wall aspect ratio (h_w/ℓ_w), size of anchor block, t, and reinforcement detailing (to prevent breakout failure) and confinement of base panel near the corners of the panel, i.e. regions of expected highest compressive strains (to increase the maximum attainable compressive strain) are of particular importance.

Longitudinal and transverse panel reinforcement and thickness of vertical stiffeners, t_{iw}, are less significant as long as the panel behaves mainly as a rigid body.

2.6.6 Parameters analysis

A summary of the experimental results are given in Table 2.4. Dimensions and reinforcement details of the tested specimens are identical with only minor variations. Variable considered in the experimental program are: (1) anchor block size and reinforcement details of its vicinity, (2) length of steel anchor/ anchor block size, and (3) type of steel anchor.

Table 2.4: Overview of the experimental results

Test	anchor block size [mm]	steel anchor type	Force in Tension anchor due to tightening [kN]	Force in Compression anchor due to tightening [kN]	Failure load [kN]	Failure mode
Test1	150	Grade 75	57.2	58.9	24.5	concrete breakout
Test2	330	Threaded anchor – Type I	34.8	30.0	50.8	steel rupture
Test3	550	Threaded anchor – Type I	12.5	1.8	51.5	steel rupture
Test4	605	Threaded anchor – Type II	17.8	3.1	66.5	compression failure

2.6.6.1 Effect of strengthening test specimen

Concrete anchor block should be sized to prevent premature failure due to concrete breakout. Comparing Test1 and Test2, the modification suggested is effective in providing an alternative load path to avoid concrete breakout failure. No cracks or any signs of distress are observed in

Test2 in the anchor block area. Cracks on the tension side vertical stiffeners confirmed that load has moved through the suggested path as explained in Figure 2.21. The observed failure mode has changed from breakout failure to bending failure by rupture of steel anchor. As a consequence, the failure load is approximately doubled.

2.6.6.2 Effect of varying anchor length /anchor block size

Comparing Test2 and Test3, using a longer anchor has increased the displacement capacity of the joint. For the same rupture strain, a higher deformation, and hence higher displacement capacity, is expected when using a longer anchor. The failure load is not affected by the anchor length, since both specimens failed at ~51.0 kN. Comparison between the base shear-drift response of Test2 and Test3 is given in Figure 2.48.

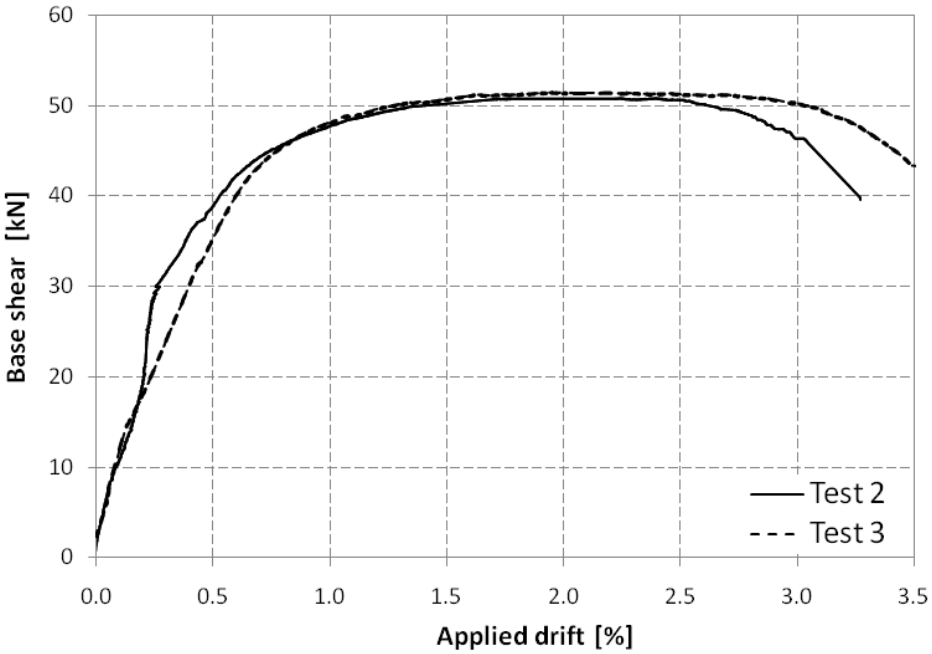

Figure 2.48: Effect of increasing anchor length/anchor block size

2.6.6.3 Effect of varying steel type

The strength and failure mode of the joint are dependent, among other factors, on the stress-strain properties of the steel anchor. Figure 2.49 compares the base shear-drift response of Test 3 and Test 4. Comparing Test 3 and Test 4, it can be concluded that using a steel type with higher ultimate and yield strength has shifted the failure mode from ductile steel failure to brittle compression failure. Although a higher failure load is achieved, displacement at failure is greatly reduced.

Displacement capacity is controlled, among other factors, by the maximum strain that can develop in the anchor. The chosen steel type should have an adequate yield plateau and maximum strain to be able to develop the desired displacement capacity. In addition, its maximum and yield strength (or steel area) should be designed with the concrete strength to avoid brittle compression failures, i.e. under reinforced behaviour is sought.

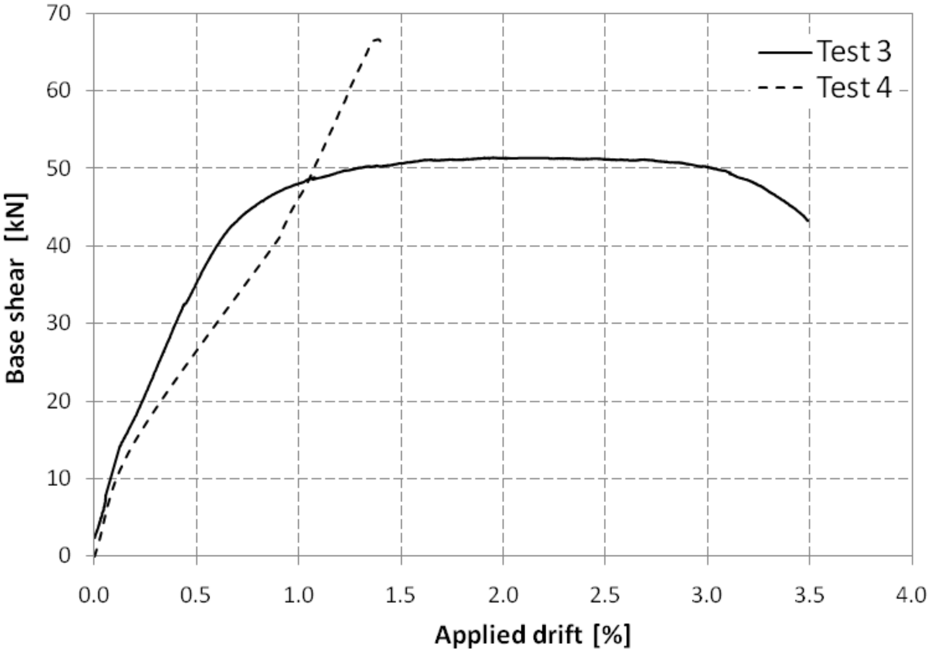

Figure 2.49: Effect of steel anchor type

2.6.7 Ductility demand

To account for ductility and inelastic behaviour in seismic designs, most of the seismic provisions, including the National Building Code of Canada (NBCC 2005), apply the "equal displacement principle". Where the EQ forces obtained by elastic analysis is reduced by the product of two modification factors, the ductility-related force modification factor, R_d and the overstrength-related force modification factor R_o. Theses modification factors are directly related to the ductility ratio and maximum drift expected for the system. The ductility ratios of Test 2 and Test 3, defined as $\Delta_{max}/\Delta_{Yield,}$ are equal to 5.3 and 5.1, respectively, where Δ_{max} is the drift at anchor rupture or load dropping to 80% of the maximum load – post peak, whichever is greater and Δ_{yield} is the drift at the onset of the steel anchor yielding in tension as determined using the strain gauges.

The test panels are required by the ITG-5.1-07 (ACI 2008) to sustain a certain amount of drift angle under cyclic load without significant degradation to the lateral capacity to be considered successful. The response under monotonic loading is construed as an envelope to the response under cyclic loads, and hence experimental results presented here can indicate whether the tested panels would be successful or not. The desired drift ratio is defined as the greater of:

1- 1.5 times drift ratio corresponding to the design displacement, or
2- the following value:

$$0.9 < 0.8\ (h_w/l_w)+0.5 < 2.5$$

where h_w is the height of the entire wall for prototype structure, and l_w is the length of the entire wall in the direction of the shear wall. For the tested specimens, this value is equal to 2.5%. Both specimens that failed in a ductile manner, Test 2 and 3, exceeded this value. Test 2 and 3 sustained a maximum drift of 3.27% and 3.5%, respectively. It is worthy of mention however that under cyclic loading, the maximum drift is likely to be reduced.

2.7 Basis for development of response prediction model

The moment-rotation response of the joint can be predicted using the basic principles of force equilibrium and compatibility of deformations, together with concrete and steel stress-strain relationships. The concrete panels are assumed to behave primarily as rigid bodies. Deformation and stiffness are governed by gap opening at the horizontal joint between the base panel and the foundation.

For small moments, where the resultant force is within the middle third of the connection, the entire contact area between the two panels will be under compression and anchors are dormant at this stage. For higher moments, where the resultant force falls outside the middle third, uplift on one side is expected. Acting moment will induce compressive bearing stresses at one side, and tension stresses in the anchors located in the other side. Free body diagram and deformed shape are depicted in Figure 2.50. Conventional sectional analysis cannot be applied for two reasons: (1) due to lack of bond, strain compatibility between steel anchor and surrounding concrete is violated at the critical section. Consequently, for a given loading state, a unique solution for the neutral axis depth, c, cannot be found, and (2) plane sections no longer remain plane as a result of considerable gap opening (refer to Figure 2.45). An assessment of applicability of analysis procedures available in the literature for joints with comparable characteristics is undertaken.

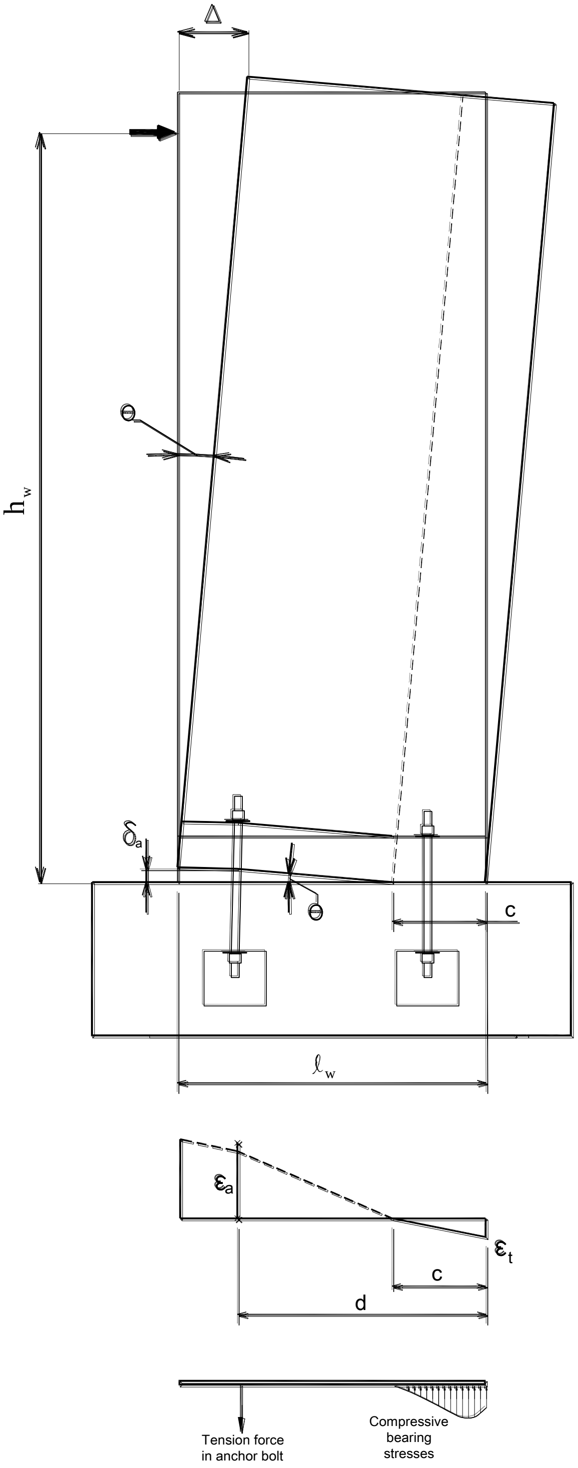

Figure 2.50: Analysis of the joint behaviour

Pampanin et al. (2001) proposed an iterative sectional procedure to analyse the behavior of precast concrete beam-column connections. In their study, they swapped the strain compatibility condition, used in conventional sectional analysis, by an equality condition on the global top deformation between the precast member and an analogous monolithic member. The applicability of this condition to anchor-jointed precast structural wall system is doubtful.

Several studies have been carried out to characterize the behaviour of unbonded post-tensioned precast wall system. Suggested analytical procedures assumed that the wall is designed to respond mainly in flexural and that shear sliding is prevented. Perez et al. (2007) approximated the nonlinear behaviour of unbonded post-tensioned precast wall system using tri-linear idealization. Mathematical formulas were developed to predict critical points on the response. The critical points are: (1) effective linear limit, (2) yielding of post-tensioning steel, and (3) crushing of concrete in compression. Aaleti and Sritharan (2009) suggested a simplified tri-linear relation between base rotation and the neutral axis depth. This relation is based on experimental and analytical observations. The neutral axis depth is equal to the wall length at zero rotation. On the other hand, it basically remains constant beyond ~0.5% rotation. An illustration of the suggested relation is shown in Figure 2.51. Suggested relation is comparable to the relation observed in the current study (refer to Figure 2.44). Using the proposed relation for the neutral axis depth and principles of equilibrium and deformation compatibility, full moment-drift relationship could be established. The applicability of the simplified tri-linear relation between base rotation and the neutral axis depth must be confirmed and/or modified using data from further experimental and analytical investigations.

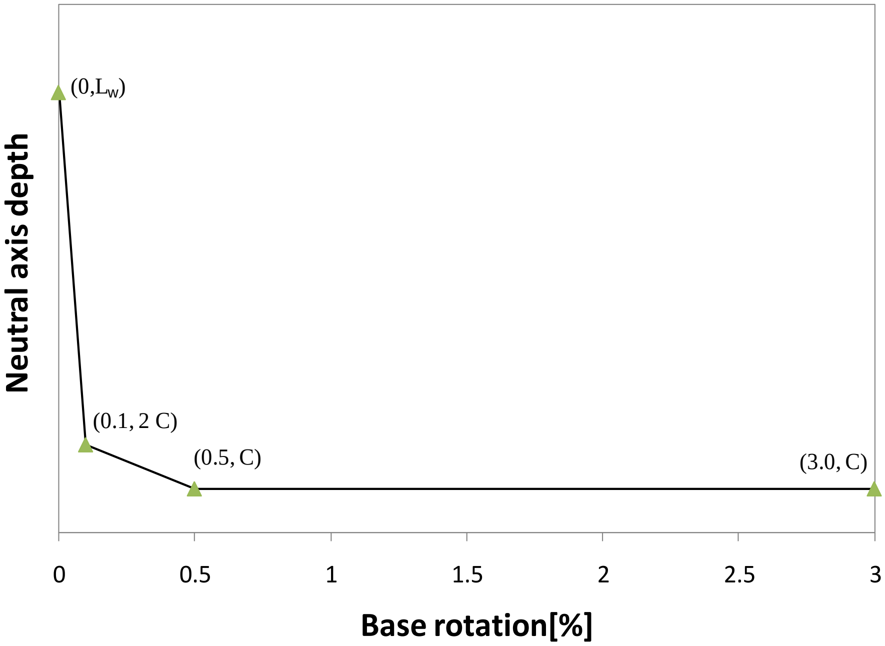

Figure 2.51: illustration of the tri-linear idealization of the neutral axis depth versus base rotation (after Aaleti and Sritharan 2009)

It is imperative to note that in all methods, panel is assumed to move as a rigid body, i.e. angle between the panel horizontal edge and the horizontal is equal to the drift angle, θ. Consequently, the elongation of the steel anchor is equal to θ×(d-c). This assumption, though confirmed for unbonded post-tensioned precast wall systems, contradicts experimental observation as illustrated in Figure 2.44. Considering the limited number of tests, it is premature to develop reliable analysis procedures for the anchor-jointed precast structural wall system.

However, the method suggested by Aaleti and Sritharan (2009) is used to predict the behaviour of Test2 and Test3 as shown in Figure 2.52 and Figure 2.53. This method is able to provide an accurate prediction of the decompression load and a reasonable estimate for the failure load.

Nevertheless, the predicted initial stiffness is higher than the observed one. The analysis procedure needs to be adjusted and fine tuned to be able to reliably predict the behaviour of anchor-jointed precast structural shear walls.

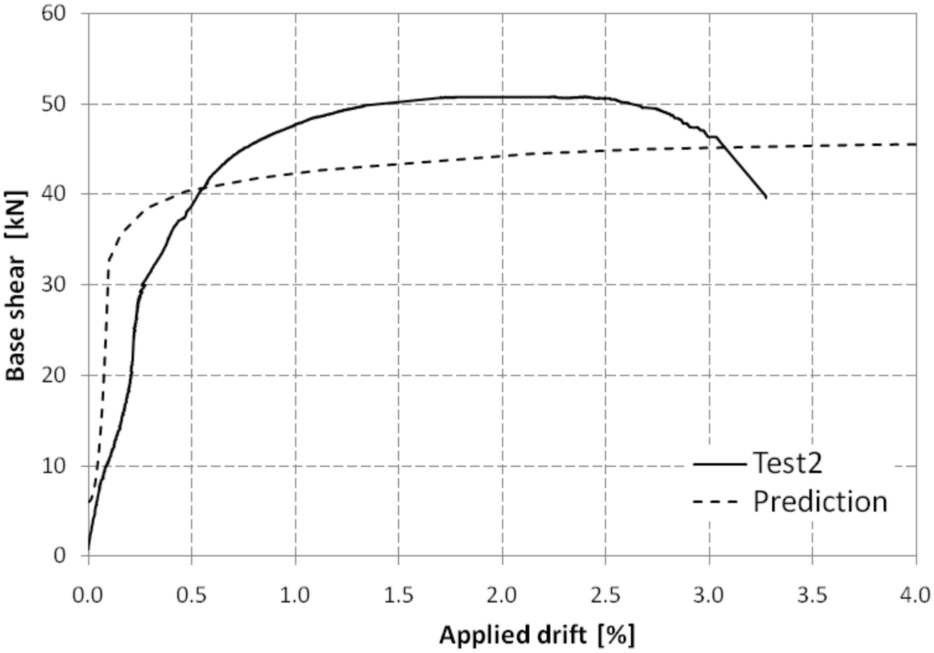

Figure 2.52: prediction of base shear-drift response of Test2

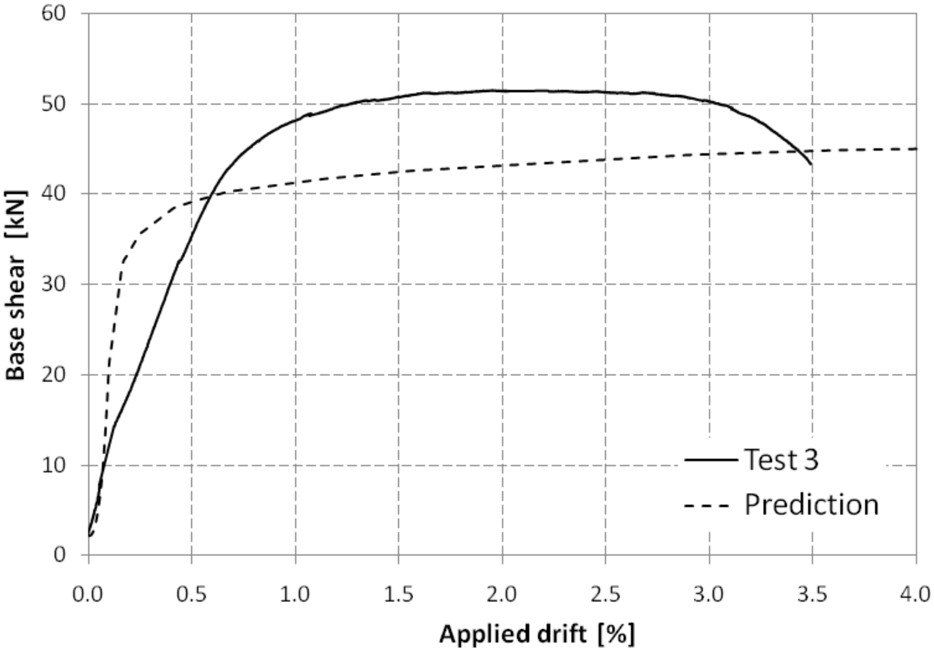

Figure 2.53: prediction of base shear-drift response of Test3

2.8 Summary and Conclusions

In this study, a new innovative jointing technique for connecting precast concrete shear walls is conceptually developed and tested. Four reduced scale specimens, comprising of a base block and precast panel jointed using two anchor bolts, are tested under monotonically increasing horizontal displacement. Tests are conducted to study the behaviour of the proposed joint under bending moments, which mainly governs the behaviour of lower joints. Test results are used to characterize the behaviour of such connections; mainly determining lateral strength and associated possible modes of failure. Key parameters dominating the behaviour are identified and their importance are assessed. Available analytical procedures, developed for analogous joint, to predict the behaviour of the connection for design purposes are reviewed and their applicability to the proposed system is assessed. This work lays out the basis towards developing design procedures, which is a corner stone towards acceptance and recognition of this system as a lateral-load-resisting system by relevant codes.

This study shows that anchor-jointed precast structural wall system provides a feasible alternative to conventional cast-in-place shear walls in low-to-medium seismic regions. The system has desirable seismic characteristics and is easy to construct. The following conclusions can be drawn from the test results:

- The ultimate capacity of the joint is attained upon one of the following: (1) rupture of steel anchor, (2) concrete compression failure, or (3) concrete breakout failure. A successful design should avoid brittle concrete failures.
- The originally proposed panel design is inherently weak in resisting breakout failure. This weakness impedes the system from resisting higher levels of lateral loads. A modification of the panel geometry and reinforcement by increasing the anchor block size is suggested and tested. The detail used in strengthening the test specimens against breakout failure is successful in increasing breakout capacity and avoiding this brittle failure mode. This detail is easily applicable to new constructions.
- In order for the joints to achieve satisfactory performance, the concrete breakout strength must be greater than the tensile ultimate strength of the anchors. In addition, the area of

steel should be limited to ensure that steel yields before concrete crushes under bearing stresses.

- Joint may be designed such that all damage and inelastic deformations are concentrated in the anchors. Following a damaging earthquake event, only damaged anchor bolts would need to be replaced. Anchor may act as a structural fuse.
- The system is able to undergo large inelastic deformation with little damage to the concrete panel. Seismic demand up to a 3.5% of drift could be attained by the proposed joint configurations with minimum apparent damage to the precast wall connection. This level represents typical seismic demand for low to moderate seismicity.
- As the anchor length is increased, the displacement capacity of the joint is also increased. Anchor length is directly dictated by the anchor block size.

CHAPTER 3

Lateral Resistance of Anchor-Jointed Precast Structural Wall System: Nonlinear Model Development

3.1 Introduction

Enormous capabilities are available now in nonlinear finite element modelling allowing replication of actual physical behaviour with greater accuracy. This research aims at developing a nonlinear finite element modelling technique that is capable of accurately mimicking the structural behaviour and capturing possible failure modes of the anchor-jointed precast structural wall system subjected to lateral load. Conceptual development of the system is presented in Chapter 2. Conducting a large experimental program to study this behaviour might be prohibitively expensive. Hence, using nonlinear finite element analysis supported only by a few number of experimental tests can help in understanding the structural behaviour, developing a practical design, conducting parametric studies and examining different improvement strategies for strength, ductility, and/or energy dissipation of the system. The intricacy of such analysis is dictated by the complexity of behaviour.

To augment the experimental work, a non-linear finite element model for the anchor-jointed precast structural wall system is developed. First, the structural behaviour of the system is briefly discussed identifying main force transfer mechanism through the joint. Then, the details of the numerical model are given, including an overview of the material models, contact modeling, and hourglass control. Model development process involves fine tuning and validating modeling parameters such as material properties, material model parameters, element size, mesh layout, and contact definitions. First the structural behaviour of the system under bending moments and associated failure modes are studied and modeled. Bending associated failure modes are: concrete breakout and steel rupture. Then tests involving shear behaviour, shear friction and dowel action mechanisms, are modelled. Models are verified against experimental data available in the literature. Finally, application of anchor pretension is discussed.

3.2 Factors governing the structural behaviour of the precast shear wall systems

Shear walls are known for their inherently high strength and stiffness due to their relatively large dimensions. However, the panel-to-panel and base panel-to-foundation joints are considered areas of reduced strength and stiffness when compared to the concrete panels. It is observed experimentally that concrete panels behave primarily as rigid bodies and the deformation and damage are concentrated within the joints. Axial, bending, and shear loads are transmitted through the joints. The system behaviour is mainly governed by its joints (Fintel 1977 and Soudki et al. 1996). Thus, special attention has been directed towards modelling the connection and its vicinity. ITG-5.1-07 (ACI 2008) recommends that capacity design principals should be applied to prevent/minimize joints openings other than the base joint, i.e. only base joint opening is allowed. Therefore, this work is focused on modelling the base panel-to-foundation joint. However, discussion is also applicable to the panel-to-panel joints.

3.3 Structural behaviour and Model development

For the system to resist lateral loads it must be ensured that compression and shear forces, in addition to the applied bending moments, are safely transferred through the joints. A clear and safe load path all the way to the foundation needs to be created. As the wall is loaded horizontally, tension side starts to uplift creating a single gap between the base panel and the foundation. Bending moments are transferred through a couple of tension force in the tension side anchor and a compressive force transferred through direct bearing between foundation and base panel. Whereas shear forces are transferred through shear friction along the contact area at the compression side and dowel action of the anchor bolts as depicted in Figure 3.1.

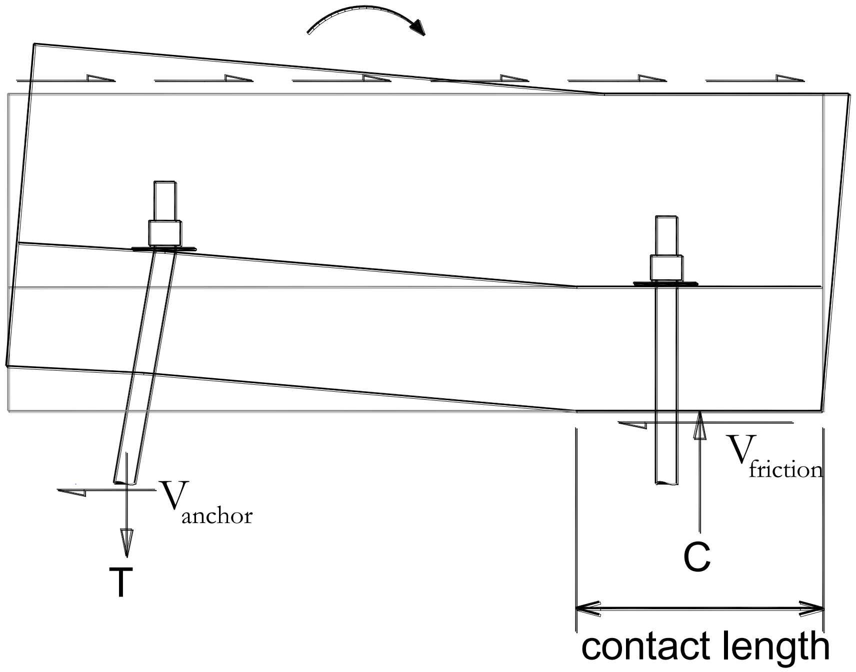

Figure 3.1: force transfer across joint

Model development involves locating and isolating physical phenomenon and failure modes governing the structural behaviour at the joint. Each of them is studied and modelled. In the following work, development of the model is divided into two main sections. The first studies the transfer of flexural bending moments, while the second deals with the shear force transfer. Structural behaviour and all potential failure modes are examined. Tests involving subassemblies with analogous failure modes and/or similar joints reported in the literature are modelled using a rational modelling technique. To validate the developed models, correlative studies including failure mode, failure load, and load-displacement relationship are conducted.

3.4 Numerical Model

The proposed system is comprised of an assemblage of three components: concrete panel, base, and steel anchors. Anchor-jointed connections exhibit nonlinear structural behaviour, where nonlinearity results from the geometrical discontinuities and interaction between different joint components. The chosen numerical tool must be able to handle the expected interactions between components such as gap opening/closing, slip and associated frictional and dowel forces, nonlinear material behaviour, and stress concentration. Numerical analyses are carried out using the commercial software LS-DYNA (LSTC 1998 and LSTC 2009), which is a general purpose implicit/explicit finite element program commonly used for nonlinear transit analysis. The program contains a rich library of material models capable of representing the complex behaviour of concrete and steel materials. Also, a large number of contact types and advanced search algorithms are available allowing difficult contact problems to be treated easily.

Although the current problem deals with quasistatic loading, explicit analysis is chosen for a number of reasons: (1) Numerical difficulties arising with nonlinearities and progressive damage/failure in implicit analysis, (2) some material models and elements within LS-DYNA are only available for the explicit solver, and (3) potential savings in CPU cost. Generally for small problems, implicit solvers are much faster but as the elements number and/or the behavioural nonlinearities increase, the CPU time increases linearly for explicit solvers versus exponentially for implicit solvers. Therefore, for large problems, explicit solvers might be faster.

Discussion given below will deal with general issues faced with nonlinear modelling applicable to numerous finite element analysis packages, along with some details specific to LS-DYNA. Further in-depth discussion of the program can be found in the user and theory manuals (LSTC 1998 and LSTC 2009).

3.4.1 Simulation of quasi-static tests using implicit finite element analysis

For Explicit time integration finite element analysis (as the one used in LS-DYNA), the solution is obtained by solving the linearized equilibrium equation given below.

$$M\ddot{x}^{n+1} + D\dot{x}^{n+1} + K_t(x^n)\Delta x = P(x^n)^{n+1} - F(x^n) \tag{3.1}$$

where M, D, K_t are the mass, damping, and tangent stiffness matrices, $\ddot{x}^{n+1}$,$\dot{x}^{n+1}$, x^n, and Δx are the acceleration, velocity, coordinate, and displacement vectors, $P(x^n)^{n+1}$ is the external load vector, $F(x^n)$ is the stress divergence vector, and the superscripts n and n+1 indicate the time increment.

Equation 3.1 includes terms for inertia and damping forces (terms involving M and D). Hence, when simulating static and quasi-static tests, analyst must ensure that the inertia and damping forces remain negligibly small throughout the analysis. Dynamic terms are greatly affected by material density (mass) and load application time. To eliminate dynamic effects, material density have to be decreased and/or load application time increased to be significantly larger than the structural natural period. In addition, boundary and contact conditions should be selected carefully to match the static test and to prevent oscillation. Decreasing the material density will add to the run time considerably. Thus, mass-and/or-time-scaling might be necessary to force the simulation running time into a reasonable time frame. However analyst must ensure that this procedure would not affect the accuracy of the results.

As a check, the system kinetic energy should be insignificant compared to the internal energy. Static equilibrium should also be checked, and any disequilibrium implies the existence of dynamic effects.

3.4.2 Material models

A crucial aspect of the model is the definition of the mechanical properties of concrete and steel materials. In the following sections, main aspects of the behaviour of both concrete and steel will be reviewed together with material models to represent this behaviour in finite element analysis.

3.4.2.1 Concrete

3.4.2.1.1 Concrete behaviour

Concrete exhibits very complex behaviour, due to its nonlinear behaviour under compressive and tensile stresses, bi-axial stiffening, size-effects, difficulty of defining failure surfaces under multi-axial stress state, and interaction between concrete and reinforcement. Moreover, cracking is a critical feature of the concrete behaviour under both service and ultimate loads. Concrete is a heterogeneous material; in the realm of finite element, it is approximated by an equivalent homogeneous continuum with average stresses and strains.

Although, it is common to ignore tensile resistance of cracked concrete in design, it is, in contrast, of extreme importance when conducting finite element analyses (Elighausen et.al. 2006). Behaviour of a concrete member is critically influenced by cracking, which is of higher significance when modelling lightly reinforced concrete members or members critical in tension or shear. Also, it must be considered when accurate prediction of deflection is sought.

Cracking is accompanied by the formation of a narrow band of intense straining (localization of deformation). As a crack propagates, the damaged zone at the crack tip is known as the fracture process zone (Figure 3.2a). Width of the fracture process zone is known as the crack band width or the characteristic width, w_c, (Figure 3.2b). In this zone, microcracks are assumed to be uniformly spread. Cohesive stresses are still transferred across the developing micro cracks and do not drop suddenly to zero, it decreases with accumulated effective plastic strain, i.e. increasing crack width as shown in Figure 3.2c. Stress-softening is attributed to the reduction of the effective area due to the presence of micro cracks. Tensile stresses distribution across a developing crack is shown in Figure 3.2(d).

The actual formation of a crack will consume a certain energy known as the fracture energy, G_{Ft}, which is defined as the amount of energy consumed in the formation of a unit area of the crack surface i.e. area under the load-displacement curve divided by the crack area for a standard specimen. Propagation of the crack in concrete is dependent on the fracture energy. Fracture energy can be estimated using the equation proposed by CEB-FIP model code (1990), with a coefficient of variation of 33.3 %.

$$G_{Ft} = (0.0469\, d_a^2 - 0.5\, d_a + 26) \left(\frac{f_c'}{10} \right)^{0.7} \tag{3.2}$$

where G_{Ft} is in N/m, f'_c is the concrete compressive strength in MPa, d_a is the maximum aggregate size in mm.

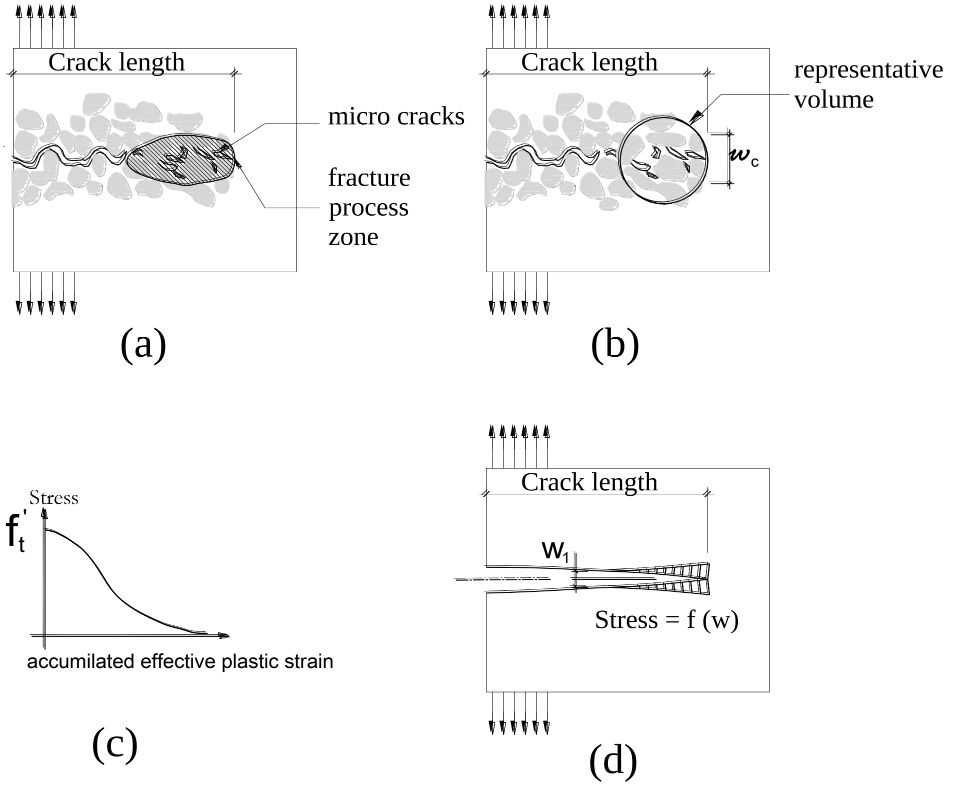

(a) (b) (c) (d)

Figure 3.2: (a) fracture process zone (b) representative volume (c) post-cracking softening response for concrete (d) tensile stress across a developing crack (after Bažant and Oh 1983)

On the other hand, for the behaviour of concrete under compression, it has been observed that deformations after peak stresses are also concentrated in certain zones (Santiago and Hilsdorf 1973). The determination of the fracture energy in compression is as important as the determination of the fracture energy in tension (Nakamura and Higai 1999), particularly for structures susceptible to compressive failure under flexural and shear-compression. Fracture energy in compression can be estimated using the equation proposed by Nakamura and Higai (1999)

$$G_{Fc} = 250\ G_{Ft} \tag{3.3}$$

3.4.2.1.2 Concrete material models in LS-DYNA

Several material models are available in the LS-DYNA library such as *MAT_016*, *MAT_025*, *MAT_072R3, MAT_078*, *MAT_084*, *MAT_096* and *MAT_159*. For this study, two material models for concrete are considered: (1) *MAT_072R3* (*MAT_concrete_damage_rel3*) and (2) *MAT_159* (*MAT_CSCM*). Understanding the model behaviour and model parameter is essential to a successful simulation. Hence a brief description of both models and their parameters are given.

3.4.2.1.2.1 Mat_concrete_damage_rel3 (MAT_072R3)

This material model has been developed by Malvar et al. (1997) and has proven efficient in predicting the response of standard uniaxial, biaxial, and triaxial concrete tests under both tension and compression (Schwer and Malvar 2005, Yonten et. al. 2005, and Tu and Lu 2009). Model *MAT_072R3* includes parameter generation capability that requires the user to input only the concrete compressive strength, f'_c (Schwer and Malvar 2005). A one parameter model is very attractive and easy to use. However, analyst must be careful in using the default parameters as it might yield erroneous results in some cases.

The model utilizes a plasticity based formulation with three independent dynamic failure surfaces namely: initial yield, maximum, and residual. The shape of the failure surfaces is a function of the hydrostatic pressure of the element, P and eight constants that need to be determined from experimental data. The failure surfaces are given by:

$$\Delta\sigma_y = a_{0y} + \frac{P}{a_{1y} + a_{2y}P} \quad \text{(initial yield surface)} \qquad (3.4)$$

$$\Delta\sigma_m = a_0 + \frac{P}{a_1 + a_2 P} \quad \text{(maximum failure surface)} \tag{3.5}$$

$$\Delta\sigma_r = a_{0f} + \frac{P}{a_{1f} + a_{2f} P} \quad \text{(residual failure surface)} \tag{3.6}$$

Upon defining the three failure surfaces, the loading surface representing the strain hardening, $\Delta\sigma$, is given by:

$$\Delta\sigma = \eta(\lambda)\ \Delta\sigma_m + (1-\eta(\lambda))\ \Delta\sigma_{min} \tag{3.7}$$

where $\eta(\lambda)$ is the yield stress function, a user-defined function of the modified effective plastic strain, λ. This function, $\eta\ (\lambda)$, ranges between 0→1 and should be calibrated using triaxial tests data under different confining pressures. $\Delta\sigma_{min}$ is equal to the initial yield surface, $\Delta\sigma_y$,if $\lambda < \lambda_{max}$ or the residual strength, $\Delta\sigma_r$, otherwise. The modified effective plastic strain is given by

$$\lambda = \begin{cases} \displaystyle\int_0^{\overline{\varepsilon}_p} \frac{d\overline{\varepsilon_p}}{\left[1 + P/f_t^{'}\right]^{b_1}} & , P \geq 0 \\ \\ \displaystyle\int_0^{\overline{\varepsilon}_p} \frac{d\overline{\varepsilon_p}}{\left[1 + P/f_t^{'}\right]^{b_2}} & , P < 0 \end{cases} \tag{3.8}$$

where $d\overline{\varepsilon_p}$ is the effective plastic strain increment and b_1 and b_2 are the damage parameters in compression and tension, respectively. The choice of the parameters b_1 and b_2 is a main factor governing the shape of the strain softening branches in compression and tension, respectively.

Mat_072R3 includes the effects of cracking by employing the smeared crack band model. In the model development conducted by Bažant and Cedolin (1979), the stress-strain relations are linked to fracture mechanics. A comprehensive description of the model can be found in Bažant (1985). Cracking is considered by reducing the normal stiffness across the cracks and the shear stiffness, gradually. In the same time, the stiffness parallel to the cracks is unaffected i.e. an orthotropic stiffness matrix for the cracked concrete is introduced (Bažant and Cedolin 1979). This reduction of stresses in concrete allows for stresses to be transferred to the reinforcement. In this model, crack initiation is based on strength criterion, i.e. when the maximum principal stress reaches the concrete tensile capacity, f'_t. On the other hand, propagation of the crack within the finite elements is based on fracture mechanics criterion, i.e. considering fracture energy (Bažant and Cedolin 1979). Smeared cracks are oriented perpendicular to the maximum principal stresses. The crack band model is defined by three material parameters: f'_t, G_{Ft}, and w_c. G_{Ft} is controlled by the input parameter b_2 and f'_t. For results to be independent of the mesh size, these parameters have to be adjusted to the chosen element size. The parameter w_c, is less significant in case of structures where a single crack is expected, e.g. non-reinforced elements. Thus different values of w_c gives equally good results. For reinforced elements, the w_c parameter refers to the minimum possible crack spacing (Bažant 1992).

3.4.2.1.2.2 Continuous Surface Cap Model (MAT_CSCM)

Model *MAT_CSCM* is an elasto-plastic damage model that was developed originally to model concrete in crashworthiness simulations (Murry 2004). The model includes isotropic constitutive equations, together with yield and hardening surfaces and damage formulations to model the softening behaviour and modulus reduction exhibited by concrete. The constitutive model utilizes a cap model with smooth intersection between the failure surface and hardening cap as illustrated in Figure 3.3. The model has been used successfully to predict standard uniaxial, biaxial, and triaxial concrete tests under both tension and compression (Murry et al. 2004). The user has the option of supplying all the model parameters or using the default properties by defining only the concrete strength and the maximum aggregate size.

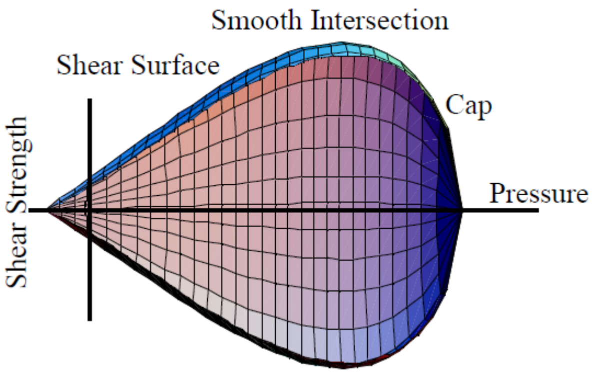

Figure 3.3: General shape of shear failure and cap hardening surface in two dimensions (Murry 2004)

The yield surface and the shear failure surface are formulated in terms of three stress invariants ($J_{1\rightarrow3}$) as given in Equations 3.9 and 3.10, respectively. In these equations, F_f is the shear failure surface, F_C is the hardening cap, and R is the Rubin three-invariant reduction factor. The values for α, β, λ, and θ should be determined from experimental data.

$$f(J_1, J_2', J_3') = J_2' - R\, F_f^2\, F_c \tag{3.9}$$

$$F_f(J_1) = \alpha - \lambda\, e^{-\beta J_1} + \theta\, J_1 \tag{3.10}$$

Concrete softening behaviour is modeled using the damage formulation shown in Equation 3.11, where σ^d and σ^{vp} are the stress tensors with and without damage, respectively. The damage parameter, d, ranges from zero for no damage to unity for complete damage. Damage is initiated when a strain-based energy term exceeds a damage threshold, r_o. Two distinct formulations, initiation and accumulation of brittle (tension) and ductile (compression) damage are defined. Equations 3.12 and 3.13 define the brittle and ductile damage parameter as a function of $\tau_{brittle}$ and $\tau_{ductile}$, which represent instantaneous strain energy-type terms for damage accumulation. The parameters A, B, C, and D define the shape of strain softening branch of the stress-strain relationship. Two of these parameters, B and D, are user defined, while A and C are internally calculated for each element to ensure constant strain energy is maintained regardless of the element size.

$$\sigma_{ij}^{d} = (1 - d)\, \sigma_{ij}^{vp} \tag{3.11}$$

$$d(\tau_{brittle}) = \frac{0.999}{D}\left[\frac{1 + D}{1 + D\, e^{-C(\tau_{brittle} - r_{o\ brittle})}}\right] \tag{3.12}$$

$$d(\tau_{ductile}) = \frac{d_{max}}{B}\left[\frac{1 + B}{1 + B\, e^{-A(\tau_{ductile} - r_{o\ ductile})}}\right] \tag{3.13}$$

3.4.2.2 Steel

Steel material behaviour is not as complicated as concrete. Steel is modelled using material model *MAT_024* (*MAT_piecewise_linear_plasticity*). This model is suitable for modelling isotropic and kinematic hardening plasticity materials such as steel. This model is favoured because of its flexibility regarding the definition of the stress-strain curve. An arbitrary multilinear idealization of the smooth stress-strain relationship could be defined. A built-in failure criterion is optional. Solid elements are removed from the model (i.e. failed) upon their maximum principal plastic strain reaching a specified value, resembling rupture of the steel material.

3.4.3 Contact modelling

The interaction between any two parts that come into contact during simulation (for instance panel and base or anchor bolt and panel) is modeled in the realm of finite elements by defining a contact. Two spring element, normal and parallel to the contact surface, are introduced between adjacent nodes on the surfaces that are in contact. Understanding the contact treatment is crucial for successful modelling. Hence, the basics of contact modeling between solid elements in LS-DYNA are briefly discussed. Discussion is still applicable to a number of other finite element analysis packages. Discussion is limited to the penalty method, which is one of the most common methods to treat contact.

For each time step, contact algorithm will search for any slave node that penetrates the master surface. For each penetrating node, two forces are applied: 1) a restoring force normal to the penetrated segment, F_n, Equation 3.14, 2) a friction force parallel to the penetrated surface, F_s, Equation 3.15, as shown in Figure 3.4. The restoring force will depend on the penetration depth, d, and the spring stiffness, k.

Friction forces in LS-DYNA are based on Coulomb formulation (LSTC 1998), where they are applied as equivalent elastic-plastic spring to nodes in contact with a surface. The friction force depends on the instantaneous friction coefficient, μ[†], and the normal force, F_n, and is governed by Equation 3.15.

$$F_n = k \cdot d \tag{3.14}$$

$$F_s \leq \mu \cdot F_n \tag{3.15}$$

Once the acting force reaches the maximum possible friction force, $\mu . F_n$, the two surfaces start to slide and F_s remains constant. Further details are given in LS-DYNA keyword and theoretical manuals (LSTC 1998 and LSTC 2009).

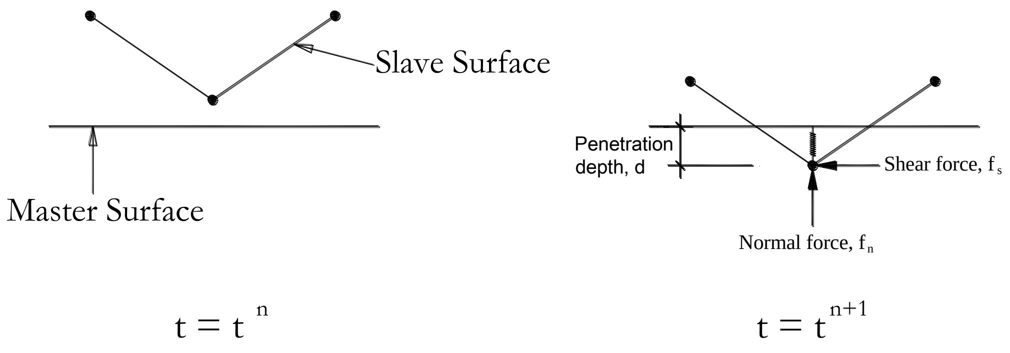

Figure 3.4: Contact forces

Two options available in LS-DYNA are used to simplify the contact definition: 1) the *automatic* option, which allows the slave and master surface to be generated internally from the part's ID given in the contact definition card, 2) the *surface_to_surface* option, which uses two way treatment of the contact i.e. the slave nodes are checked for penetration of the master surface as

---

[†] LS-Dyna determines the instantaneous friction coefficient μ from static and dynamic friction coefficients μ_s, μ_d, defined in the input file. Instantaneous function coefficient $\mu = \mu_d + (\mu_d - \mu_s) \cdot e^{-c|v|}$, where c is the decay constant and v is the relative velocity between the slave node and the master node. In this study, μ_d and μ_s are equal, i.e. μ is constant

well as the master nodes are checked for penetration of the slave surface. In this case, definition of the slave and master surfaces is arbitrary as results will be identical.

Inherently, penalty method may induce spurious numerical oscillation in the contact penalty forces. Often, amplitudes of such oscillation remains below a reasonable limit and the averaged forces are representative of the actual behaviour. Measures such as using a finer mesh, reducing time step, applying the load over a longer period, or increasing the viscous damping coefficient[‡] will reduce the oscillation amplitude but would definitely increase the run time.

3.4.4 Numerical Model

In this work, 8-noded brick elements with one integration point are used to model plain concrete and steel anchors (element form 1 in LS-DYNA). Both *MAT_072R3 and MAT_159* are used to model concrete, while *MAT_024* is used to model steel. Reinforcement is modelled using two-node beam elements and perfect bond between concrete and steel is assumed, e.g. beam and brick elements are connected to the same nodes. Contact is defined between different parts using the algorithm *contact_automatic_surface_to_surface*. In all developed models, loads are applied in a displacement controlled fashion to allow the model to capture the post-peak behaviour.

3.4.5 Hourglass control

Hourglass modes are unrealistic modes of vibration associated with elements with reduced integration points such as the one used in this study. Reduced integration elements are favoured for their computational efficiency. Therefore, elements hourglassing need to be controlled.

[‡] VCD, Defined in the second card of the contact definition

Hourglass modes are controlled by introducing artificial viscosity to dampen the vibration. Different forms of hourglass control are available in LS-DYNA. A stiffness form of hourglass control, IHQ= 4 in the **control_hourglass* card, is recommended for structural analysis and is used in the current study. Hourglass energy should be monitored throughout the analysis to ensure that it constitutes only a trivial fraction of the internal energy. The cards **control_energy* and **database_matsum* are invoked to enable hourglass energy monitoring.

3.5 Structural behaviour and failure modes under bending moment

The behaviour under bending moments governs the response of lower joints of a shear wall. The structural behavior of the proposed joint, under bending, is similar to the connection between a rigid steel column base plate and its supporting concrete footing. For small moments, where the resultant force is within the middle third of the connection, the entire contact area between the two panels will be under compression and anchors are inactive at this stage. For higher moments where the resultant force falls outside the middle third, uplift on one side is expected. Acting moment will induce compressive bearing stresses at one side, and tension forces in the other side that has to be resisted by the anchor. Static equilibrium of the connection is depicted in Figure 3.5. Three failure modes might be triggered by this stress distribution as shown in Figure 3.6; (1) breakout of concrete cone. (2) yielding and eventually rupture in steel anchor shaft. (3) concrete crushing under excessive bearing stress.

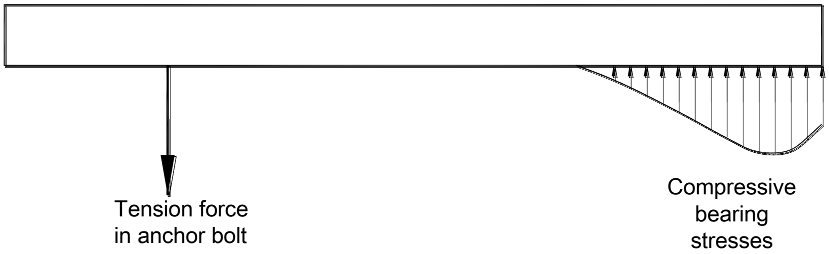

Figure 3.5: Static equilibrium under bending moments

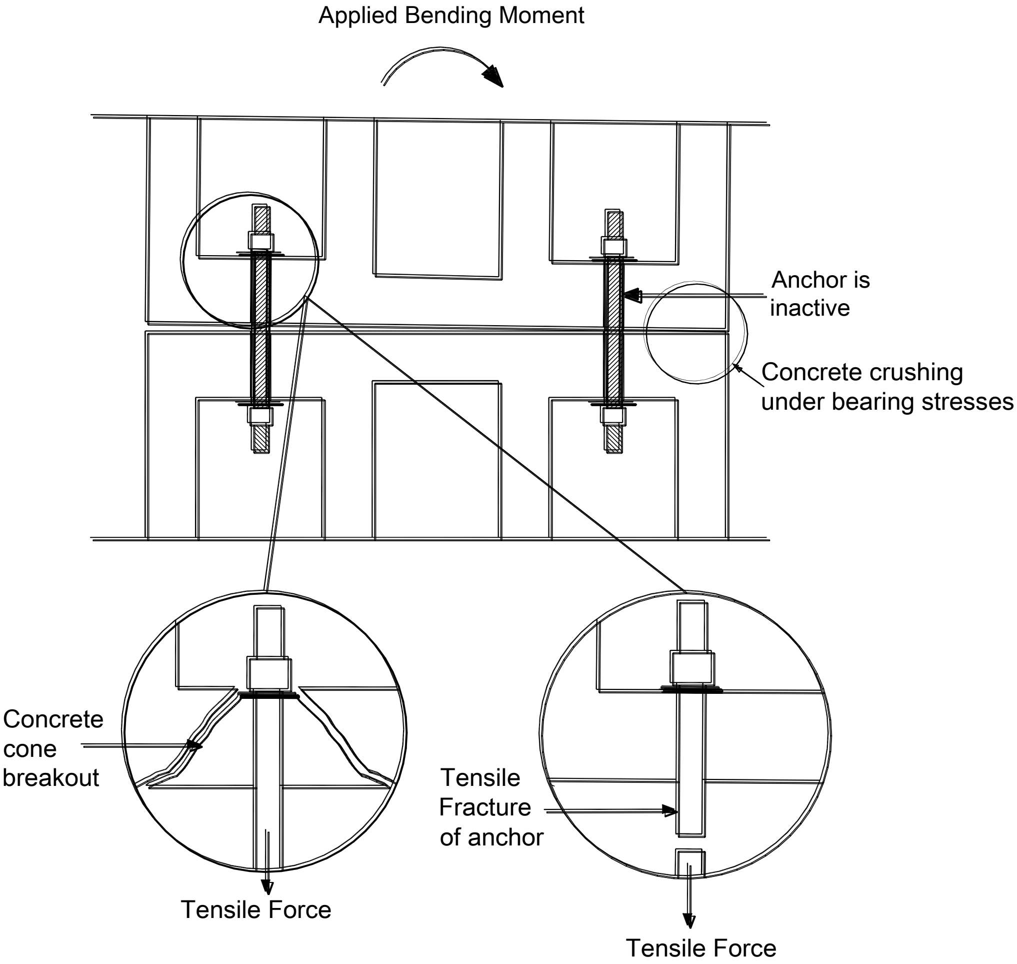

Figure 3.6: Expected failure modes

3.5.1 Concrete cone breakout failure mode

Concrete breakout failure is initiated by micro-cracking in concrete beneath the anchor nut and washer due to high circumferential tensile stresses. Under increasing load, micro-cracks join to form a macro-crack that propagates towards the other side pushing out a cone-like plug of concrete as illustrated in Figure 3.6. The load carrying capacity is dependent on the strength of the concrete. Rebar contribution to the capacity is minor and considered only if the rebar is oriented to resist the cone propagation. Rebar contribution is limited to a maximum of 15% of the concrete breakout strength. In general, the concrete cone failure surface is inclined at about 35° with respect to the free surface (Fuchs et al. 1995).

3.5.1.1 Experimental study by Primavera et al. (1997)

Concrete breakout failure of the proposed joint is fairly similar to breakout of cast-in-place anchors. Breakout tests of cast-in-place anchors carried out by Primavera et al. (1997) are selected from the literature to validate the finite element model. Five identical specimens, denoted Group-H, were tested. The dimensions of the specimens are depicted in Figure 3.7. The concrete strength was 51.4 MPa. The observed failure mode was brittle with no noticeable yielding of the anchor. The failure load of the five specimens ranged from 112.7 to 126.7 kN, with an average of 120.5 kN, and a coefficient of variation of 4.3%.

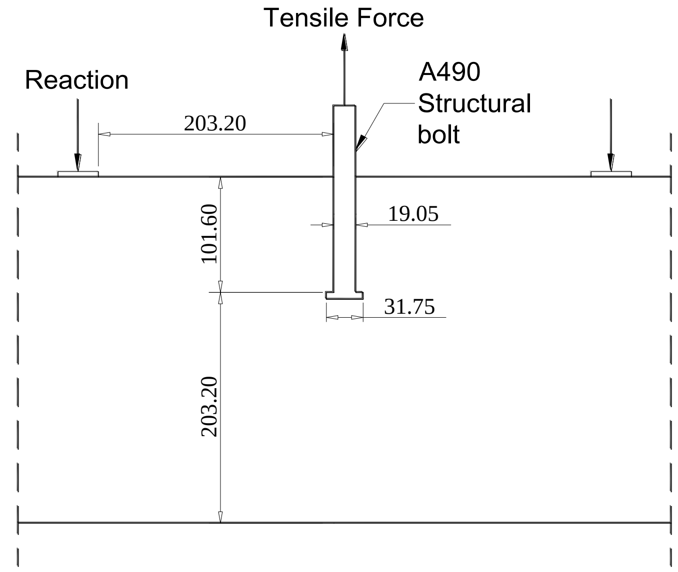

* Dimensions in mms

Figure 3.7: Group-H specimens tested by Primavera et al. (1997)

3.5.1.1.1 Finite Element model for Group-H specimens

Due to symmetry in both orthogonal directions, only one-quarter of the specimen is modeled. The assigned material properties are given in Table 3.1. All nodes across the axes of symmetry are restrained by roller support condition to uphold symmetry. Nodes corresponding to the outer edge of the top and bottom faces are restrained in the vertical Y-direction. Vertical loading is applied as an imposed upward displacement at nodes at the top surface of the anchor bolt. The overall dimensions, supports and loading conditions are depicted in Figure 3.8.

Table 3.1: material properties used for modeling Primavera et. al. (1997)

Concrete			
$f_c'^{\dagger}$ [MPa]	$f_t'^{\ddagger}$ [MPa]	$d_a^{\ddagger}$ [mm]	G_{Ft}^{*} [N/mm]
51.4	4.16	10	80.80x10^{-3}
Steel			
E [MPa]	E_{sh} [MPa]	f_y [MPa]	f_u [MPa]
200000	2000	896	1034

† Reported; ‡ Estimated; * Calculated

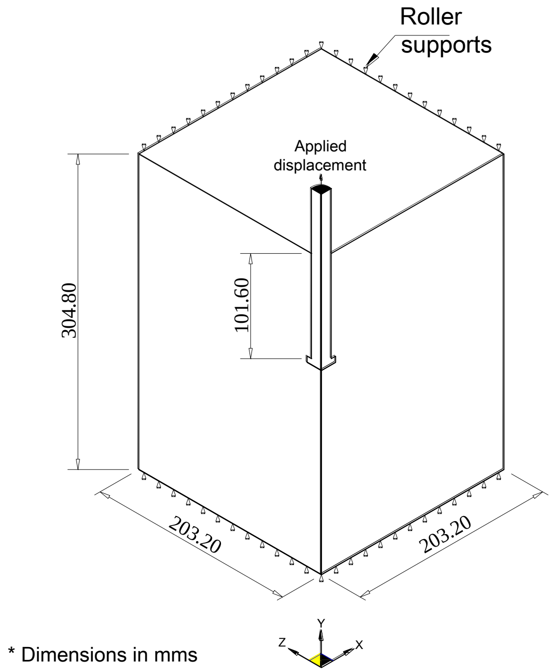

Figure 3.8: One-quarter model for Group-H specimens

Concrete block and anchor are modelled after specimen geometry. Three different finite element uniform meshes are used to study the effect of element size. Different meshes are shown in Figure 3.9. In all models, the mesh for the steel anchor is not modified.

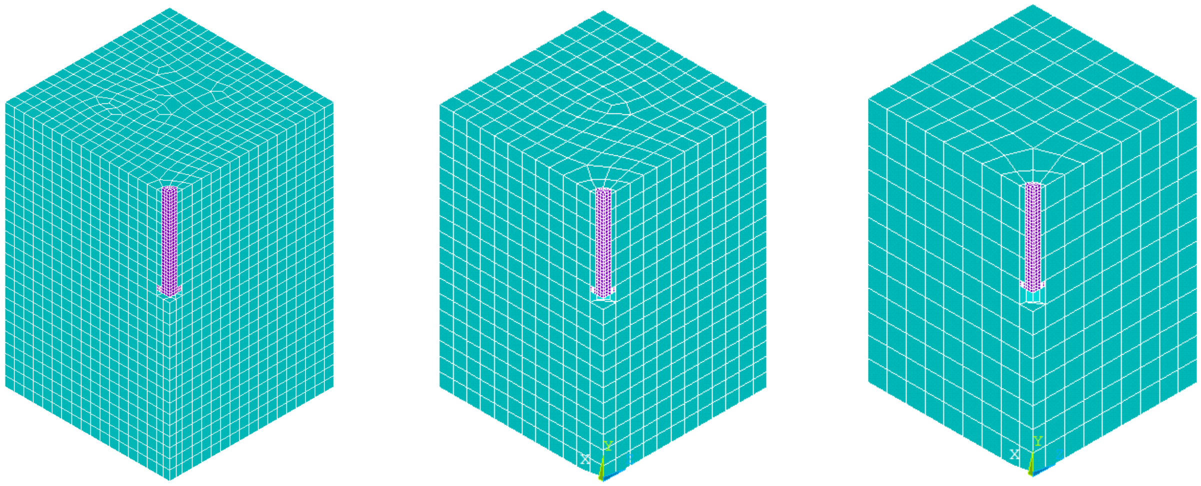
Mesh P1

Mesh P2

Mesh P3

Figure 3.9: Finite element meshes

3.5.1.1.2 Analysis results of Group-H model

Discussion will be divided into two sections: The first section discusses models where *MAT_072R3* is used to simulate concrete, with models using *MAT_159* discussed subsequently.

3.5.1.1.2.1 Models with MAT_072R3

3.5.1.1.2.1.1 Finite element mesh and model parameters

For a smeared crack model, the parameters defining the softening branch of the tensile behaviour are not material constant. These parameters should be adjusted based on the element size to ensure objectivity with regards to mesh choice. The area under the stress-strain curve should be adjusted to G_{Ft}/h_c, where h_c is the characteristic length of the element (Malvar et al. 1997). For the material model *MAT_072R3*, the input parameter b_2[§] governs the softening branch of the stress-strain behaviour of concrete subjected to a uniaxial tensile test, as shown by Equation 3.8. Consequently, b_2 governs the fracture energy, G_{Ft}. A pre-analysis should be carried out for a single element under tensile stresses, varying the parameter b_2 until the area under the obtained stress-strain curve coincides with G_{Ft}/h_c (see Figure 3.10). As mentioned earlier, the parameter w_c is less important as the specimen contains no reinforcement. Different values for w_c lead to reasonably equal results should the parameter b_2 is adjusted for each value.

The predicted direction of propagation of the crack might be influenced by mesh topology. If the crack direction is not known, using a uniform square mesh would be most suitable as any other mesh might be biased favouring a number of crack paths over others. Also, a uniform square

---

[§] Defined in the seventh card of *MAT_072R3*.

mesh would preserve the width of the crack band, w_c, throughout the crack propagation (Bažant and Oh 1983).

The element size should be chosen to correspond to the representative volume (see Figure 3.2 (b)), which is proportional to the maximum aggregate size. Bažant and Oh (1983) suggests a representative volume not less than 1.5 times the maximum aggregate size. However, a relatively smaller value could be used with high strength concrete as it is more homogeneous.

For the three different finite element meshes used in this study, the model parameters are given in Table 3.2. The stress-strain curves for a single element analysis are shown in Figure 3.10.

Table 3.2: Model parameters

Model	Average element size [mm]	b_2	w_c [mm]	Area† [N/mm^2]
P1	11.89	−0.53	25.40	6.73x10^{-3}
P2	16.98	+0.75	25.40	4.76x10^{-3}
P3	24.59	+2.20	25.40	3.29x10^{-3}

† Area under the stress-strain curve for a single element analysis

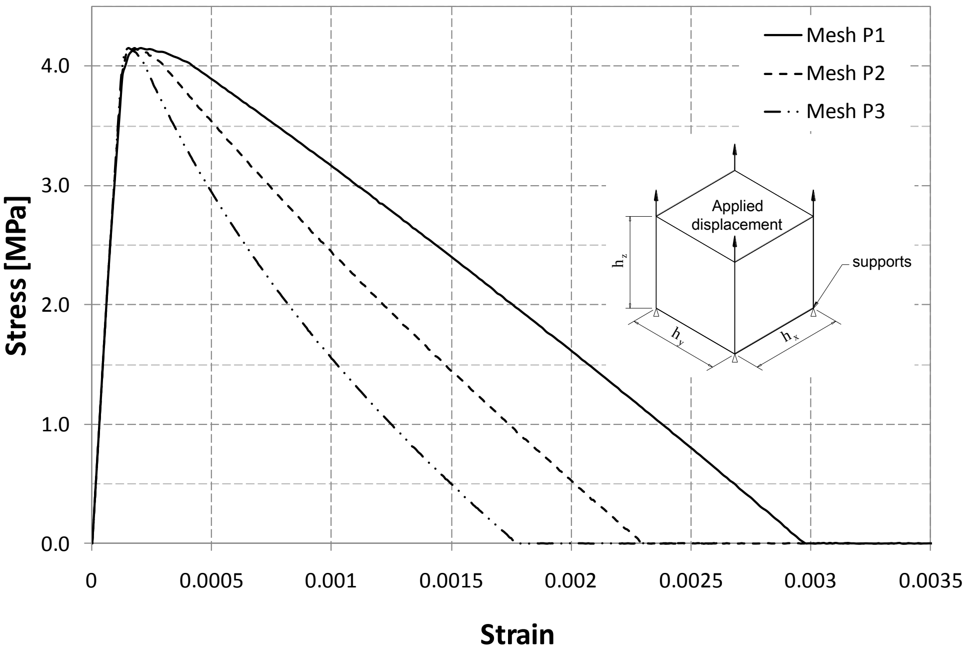

Figure 3.10: Single element tensile stress-strain curve for different element sizes (MAT_072R3)

Figure 3.11 shows the load-deflection curves of the 5 specimens (H-Group) together with the three models. The predicted maximum loads, 132.4 and 128.0 kN for model P1 and P2, respectively, are in reasonable agreement with the experimental values ranging from 112.7 to 126.7 kN. For model P3, failure load is 103.65 kN indicating a loss of accuracy with increased element size. As seen from Figure 3.11, the failure load of the two meshes P1 and P2 are fairly close demonstrating objectivity with regards to element size. Initial stiffness of the experiments could not be captured by the model. Unfortunately, the model is not able to capture the post-peak softening experienced by some of the tested specimens. However, considering the brittle nature of the failure and the scatter of the test specimen results, the results of the numerical model can be considered acceptable. Moreover, the contribution of the post-peak response of the breakout failure to the overall joint response is negligible. The ductility of the joint is dependent on avoiding such brittle failure and allowing the steel anchor to yield without triggering a breakout failure. The crack pattern, shown in Figure 3.12, matches the experimentally observed one. After reaching the maximum load, as crack propagates, steel disk and the concrete around the fracture surface drastically get unloaded, releasing the elastic energy stored in the system (see Figure 3.13). The stresses in the steel anchor remain below the yield stresses throughout the simulation, except for few elements at the head-shaft connection area where stress concentration is expected. Generally, the failure mode and failure load are simulated with reasonable accuracy.

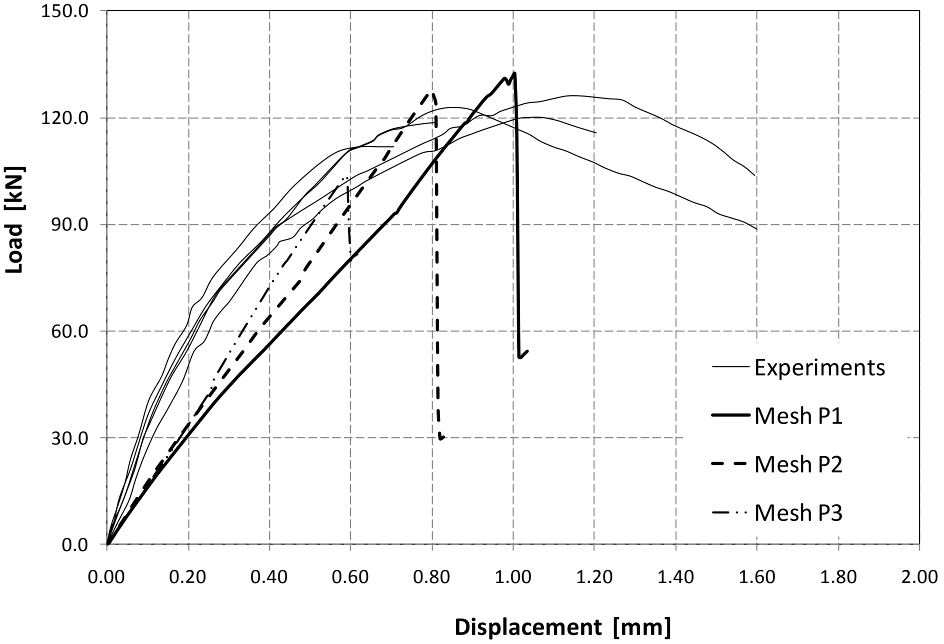

Figure 3.11: Model versus Tests load-Displacement response (MAT_072R3)

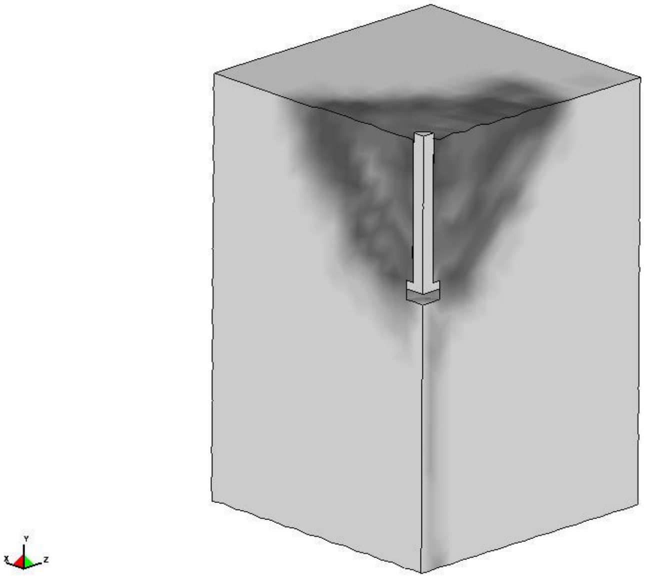

Figure 3.12: Crack pattern (MAT_072R3)

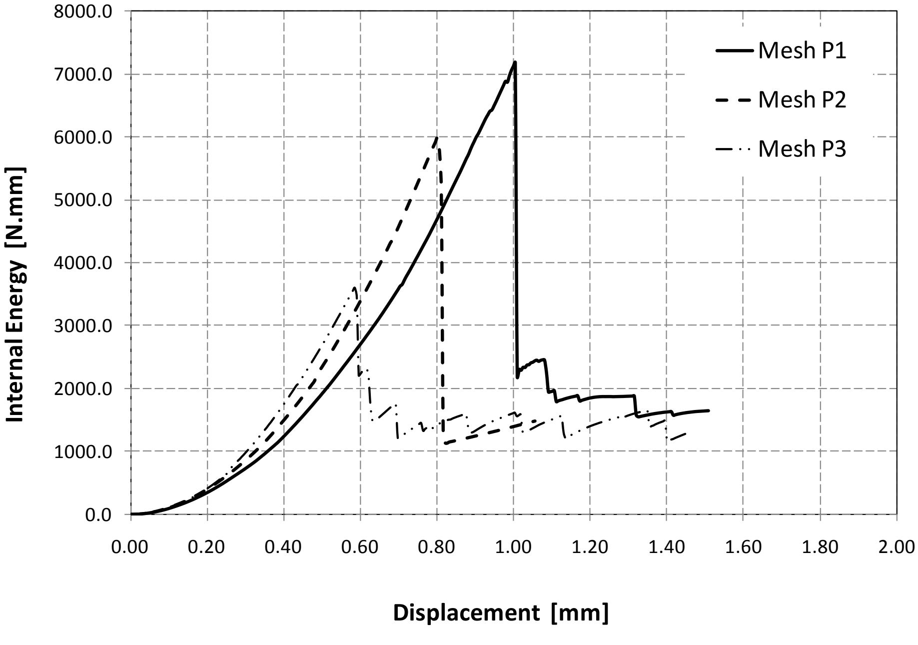

Figure 3.13: Internal energy of the model (MAT_072R3)

3.5.1.1.2.1.2 Parameters sensitivity study

The model behaviour, and in particular the failure load, is sensitive to the material tensile strength, f'_t, and the fracture energy, G_{Ft}. Analyst should be caution when choosing these parameters. A parametric study is carried out to examine the sensitivity of selected material properties on the numerical response. For the following sensitivity analyses, model P2 is chosen as a reference.

3.5.1.1.2.1.2.1 Tensile strength

Different formulas are available in the literature for estimating the tensile strength as a function of the compressive strength. To evaluate the effect of the input tensile strength on the model behaviour, different values for the tensile strength are used. In addition to the model default value (calculated using CEB-FIP model code 1990), two values representing the maximum and minimum estimates for the tensile strength are used. However, the fracture energy is maintained at $G_{Ft}=80.80\text{x}10^{-3}$ N/mm by adjusting b_2 (see Table 3.3 and Figure 3.14). All other parameters are kept constant. Load-displacement curves of the models are shown in Figure 3.15. Considering the difference in the assigned values, failure load has not varied as much. An increase in the tensile strength results in a minor increase of the failure load.

Table 3.3: Effect of concrete tensile strength on model behaviour

	Model 1a	Reference model	Model 1b
f'_t [Mpa]	$0.33\sqrt{f'_c}$	$1.4\left(\frac{f'_c}{10}\right)^{2/3}$	$0.12\,f'_c$
	2.37	4.16	6.16
[ratio]	0.57	1.00	1.48
b_2	-1.30	+0.75	+2.30
P_{max}[kN]	113.1	128.0	132.1
[ratio]	0.88	1.00	1.03

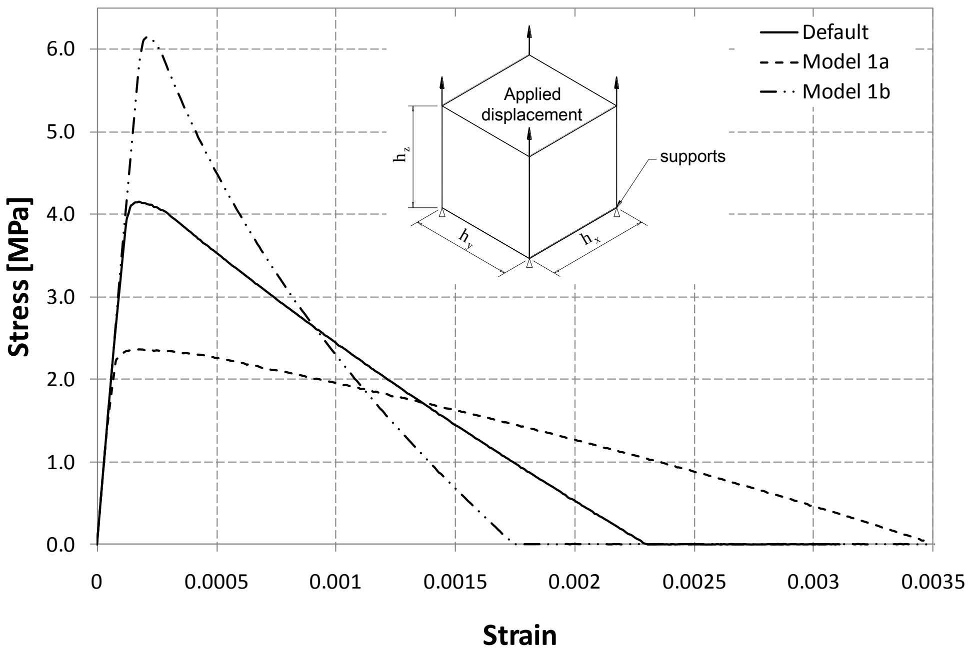

Figure 3.14: Single element stress-strain curves for different assigned tensile strength (MAT_072R3)

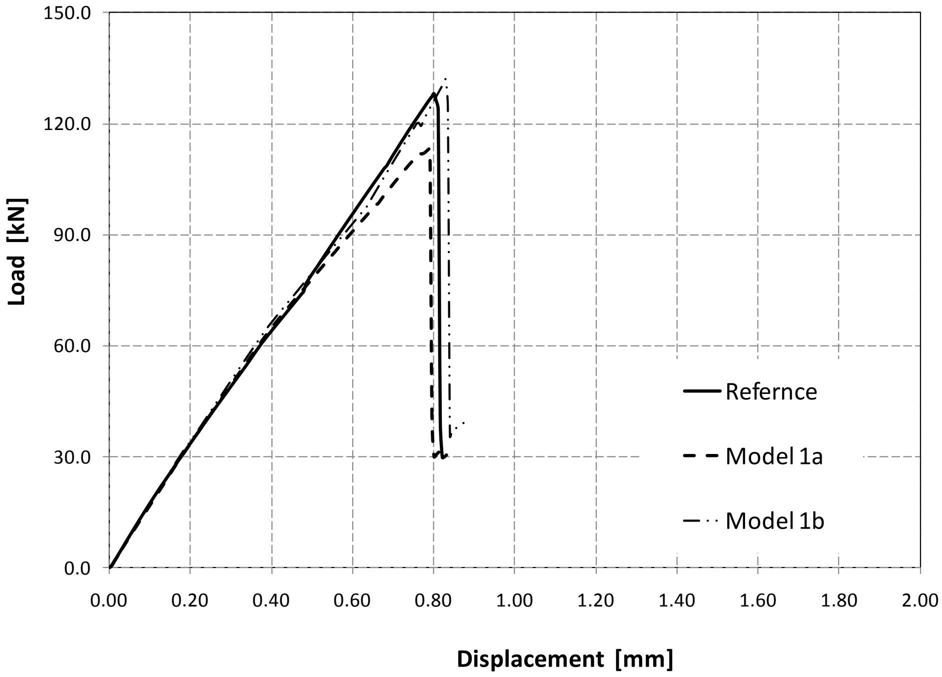

Figure 3.15: Effect of assigned tensile strength on model load-deflection response (MAT_072R3)

3.5.1.1.2.1.2.2 Fracture energy

As mentioned earlier, a 33.3 % C.O.V. is expected for the fracture energy G_{Ft} calculated using Equation 3.2. Different values for the fracture energy are considered by varying b_2 (see Table 3.4 and Figure 3.16). Load-displacement curves of the models are shown in Figure 3.17. Failure load is sensitive to the input fracture energy as it significantly increases with increasing fracture energy. The effect of the fracture energy is more pronounced than that of tensile strength. Analyst should try to find the most accurate value, for fracture energy, available either from tests or available formulas. It is noticed that reducing fracture energy will shift the failure mode towards a concrete splitting mode.

Table 3.4: Effect of concrete fracture energy on model behaviour

	Model 2a	Reference model	Model 2b
Fracture Energy [N.mm]	53.33x10^{-3}	80.80x10^{-3}	107.46x10^{-3}
[ratio]	0.66	1.00	1.33
b_2	+2.38	+0.75	-0.31
P_{max}[kN]	95.3	128.0	153.5
[ratio]	0.74	1.00	1.20

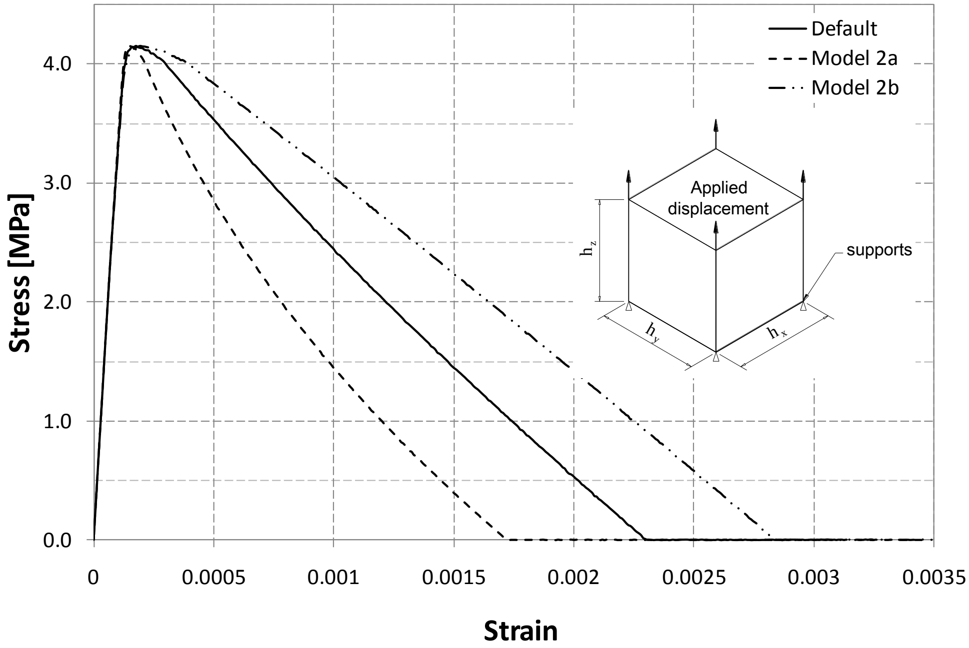

Figure 3.16: Single element stress-strain curves for different assigned fracture energy (MAT_072R3)

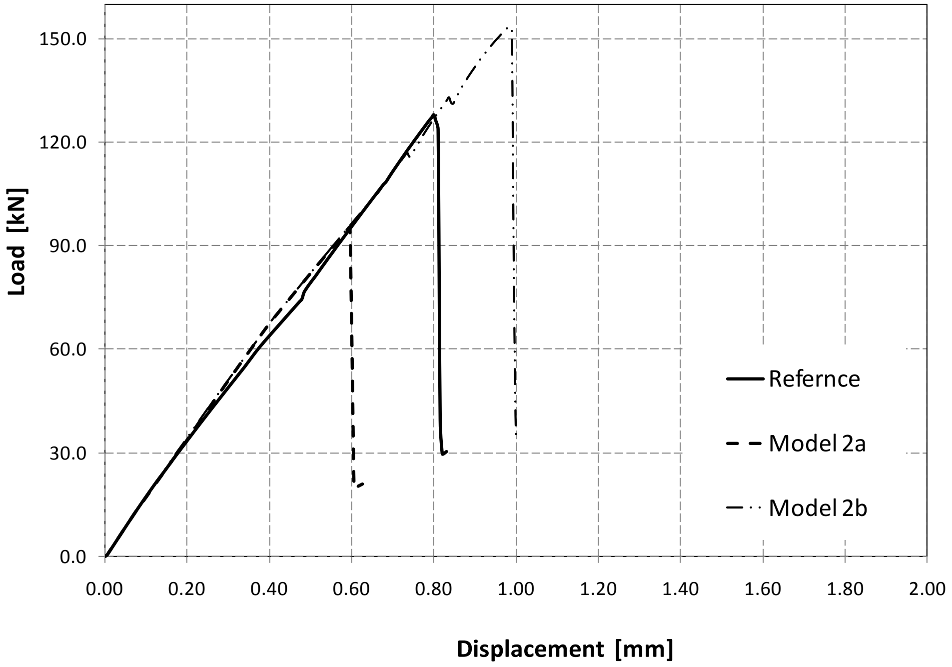

Figure 3.17: Effect of fracture energy on model load-deflection response (MAT_072R3)

3.5.1.1.2.2 Models with MAT_159

Figure 3.18 shows the load-deflection curves of the 5 specimens (H-Group) together with the three models using *MAT_159*. The predicted maximum loads, 128.8, 135.4 and 129.4 kN for model P1, P2, and P3, respectively, are in reasonable agreement with the experimental values which ranges between 112.7 to 126.7 kN. The material model parameters are identical for all three meshes used. This is unlike *MAT_072R3* parameters that have to be adjusted according to the element size. Initial stiffness of the model is less than the experimental one. The model is able to capture the post-peak softening experienced by some of the tested specimens. Compared to *MAT_072R3*, a greater ductility and slightly higher peak loads are achieved. Nevertheless, ultimate load is overestimated by approximately 10 %. The stresses in the steel anchor remain below the yield stresses throughout the simulation, except for few elements at the head-shaft connection area where stress concentration is expected. In general, the overall behaviour of the specimens is adequately simulated.

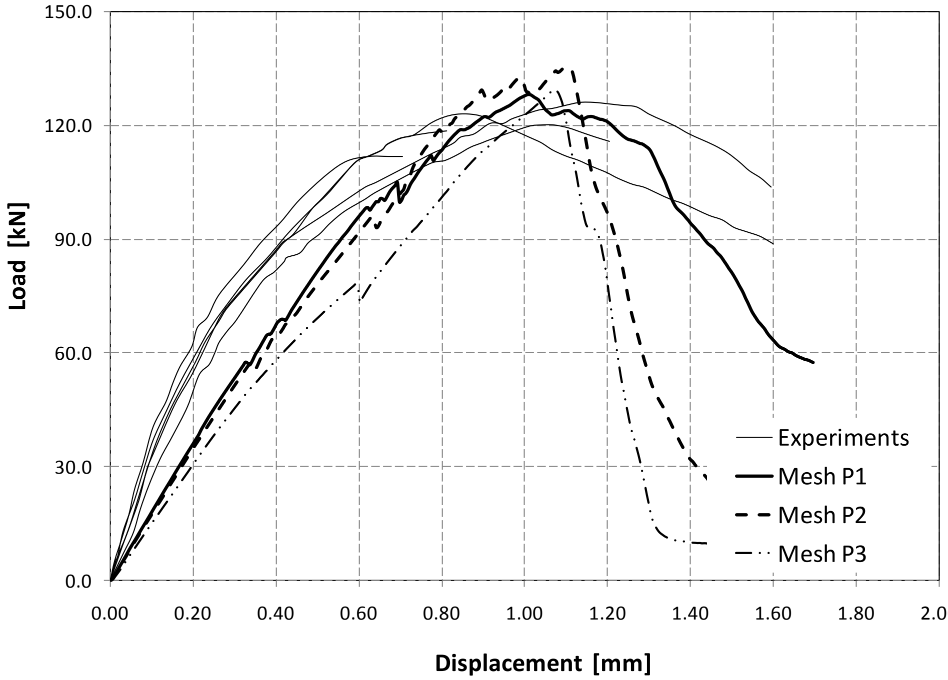

Figure 3.18: Model versus Tests load-Displacement response (MAT_159)

3.5.2 Rupture of steel anchor failure mode

Steel failure is attained by yielding and fracturing of the steel anchor. The failure starts with yielding and necking of the steel, followed by steel fracture, as shown in Figure 3.6 and Figure 3.19. The load carrying capacity depends only on the strength of the steel. Although the modeling of such a failure mode is rather uncomplicated, a simplified model is built to verify the suitability of the proposed material model, stress-strain relationship, and failure criterion.

Generally, two different types of stresses and strains could be defined for steel material; engineering and real stresses. Engineering stresses are defined as the load divided by a constant, original area, while true stresses are defined as the load divided by a variable, instantaneous area. Engineering strains are the total elongation divided by the original length, while true (natural) strain is the sum of the infinitesimal strains calculated using the instantaneous length. The area of an anchor subjected to a tensile load constantly changes with loading. In the linear elastic range, the change in the area is uniform due to the Poisson’s effect. Whereas in the plastic range, a neck is formed causing the change in the area to be more rapid. Both stress-strain relationships are almost identical in the elastic range. Whereas beyond the proportionality limit, the engineering stress rises and then falls after going through a maximum, while true stress continue to rises until failure. Engineering stress-strain relationship is commonly used for design purposes but it does not give true indication of the material behaviour necessary for finite element analysis. This is especially true if the plastic behaviour and failure are of particular interest. Thus, models used herein will be defined using the true stresses rather than engineering stresses. The true stress-strain curve can be estimated based on the engineering stress-strain relationship (Dowling 2007). Up to the onset of necking and assuming that specimen volume remains constant, Equations 3.16 and 3.17 may be used to estimate the true stresses and strains. Beyond necking, Equations 3.18, 3.19, and 3.20 are used.

$$\sigma_t = \sigma \;.\; (1+\varepsilon) \qquad (3.16)$$

$$\varepsilon_t = \ln(1+\varepsilon) \qquad (3.17)$$

$$\sigma_t = C\ \varepsilon_t^n \tag{3.18}$$

$$n = \ln(1+\varepsilon_u) \tag{3.19}$$

$$C = \frac{\sigma_u\ e^n}{n^n} \tag{3.20}$$

where σ and ε are the engineering stresses and strains, σ_t and ε_t are the true stresses and strains, C is the strength coefficient, n is the strain hardening exponent, σ_u, ε_u are the maximum engineering stress and the corresponding strain and e is the natural logarithm base (≈ 2.718).

Figure 3.19: Necking, and fracture of a 1" threaded bar under direct tension test

A model representing 1″ threaded bar under axial tension is shown in Figure 3.20(a). The model consists of an anchor shaft with the diameter of the thread root and two nuts modeled as integrated parts of the shaft. Chosen element size is 6.0 mm. *Mat_024* is used to model the steel anchor, whereas a linear elastic material model is assigned to the two nuts. Reported engineering stresses and estimated true stresses are illustrated in Figure 3.21. Equal and opposite displacements are prescribed at the inner surface of the nut, driving the two nuts away from each other. The model is able to capture the necking that occurred during the test as shown in Figure 3.20 (b and c). As shown in Figure 3.22, using the engineering stress-strain relationship underestimates the resistance in the plastic range and the model fails prematurely at lower displacement. This confirms the adequacy of using real stress-strain relationship. A maximum plastic strain at failure of 0.22 is used in the material model. This value of maximum strain, while it is unrealistic and overestimates the material ductility, is necessary for the model to achieve the total displacement observed during testing. However since it is able to replicate with reasonable accuracy the load-total displacement relationship, it is used in subsequent models.

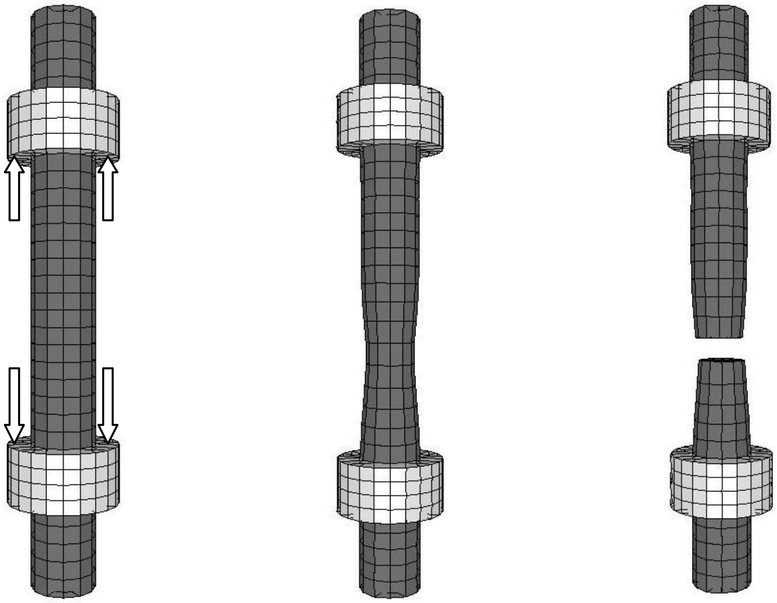

(a) (b) (c)

Figure 3.20: Finite element modeling of 1"threaded bar subjected to tensile load (a) mesh and loading (b) deformed shape at imminent failure (c) failure

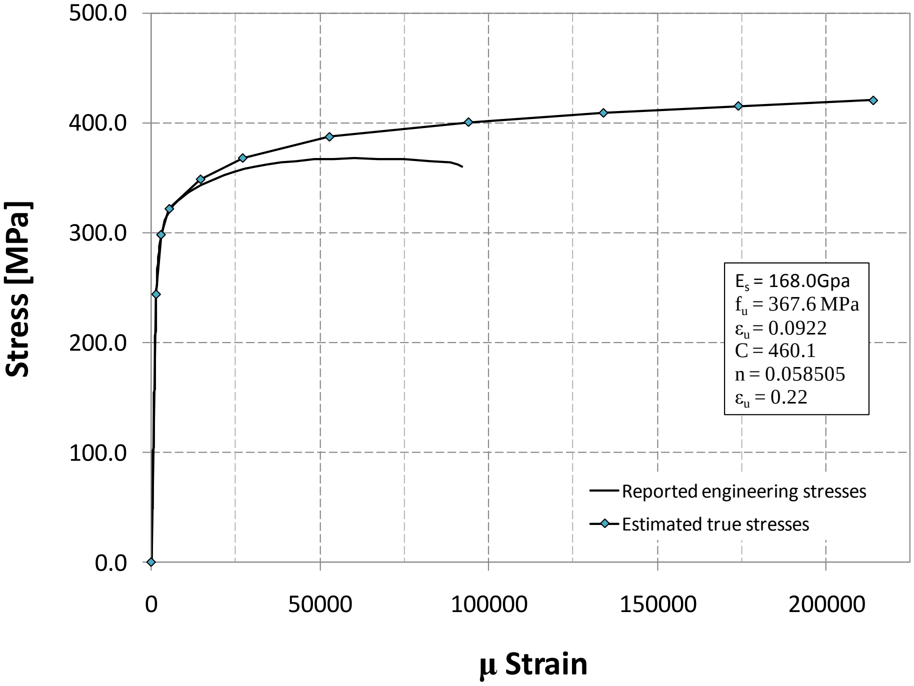

Figure 3.21: Stress-strain relationship

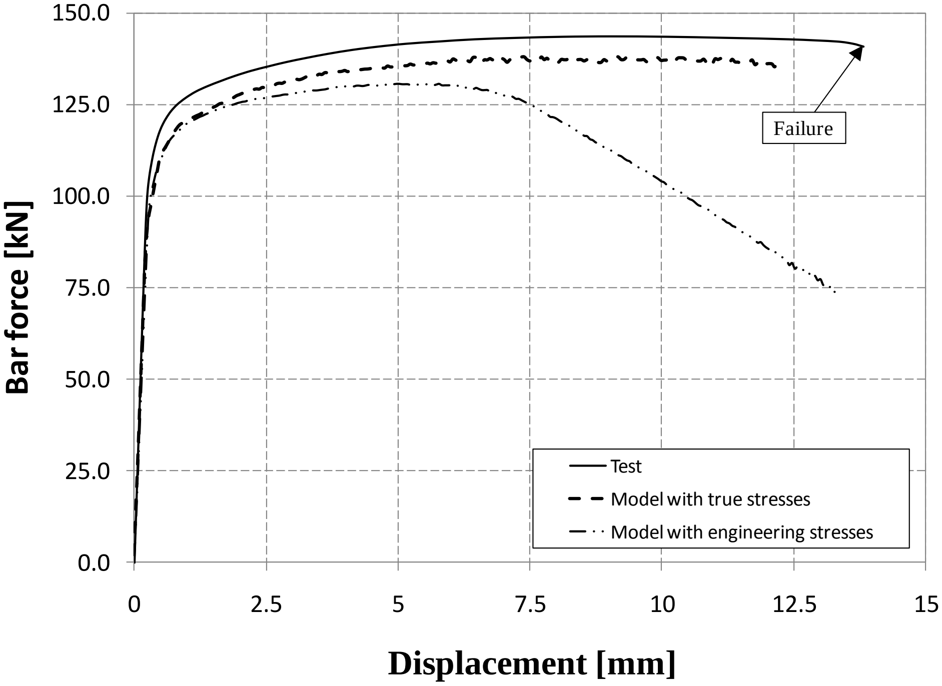

Figure 3.22: Experimental vs. model load-displacement curve for anchor bolt under direct tension

3.6 Structural behaviour and failure modes under shearing load

The behaviour under shearing loads governs the response of upper joints of a shear wall. Shear behaviour also contributes to the overall response of lower joints. Shear forces are transferred across the joint by two mechanisms: 1) shear friction and 2) Dowel action. Initially, shear force is fully resisted by friction associated with net compressive resultant applied at the panel-to-panel interface, while anchors are not loaded in shear. The friction force R is given by:

$$R = \mu \cdot C \tag{3.21}$$

where μ is the friction coefficient between the two concrete surfaces and C is the resultant compressive force at the panel-to-panel interface. When the applied shear force exceeds the value given by Equation 3.21, slip across joint surface is initiated. Relative displacement between panels will cause continuity bars to deform. The resistance of the bars to deformation is attributed to the dowel action mechanism, which will contribute to the connection shear resistance. There are three mechanisms associated with dowel action, namely shear, flexural, and kinking action of reinforcement (Paulay et al. 1974). The shear capacity is governed by steel strength, as shown in Figure 3.23. However, when large rebars are used, the concrete stresses around the rebars increases significantly, thus shear capacity might be governed by concrete strength rather than steel.

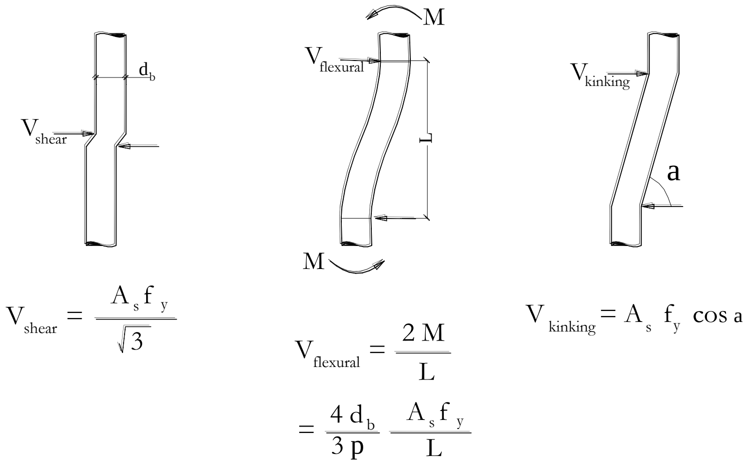

$$V_{shear} = \frac{A_s f_y}{\sqrt{3}}$$

$$V_{flexural} = \frac{2M}{L} = \frac{4 d_b}{3 p} \frac{A_s f_y}{L}$$

$$V_{kinking} = A_s f_y \cos a$$

Figure 3.23: Dowel action mechanisms (after Paulay et al. 1974)

3.6.1 Experimental study by Foerster et al. (1989)

The shear behaviour of the connection between load bearing wall panels was studied experimentally by Foerster et al. (1989). The tested connection consisted of two identical panels, with over all dimensions of 1660 x 1290 mm and 200-mm thickness. The chosen connection dimensions correspond to a prototype scale of the precast panels typically used in high rise construction. Three specimens were tested: SP11, SP12, and SP12C. For Specimen SP11, panels were connected using dry pack grout only. For other specimens, in addition to the dry pack grout, two 25M-Grade-400W mild steel reinforcing continuity bars were used. Continuity across the joint was achieved through welding of the rebar protruding from one panel to a steel angle embedded in the other panel (see Figure 3.25). Specimens were identical in all other aspects. Specimens were preloaded with a uniform pressure of 2.0 MPa (corresponds to 408 kN), normal to the joint to simulate the effect of gravity loads. Horizontal load was then applied incrementally up to either failure or a state of loss of load carrying capacity. Test results of one sample of the continuity bars indicated a yield and ultimate strength of 457.3 and 643.2 MPa, respectively. The concrete strength of specimen SP12C was f'_c = 43.2 MPa. The observed shear load-slip diagram is presented in Figure 3.24. For specimens SP11 and SP12, the initial peak load corresponds to the cracking of the dry pack grout. Specimen SP12C was chosen to be modelled as the dry pack joint in this specimen was cracked prior to testing. Therefore, its load-slip response is similar to the proposed joint which does not use dry pack. Comparing results of SP12 and SP12C, the dry pack grout only affects the first part of the load-slip curve. Specimen SP11, after cracking of dry pack grout, resisted a shear force of 371 kN, implying a friction coefficient, μ=0.91. This friction coefficient is used in the finite element model.

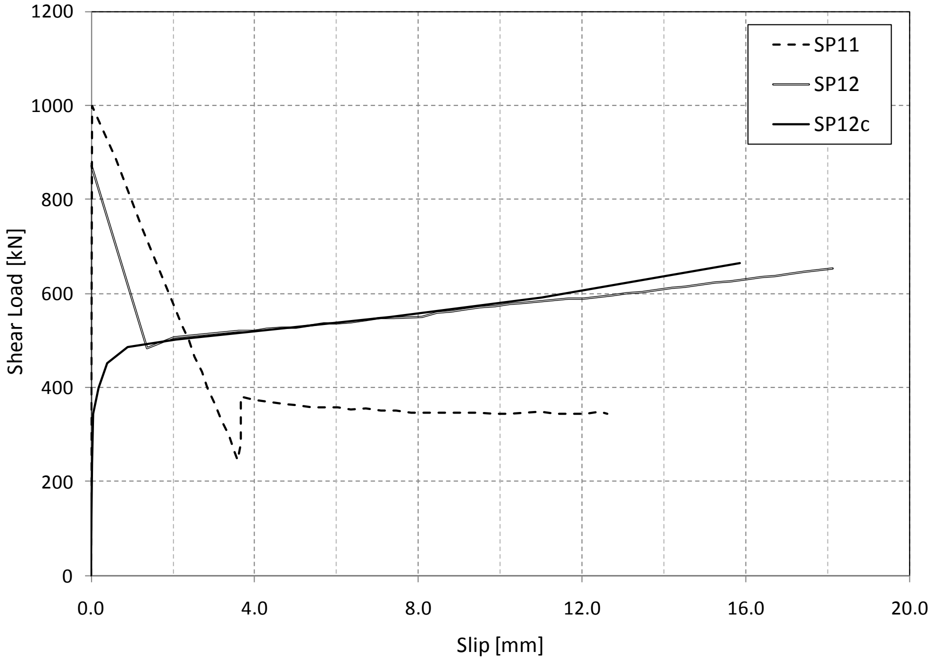

Figure 3.24: Observed Shear load-slip curve (after Foerster et al. 1989)

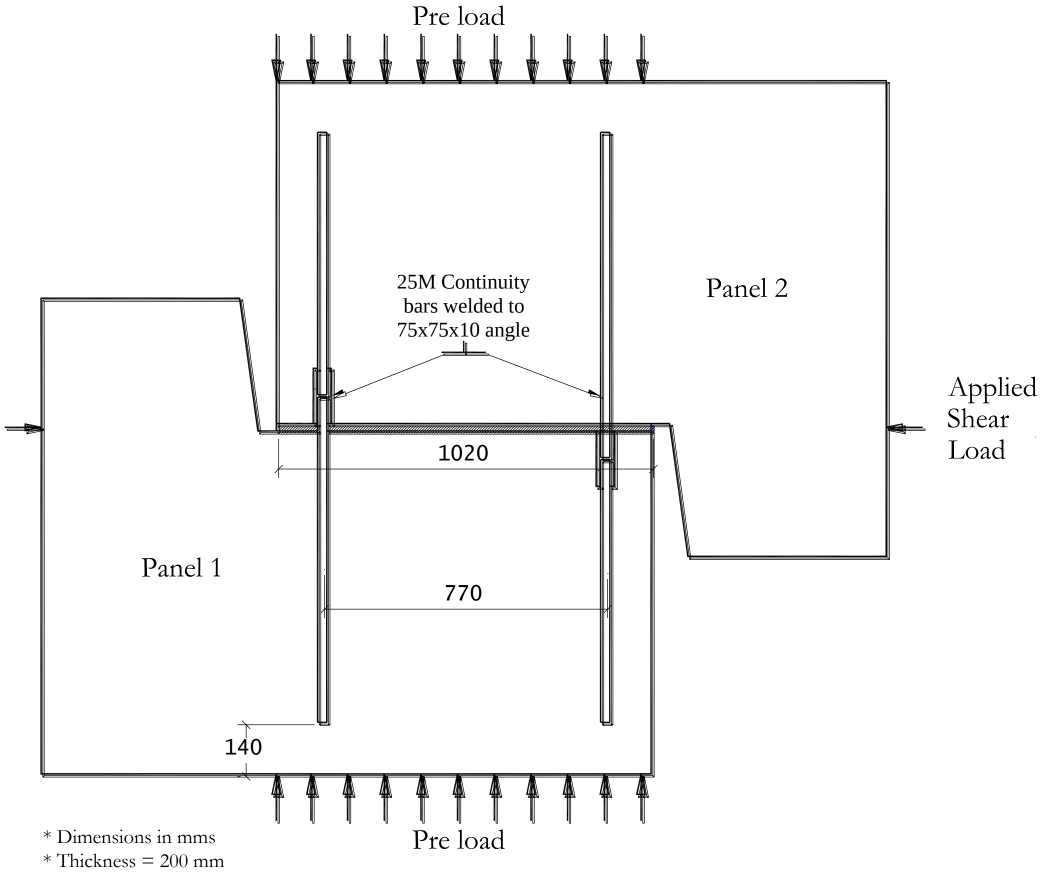

Figure 3.25: Specimen SP12 and SP12C (after Foerster et al. 1989)

3.6.1.1 Finite Element model for SP12C

The concrete panels and the continuity bars are modelled after the specimen geometry. A friction coefficient, obtained from Specimen SP11, of μ=0.91 is assigned to the contact defined between the two panels. The steel rebar properties listed in Table 3.5 are used in the model. The performance of different concrete constitutive models is assessed. The loading and support conditions of the model match those of the experiment. Boundary conditions and applied loads are depicted in Figure 3.26. Each continuity bars was modelled as a continuous part, no effort is made to model the connecting steel angle. Finite element model and mesh are depicted in Figure 3.28 and Figure 3.29.

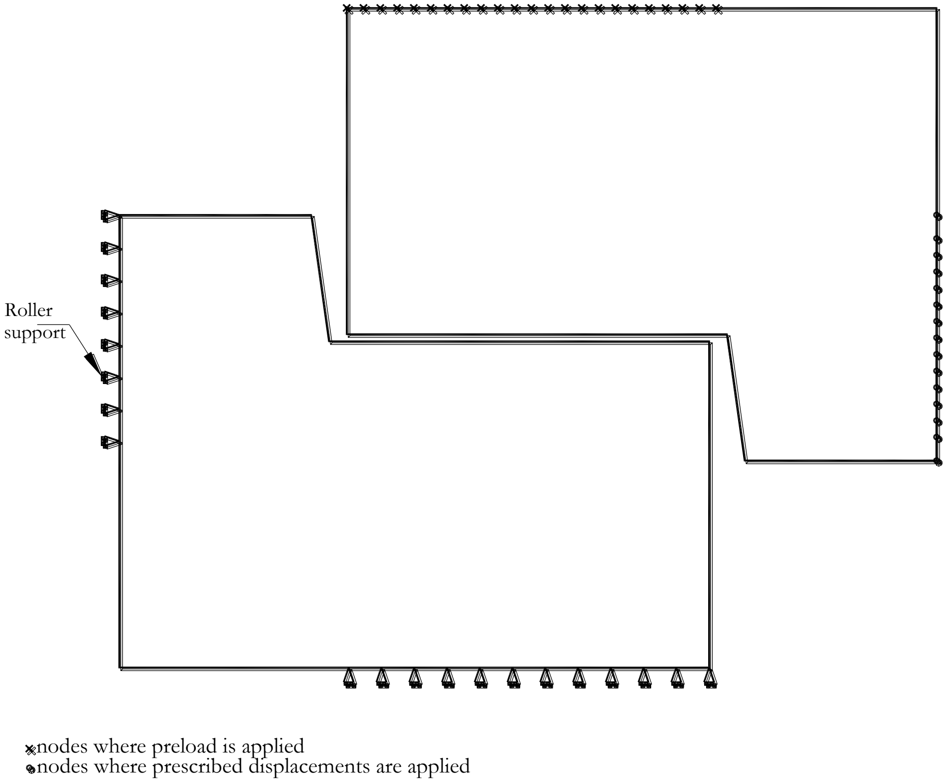

Figure 3.26: boundary conditions and applied loads on the FE model (Specimen SP12C)

Table 3.5: steel material properties for continuity bars (Specimen SP12C)

E [MPa]	E_{sh} [MPa]	f_y [MPa]
200000	3000	457.3

After a sample bar tested by Foerster (1987)

Vertical pressure and horizontal displacement are applied sequentially. A ramping pressure normal to the joint is applied. Upon reaching the desired value of 2.0 MPa, the pressure is kept constant and a ramping prescribed horizontal displacement is applied and the corresponding force is monitored (see Figure 3.30).

A preliminary model is developed to investigate and verify the sliding frictional behaviour of the two panels, i.e. without including the continuity bars in the model. First attempts have not been successful in capturing actual sliding force, as unexpectedly higher slip forces are observed. In addition, if the model is re-run, it does not necessarily reproduce the same slip force. Close inspection of the deformed shape shows that snagging between the two sliding panels takes place. One or more nodes of the sliding part snags a node from the bottom part and cause the sliding block to lock, i.e. no sliding occurs until snagging is released (see Figure 3.27). Snagging usually takes place as sharp corners of a part come into contact with other parts. Snagging results in unexpectedly higher slip forces. Penalty forces coming from the penalty method can cause snagging. Corner radiusing would eliminate snagging and the model behaves as expected. This confirms the well known modelling rule that sharp edges should be avoided. A similar observation was made by Reid and Hiser (2004).


(a) (b)

Figure 3.27: Snagging of edge node (after Reid and Hiser 2004) (a) applied load (b) sliding block locks due to snagging of edge point

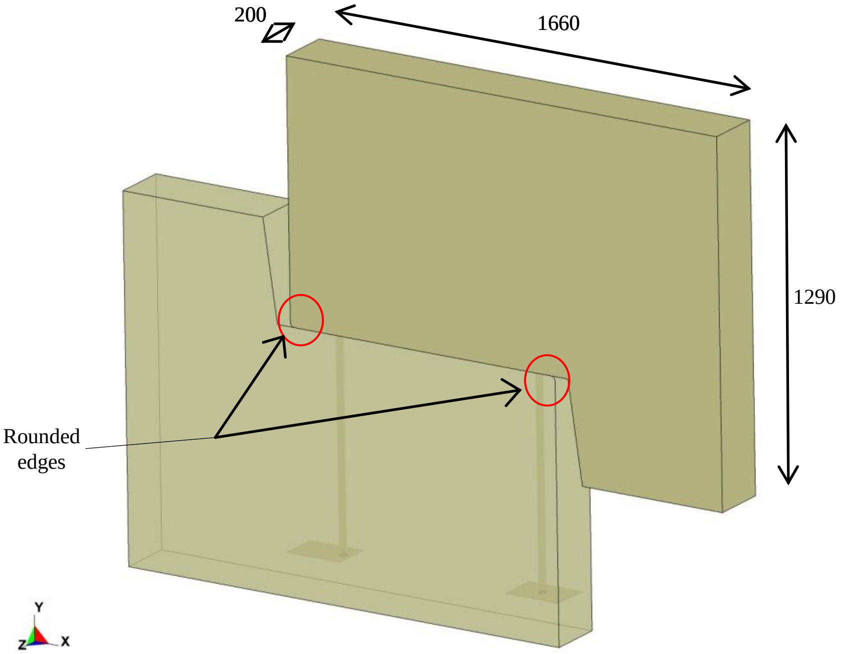

Overall view(Dimensions in mm)

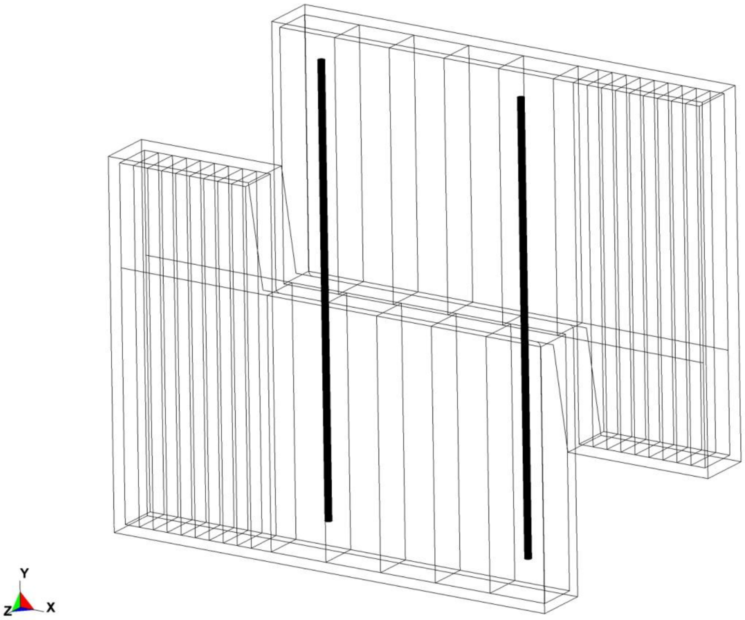

Continuity and regular reinforcement

Figure 3.28: Finite element model for SP12C

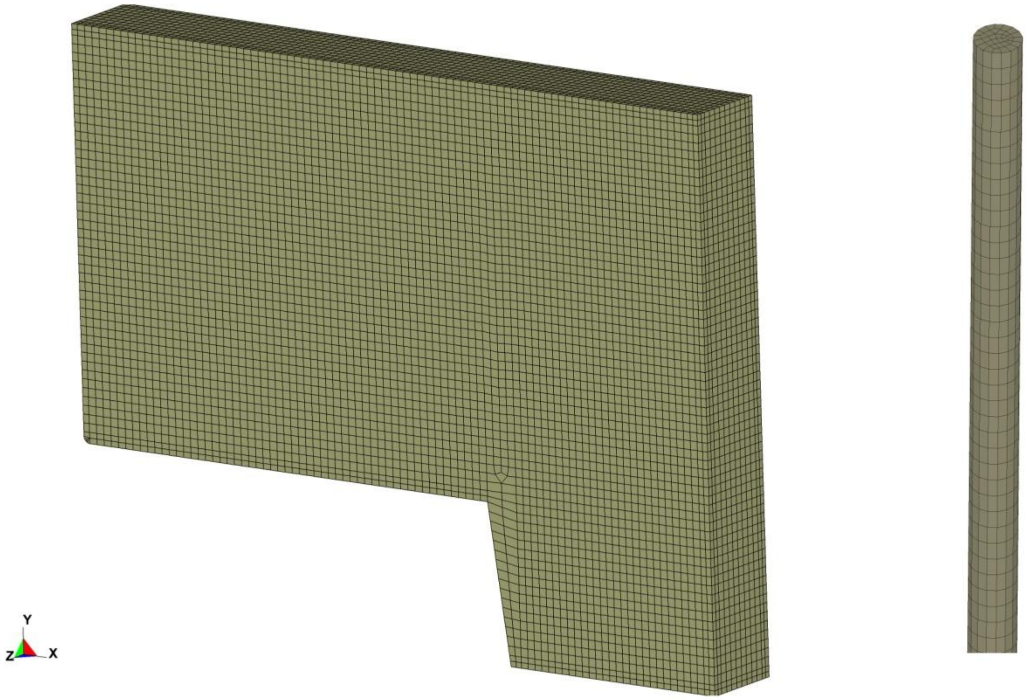

Upper panel

continuity reinforcement

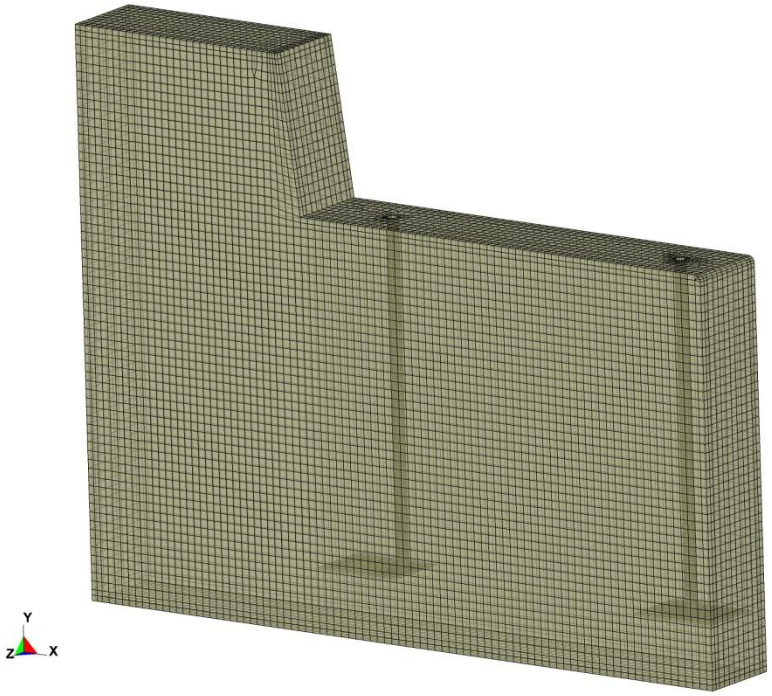

Lower panel

Figure 3.29: Finite element mesh of concrete panels and continuity reinforcement

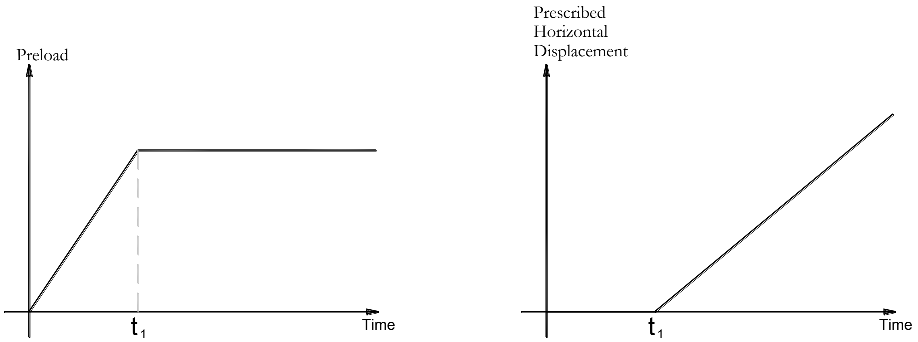

Figure 3.30: sequential load application

3.6.1.2 Analysis Results of Specimen SP12C

A pilot model is developed with linear elastic constitutive model (*MAT_ELASTIC or MAT_001*) utilized to model concrete, i.e. aspects of concrete behaviour like damage and cracking are ignored for the time being. The model results versus experimental shear load-slip curves are shown in Figure 3.31. In general, agreement between the predicted and measured responses is reasonably good. However, initial stiffness of the model is less than that observed experimentally. The model predicts that slip occurs at a lower level of horizontal force. Vertical and horizontal force transfer is discussed in the following section.

Due to bond between continuity bars and concrete, a portion of the vertical load will be transferred through continuity bars, thus reducing the effective vertical force on the connection. The predicted initial force in the continuity bars is 71.7 kN. As joint slips, some extent of debonding between concrete and continuity bars at the joint surface occurs. A larger portion of the vertical force is transferred through continuity bars. An increase in the bars vertical force, accompanied by a decrease of the effective vertical force on the connection, is observed as depicted in Figure 3.32. Increased joint slip causes continuity bars to kink (refer to Figures 3.32 and 3.23). Tension force builds up in the continuity bars due to the vertical component of the kinking force, thus reducing its initial compressive force and inducing a clamping force that increases the effective vertical force on the joint.

Break down of the model horizontal force resistance is depicted in Figure 3.34. As described earlier, two mechanisms are responsible for the horizontal force resistance. The portion of the horizontal force resisted by the shear friction mechanism is linearly proportional to the effective vertical force transferred through the joint surface (refer to Equation 3.21). A similar trend of variation with the applied slip is observed. The remainder of the force is furnished by continuity rebars credited to the dowel action mechanism. Unfortunately, only total horizontal and vertical forces were recorded during the experiment. Thus, correlation with the model forces could not be made. Dowel action force is discussed in the following section.

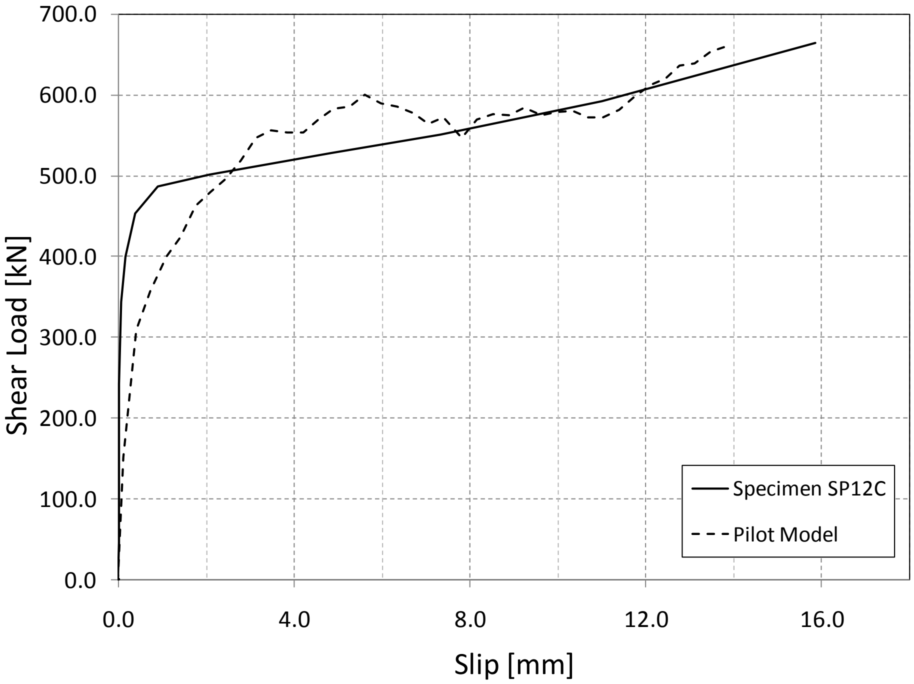

Figure 3.31: Model versus experimental shear load-slip response of specimen SP12C

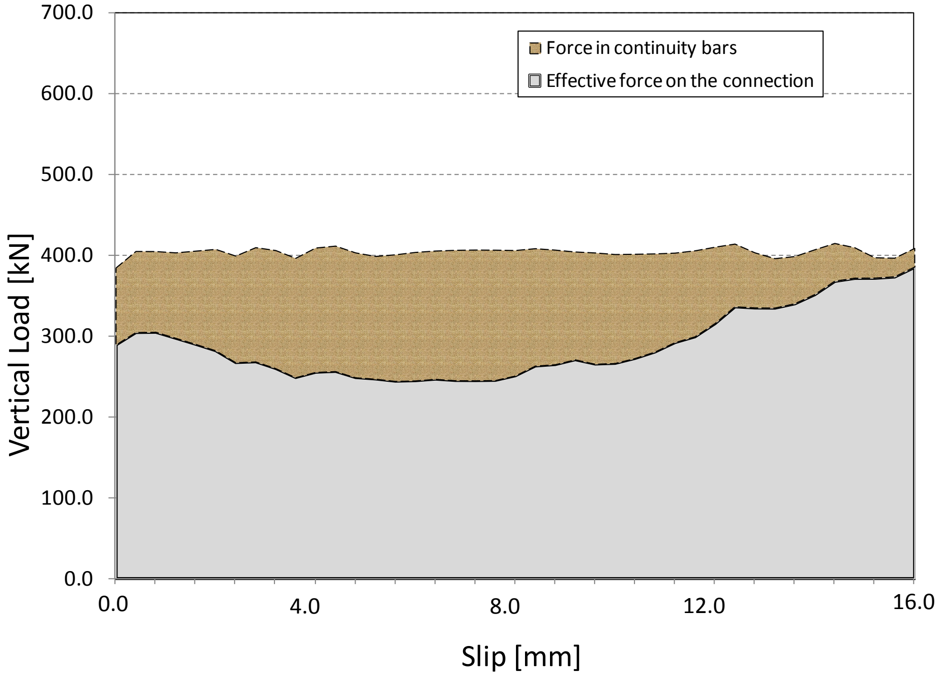

Figure 3.32: Vertical forces transfer

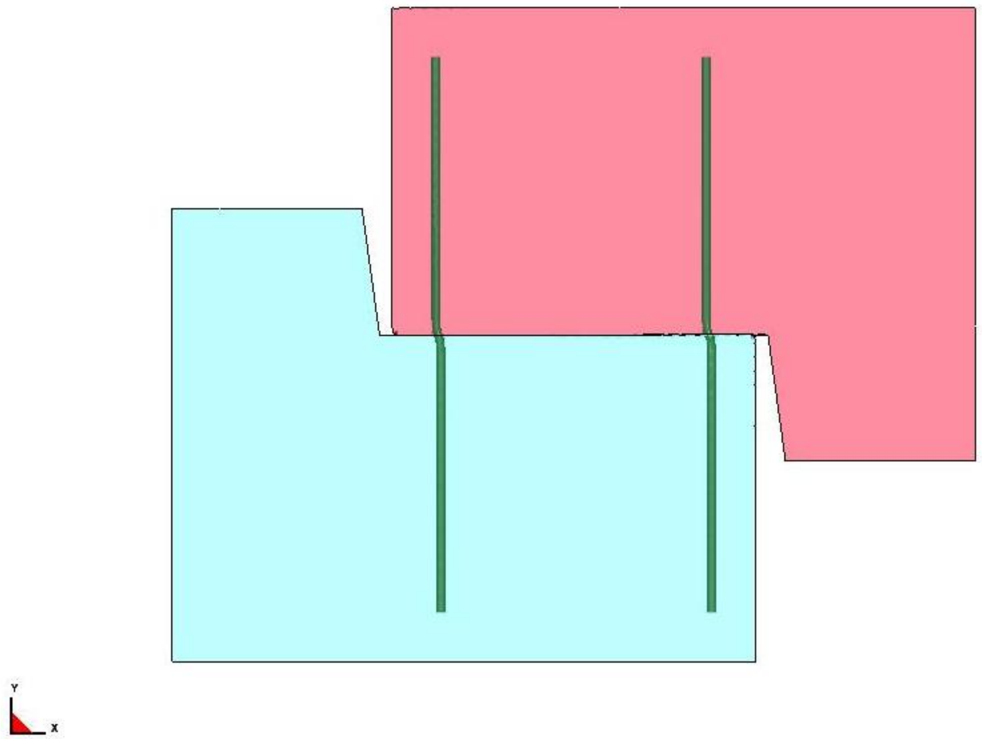

Figure 3.33: deformed shape of the connecting rods at maximum slip

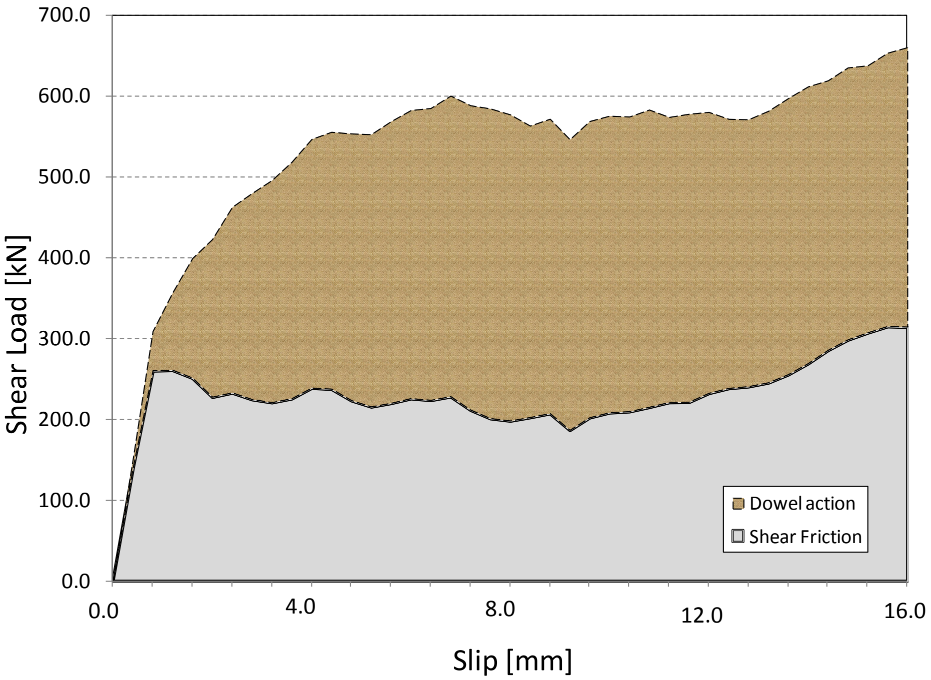

Figure 3.34: Components of horizontal force

3.6.1.2.1 Effect of concrete constitutive models on model behaviour

The concrete constitutive model affects overall model behaviour including horizontal and vertical force transfer. However, the dowel action forces are probably the most affected, as explained below. As slip increases, bearing stresses in concrete around the anchors increase and concrete tends to soften allowing a progression of the damaged region and thus an increase of the deformed length. An increase in the deformed length will cause the governing mechanism of the dowel action to shift from shear to flexure to, finally, a kinking mechanism (refer to Figure 3.23). Furthermore, strength of the surrounding concrete in bearing might govern the connection strength (Paulay et al. 1974). Damage in this case is related to compression. Hence, the material model parameters governing the concrete fracture energy in compression need to be chosen carefully. The reader is referred to Equation 3.3 for calculation of fracture energy in compression.

Figure 3.35 depicts the shear load-slip response, while Figure 3.36 and Figure 3.37 show the effect of concrete constitutive model on different force components. Dowel action force resulting from shear mechanism can be calculated as:

$$V_{shear} = \frac{A_s\ f_u}{\sqrt{3}} = \frac{2 \text{ x } 500 \text{ x } 462.8}{\sqrt{3}} = 371 \text{ kN} \qquad (3.23)$$

where A_s is the area of the anchor bar and f_u is the ultimate strength of steel. The dowel action mechanism is governed by the shear mechanism as seen from the proximity of the level of dowel action force to the one predicted by the shear mode equation.

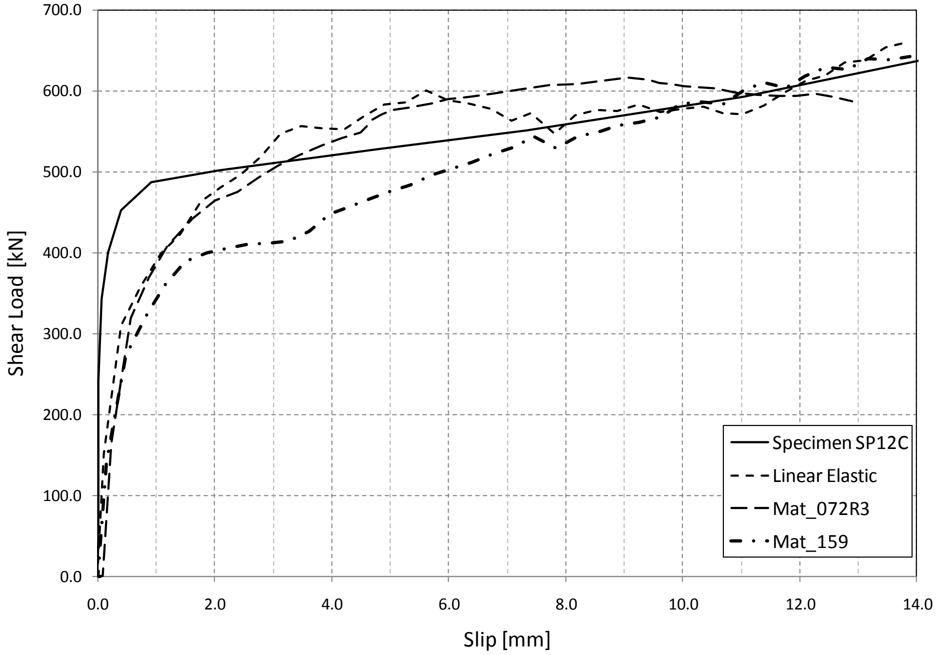

Figure 3.35: Effect of concrete constitutive model on shear load-slip response

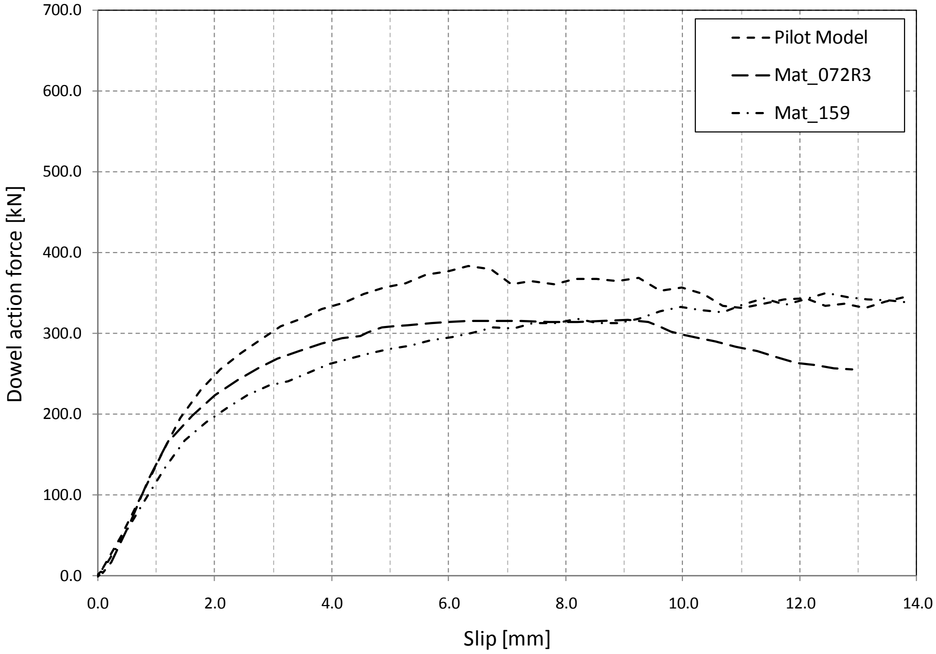

Figure 3.36: Effect of concrete constitutive model on dowel action forces

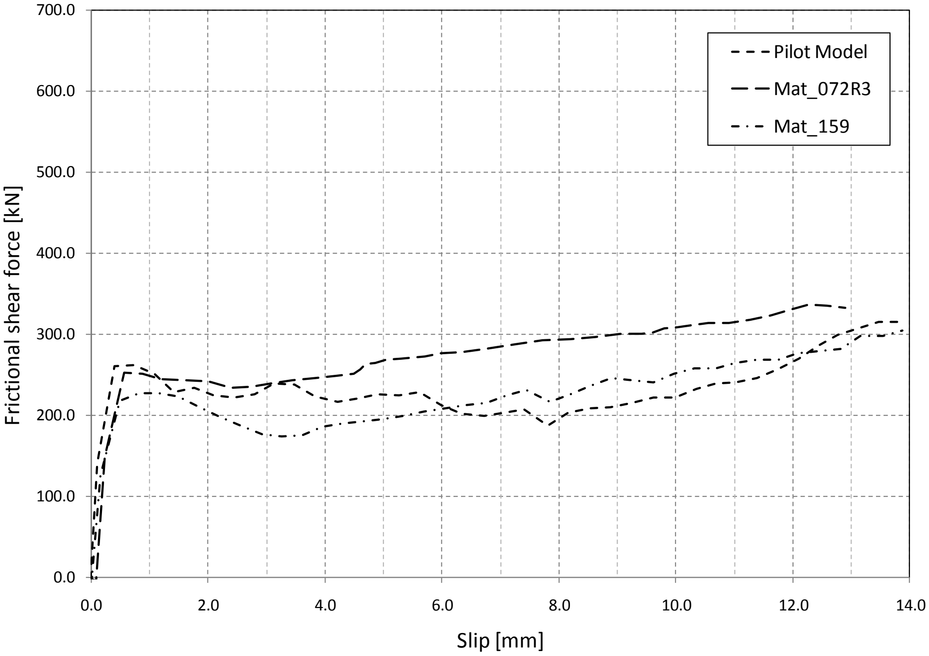

Figure 3.37: Effect of concrete constitutive model on frictional forces

3.7 Modeling pretension forces in anchors due to nut tightening

As the nut is tightened, anchor is forced to elongate inducing tensile stresses in the anchor and clamping force on the joint. Clamping forces are expected to influence some aspects of the joint behaviour including the shear friction resistance, the initial stiffness, and the decompression moment[**]. To model preloading, initial tensile stresses are applied to all elements belonging to the anchor shank. These stresses are applied along the anchor longitudinal axis using the keyword, *initial_stress_solid*. A more comprehensive study on applying preload can be found in Kuarswamy (2010).

[**] Moment at which the joint gap opening is initiated.

A simplified model is developed to explore the capabilities and limitation of the technique. The model consists of two blocks representing concrete pieces connected using an anchor with two nuts. The two nuts are modeled as an integrated part of the shaft. The FE model is depicted in Figure 3.38. Stresses in the anchor and blocks are depicted in Figure 3.39. It is observed that the initially applied axial stresses are decreased till reaching equilibrium state due to deformation of the upper and lower blocks. To reach a specific value for initial clamping, a few trials involving applying a higher initial stresses are required. This higher initial stress must be less than the assigned yield stress of the material to avoid unrealistic nonlinear material behaviour.

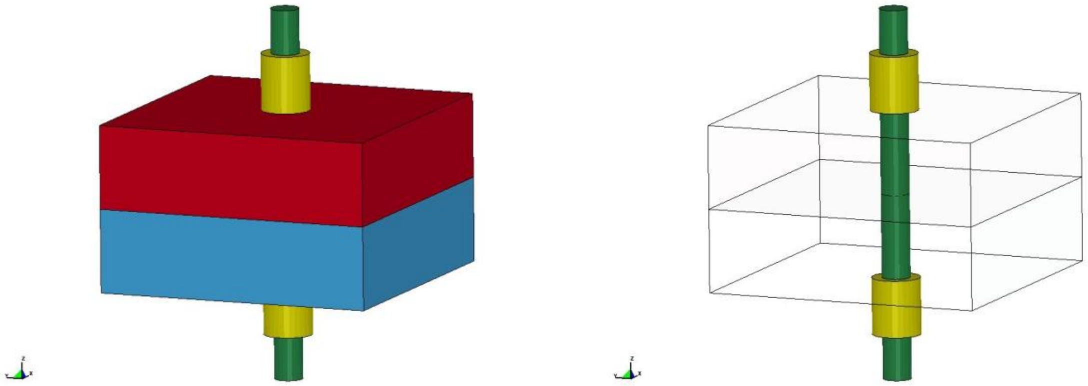

Figure 3.38: Finite element model for pretensioning anchor

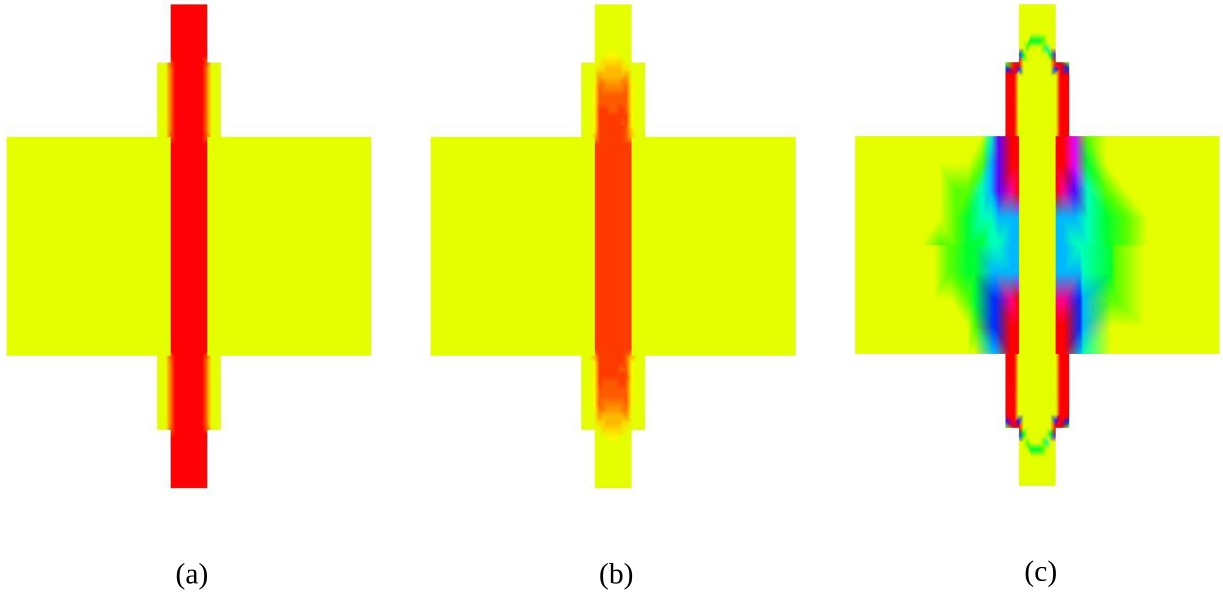
(a) (b) (c)

Figure 3.39: Prestressing stresses (a) initial pretension (b) tensile stresses in the anchor at equilibrium state (c) compressive stresses in blocks at equilibrium state

3.8 Conclusions

Through a model development process, material properties, material model parameters, element size, mesh layout, and contact definitions are examined and fine-tuned to accurately capture the behaviour of anchor-jointed precast structural wall system. The model development considers capturing different possible failure modes and phenomenon governing the behaviour including: concrete breakout, rupture of steel anchor, dowel action, shear friction, and anchor pretensioning. Tests involving subassemblies with analogous failure modes and/or similar joints reported in the literature are modelled. Accuracy of the numerical results depend on the finite element model parameters selection. This research focuses on identifying the critical parameters influencing the behaviour of the model. Based on critical analysis of the models, the following conclusions can be drawn:

- For the breakout failure mode, FE model is able to predict the concrete cone breakout failure load provided that the material model parameters governing the concrete fracture energy in tension are chosen rationally.
- Both *MAT_072R3* and *MAT_159* can be used to predict concrete behaviour. The two models could be used to predict the failure load and failure mode with reasonable accuracy. However, predictions using MAT_159 are better with regards to the load-displacement curves. It is more convenient to use material model *MAT_159* for modelling concrete. Unlike *MAT_072R3,* internal parameters are automatically adjusted by the material model for each element as a function of the element size to ensure constant fracture energy is maintained regardless of the element size.
- Modelling of steel anchor yielding and rupturing is possible using material model no.24. Failure criteria specifying the maximum principal strain at failure is able to capture the true behaviour of an anchor subjected to tensile loads provided that the true stress-strain curves are used.
- For shear force transfer, dowel action forces may be governed by concrete softening rather than steel strength for large-diameter bars. Softening in this case is related to damage in compression. Hence, the material model parameters governing the concrete fracture energy in compression need to be chosen rationally
- Anchor pretension is modelled successfully by assigning an initial tensile stresses to the anchor shaft. It is observed that the axial stresses applied initially are decreased till reaching equilibrium state due to deformation of the upper and lower blocks. A few trials are needed to reach a specific pretension force.

- The numerical response obtained from all simulations provides a reasonable correlation with the experimental data with regards to failure load and failure modes. Thus, features of these models including material properties, material model parameters, element size, mesh layout, and contact definitions can be used with confidence to build a reliable model to predict the behaviour and failure modes of the proposed joint.

CHAPTER 4

Lateral Resistance of Anchor-Jointed Precast Structural Wall System: Nonlinear Model and Parametric study

4.1 Introduction

A new innovative jointing technique for connecting precast concrete structural walls has been conceptually developed and tested as explained in Chapter 2. In this system, panels are connected using anchor bolts which may act as structural fuses during an earthquake event. Damage is concentrated in the yielding of the anchor bolt with minimum damage to the concrete panels minimizing capital loss. As described in Chapter 3, critical model parameters are examined and fine-tuned. Tests involving subassemblies with analogous failure modes and/or similar joints reported in the literature are modelled. The numerical response obtained from all simulations provides a reasonable correlation with the experimental data with regards to failure load and failure modes. Information and insight gained from conducted simulations are implemented to build a reliable model for the anchor-jointed precast structural wall system.

The modelling procedures and numerical results are presented. Details of the model are introduced first. A pilot model using linear elastic material formulation is used to check the force transfer mechanisms and equilibrium. Following that, the model is verified against experimental data presented in Chapter 2. Finally, a parametric study to assess the effects of selected parameters on the response of the anchor-jointed precast structural wall system to monotonic lateral loads is conducted using the validated numerical model. These parameters are selected to represent possible variations in the tested specimens. Three parameters are considered: (1) gravity loads, (2) anchor pretension force, and (3) anchor length.

4.2 Finite Element Model

The precast concrete panel, the concrete base block and the steel anchors are modelled after the specimen geometry. 8-noded brick elements with one integration point are used to model plain concrete and steel anchors (element form 1 in LS-DYNA). Reinforcement is modelled using two-node beam elements. Beam and brick elements are connected to the same nodes, i.e. perfect bond is assumed. Both *MAT_072R3 and MAT_159* are used to model concrete, while *MAT_024* is used to model steel material. Contact is defined between different parts using the algorithm *contact_automatic_surface_to_surface*. Bottom nodes of the concrete base block, defined as Group 2, and nodes on the top surface corresponding to the locations of the tie-down beam, defined as Group 3, are restrained from global X, Y and Z movements. To prevent out-of-plane movement, i.e. Z-displacement, a group of nodes corresponding to the position of the out-of-plane bracing is restrained from movement in the Z-direction. Lateral load is applied through a ramping X-displacement applied at the mid-depth of the head beam at the pushing end. Finite element model and mesh are depicted in Figures 4.1 and 4.2. A coarser finite element mesh is used for the concrete base block; the element size for the precast panel and the concrete base block are approximately 16 and 50 mm, respectively. In addition, linear elastic material model is used for the concrete base block and the head beam. A friction coefficient of 0.5 is assumed for the contact between base and panel (Contact1 in Table 4.1). This value is recommended as a lower bound for unbounded post-tensioned precast structural wall joints by ITG-5.2-09 (ACI 2009). However, a sensitivity analysis varying the friction coefficient between 0.3 and 1.0 showed that its effect is minor. This is conceivable as the panels mainly behave in bending and no vertical load was applied. For all other contacts definition, the friction coefficient is assigned to a small value to maintain numerical stability. The model consists of 4398 beam elements and 87016 solid elements. The true stress-strain relationship is deduced from the given engineering stress-strain relationship and is used in the model as detailed in Section 3.5.2. Pretensioning stresses are applied prior to lateral loading as explained in Section 3.7. A few trials are required to achieve the pretensioning force observed during testing. Horizontal loading is applied after equilibrium, due to pretensioning load, is reached to be able to verify the anchor preload prior to load application.

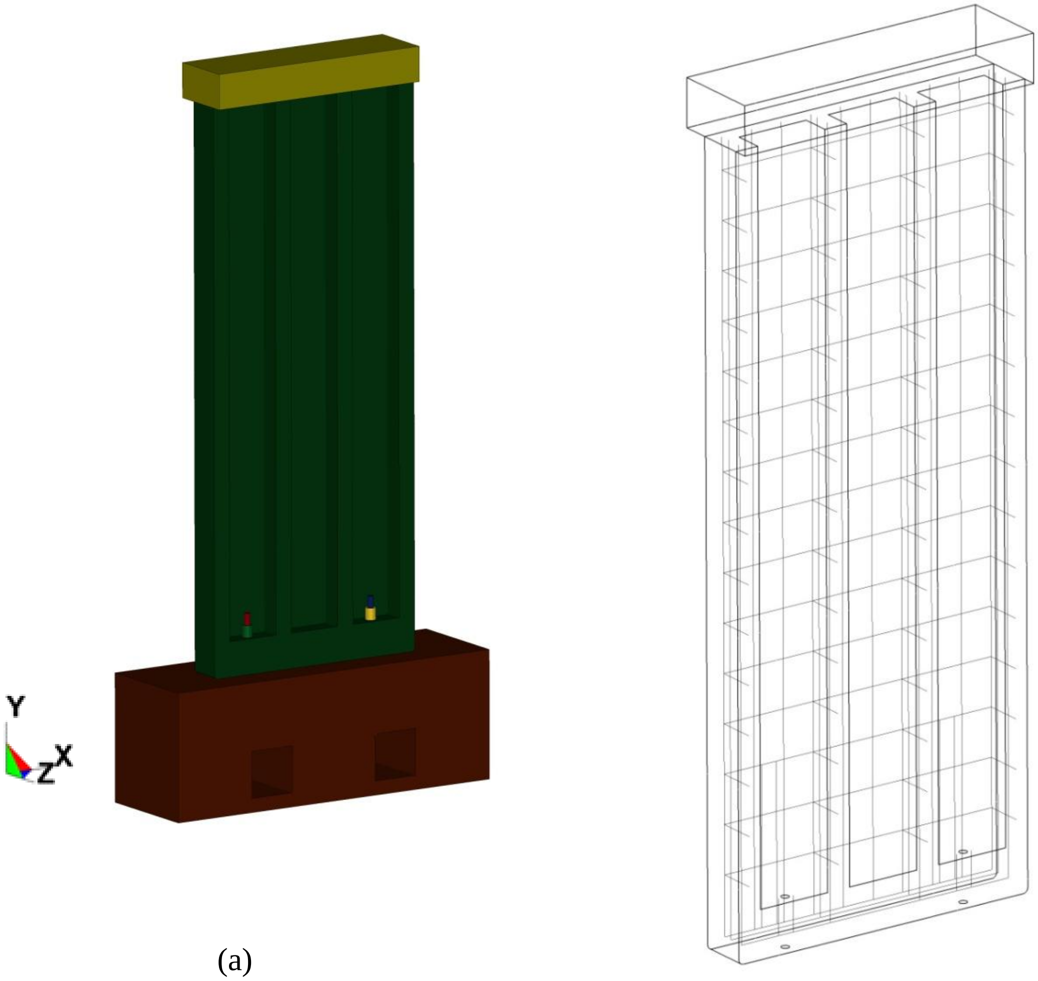

(a)

(b)

Figure 4.1: Generic model of El Semelawy et al. specimens (a) overall view (b) Precast concrete panel reinforcement

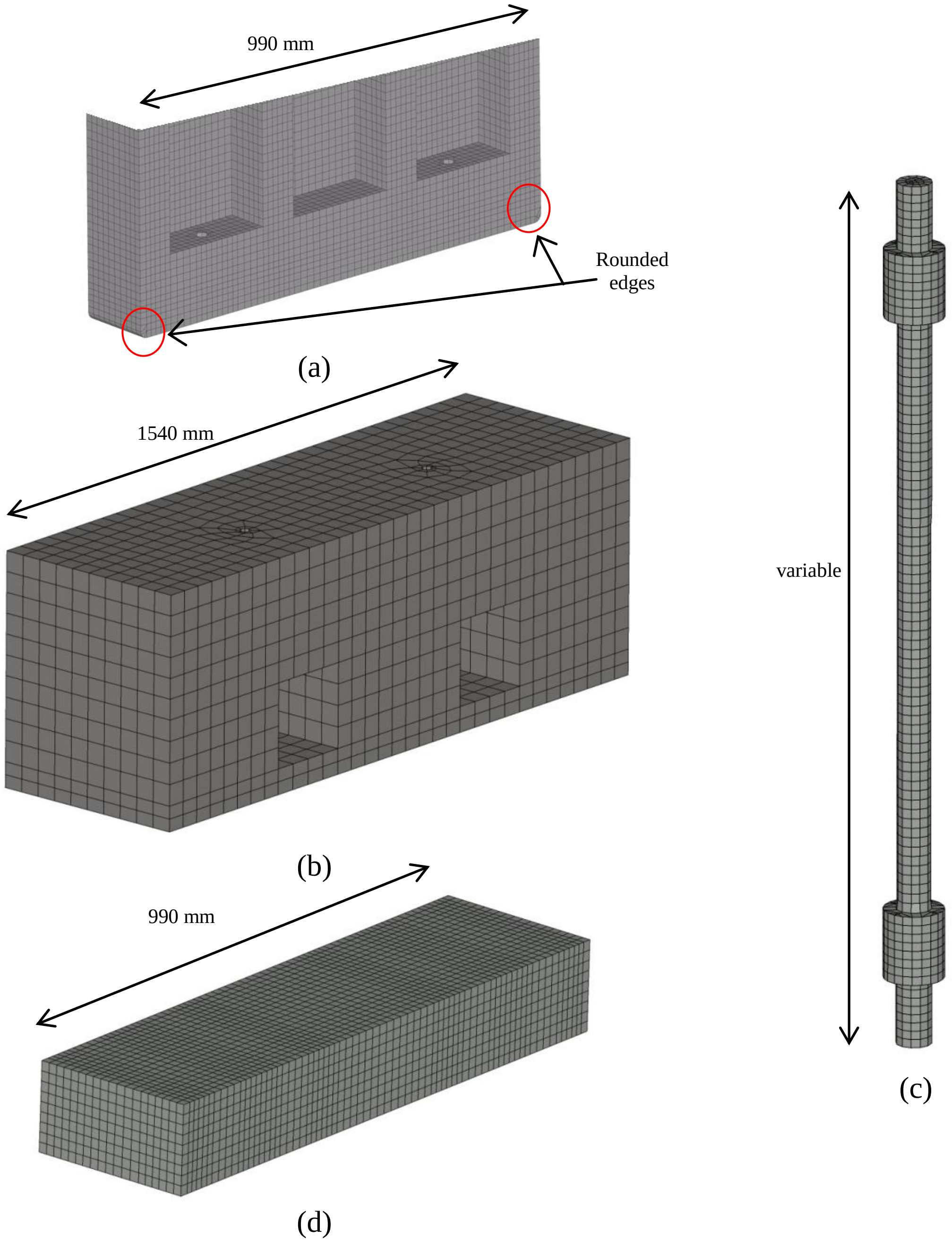

Figure 4.2: Finite element mesh (a) anchor block region (b) anchor bolts (c) concrete base block (d) head beam

Note: (a), (b), (c), and (d) are drawn to different scales for clarity

4.2.1.1 Preliminary model

A Preliminary model, employing linear elastic material models for both concrete panel and steel anchor, is created. The model is intended for checking the static equilibrium and the force transfer mechanisms. Linear elastic material models are employed to avoid the complex effect from materials nonlinearities on the behaviour for the time being. To facilitate equilibrium check, load is applied as a ramping X-force, not displacement, applied at the mid-depth of the head beam at the pushing end. A total of 9 contacts are defined for this model. The contacts definitions and the physical representation of the contact forces are listed in Table 4.1.

The model load-drift response is provided in Figure 4.3, showing a linear behaviour as expected. As shown in Figure 4.4, the sum of horizontal reactions oscillates around the external applied force horizontal force. Generally, disequilibrium between applied loads and reactions is tolerable. Oscillation observed in Figure 4.3 and Figure 4.4 may be traced back to the application of contacts utilizing the penalty method as explained in Section 3.4.3. To minimize this oscillation, load application time needs to be increased. Unfortunately, this might not be feasible due to excessive running time. Vertical equilibrium is illustrated in Figure 4.5, which is maintained throughout the analysis. Total, internal, kinetic, and hourglass energies of the model are depicted in Figure 4.6. The kinetic energy is negligible compared to the internal energy, indicating a negligible inertia and damping forces, i.e. minor dynamic effect. In addition, hourglass energy only constitutes a trivial fraction of the internal energy. The model is acceptable with regards to static equilibrium and energy aspects.

The model is able to capture the following key transfer mechanisms observed experimentally:

(1) Bending moment at the joint level is resisted by a couple of vertical forces. The first is the compressive force transmitted through contact1, while the other is the tensile force in the tension side anchor (refer to Figure 4.7).

(2) Shear force at the joint level is transferred through the shear friction force (horizontal component of contact1) and the dowel action force of the tension side anchor (refer to Figure 4.8).

The developed model is capable of representing the complex force transfer behaviour of the anchor-jointed precast structural wall system.

Table 4.1: Contact definition for the preliminary model

	Part 1	Part 2	Vertical component	Horizontal component
Contact1	concrete panel	base block	compressive force due to direct contact	shear friction force
Contact2	concrete panel	tension side anchor shaft		dowel action force in the tension side anchor
Contact3	concrete panel	compression side anchor shaft		dowel action force in the compression side anchor
Contact4	base block	tension side anchor shaft		dowel action force in the tension side anchor
Contact5	base block	compression side anchor shaft		dowel action force in the compression side anchor
Contact6	concrete panel	tension side anchor nut	vertical force in tension side anchor	
Contact7	base block	tension side anchor nut	vertical force in tension side anchor	
Contact8	concrete panel	compression side anchor nut	vertical force in compression side anchor	
Contact9	base block	compression side anchor nut	vertical force in compression side anchor	

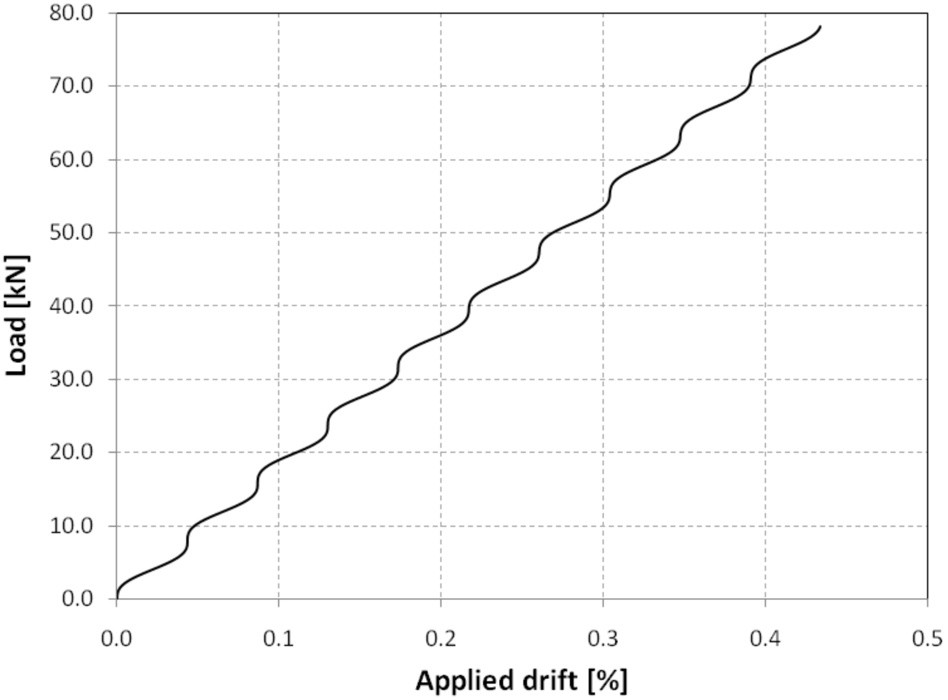

Figure 4.3: Preliminary model load-drift response

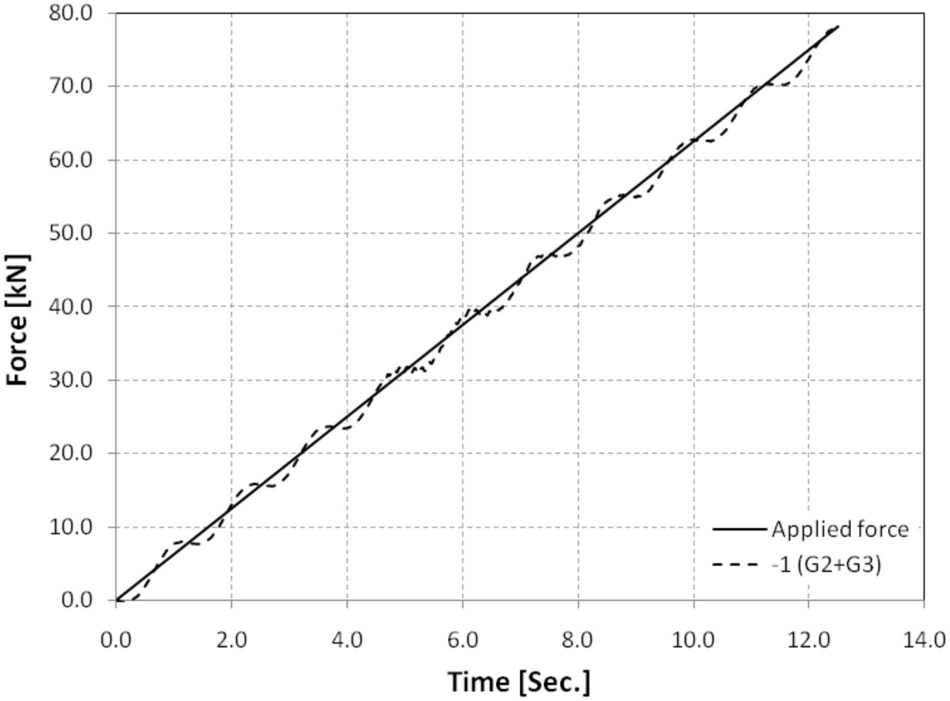

Figure 4.4: Horizontal-force equilibrium of the preliminary model

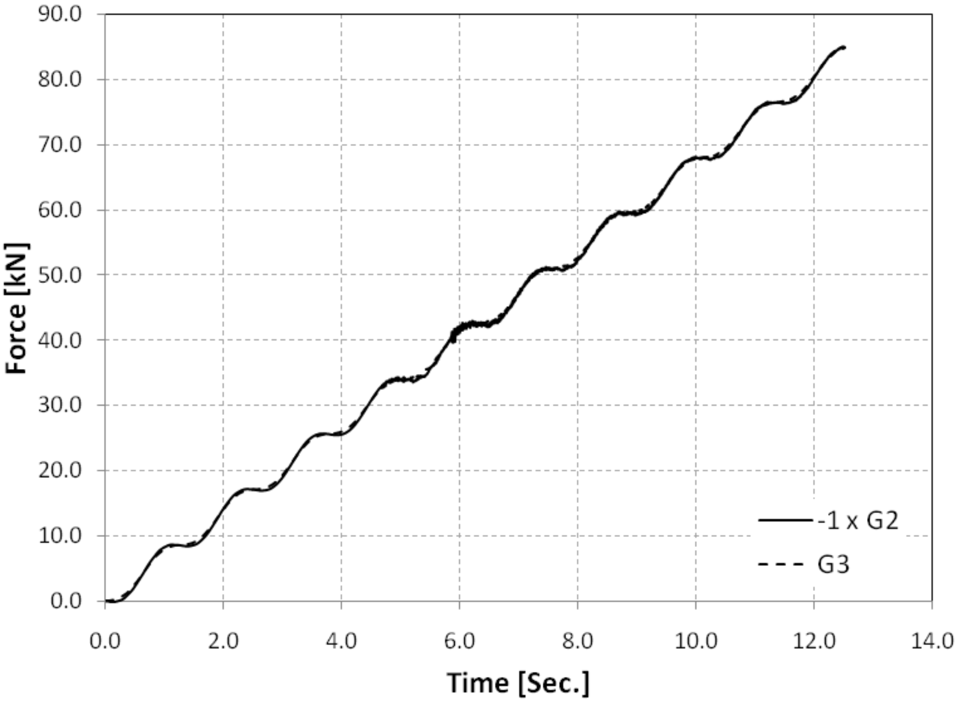

Figure 4.5: Vertical-force equilibrium of the preliminary model

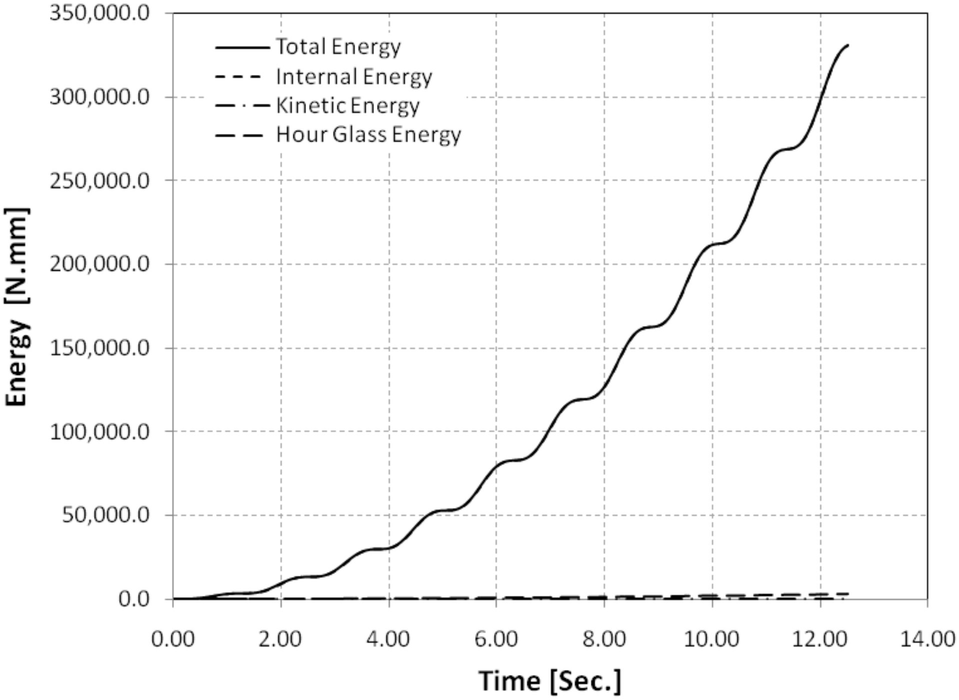

Figure 4.6: Kinetic, internal, total energy of the preliminary model

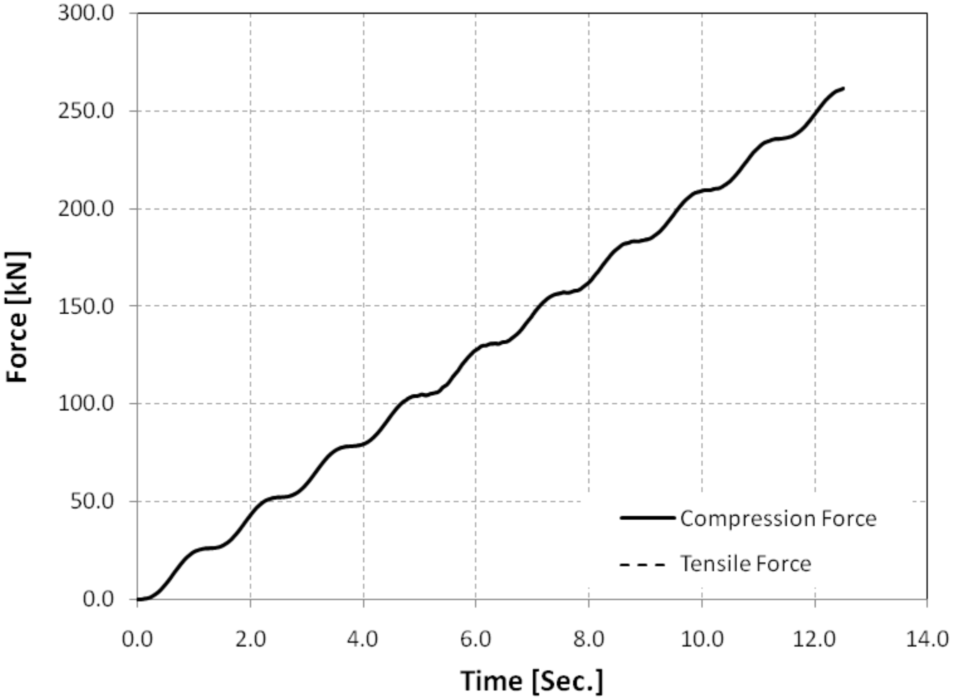

Figure 4.7: Couple forces resisting bending moment at the joint level

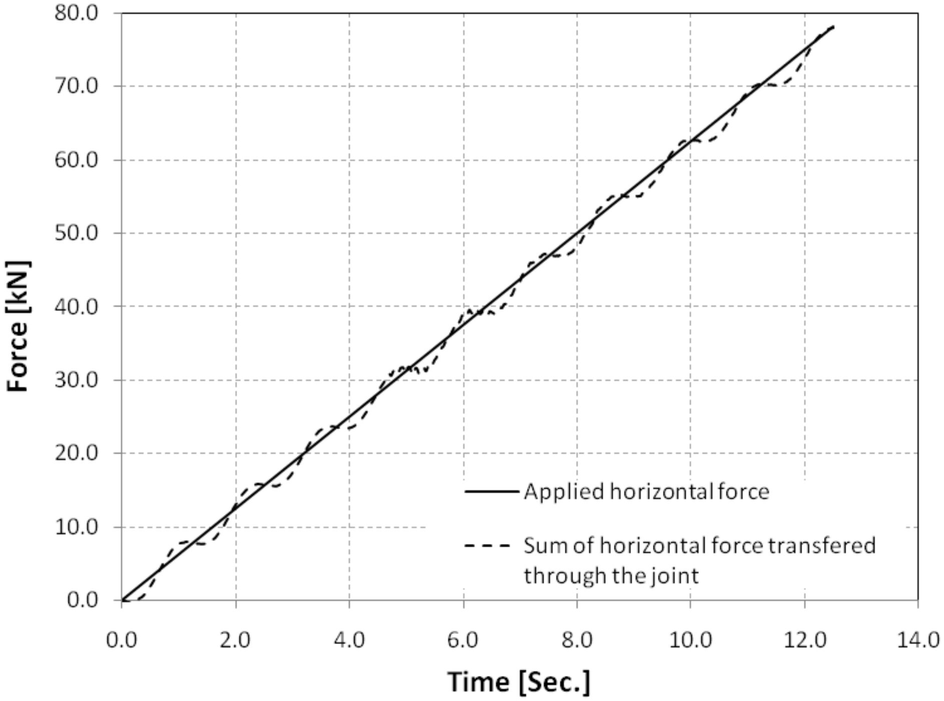

Figure 4.8: Horizontal force transfer at the joint

4.2.1.2 Analysis results of the tested specimens

The preliminary model is extended to simulate the tested specimens (detailed in Chapter 2). *Mat_072R3* and *MAT_159* are used to model concrete, while *MAT_024* is used to model steel. The experimental load-drift responses are illustrated in Figures 4.9 through 4.12, together with the results of different models. A summary of the results, including failure load and failure mode, are listed in Table 4.2. To assess the accuracy of the developed model, correlative studies between experimental and numerical model are undertaken.

4.2.1.2.1 Failure load and failure mode

In general, the models are able to capture the failure mode and the associated failure load with reasonable accuracy. Only model for Test4, using *MAT_159*, fails to predict the failure mode observed in the experiment. The failure is wrongly predicted to be a compression failure, while a tension rupture failure was observed during testing. In all other models, the failure modes are captured accurately. The accuracy of the failure load is higher for joints failed by steel rupture (average 1.06 of the experimental load, for Test 2 and Test 3). This might be traced back to the difficulty of modelling the complex nonlinear behavoiur of concrete under both tensile and compressive stresses versus the relative simplicity of modelling steel material.

4.2.1.2.2 Load-drift response

In all conducted simulations, the models over predict the initial lateral stiffness of the joint. The discrepancy between the numerical model and the test can be attributed to a variety of sources including imperfections originated from test assembly. In addition, geometric nonlinearity caused mainly by the material discontinuity of the assemblage itself and material non-linearities of the system make it more difficult to predict the response under external lateral loading. Also, Initial stiffness is greatly affected by the “lack of fit”, and as a result, disagreement between experimental stiffness of similar joints can occur (Bursi and Jaspart 1997).

The ultimate drift is reasonably captured for specimens that failed in a ductile manner (Test 2 and Test 3). However, for the other tests, the maximum drift at failure is under predicted, this could also be attributed to the complexity of the concrete behaviour modelling.

From the figures, it is observed that the predicted stiffness of the model after gap opening is slightly higher than the experimental ones. A source of error is possibly the readings of the horizontal and vertical LVDT’s. As the panel is loaded, it deflects and rotates. A component of the lateral deflection contributes to the vertical measurement and vice versa.

4.2.1.2.3 Damage pattern

The damage pattern predicted by the models is fairly similar to that of the test as illustrated in Figure 4.13 and Figure 4.14. For Test 1, Figure 4.13 shows a clear damage in the anchor block area where as no other damage elsewhere in the panel. For Test 2, the damage pattern predicts well the cracks that develop in the tension side stiffeners. The FEM effectively captures the damage pattern observed during testing.

4.2.1.2.4 Forces in tension anchors

Forces observed in tension side anchor in Test 2 and Test 3 are presented in Figure 4.15 and Figure 4.16. Predicted anchor forces compare well with the measured values observed in Test 2 and Test 3 which failed due to anchor rupture.

4.2.1.2.5 Forces in bonded reinforcement

The axial forces in panel reinforcement, of Test3 model, are depicted in Figure 4.17. Higher forces are developed in vertical bars in the stiffeners, especially bars just above the anchor block. This matches the experimental observation of concrete cracking above the anchor block area.

Table 4.2: Summary of the models results

Model		Model failure mode	Model failure load [kN]	Model/Experimental
Test1	Mat_072	concrete breakout	33.7	1.38
	Mat_159	concrete breakout	28.0	1.14
Test2	Mat_072	steel rupture	55.2	1.08
	Mat_159	steel rupture	52.8	1.04
Test3	Mat_072	steel rupture	55.4	1.08
	Mat_159	steel rupture	54.0	1.05
Test4	Mat_072	compression failure	68.5	1.03
	Mat_159	steel rupture[†]	99.7	1.50

[†] Model is not able to capture the specimen failure mode (compression failure)

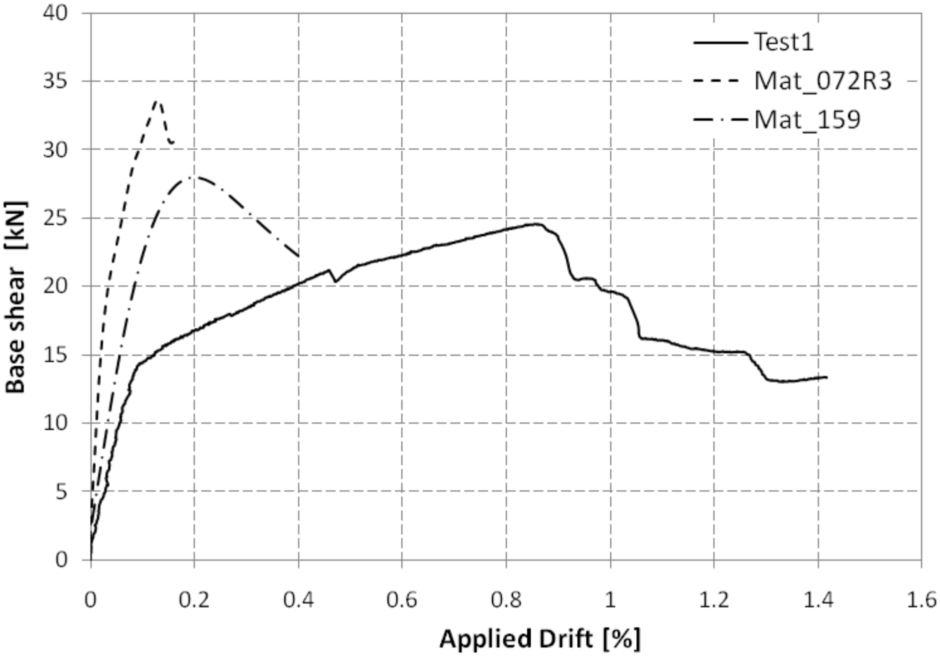

Figure 4.9: Load-drift response of Test1

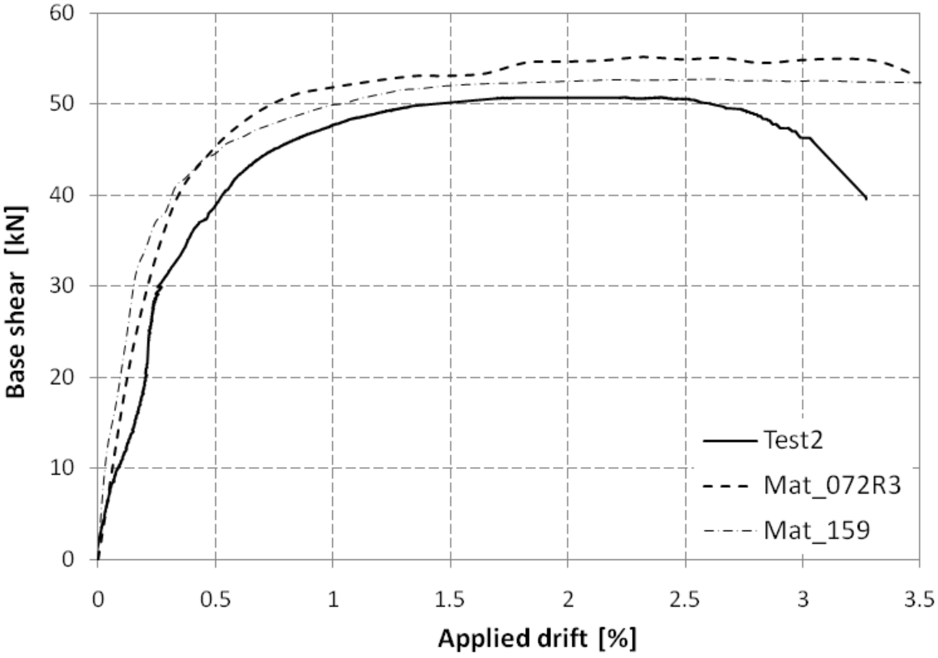

Figure 4.10: Load-drift response of Test2

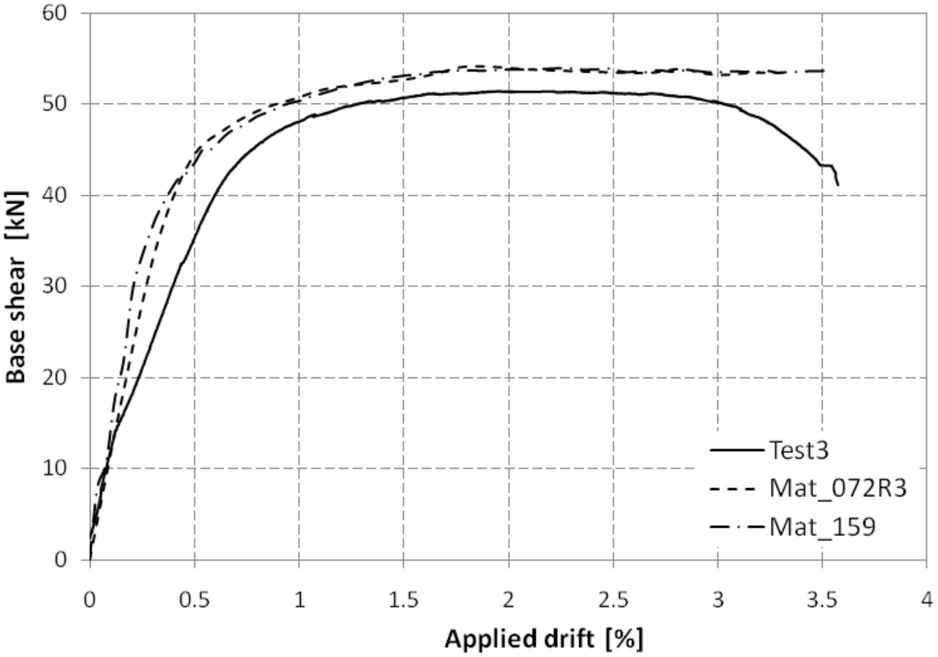

Figure 4.11: Load-drift response of Test3

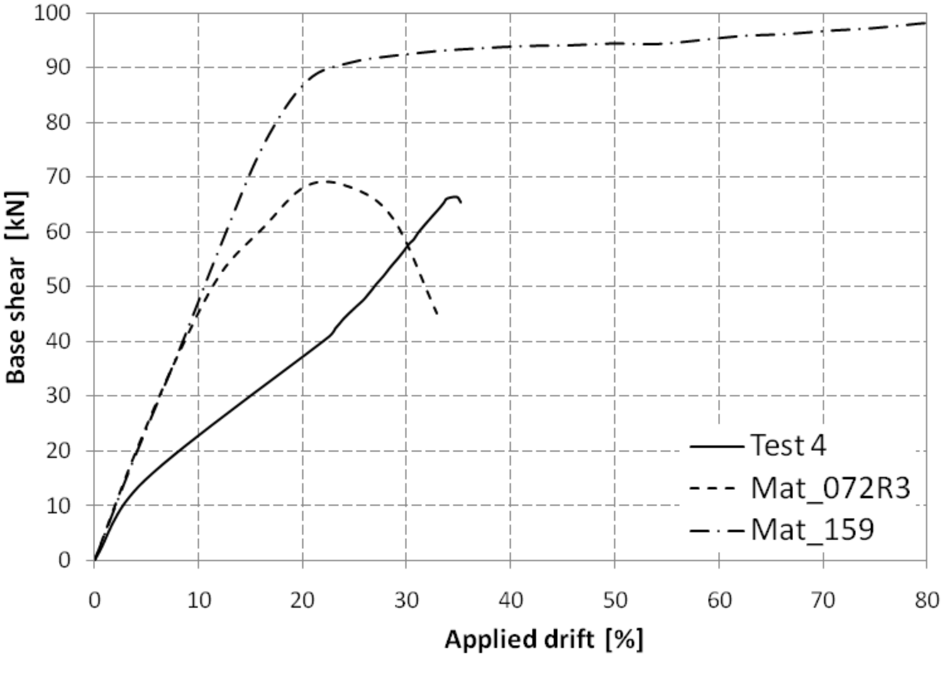

Figure 4.12: Load-drift response of Test4

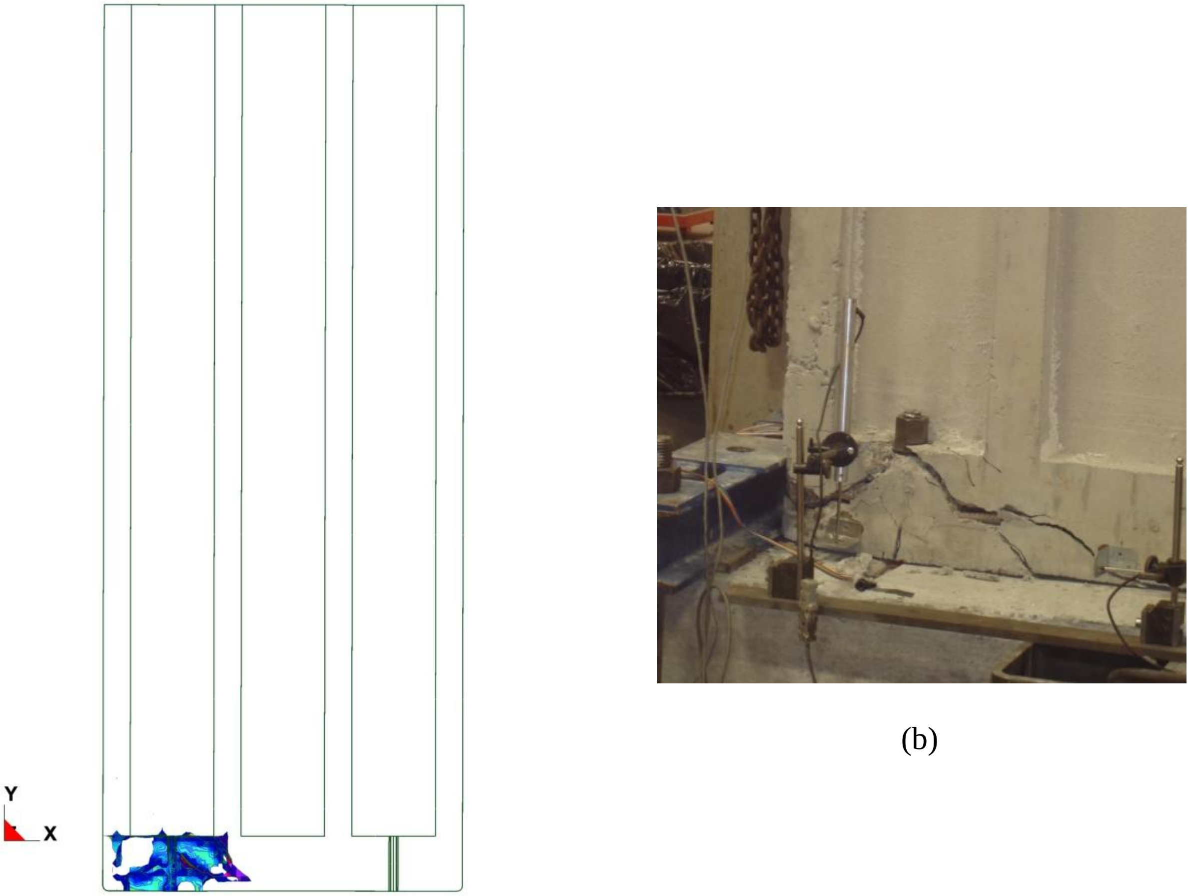

(b)

(a)

Figure 4.13: Damage pattern for Test1 (concrete breakout failure mode) (a) Model (b) Test

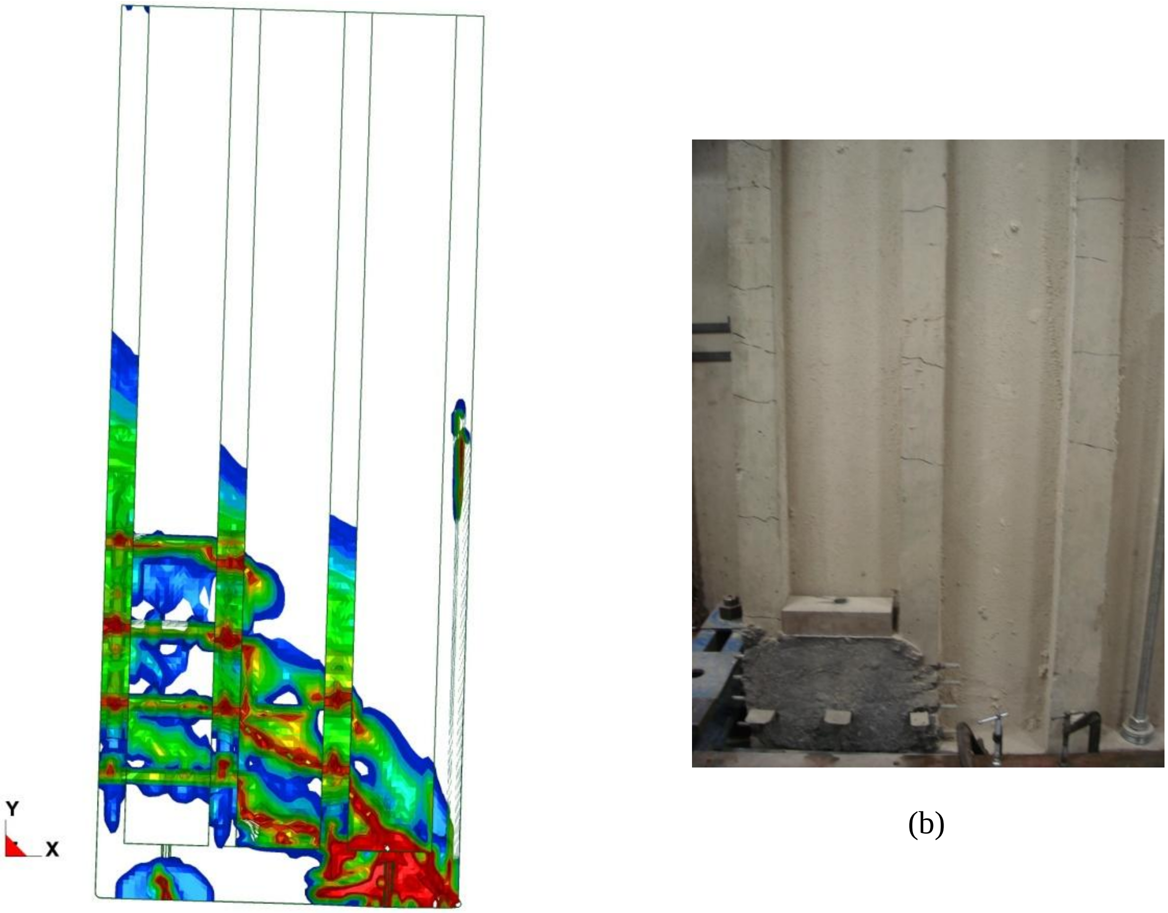

(b)

(a)

Figure 4.14: Damage pattern for Test2 (steel rupture failure mode) (a) Model (b) Test

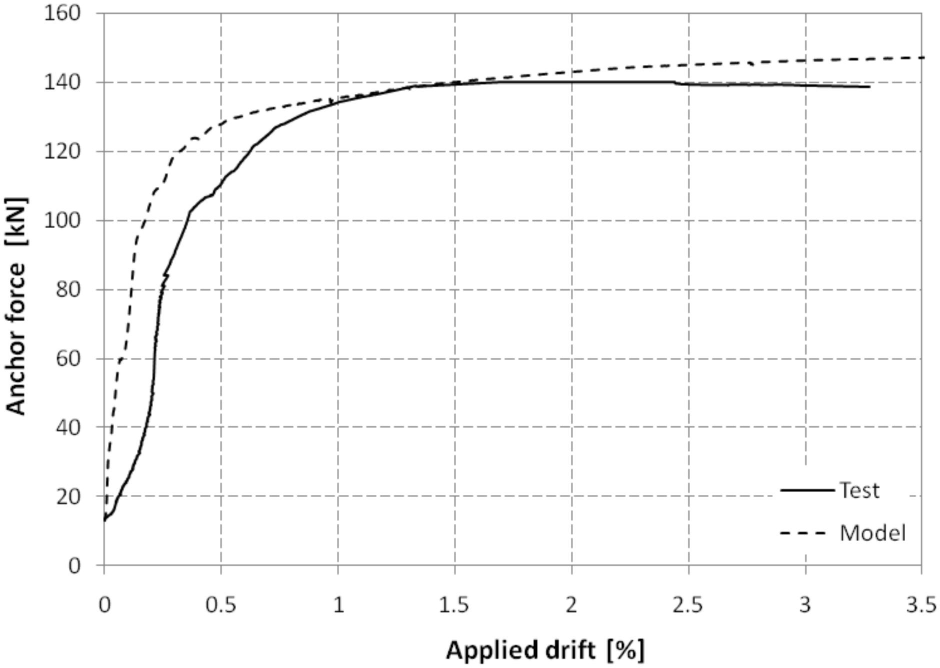

Figure 4.15: Correlation between tension side anchor forces for Test2

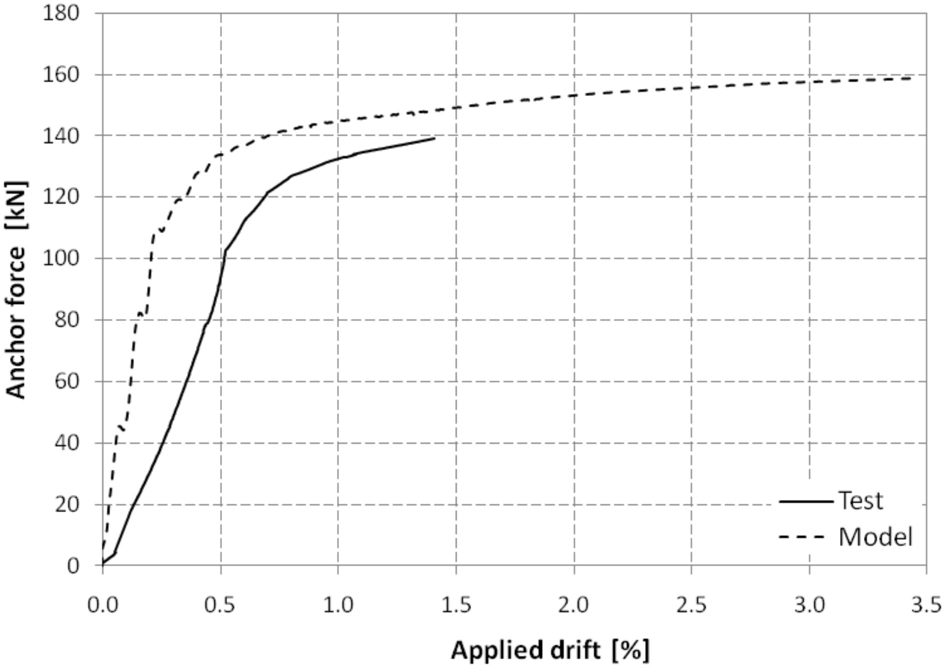

Figure 4.16: Correlation between tension side anchor forces for Test3
(Note: experimental date past a drift of ~1.5% was corrupted)

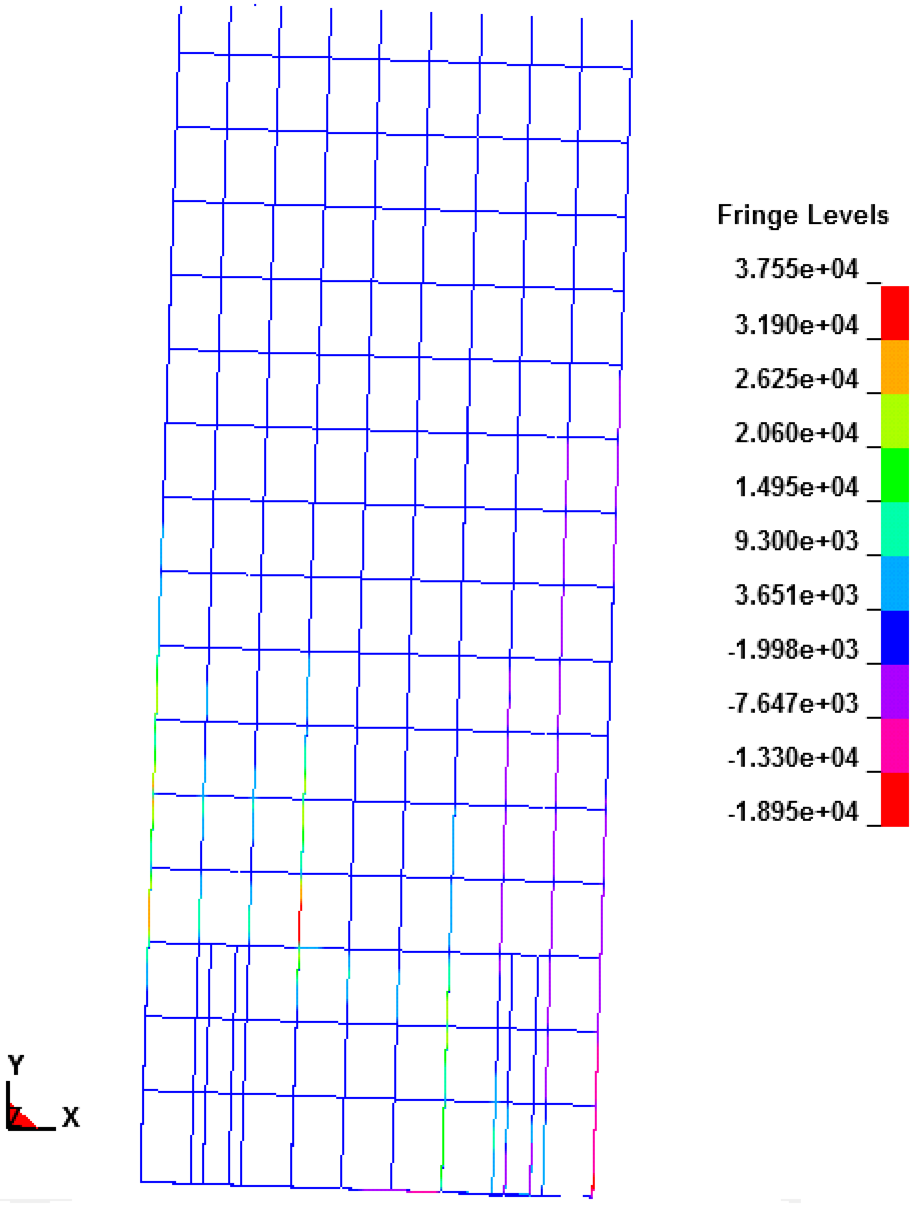

Figure 4.17: Forces in the panel reinforcement (Test3 model)

4.3 Parametric study

In general, the model correlates well with the experimental results with regards to failure load and failure mode. Particularly, greater accuracy of the predicted response is achieved with panels that failed in a ductile manner. Considering the capabilities of the model, it is possible to utilize it beyond the available test data. The parametric study is conducted to investigate the effect of some parameters that may affect the behaviour but were not studied experimentally in the current program. For the parametric study conducted herein, model *MAT_072R3* is used for concrete as it is more capable of capturing compression failure mode compared to *MAT_159*.

4.3.1 Effects of varying gravity loads

Gravity loads are applied as a constant pressure at the top surface of the top beam (see Figure 4.18). Applied load is causing a uniform pressure at the joint level. Normal pressure at joint level is varied between 0.0 and 4.0 MPa; which are typical stresses due to gravity loads at the base of a shear wall in medium-rise buildings. Figure 4.19 shows the effect of the normal pressure on the load-applied deformation response. Normal pressure, failure load, and maximum drifts are listed in Table 4.3. Results show that increasing the vertical applied pressure would greatly enhance the ultimate capacity. Increasing the pressure from zero to 4.0 MPa, boostes the ultimate capacity up from 58.3 kN to 165.1 kN, and leads to a slight decrease in the maximum drift. This increase is approximately equal to the overturning moment caused by the gravity load. With increased pressure, the nonlinearity of the behaviour due to gap opening is decreased. Increased pressure might trigger an early brittle failure due to concrete crushing. However, under the applied pressure levels, such a failure mode has not been triggered. Figure 4.20 shows the variation of tension side anchor forces versus the applied drift. As shown in the figure, yielding of the anchor is observed in all cases. Joints that are subjected to a pressure below 4 MPa are able to sustain an ultimate drift of 3.8 %.

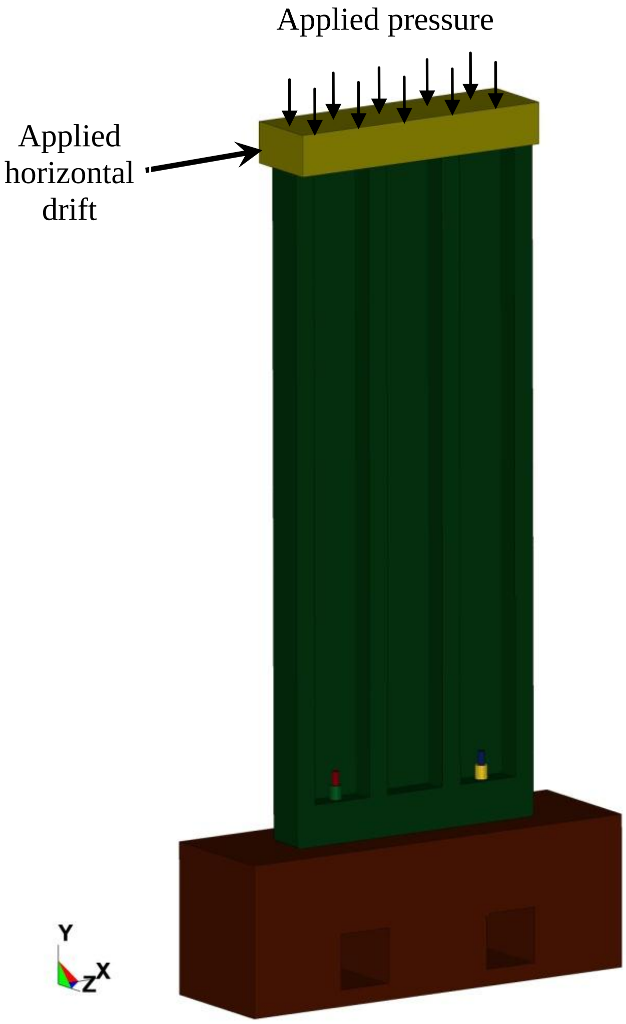

Figure 4.18: Applied pressure to the Anchor-jointed precast structural wall system model

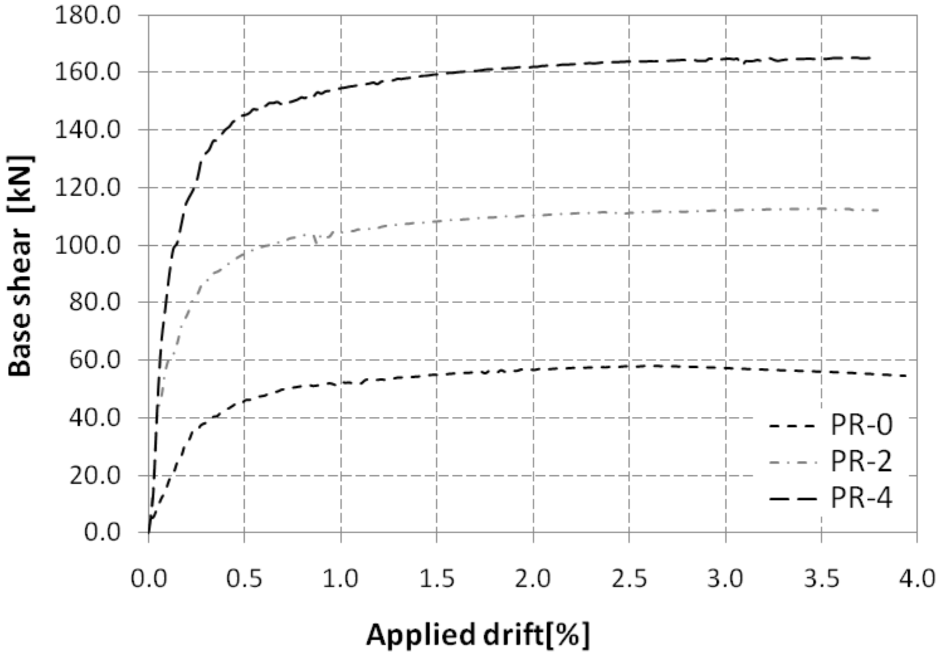

Figure 4.19: Effect of gravity load on the numerical response of the system

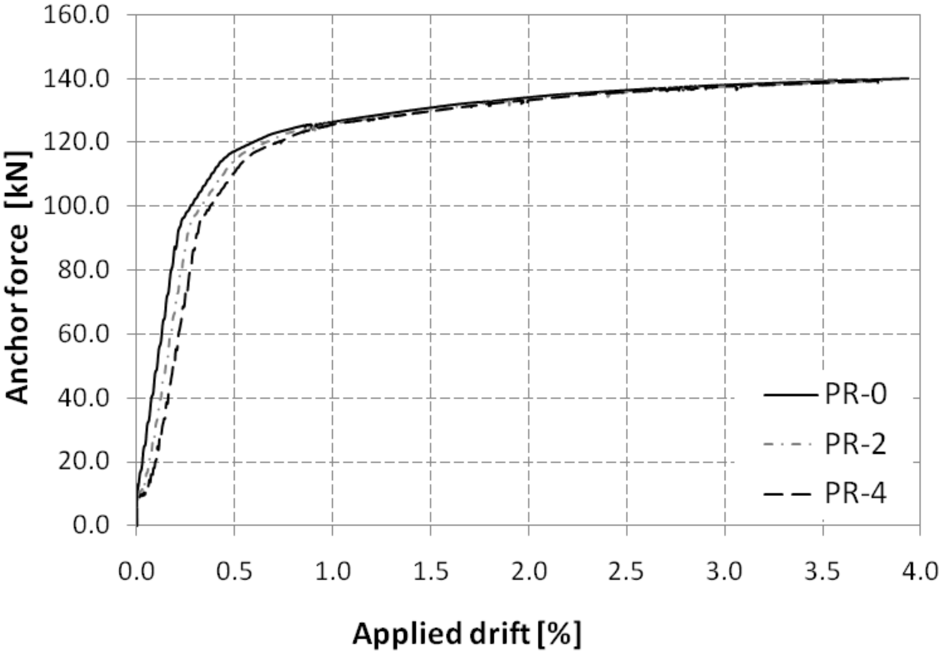

Figure 4.20: Effect of gravity loads on tension side anchor forces

Table 4.3: Effect of gravity loads

Model	Normal stress at joint [MPa]	Failure load [kN]	Maximum drift [%]
PR-0	0.0	58.3	4.94
PR-2	2.0	112.6	3.80
PR-4	4.0	165.1	3.78

4.3.2 Effect of varying anchor bar length/anchor block size

The anchor block size is varied between 150 and 575 mm, which results in a total anchor length varying between 440 and 865 mm as depicted in Figure 4.21. The response predicted by the numerical model is shown in Figure 4.22. The numerical results are also summarized in Table 4.4. The failure mode depends on the anchor block size. Model AL-150 fails in a brittle manner. The short anchor block size, 150 mm, is not able to resist the tensile stresses developed due to anchor load. The failure mode is governed by concrete breakout. Increasing the anchor block size shifts the failure mode towards a more ductile failure by yielding and rupturing of steel anchor. As a result, the failure load is increased from 36.3 kN for Model AL-150 to ~58.6 kN for other models. If concrete breakout failure is avoided, increasing the anchor length would not practically affect the failure load as seen from comparing the results of models AL-330 and AL-575. One of the most significant effects of increasing anchor length is the enhancement of the deformation capacity and, consequently, the improvement in the energy dissipation capabilities. Increasing the anchor length from 330 mm to 575 mm results in 32% and 29% enhancement of the maximum drift and energy absorption, respectively. Since there is no bond between the anchors and the surrounding concrete, strain along the anchor is constant. Hence, the longer bar develops larger displacement at the same strain level. Varying the anchor bar length is an efficient parameter that may be used to reach a target performance level of ductility. Figure 4.23 shows the variation of the tension side anchor force with the drift applied during simulation. Yielding is observed in models AL-330 and AL-575. Yielding of model AL-330, which includes a shorter anchor, starts at smaller drift. On the other hand, failure occurs before yielding for model AL-150. As explained in Section 2.6.6.2, an increase in the anchor length is expected to reduce the joint lateral stiffness. However, comparing results of models AL-330 and AL-575, this reduction is insignificant.

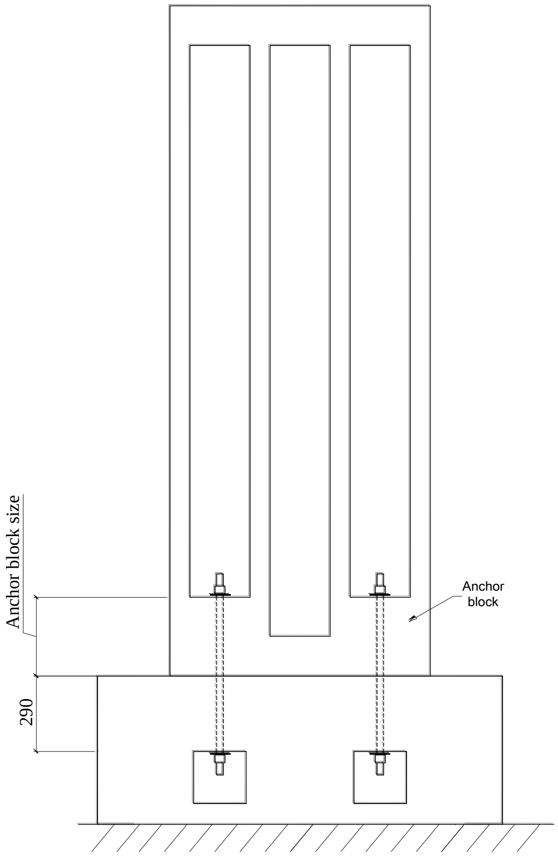

Figure 4.21: Models of varying anchor block size

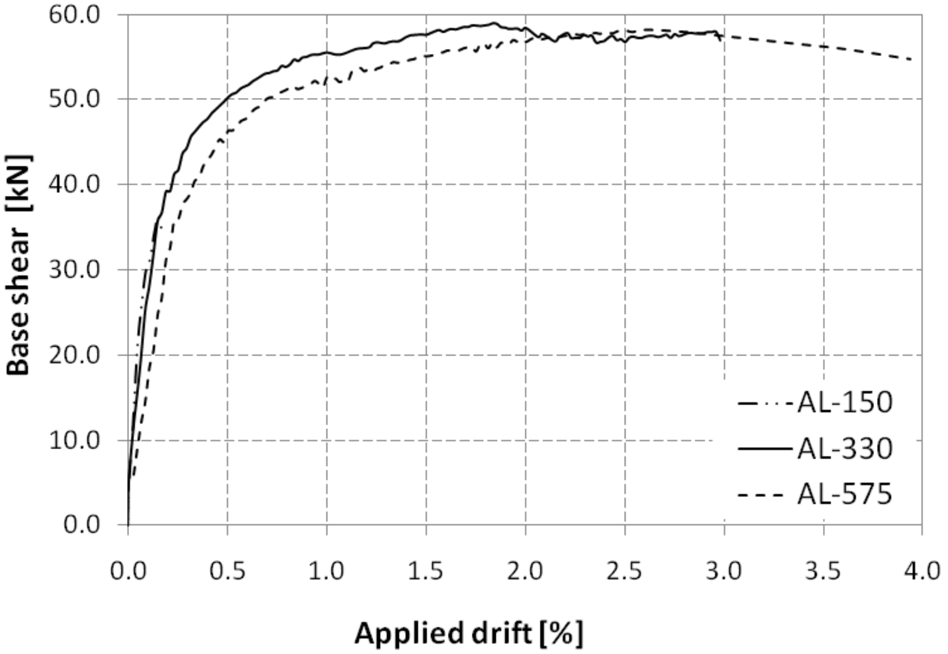

Figure 4.22: Effect of varying anchor length on the numerical response of the system

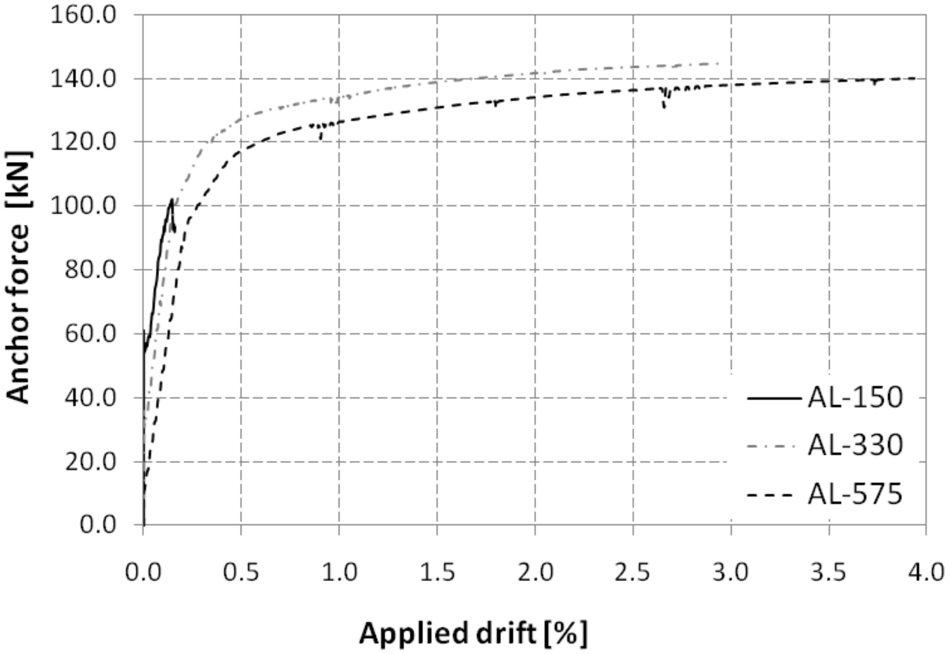

Figure 4.23: Effect of varying anchor length on tension side anchor force

Table 4.4: Effect of varying anchor length

Model	Anchor block size [mm]	Total anchor length [mm]	Failure load [kN]	Maximum drift [%]	Failure mode
AL-150	150	440	36.3	0.15	Concrete breakout
AL-330	330	620	58.9	2.98	Anchor rupture
AL-575	575	865	58.3	3.94	Anchor rupture

4.3.3 Effects of varying anchor pretension load

The initial pretensioning stresses are varied between 0.0 to 240.0 MPa. These stresses are applied to the elements belonging to the anchor shaft as explained in Section 3.7. Initial stresses are then decreased till reaching an equilibrium state. Response predicted by the numerical model is given in Table 4.5. The results indicated that increasing the pretension force, increases the force losses. At pretensioning level of 60.0 MPa, losses are 12.2% versus 26.8% for 240.0 MPa. As shown in Figure 4.24, varying pretensioning force has minor effects on the base shear-lateral drift relationship. Only minor increases of the initial stiffness and the gap-opening load are observed with increased pretensioning. Also, the ultimate drift is slightly decreased, as part of the anchor ductility is already utilized prior to loading. Practically, the failure load is not affected. Figure 4.25 shows the variation of the tension anchor forces during simulations. In general, anchor pretensioning force has an insignificant effect on the response.

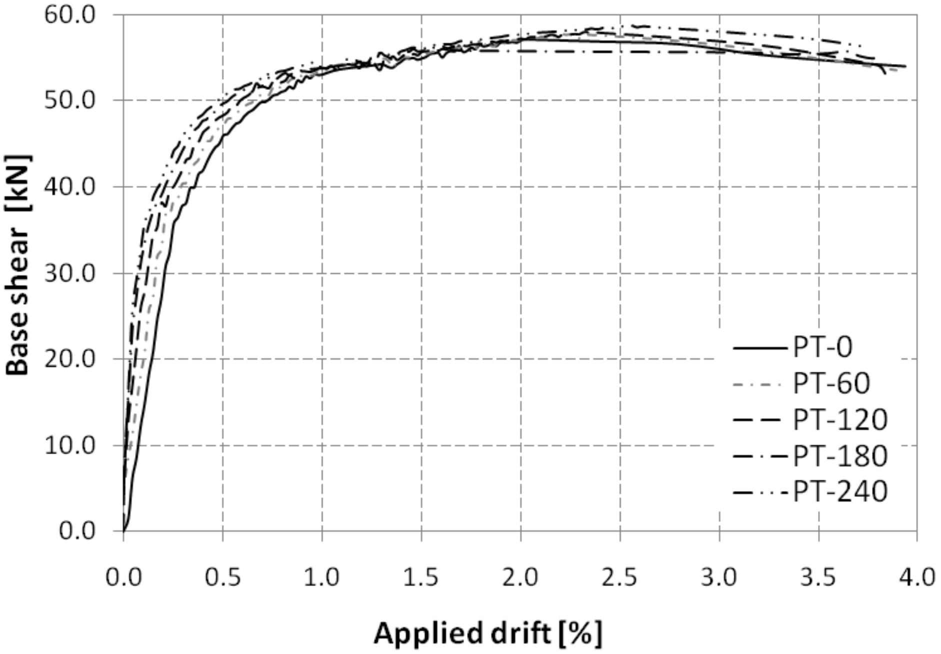

Figure 4.24: Effect of pretensioning load on the numerical response of the system

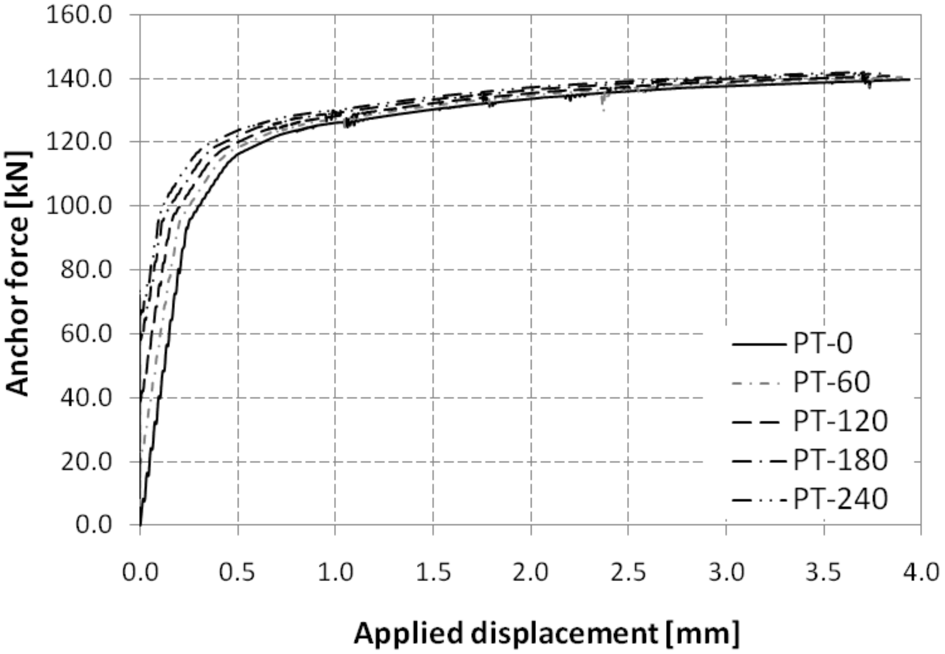

Figure 4.25: effect of pretensioning force on tension side anchor force

Table 4.5: Effect of pretensioning load on the numerical response of the system

Model	Initial Pretensioning stress [MPa]	Pretensioning at equilibrium state [MPa]	Maximum load [kN]	Maximum drift [mm]
PT-0	0.0	0.0	57.0	3.94
PT-60	60.0	52.7	57.8	3.90
PT-120	120.0	105.7	58.0	3.83
PT-180	180.0	155.9	56.7	3.81
PT-240	240.0	175.6	58.6	3.71

4.4 Summary and conclusion

Information and insight gained from simulations presented in Chapter 3 are implemented to build a consistent model for the anchor-jointed precast structural wall system. A rational model is developed. The model is verified against the results of the experimental program discussed in Chapter 2. The non-linear finite element model is used to investigate the effect of selected parameters on the system response. Based on the conducted simulations, the following conclusions can be drawn:

- Nonlinear finite element analysis has great capabilities. It is able to accurately model complex force transfer and captures different failure modes and phenomenon governing the behaviour of anchor-jointed precast concrete shear wall system.
- The proposed 3D modeling technique is general and can be applied for accurate modeling of different jointing techniques.

- The developed model shows acceptable correlations with the experimental data as to failure mode and failure load of the system. However, the model over predicts the system's initial stiffness for all models. In addition, simulations under predicts the system's ductility in case of brittle failures.
- Further research is required to improve the model prediction with regards to initial stiffness and ductility of the system.
- Applying gravity loads greatly enhances the lateral capacity of the system. An increase of normal pressure from 0 to 4.0 MPa leads to a 283% increase of lateral capacity.
- Increasing the anchor length enhances the ductility of the joint without affecting the failure load. An increase of 32% in ductility is observed with increasing anchor length from 620 to 865 mm.
- Varying the anchor bar length is an efficient parameter that may be used to reach a target performance level of ductility.
- Varying pretensioning force has minor effects on the lateral response of the system.

CHAPTER 5

Design of Prestressed Concrete Flat Slab Using Modern Heuristic Optimization Techniques

5.1 Introduction

Prestressed flat-slab system is one of the most widely used structural systems for residential buildings, office buildings, and parking garages in North America. The system is economic, easy to built, and efficient both structurally and architecturally. Inherit redundancy of the system offers alternative load paths allowing the system to withstand extremely high gravity loads; prestressing overcomes concrete weakness in tension and results in improved serviceability and durability (Collins and Mitchell 1997). The system uses the simplest formwork and reinforcement arrangement which expedites the construction process. The absence of beams offers architectural flexibility, easier arrangement of pipes underneath the slab, and more clear space.

In the previous chapters, a system for resisting later load has been developed. To augment the design of a building, the prestressed flat slab system is chosen as the main flooring system and its design is optimized. It is believed that a building combining precast shear walls as lateral-load-resisting system and prestressing flat slab for resisting gravity loads would be the most economic in terms of costs of construction and repairs.

The design process of the post-tensioned flat-slab system to resist gravity loads is pretty well defined in codes of practice all over the world. Considering the infinite number of feasible designs, the objective of this study is to develop a robust numerical tool to aid in designing prestressed flat slabs for minimum cost. The tool should be general, flexible, and relatively easy to use. Furthermore, more practical design optimization examples should be published to close the gap between research and industrial applications (Cohn and Dinovitzer 1994).

Trying to find the lowest cost solution, the current study attempts to consider all the design variables in the optimization process. This would, no doubt, complicate the optimization procedure and necessitate the use of modern heuristics as opposed to exact methods used in previous studies. In addition, the method of structural analysis, Finite Element method with tendons explicitly modeled, is selected to for its generality and flexibility to enable practicing engineers to optimize the design of irregular slabs with regard to plan and loading, if needed.

Although the objective function, cost, is simple and monotonic, the optimization problem is quiet challenging due to the complexity and nonlinearity of the constraints in addition to the discreteness of some of the variables. As a demonstration problem, the optimum design of a square prestressed flat slab is sought.

First, the optimization problem, objective function and constraints, are formulated and the demonstration problem is presented. Then, principles and assumptions used for structural analysis and design are given. Following that, integration of the analysis, design, and optimization is explained. Finally, different optimization techniques are used to find an optimum solution for the demonstration problem. Each technique is discussed and its efficiency is evaluated.

5.2 Formulation of the Optimization Problem

The objective of the optimization procedures developed herein is to minimize the cost of the slab while satisfying all relevant strength and serviceability limit states specified by the Canadian code CSA A23.3. It should be noted that other codes of practice have similar limitations, which probably will not affect the optimization procedures. The selected objective function is the total material cost, which consists of the cost of the concrete material and the prestressing cables. The optimization problem can be defined as:

minimize:

$$C(\mathbf{V},\mathbf{E}) = C_c \,.\, V_c + \sum_{i=1}^{n} C_s \,.\, L_s \tag{5.1}$$

Subject to:

$$\frac{G_i(\mathbf{V},\mathbf{E})}{g_i} \leq 1.0 \tag{5.2}$$

where

C = objective function (cost)
C_c = cost of unit volume of concrete
V_c = total volume of concrete
C_s = cost of unit length of a prestressing tendon
L_s = length of a prestressing tendon
G_i = a constraint function (detailed in Table 5.2), i=1→6

g_i = corresponding allowable limit (detailed in Table 5.2)
V = $\{v_1, v_2, v_3, v_4, v_5\}$
E = $\{e_{1x}, e_{1y}, e_{2x}, e_{2y} \ldots\ldots\ldots\ldots\}$

The design variables, **V** and **E**, are defined in Table 5.1. Behavioral constraints dictated by the Canadian code are presented in Table 5.2.

Table 5.1: Design variables

v_1	=	thickness of the concrete slab (t)
v_2	=	total number of prestressing tendons in the X-Direction (N_x)
v_3	=	total number of prestressing tendons in the Y-Direction (N_y)
v_4	=	tendon size of the X-Direction tendons (D_x)
v_5	=	tendon size of the Y-Direction tendons (D_y)
$e_{1x}, e_{2x}, e_{3x}, \ldots$	=	eccentricities defining the tendon profile in the X-Dir
$e_{1y}, e_{2y}, e_{3y}, \ldots$	=	eccentricities defining the tendon profile in the Y-Dir

Table 5.2: Constraints specified by the Canadian code (CSA A23.3)

	Constraint	Clause	Limit	function/ Symbol
1	Stresses in concrete (initial stage)	18.3.1.1	$-0.6f'_c < S_{conc.} < 0.5\sqrt{f'_c}$	G_1
2	stresses in concrete (final stage)	18.3.2	$-0.6f'_c < S_{conc.} < 0.5\sqrt{f'_c}$	G_2
3	Stresses in steel tendons	18.4	$S_{tendon} < 0.7\, f_{pu}$	G_3
4	Ultimate moment	18.6.2 (a)	$M_r > M_f$	G_4
5	Minimum Factored Resistance	18.7	$M_r > 1.2\, M_{cr}$	G_5
6	Punching shear*	13.3	$v_r > v_f$	G_6
7	Max/Min eccentricity **	7.9 & 6.6.6 (Annex A)	$\lvert e \rvert \le 1 - \frac{2 \cdot d_c}{t}$	E

* Punching shear will also depend on the column dimension, which was taken as a constant in this study

**directly related to the specified minimum concrete cover and tendon diameter (see Figure 5.2) where:

f'_c = specified compressive strength of concrete

S_{conc} = stresses in concrete (obtained from FE analysis) for initial and final loading stages

f_{pu} = Specified tensile strength of prestressing tendons

S_{tendon} = stresses in prestressing tendon (obtained from FE analysis)

v_r = factored shear stress resistance

v_f = factored shear stress

M_r = factored moment resistance

M_f = Factored moment

M_{cr} = cracking moment

e = eccentricity of the prestressing tendon at a specified key point - defined as a ratio to the thickness ranging from -1 to 1

d_c = distance from extreme fibre to the centre of the longitudinal prestressing tendon located close to it (see Figure 5.2)

t = thickness of the concrete slab

In the developed algorithm, users need to define the cost of unit volume of concrete and the cost per unit length of chosen tendon sizes. The unit cost of the structural concrete and steel depends on a number of conditions such as the provider and the site location. For more practical results, the cost provided should also include the construction cost. Table 5.3 lists the materials costs that are used in this work.

Table 5.3: Structural materials cost

Concrete Cost	130 $/m^3
Prestressing tendons	
(1) 9 mm diameter	0.557 $/m′
(2) 13 mm diameter	0.984 $/m′
(3) 15 mm diameter	1.378 $/m′

The design variables can be categorized into two categories. The first one, **V**, includes the variables contributing directly to the objective function (cost). While the second category, **E**, includes the variables defining the prestressing cable profile. In this work, the cable profile is defined by the eccentricity at key points. Eccentricity is defined as a ratio to the thickness ranging from -1.0 to 1.0. The cable profile variables group, **E**, does not contribute directly to the objective function (Cost). If chosen rationally, tensile stresses in concrete are reduced, allowing the choice of slimmer thickness and fewer and smaller diameter tendons; thereby reducing the cost indirectly.

The number of variables of the second category depends on the structural plan layout (i.e. columns arrangement, no. of spans, etc.) and the chosen profile (i.e. straight, triangular, trapezoidal, or parabolic shape). An isolated square flat slab 5m x 5m in plan supported on four columns at its corners is selected to be optimized. The optimum solution of this problem can be found easily by hand calculations, and thus it could be used to evaluate several optimization techniques proposed here. Dead load consists of the own weight of the slab (normal weight concrete at 24 kN/m^3) plus a 2.4 kPa superimposed dead loads, live load of 2.4 kPa. The concrete compressive strength is taken as 40 MPa, concrete cover as 40 mm, and prestressing steel strength as 1860 MPa. For this specific problem, a parabolic cable profile is adapted. Three key points in each of the two perpendicular directions are selected; eccentricities at these points are denoted [e_{1x}, e_{2x}, e_{3x} ,e_{1y}, e_{2y}, e_{3y}]. As shown in Figure 5.1, the chosen key points were located at both ends and at centre.

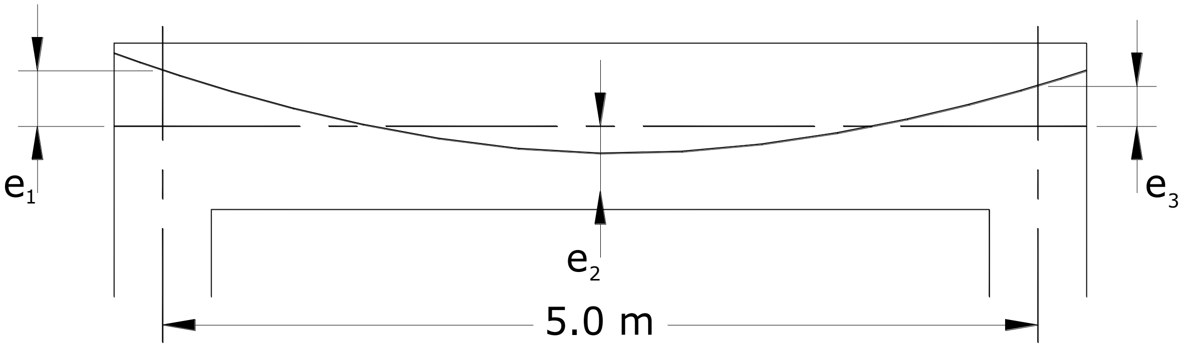

Figure 5.1: Cross-section showing variables defining tendon profile

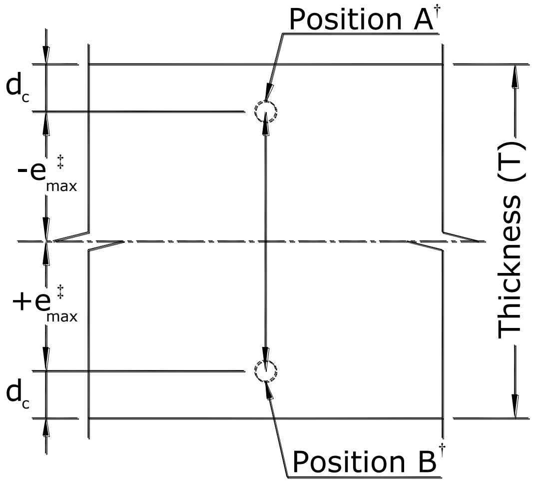

† *prestressing tendon can be located at any point on the line connecting position A and B*
‡ *positive eccentricity means that the tendon is located below the centre line*

Figure 5.2: Cross-section showing the Max/Min eccentricity at a certain location

5.3 Structural Analysis

Structural analysis of the system can be carried out using different methods. Finite Element (FE) analysis, equivalent frame method, and yield line theory are all valid analysis methods. The finite element method is chosen for its generality and ability to model irregular structures and loading conditions.

In the Finite element analysis, concrete slab is modelled using a consistent triangular shell element that was originally developed by Koziey and Mirza (1997). The element utilizes a consistent formulation, which employs a cubic interpolation for displacements and quadratic interpolation for rotations. Consistent formulation frees the element of problems such as shear locking. The element consists of 13 nodes as shown in Figure 5.3 (a). Displacements degrees of freedom are interpolated using ten nodes, while rotational ones are interpolated using six nodes.

Steel tendon is modelled as a discrete integral part of the shell element as depicted in Figure 5.3 (b&c). Tendon element is defined using four nodes; each node has three translational degrees of freedom. For each tendon element, stiffness matrix [12x12] and force vector [12x1] are evaluated using Gaussian integration, and then transformed into the degrees of freedom of the shell element [91x91] using a transformation matrix [12x91]. The outcome is then added to the shell element stiffness matrix and load vector respectively. Prestressing is applied to the tendon elements as prescribed strain. Simplified arithmetic expressions for the formulation of the stiffness matrix of the tendon element are in given in Appendix V. Tendon element can be arbitrary placed within the shell element, and does not need to be connected to the shell element through element nodes which eliminates the need to re-mesh every time the number of tendons changes facilitating the optimization process.

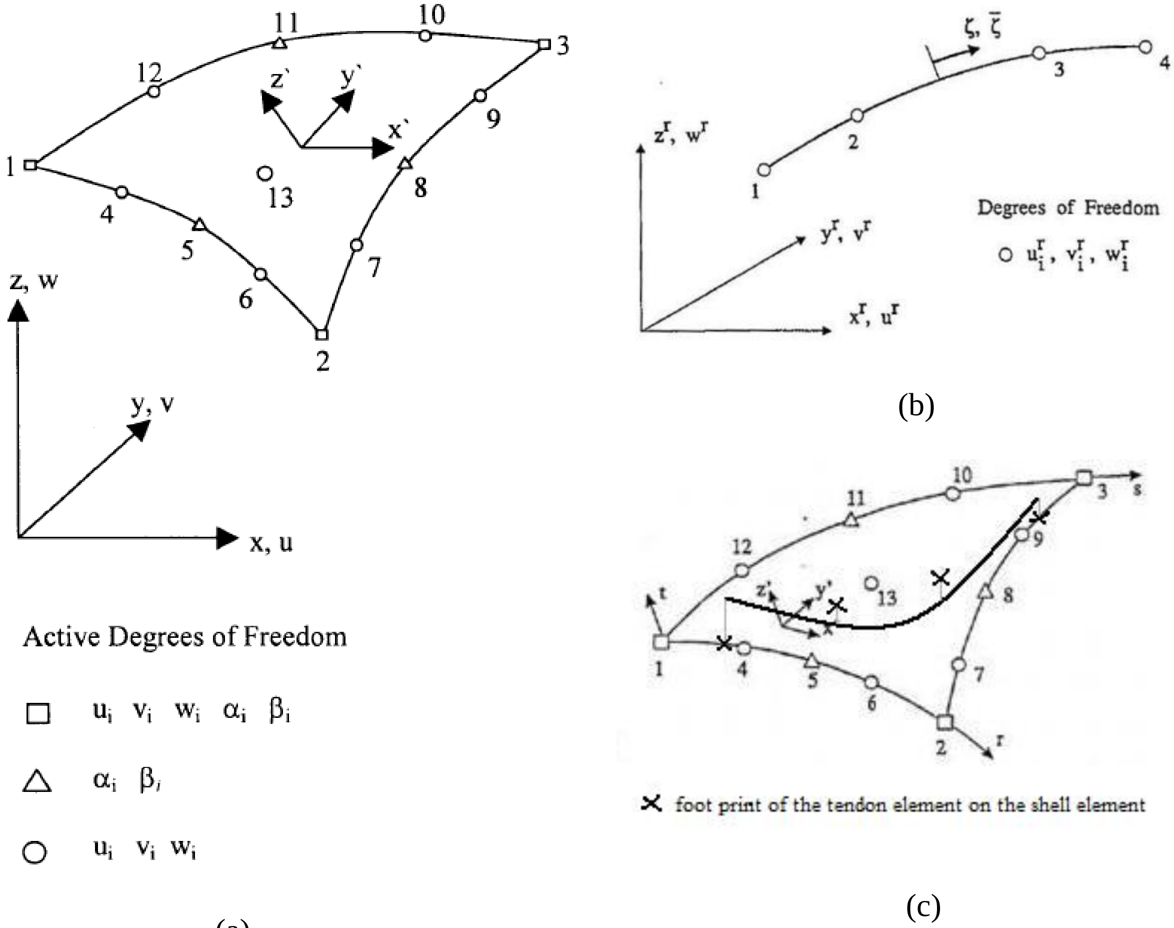

(a)

(b)

(c)

Figure 5.3: Coordinates and degrees of freedom of the elements used (a) consistent shell element (b) tendon element (c) tendon element included in a shell element

5.4 Structural Design

The slab is designed to behave as a fully prestressed concrete member, reinforced with fully bonded prestressing tendons, with no regular rebars. The types of loads considered are the gravitational dead and live loads. Lateral loading is not considered as it is common to use other structural elements such as shear walls to resist lateral loads. In the analysis, final prestressing force is approximated as 90% of the initial force. In the design process, prestressing tendons are assumed to be evenly distributed to the middle strip and the column strip. Pre-stressing strain is assumed to be at its maximum allowable limit and is not considered as a variable in the optimization process.

For working limit state, constraint 1, 2, and 3, the outcome of the finite element analysis, stresses at integration points, are compared to the relevant allowable stresses. On the other hand, for ultimate limit state checks, constraints 4, 5, and 6 are calculated explicitly using relevant code equations. All the design constraints are formulated as the ratio of the demand dictated by the applied loads, i.e. outcome of the structural analysis, to the resistance provided by the concrete section and tendons. A constraint would be active if its value is equal to unity, while a value less than unity means that suggested solution is in the feasible range (see Appendix IV).

From optimization point of view, it would be complicated to apply constraint no.7; where the upper and lower limits of the cable profile variables, **E**, depend on another variable, which is the slab thickness, $\mathbf{v}_1$ (see Figure 5.2). To avoid this dilemma, a new variable, $\mathbf{E}_{\mathrm{Ratio}}$, ranging from –1.0 to 1.0, is to replace **E** within the optimization procedure, where:

$$\mathbf{E} = \mathbf{E}_{Ratio} \cdot e_{Max/Min} \tag{5.3}$$

where:

$$e_{Max/Min} = 1 - \frac{d_c}{t/2} \tag{5.4}$$

This way, the proposed **E** will always be within the feasible range. For convenience, the optimization results are changed back and reported in terms of the original variable, **E**.

5.5 Integration of Analysis, Design, and Optimization

Structural analysis and design are coded using FORTRAN and then coupled with optimization. A pre-processor is developed and integrated into the finite element code to build the input files for each new set of variables suggested by the optimization procedure. The procedure to achieve an optimum design of the prestressed concrete flat slab system follows the algorithm illustrated in Figure 5.4.

```
Procedure Design-Optimization
    Input date: system plan dimension (FE mesh), supports
      locations, material properties, material cost, loading,
      variables limits.
    While optimum solution not found
        Generate a new set of variables V, E.
        Procedure Analysis/Design
            Generate input files for the FE analysis
            Analyze of the system using FE analysis
            Calculate the constraints values
        End Analysis/Design
        Calculate the objective function(s)
    End While
End Design-Optimization
```

Figure 5.4: Procedure for evaluation of optimum design of prestressed concrete slab system

5.6 Optimization Procedure

The objective function, cost, is a monotonic linear function with its minima at the immaterial solution of zero slab thickness and number of cables. Therefore, possible minima must be allocated at an active constraint. If the intersections of the constraint hyper-planes would yield a convex search space, then direct search methods would be suitable for optimization. On the other hand, if the intersections yield a non-convex search space, the intersections of the constraints with the objective function, would yield a number of potential local minima (see Figure 5.5). This would necessitate the use of a global optimization technique.

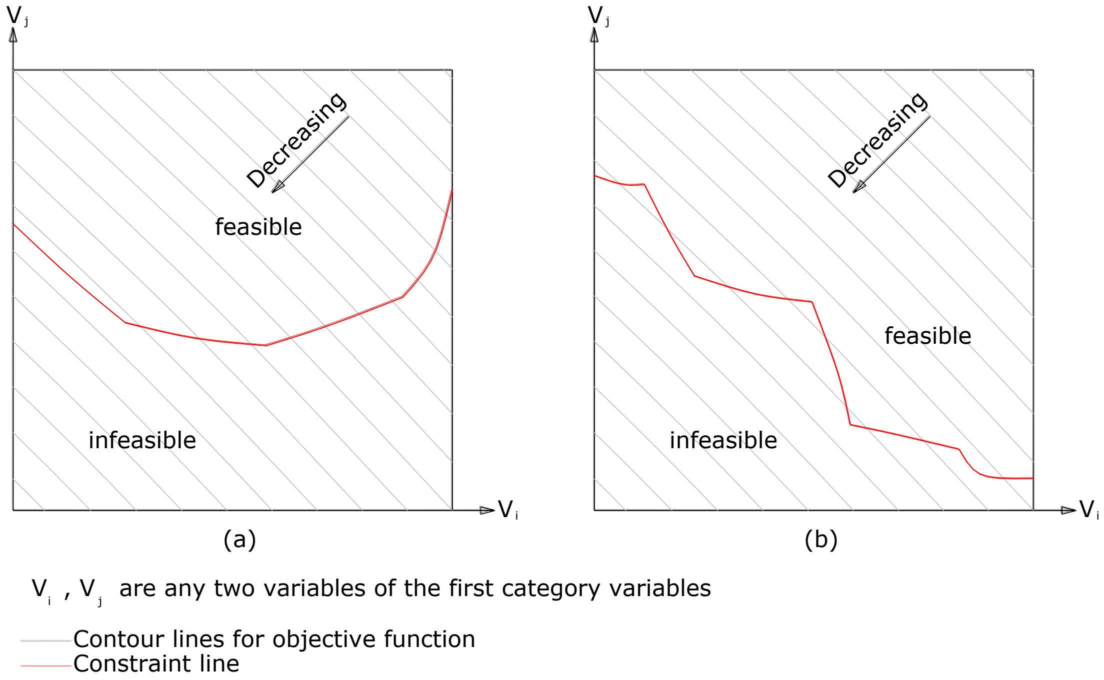

Figure 5.5: (a) convex search space (b) non-convex search space

Direct search methods greatly depend on the initial search point. If different starting search points yield different minima, then there is a strong indication that the search space is non-convex. Two direct search methods are applied to the function at hand. These are the Nelder-Mead search and the Sequential Quadratic Programming (for further details, refer to Rao 1996). In both cases, the discrete variables are treated as continuous variables and rounded to the nearest discrete value. The discrete nature of some of the variables prevents the latter method from approximating the trust region of the search and therefore does not move from the starting point. The Nelder-Mead search is unable to find a satisfactory solution unless a very close point to the optima is chosen as the starting point. This is shown in Table 5.4. Therefore it is concluded that multiple optima might exist, possibly due to the complexity of the constraints and their nonlinearity, in addition to the discreteness of some of the variables.

Table 5.4: Results of the Nedler-Mead direct search method

	Run1		Run2		Run3	
	Initial point	Solution	Initial point	Solution	Initial point	Solution
V_1	150	147	200	209	350	287
V_2	14	14	24	24	35	36
V_3	14	14	24	24	35	34
V_4	15-mm dia.	15-mm dia.	13-mm dia.	13-mm dia.	9-mm dia.	9-mm dia.
V_5	15-mm dia.	15-mm dia.	13-mm dia.	13-mm dia.	9-mm dia.	9-mm dia.
e_{1x}	-0.1633	-0.1595	-0.3000	-0.3000	-0.5400	-0.4919
e_{2x}	0.4200	0.4102	0.5100	0.5100	0.5400	0.4827
e_{3x}	-0.1633	-0.1595	-0.3000	-0.3000	-0.5400	-0.4848
e_{1y}	-0.1633	-0.1595	-0.3000	-0.3000	-0.5400	-0.4737
e_{2y}	0.4200	0.4102	0.5100	0.5100	0.5400	0.5379
e_{3y}	-0.1633	-0.1595	-0.3000	-0.3000	-0.5400	-0.5240
Cost	680.49	670.73	886.33	915.59	1333.33	1128.30
Constraints						
G_1	1.0011	0.9973	1.1355	1.0901	0.8079	1.0110
G_2	0.6964	0.8646	0.6596	0.6408	0.5293	0.6297
G_3	0.9122	0.9127	0.9308	0.9291	0.9178	0.9245
$G_{4\text{-}X}$	0.4359	0.4525	0.2727	0.2546	0.1680	0.1896
$G_{4\text{-}Y}$	0.5298	0.5652	0.3391	0.3249	0.2851	0.3244
$G_{5\text{-}X}$	0.5298	0.5652	0.3391	0.3249	0.2851	0.3083
$G_{5\text{-}Y}$	0.5683	0.5915	0.5481	0.5522	0.8290	0.7416
G_6	0.5683	0.5915	0.5481	0.5522	0.8290	0.7152

Given the findings of the previous trials, it is concluded that a global optimization technique is needed. Of the available global search techniques, Genetic Algorithms (GAs) are utilized. GAs are general purpose random search methods that are inspired by the natural genetic evolution. GAs are applicable to many engineering fields, for further details on the technique and the genetic operators, the reader is referred to Herrera et al. (1998). Optimization is carried out on the two categories of variables, **V** and **E**, simultaneously. Constraints are applied using penalty functions. Penalty functions are linearly proportionate to the level of constraint violation. The objective function is given by:

$$C(\mathbf{V},\mathbf{E}) = \begin{cases} C_c \,.\, V_c + \sum_{i=1}^{n} C_s \,.\, L_s & ,\mathit{if\ all\ const.} \leq 1.0 \text{ (i.e. feasible solution)} \\ K + \sum_{i=1}^{8} \max(P_i, 0) & ,\mathit{else} \end{cases} \tag{5.5}$$

where:

K = a large positive constant representing a high slab cost
$P_i = w \times (G_i - 1)$, i=1→6
w = weighting constant

The constant K ensures that all infeasible solutions assume a higher cost than any other point in the feasible domain, whereas the constant w ensures that the infeasible solutions are penalized significantly so as to direct the search back into the feasible domain. However, it should not be chosen of a high positive value, otherwise it will hamper the search from finding solutions that exist on the constraint boundary (Michalewicz and Fogel, 2004). An order of magnitude analysis is conducted on the objective function and the constraint functions and it is found that the largest possible cost would be $4000; therefore K is assigned that value, whereas the weight w is assigned the value of 10. The applied ranges for the different variables are specified in Table 5.5. Note that the limit for the second category variables, **E**, is applied implicitly using the variable, $\mathbf{E}_{\text{Ratio}}$, as explained above.

Table 5.5: Upper and lower limits of the design variables

Variable	*Upper limit*	*Lower limit*
$\mathbf{v}_1$	90 mm	500 mm
$\mathbf{v}_2$	1	49
$\mathbf{v}_3$	1	49
$\mathbf{v}_4$	1	3
$\mathbf{v}_5$	1	3

Table 5.6 shows the results of three analyses, labeled Run1, Run2, and Run3, by the GAs. The objective function versus Generation (iteration) curve for Run1 is depicted in Figure 5.6. The variability of the optimum solution obtained from different runs indicates that there can be multiple optima along the boundary of the active constraint. It is concluded that the search should be conducted along the boundary of the constraint to achieve better results.

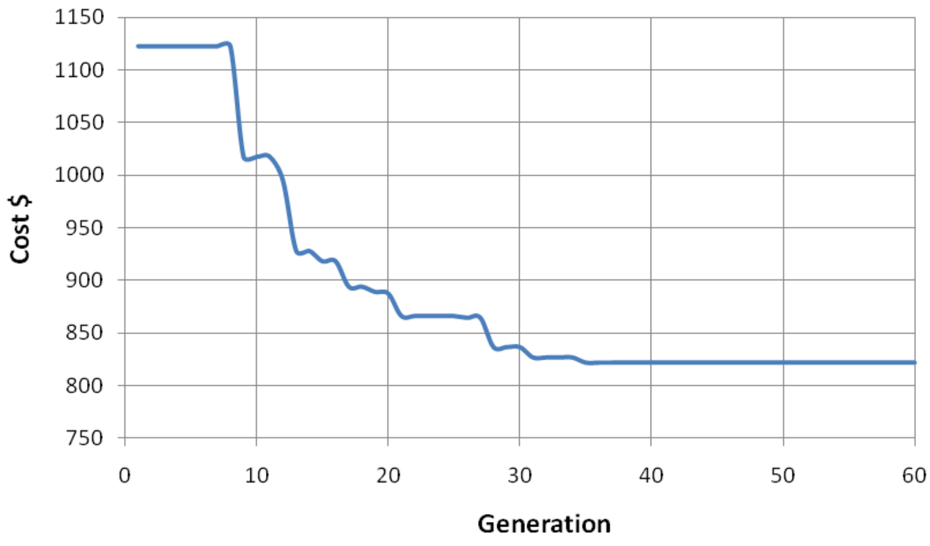

Figure 5.6: Objective function vs. generation (iteration) for the Genetic Algorithm – Run1

Table 5.6: Results of optimization using Genetic Algorithms

	Run1	Run2	Run3
Obtained Solution			
V_1	218	199	198
V_2	10	12	33
V_3	13	13	27
V_4	13-mm dia.	13-mm dia.	9-mm dia.
V_5	13-mm dia.	13-mm dia.	9-mm dia.
e_{1x}	0.1283	-0.2161	0.3668
e_{2x}	0.4087	0.4348	0.5012
e_{3x}	-0.1860	-0.0998	0.2918
e_{1y}	0.4696	0.2144	0.4881
e_{2y}	0.5759	0.3978	0.5548
e_{3y}	-0.0327	0.5873	0.5177
Cost	821.68	769.77	810.90
Constraints			
G_1	0.9892	0.9472	0.9930
G_2	0.7582	0.7866	0.8191
G_3	0.8974	0.8997	0.9206
$G_{4\text{-}X}$	0.2431	0.2880	0.2732
$G_{4\text{-}Y}$	0.5162	0.6240	0.4902
$G_{5\text{-}X}$	0.6559	0.6699	0.4122
$G_{5\text{-}Y}$	0.7702	0.8292	0.6721
G_6	0.9276	0.8730	0.6000

Now, realizing the different effects of the two variable categories on the objective function, it is decided to uncouple them when searching for the Optima. It is thought that the best solution would be found searching along the boundaries of the constraints. The procedure steps are as follows: First, search along the first category variables, **V**, using genetic algorithm, while the second category variables, **E**, are kept constant, to minimize the cost. Minimum cost typically exists at an active constraint. Secondly, using optimum **V'**s from previous step, a search for new **E**'s is conducted within the feasible space at which the constraint would be furthest from the boundary (see Figure 5.7). The objective function representing the distance away from the constraint boundary can be expressed as follows:

minimize:

$$D = \begin{cases} Max(\mathrm{G_i}) - 1 & ,if\ \ all\ \ const.\ \le\ 1.0\ \ \text{(i.e. feasible solution)} \\ 1 + \sum_{i=1}^{8} \max(P_{\mathrm{i2}}, 0) & ,else \end{cases} \tag{5.6}$$

where

D = proposed objective function, representing the distance away from the constraint boundary

G_i = constraint functions values, i = 1→ 6

P_{i2} = $(G_i - 1)$, i=1→6

This search zigzags in the feasible vicinity close to a constraint line as shown in Figure 5.7. The search starts at eccentricities equal to zero and moves forward until an optimum solution is found. The procedure moves towards the optimum solution, but its computational time is dependent on the initial guess of **E**, given by the designer. Thus excessive computational time might be the drawback of this method. Results of successive runs of genetic algorithms are shown in Figure 5.7.

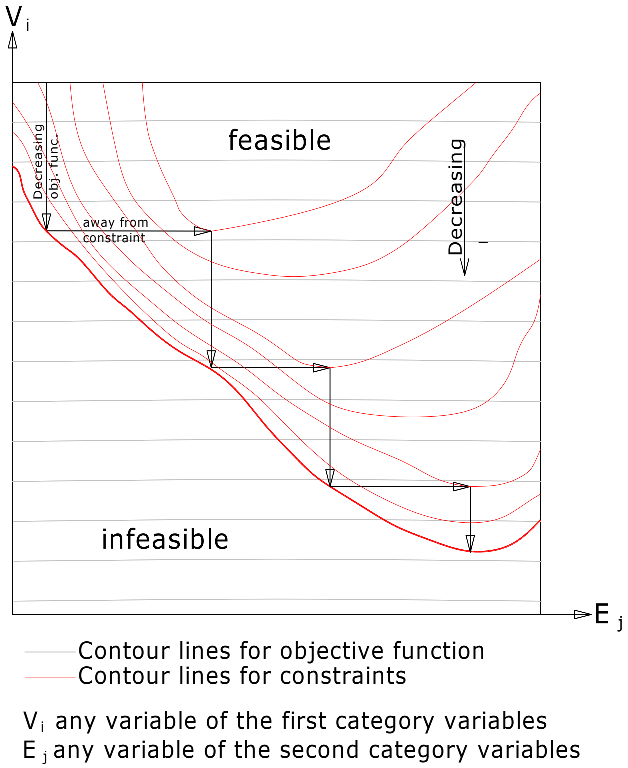

Figure 5.7: Searching for the optima along a constraint boundary

Table 5.7: Results of optimization along constraint boundary

Obtained Solution	Step 1		Step 2		Step 3		Step 4
	Minimizing		Minimizing		Minimizing		Minimizing
	Cost	Distance	Cost	Distance	Cost	Distance	Cost
V_1	199	199	179	179	175	175	159
V_2	28	28	19	19	31	31	37
V_3	27	27	30	30	17	17	31
V_4	13-mm dia.	13-mm dia.	13-mm dia.	13-mm dia.	9-mm dia.	9-mm dia.	9-mm dia.
V_5	13-mm dia.	13-mm dia.	9-mm dia.	9-mm dia.	13-mm dia.	13-mm dia.	9-mm dia.
e_{1x}	0.0000	0.2545	0.2354	-0.0891	-0.0875	0.2767	0.2533
e_{2x}	0.0000	0.3251	0.3007	0.3555	0.3489	0.4355	0.3986
e_{3x}	0.0000	0.2235	0.2067	-0.0566	-0.0555	0.2121	0.1941
e_{1y}	0.0000	0.1566	0.1448	0.4541	0.4457	-0.0209	-0.0191
e_{2y}	0.0000	0.3772	0.3488	0.3790	0.3720	0.5429	0.4969
e_{3y}	0.0000	0.1595	0.1475	0.4508	0.4425	0.1530	0.1401
Cost (C)	917.35	917.36	758.93	758.95	738.90	738.90	706.49
Constraints							
G_1	0.9710	0.8871	0.9857	0.9182	0.9904	0.9096	0.8965
G_2	0.8244	0.5879	0.9387	0.9138	0.9589	0.9067	0.9896
G_3	0.9406	0.9369	0.9229	0.9182	0.9310	0.9228	0.9373

G_{4-X}	0.2995	0.2693	0.3306	0.3267	0.3395	0.3399	0.3946
G_{4-Y}	0.5245	0.3475	0.3603	0.3500	0.9209	0.8098	0.5317
G_{5-X}	0.5119	0.3378	0.8369	0.8167	0.3510	0.3008	0.4609
G_{5-Y}	0.8771	0.5835	0.5628	0.5473	0.9605	0.8451	0.5798
G_6	0.8689	0.5760	0.9218	0.8997	0.5438	0.4673	0.5375
Distance (D)	-0.0290	-0.0631	-0.0143	-0.0818	-0.0096	-0.0772	-0.0104

The zigzagging moves along the boundary of the constraints show that an optimization approach should drive the search points in the early phases towards the constraint boundary in addition to its drive towards the minimum cost. Bearing in mind that there are some variables that do not affect the cost function but are rather related to the constraint boundary, a good portion of the search space becomes unnecessary to approach for cost minimization. To create this extra drive towards the constraint boundary, optimization of the two objective functions, Cost and Distance (defined previously as C and D), should be carried out simultaneously. A multi-objective evolutionary algorithm using the strength Pareto approach, Zitzler and Thiele (1999),is used for this purpose. As the two objective functions are in conflict, the multi-objective evolutionary algorithm finds a group of non-dominated solutions rather than a single point solution. This set is known as Pareto-optimal solutions, which are superior to all other solutions in the search space i.e. any of the objective functions of the Pareto-optimal solutions cannot be improved without degradation in the other objective function. A more detailed presentation of the algorithm can be found in Zitzler and Thiele (1999). Due to the random nature of this search method, outcome obtained by repeating the analysis might be a little different. To examine this, three independent analyses using the same algorithm are reported. Results are shown in Figure 5.8 and Table 5.8.

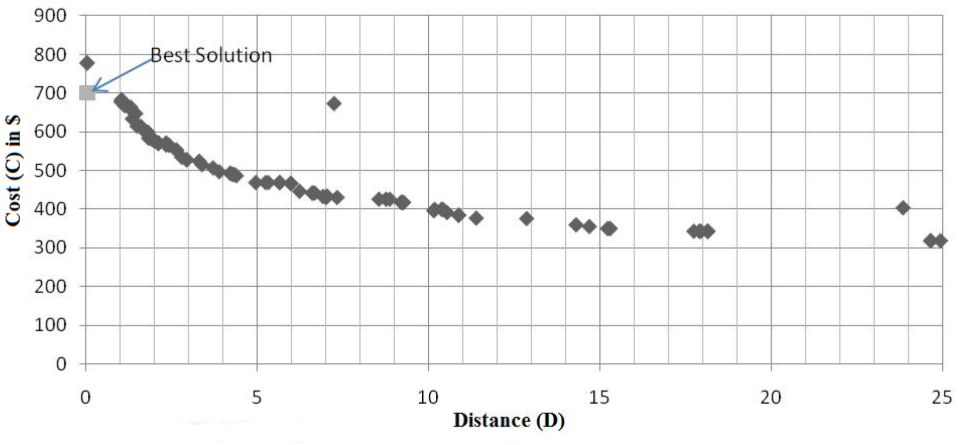

(a)

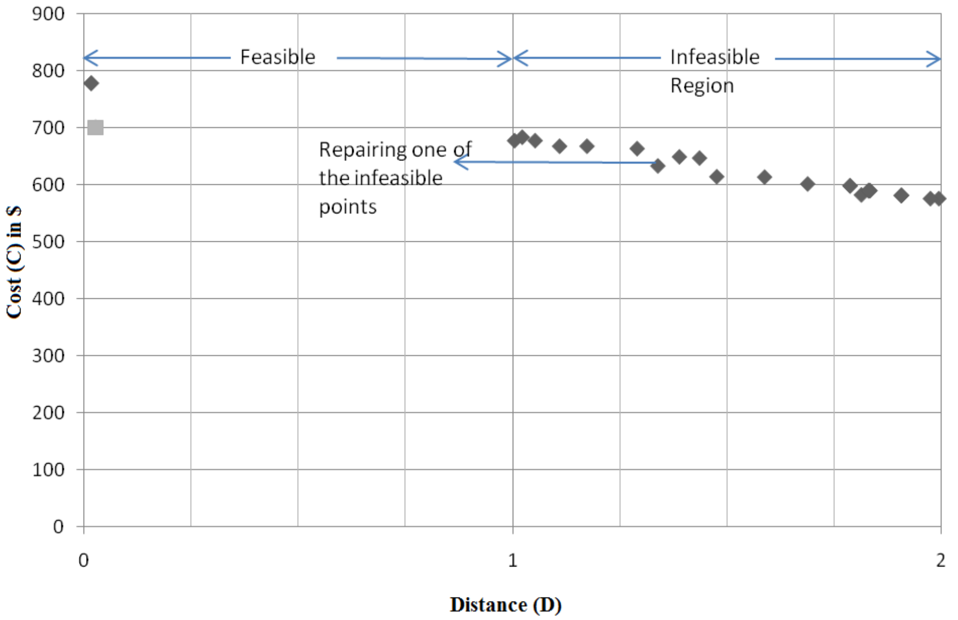

(b)

Figure 5.8: (a) Pareto-optimal solutions of the multi-objective optimization (Run1) (b) Zooming at the boundary line between feasible and infeasible solution

Table 5.8: Results of optimization using Multi-objective evolutionary algorithm

Best Solution	Run1	Run2	Run3
V_1	169	171	176
V_2	26	19	18
V_3	16	26	19
V_4	9-mm dia.	9-mm dia.	13-mm dia.
V_5	13-mm dia.	9-mm dia.	13-mm dia.
e_{1x}	0.1430	0.0348	-0.1419
e_{2x}	0.4298	0.5307	0.4640
e_{3x}	-0.0902	0.0443	-0.0031
e_{1y}	-0.1090	-0.0507	0.2007
e_{2y}	0.4012	0.3794	0.4224
e_{3y}	0.1110	0.0344	-0.0959
Cost (C)	700.54	681.33	754.08
Constraints			
G_1	0.8432	0.8949	0.7898
G_2	0.9704	0.9765	0.6669
G_3	0.9235	0.9180	0.9506
$G_{4\text{-}X}$	0.3730	0.3604	0.3225
$G_{4\text{-}Y}$	0.9725	0.6416	0.4828
$G_{5\text{-}X}$	0.3990	0.8423	0.5047
$G_{5\text{-}Y}$	0.9560	0.7244	0.6244
G_6	0.5496	0.8735	0.6401
Distance (D)	-0.0275	-0.0235	-0.0494

For further improvement, a second step in the optimization routine is suggested. One of the infeasible points is repaired using the zigzagging search procedure explained in Figure 5.7, starting with maximizing the distance away from the active constraint, D, then minimizing the cost, C, as explained in Figure 5.8 (b). For more efficient search, the upper limit imposed on the thickness should be reduced as a reduction in cost is expected at lower thickness. Outcome of the repairing process are given in Table 5.9. Results obtained from this procedure are superior to all other procedures. It is thus suggested to follow the following steps when optimizing the design of a prestressed flat slab system:

(1) Using the multi-objective evolutionary algorithm, find the Pareto-optimal solutions.

(2) Repair one of the infeasible found solutions that is close to the boundary by zigzagging along **E** first, minimizing Distance, D, and then along **V**, minimizing the cost, C.

Table 5.9: Results of repairing infeasible solution using zigzagging procedure

	Point to be repaired†	minimize Distance	minimize Cost‡
V_1	159	159	150
V_2	24	24	10
V_3	17	17	12
V_4	9-mm dia.	9-mm dia.	15-mm dia.
V_5	13-mm dia.	13-mm dia.	15-mm dia.
e_{1x}	0.1619	-0.0634	-0.0596
e_{2x}	0.4205	0.4969	0.4667
e_{3x}	-0.0421	-0.1300	-0.1221
e_{1y}	-0.1004	-0.1500	-0.1409
e_{2y}	0.3787	0.4131	0.3880
e_{3y}	-0.0573	-0.1247	-0.1171
Cost (C)	667.38	667.40	639.13
Constraints			
G_1	0.9302	0.8592	0.7505
G_2	1.1095	0.9289	0.9412
G_3	0.9216	0.9239	0.9022
$G_{4\text{-}X}$	0.4066	0.4025	0.4424
$G_{4\text{-}Y}$	0.9772	0.9508	0.6145
$G_{5\text{-}X}$	0.4547	0.4411	0.7130
$G_{5\text{-}Y}$	0.8964	0.8727	0.6220
G_6	0.5644	0.5477	0.6773
Distance (D)	+0.1095	-0.0492	-0.0588

† obtained from Run1 (infeasible solution)

‡ best solution found from all different tested optimization procedures

The obtained optimum design depends on the problem input, i.e. loads, material strength, material costs, and plan layout. Varying the relative cost of concrete and prestressing might yield a different optimum designs. For the considered problem, optimum design is not governed by a single constraint, implying that constraints are highly interrelated; a slight change in one of the design variables might change the governing constraint. Comparing different methods used in this study, the minimum thickness obtained is 150 mm and the corresponding cost is 639.1 $. This solution is ~10% cheaper than the one obtained by optimization using GAs along the constraints boundaries. For the lowest cost solutions obtained here, the optimum eccentricity at the middle section ranges between 0.9→1.0 of the maximum allowable eccentricity, $e_{max/min}$, whereas eccentricity at the edge of the slab ranges from +0.04→−0.14 of the slab thickness. Varying the cable eccentricity between theses limits will not affect the cost noticeably. It is noticed that the slab thickness is the prominent design variable governing the cost; this is conceivable considering that large volume of concrete used for slabs in general. However, to achieve savings in thickness tendon profile and/or layout need to be optimized.

5.7 Summary and Conclusion

In this study, a numerical tool that is capable of finding the optimum design of a prestressed concrete flat slab system using modern heuristic search algorithms is developed. The optimum solution must satisfy all behavioural constraints imposed by the chosen design code. The introduced numerical tool employs finite element analysis for structural analysis with prestressing modelled explicitly using tendon elements. The developed tool is general and flexible and could be used by practicing engineers for optimum design of real world problems. As a demonstration problem, the optimum design of a square prestressed flat slab supported on four columns at the corners and spanning 5.0 m is investigated. The Canadian code CSA A23.3 is chosen as the design code. Several optimization techniques have been considered and the following conclusions could be drawn from the results:

- Using the given concrete and steel costs, the main design variable governing the cost of a prestressed concrete slab is the thickness. To minimize the thickness, cable profile and/or layout need to be optimized at the same time.
- Although the objective function, cost, C, is simple and monotonic, the optimization problem is quiet challenging. The intricacy of the optimization problem could be traced back to the complexity and nonlinearity of the constraints, as well as the discreteness of some of the design variables, $v_{2\rightarrow5}$. Considering the monotonic nature of the function, optimum solution must lie on an active constraint hyper line. It is also possible for multiple optima to exist.
- For the studied example, constraints are observed to be highly interrelated. A slight change in one of the design variables might change the governing design constraint.
- Direct search methods covering only a small search space are not able to find an optimum solution unless a very good, close to the optima, estimate for the initial search point is made by the designer.
- Using GA's on the whole set of the design variables at one time is not successful in finding optima. A large portion of the search space is deemed unnecessary as search should be conducted along the active constraint boundary.
- Design variables should be divided into two categories and a second objective function should be introduced to represent the distance away from the active constraint, D. Search is conducted to minimize both objective functions (cost and distance) successively until a satisfactory solution is found. This method can achieve an optimum solution but its computational time is dependent on the initial point of search given by the designer, and thus might be prohibitive.

- For better results, search should be conducted for both objective functions simultaneously using multi-objective evolutionary algorithm. Solution is then to be improved by searching along the constraint boundary using GA's.
- Comparing the results of different methods used, the suggested procedure is successful in finding an optimum design for the demonstration problem.
- Using the multi objective algorithm opens a door for including other objective functions that might be of interest to the designer such as minimum deflection, maximum reliability index, and minimum environmental impact. Of course, increasing the number of the objective functions will increase the complexity of the optimization problem.

CHAPTER 6

Conclusions and Recommendations

6.1 Introduction

The research work completed and reported in this thesis consists of two parts. The first part involves experimental development and analytical analysis of anchor-jointed precast structural wall system (Chapters 2 to 4). The second part of the study is concerned with finding an optimum design of concrete prestressed flat slab system (Chapter 5).

6.2 Summary and Conclusion

6.2.1 Anchor-jointed precast structural wall system

Precast concrete shear walls are used to resist lateral loads in medium to high rise buildings. Precast construction is quick, efficient, and economic. Generally, precast concrete shear wall response is highly dependent on the behaviour of base panel-to-foundation joint. An innovative joining technique is proposed to accelerate construction process and reduce concrete damage possibility and capital loss during an earthquake event. Panels are jointed using anchor bolts slid through prefabricated holes at the panel edges. Inspired by the jointing technique, the system is designated "anchor-jointed precast structural wall system". Steel anchors are utilized as a structural fuse, i.e. a sacrificable structural element that provides adequate structural ductility and strength during an earthquake event. Structural fuse, i.e. anchors, could be easily replaced after an earthquake, minimizing repair costs and serviceability disruptions. In this study, conceptual development of the system is carried out. A research program of combined analytical and experimental studies is initiated in this study. This work lays out the basis towards developing design procedures for the new system which is a corner stone towards acceptance and recognition of this system as a lateral-load-resisting system by relevant codes.

6.2.1.1 Experimental study

Four reduced scale specimens are tested under monotonic horizontal displacement. Each specimen comprises of two parts: a precast panel and a base block jointed through a horizontal joint using two anchor bolts. Tests are conducted to study the behaviour of the proposed joint under combined shear and bending moment which mainly govern the behaviour of lower joints. Test results are used to characterize the behaviour of such connections; mainly determining lateral strength and associated possible modes of failure. Key parameters dominating the behaviour are identified and their importance is assessed. Available analytical procedure, developed to predict the behaviour of the connection of analogous joints, is reviewed and assessed.

This study shows that anchor-jointed precast structural wall system provides a feasible alternative to conventional cast-in-place shear walls in low-to-medium seismic regions. The system has desirable seismic characteristics. The following conclusions can be drawn from the test results:

- The ultimate capacity of the joint corresponds to one of the following: (1) rupture of steel anchor, (2) concrete compression failure at the bearing edge of the panel, or (3) concrete breakout failure. A successful design should avoid brittle concrete failures.
- The originally proposed panel design is inherently weak in resisting breakout failure. This weakness impedes the system from resisting higher levels of lateral loads. A modification of the panel geometry and reinforcement by increasing the anchor block size is suggested and tested. The detail used in strengthening the test specimens against breakout failure is successful in increasing breakout capacity and avoiding this brittle failure mode. This detail is easily applicable to new constructions.
- In order for the joints to achieve satisfactory performance, the concrete breakout strength must be greater than the ultimate tensile strength of the anchors. In addition, the area of steel should be limited to ensure that steel yields before concrete crushes under bearing stresses.
- Joint may be designed to sustain all damage and inelastic deformations are concentrated in the anchors. Following a damaging earthquake event, only damaged anchor bolts would need to be replaced. Anchor may act as a structural fuse.
- The system is able to undergo large inelastic deformation with little damage to the concrete panel. Seismic demand up to a 3.5 % of drift could be attained by the proposed joint configurations with minimum apparent damage to the precast wall connection. This level represents typical seismic demand for low to moderate seismicity.

- As the anchor length is increased, the displacement capacity of the joint is also increased. Anchor length is dictated by the anchor block size.

6.2.1.2 Numerical study

First, model parameters are developed and fine-tuned. Then, a model to simulate the behaviour of anchor-jointed structural shear wall system is built and verified. Finally, the developed model is extended to study the effect of selected parameters on the specimen’s behaviour.

6.2.1.2.1 Model development

Through a model development process, material properties, material model parameters, element size, mesh layout, and contact definitions are examined and fine-tuned to accurately capture the behaviour. The model development consideres capturing different possible failure modes and phenomenon governing the behaviour including: breakout of concrete cone, rupture of steel anchor, concrete crushing, dowel action, shear friction, and anchor pretensioning. Tests involving subassemblies with analogous failure modes and/or similar joints reported in the literature are modelled. Accuracy of the numerical simulations depend on the finite element model parameters selection. The research focuses on identifying the critical parameters influencing the behaviour of the model. Based on critical analysis of the models, the following conclusions could be drawn:

- For the breakout failure mode, FE model is able to predict the concrete cone breakout failure load provided that the material model parameters governing the concrete fracture energy in tension are chosen rationally.
- Both *MAT_072R3* and *MAT_159* can be used to predict concrete behaviour with reasonable accuracy. However, it is more convenient to use material model *MAT_159* for modelling concrete. Unlike *MAT_072R3*, internal parameters are automatically adjusted by the material model for each element as a function of the element size to ensure constant fracture energy is maintained regardless of the element size.
- Modelling of steel anchor yielding and rupturing is possible using material model no.24. Failure criteria specifying the maximum principal strain at failure is able to capture the true behaviour of an anchor subjected to tensile loads provided that the true stress-strain curves are used.
- For shear force transfer, dowel action forces may be governed by concrete softening rather than steel strength for large-diameter bars. Softening in this case is related to damage in compression. Hence, the material model parameters governing the concrete fracture energy in compression need to be chosen rationally
- Anchor pretension is modelled successfully by assigning initial tensile stresses to the anchor shaft. It is observed that the axial stresses applied initially are decreased till reaching equilibrium state due to deformation of the upper and lower blocks. A few trials are needed to reach a specific pretension force.

- The numerical response obtained from all simulations provides a reasonable correlation with the experimental data with regards to failure load and failure modes. Thus, features of these models including material properties, material model parameters, element size, mesh layout, and contact definitions can be used to build a reliable model to predict the behaviour and failure modes of the proposed joint.

6.2.1.2.2 Model

Information and insight gained from simulations presented in Chapter 3 are implemented to build a consistent model for the anchor-jointed precast structural wall system. A rational model is developed. Model is verified against the results of the tests presented in Chapter 2. Based on simulations conducted, the following conclusions can be drawn:

- Nonlinear finite element analysis using LS-DYNA has great capabilities. It is able to accurately model complex force transfer and captures different failure modes governing the behaviour of anchor-jointed precast concrete shear wall system.
- The proposed 3D modeling technique is general and can be applied for accurate modeling of different jointing techniques.
- The developed model shows acceptable correlations with the experimental data as to failure mode and failure load of the system. However, the model over predicts the system’s initial stiffness. In addition, simulations under predicts the system’s ductility in case of brittle failures.

6.2.1.3 Parametric study

Considering the capabilities of the model, it is possible to utilize it beyond the available test date. A parametric study based on the verified model is conducted to evaluate the effects of selected parameters on the response of the tested specimens. Selected parameters are: (1) vertical load resembling gravity loads, (2) anchor pretension force, and (3) anchor length. Based on simulations conducted, the following conclusions can be drawn:

- Applying gravity loads greatly enhances the lateral capacity of the system. An increase of normal pressure from 0 to 4.0 MPa leads to a 283% increase of lateral capacity.
- Increasing the anchor length enhances the ductility of the joint without affecting the failure load. An increase of 32% in ductility is observed with increasing anchor length from 620 to 865 mm.
- Varying the anchor bar length is an efficient parameter that can be used to reach a target performance level of ductility.
- Varying pretensioning force has minor effects on the lateral response of the system.

6.2.1.4 Recommendation for future research

To facilitate development of design procedures for the anchor-jointed precast structural wall system, required for code approval, different aspects of the behaviour should be studied both experimentally and analytically:

- The effect of the following parameters on the response of the suggested joint under bending: (a) gravity loads (b) wall aspect ratio (h_w/ℓ_w) (c) the use of closely spaced ties at lower panel corners to provide more ductility for concrete in compression.
- The type of loading may affect the failure mode and load. The behaviour of the suggested joint under cyclic and dynamic loading should be studied. Strength, stiffness, ductility and energy dissipation are of particular interest.
- Study of the ultimate breakout strength of the anchor block.
- Testing two jointing planes (i.e. foundation and two panels).
- Behavior of the suggested joint under shear loading.
- Parameters affecting the system lateral stiffness, which in turn affects the system structural period and the seismic demand.
- Further research is required to improve the model prediction with regards to initial stiffness and ductility of the system.

6.2.2 Design optimization

In this study, a numerical tool that is capable of finding the optimum design of a prestressed concrete flat slab system using modern heuristic search algorithms is developed. The optimum solution must satisfy all behavioural constraints imposed by the chosen design code. The introduced numerical tool employs finite element analysis for structural analysis with prestressing modelled explicitly using tendon elements. The developed tool is general and flexible and can be used by practicing engineers for optimum design of real problems. As a demonstration, the optimum design of a square prestressed flat slab supported on four columns at the corners and spanning 5.0 m is investigated. The Canadian code CSA A23.3 is chosen as the design code. Several optimization techniques have been considered and the following conclusions could be drawn from the results:

- Using the given concrete and steel costs, the main design variable governing the cost of a prestressed concrete slab is the thickness. To minimize the thickness, cable profile and/or layout need to be optimized at the same time.
- Although the objective function, cost, C, is simple and monotonic, the optimization problem is quiet challenging. The intricacy of the optimization problem can be traced back to the complexity and nonlinearity of the constraints, as well as the discreteness of some of the design variables. Considering the monotonic nature of the function, optimum solution must lie on an active constraint hyper line. It is also possible for multiple optima to exist.
- For the studied example, constraints are observed to be highly interrelated. A slight change in one of the design variables might change the governing design constraint.
- Direct search methods covering only a small search space are not able to find an optimum solution unless a very good, close to the optimum, estimate for the initial search point is made by the designer.

- Using GA's on the whole set of the design variables at one time is not successful in finding optima. A large portion of the search space is deemed unnecessary as search should be conducted along the active constraint boundary.
- Design variables should be divided into two categories and a second objective function should be introduced to represent the distance away from the active constraint, D. Search is conducted to minimize both objective functions (cost and distance) successively until a satisfactory solution is found. This method can achieve an optimum solution but its computational time is dependent on the initial point of search selected by the designer, and thus might be prohibitive.
- For better results, search should be conducted for both objective functions simultaneously using multi-objective evolutionary algorithm. Solution could then be improved by searching along the constraint boundary near it using GA's.
- Comparing the results of different methods used, the suggested procedure is successful in finding an optimum design for the demonstration problem.
- Using the multi objective algorithm opens a door for including other objective functions that might be of interest to the designer such as minimum deflection, maximum reliability index, and minimum environmental impact.

REFERENCES

Aaleti, S. , Sritharan, S. "A simplified analysis method for characterizing unbonded post-tensioned precast wall systems" Engineering Structures, v 31, n 12, 2966-2975, December 2009.

ACI Committee 318, "Building code requirements for structural concrete (ACI 318-08) and commentary (ACI 318-08)" American Concrete Institute, Farmington Hills, MI, 2008.

ACI Committee 444: Models of concrete structures, "Models of Concrete Structures –state–of–the–art" Concrete International. January, 1979.

American Concrete Institute (ACI) "Acceptance Criteria for Special Unbonded Post-Tensioned Precast Structural Walls Based on Validation Testing (ACI ITG-5.1-07)" Innovation Task Group 5, Farmington Hills, MI , 2008.

American Concrete Institute (ACI) "Requirements for Design of a Special Unbonded Post-Tensioned Precast Shear Wall Satisfying ACI ITG-5.1 (ACI ITG-5.2-09) and Commentary" Innovation Task Group 5, Farmington Hills, MI, 2009.

ASTM C1611 / C1611M - 09b: Standard Test Method for Slump Flow of Self-Consolidating Concrete

ASTM C39/C39M-94: Standard Test Method for Compression Strength of Cylindrical Concrete Specimens.

ASTM C496-96: Standard Test Method for Splitting Tensile Strength of Cylindrical Concrete Specimens.

Atabay, S. and Gulay F.G. "The study of the effect of changes in cost of the materials used in 3-D shear-wall reinforced concrete structures on the optimum dimensions" Expert Systems with Applications 36(3), 4331-4337, 2009.

Balling R, Yao X "Optimization of reinforced concrete frames" ASCE Journal of Structural Engineering, 123(2), 193–202, 1997.

Bažant, Z.P. (Editor) "Fracture Mechanics of Concrete Structures" Proceedings of the First International Conference on Fracture Mechanics of Concrete Structures (FraMCoS1), held at Beaver Run Resort, Breckenridge, Colorado, USA, June 1992, Elsevier Applied Science, ISBN: 1-85166-869-1, Section 3.2.1.

Bažant, ZP, "Mechanics of Fracture and Progressive Cracking in Concrete Structures," Chapter 1 in Fracture Mechanics of Concrete: Structural Application and Numerical Calculation, Ed. G. C. Sih, Di Tomasso, A. Martinus-Nijhoff, Doordrecht-Boston 1985, 1-91. ISBN: 90-247-2960-2.

Bažant, ZP. , Cedolin, L. "Blunt Crack Band Propagation in Finite Element Analysis" ASCE J Eng Mech Div, v 105, n 2, 297-315, Apr 1979.

Bažant, ZP., Oh, B.H. "Crack Band Theory for Fracture of Concrete" Material and Structures, v 16, n 93, 155-177, May-Jun 1983.

Bora, C., Oliva, M.G., Nakaki, S.D. and Becker, R. "Development of a Precast Concrete Shear-Wall System Requiring Special Code Acceptance" PCI Journal, 2007, Vol. 52, No. 1, 122–35.

Bursi, O.S. and Jaspart, J.P. "Calibration of Finite Element Model for Isolated Bolted End-Plate Steel Connection" J. Construct. Steel Res., 1997, Vol. 44, No. 3, 225-262.

CEB-FIP Model Code 1990, Comité euro-international du béton. Thomas Telford House, London, 1993, ISBN: 0727716964.

Choi C, Kwak H "Optimum RC member design with predetermined discrete sections" ASCE Journal of Structural Engineering, 116(10), 2634–2655, 1990.

Coello CA, Christiansen AD, Santos F "A simple genetic algorithm for the design of reinforced concrete beams" Engineering with Computers, 13(4), 185–196, 1997.

Cohn MZ, Dinovitzer AS "Application of structural optimization" ASCE Journal of Structural Engineering, 120(2):617– 650, 1994.

Collins, M.P. , Mitchel, D. "Prestressed Concrete Structures" Response publication, Canada, 2006, ISBN:0-9681958-0-6.

CSA A23.3-04, *Concrete design handbook*, Cement Association of Canada, Ottawa, Ontario, Canada, 2006.

Dowling, Norman E. "Mechanical behavior of materials: engineering methods for deformation, fracture and fatigue", Publisher Pearson Prentice Hall, 2007, ISBN: 0131863126.

Eligehausen, R., Mallée, R., Silva, J.F. "Anchorage in Concrete Construction", Publisher: Ernst & Sohn, 2006, ISBN: 978-3-433-01143-0. Section 3.3.1.

Fintel, M. "Performance of precast concrete structures during Rumanian earthquake of March 4, 1977" PCI JOURNAL, Volume 22, 10-15, March/April 1977.

Foerster, H. R., "Behaviour of the connections typically used in precast concrete load-bearing shear wall panels" Ph.D. Thesis, University of Manitoba, Winnipeg, Manitoba, 1987.

Foerster, H.R., Rizkalla, S.H., and Heuvel J.S. "behaviour and design of shear connection for loadbearing wall panels" PCI journal, 102-119, Vol. 34, No. 1, January-February 1989.

Fuchs, W., Eligehausen, R., and Breen, J. E., "Concrete Capacity Design (CCD) Approach for Fastening to Concrete" ACI Structural Journal, Vol. 92, No. 1, 73-94, January-February1995.

HALLQUIST, J O. "LS-DYNA Keyword User's Manual" Version 960, Livermore Software Technology Corporation, Livermore, CA, March 2001.

HALLQUIST, J O. "LS-DYNA Theoretical Manual" Livermore Software Technology Corporation, Livermore, CA, May 1998.

Herrera F, Lozano M, Verdegay JL "Tackling real-coded genetic algorithms: Operators and tools for behavioural analysis" Artificial Intelligence Review, 12, 265–319, 1998.

Holden T, Restrepo J, Mander J B. "Seismic Performance of Precast Reinforced and Prestressed Concrete Walls" Journal of Structural Engineering 2003, 129(3), 277-424.

Hutchinson, R., Rizkalla, S., Lau, M., and Heuvel, S. "Horizontal Post-Tensioned Connections for Precast Concrete Loadbearing Shear Wall Panels" PCI Journal, V. 36, No. 6, 1991.

Kousmousis VK, Arsenis J "Genetic algorithms in optimal detailed design of reinforced concrete members". Computer-Aided Civil and Infrastructure Engineering, 13(1), 43–52, 1998.

Koziey BL "Formulation and applications of consistent shell and beam elements. Dissertation" McMaster University, Hamilton, Canada, 1993.

Koziey BL, Mirza FA. "Consistent thick shell element" Computers and Structures 65(4):531–549, 1997.

Kumarswamy KN, "Experimental and numerical analysis of structures with bolted joints subjected to impact load" Ph.D. Thesis, University of Nevada Las Vegas, Las Vegas, 2010.

Kurama Y, Pessiki S, Sause R, Lu L. "Seismic behaviour and design of unbonded post-tensioned precast concrete walls" PCI Journal, 44(3), 72–89, 1999.

Kuyucular A "Prestressing optimization of concrete slabs" Journal of Structural Engineering, 117(1), 235–254, 1991.

Lounis Z, Cohn MZ "Multiobjective optimization of prestressed concrete structure" Journal of Structural Engineering, 119(3), 794–808, 1993.

MacRae, AJ, Cohn MZ "Optimization of prestressed concrete flat plates" Journal of Structural Engineering, 113(5), 943–957, 1987.

Malvar, L. J.; Crawford, J. E.; Wesevich, J. W.; and Simons, D. "A Plasticity Concrete Material Model for DYNA3D" International Journal of Impact Engineering, V. 19, No. 9/10, 847-873, 1997.

Martí JV, González-Vidosa F "Design of prestressed concrete precast pedestrian bridges by heuristic optimization" Advances in Engineering Software, 41(7–8), 916–922, 2010.

Michalewicz Z, Fogel DB "How to Solve It: Modern Heuristics" Springer, New York, 2004.

Murphy, G., "Similitude in Engineering" Ronald Press, New York, 1960.

Murry Y.D. "Users Manual for LS-DYNA Concrete Material Model 159" US Department of Transportation, Federal Highway Administration, Publication No. FHWA-HRT-005-062, 2004.

Murry Y.D., Abu-Odeh A., Bligh R. "Evaluation of LS-DYNA Concrete Material Model 159" US Department of Transportation, Federal Highway Administration, 2004, Publication No. FHWA-HRT-005-063.

Nakamura, H., and Higai, T., "Compressive Fracture Energy and Fracture Zone Length of Concrete" JCI-C52E Seminar of post-peak behaviour of RC structures subjected to seismic loads, Vol. 2, 259-272, October 1999.

National Building Code of Canada (NBCC 2005), "National Building Code of Canada" Institute for Research in Construction, National Research Council of Canada, Ottawa, Ontario, 2005.

Pampanin S, Priestley M J N, Sritharan S. "Analytical Modeling of the Seismic Behavior of Precast Concrete Frames Designed with Ductile Connections" Journal of Earthquake Engineering (JEE) 2001, 5(3), 329-367, Imperial College Press.

Paulay, T., Park, R., and Phillips, M. H. "Horizontal construction joints in cast-in-place reinforced concrete" Shear in reinforced concrete, ACI Special Publication 42, Detroit, 1974, 599-616.

Payá I, Yepes V, González-Vidosa F, Hospitaler A "Multiobjective optimization of reinforced concrete building frames by simulated annealing" Computer-Aided Civil and Infrastructure Engineering, 23(8), 575–89, 2008.

Perez, F., Sause, F., Pessiki, S. "Analytical and experimental lateral load behavior of unbonded posttensioned precast concrete walls" Journal of Structural Engineering 133(11), 1531–1540, 2007.

Primavera, E. J., Pinelli, J-P, Kalajan, E. H., "Tensile Behaviour of Cast-in-Place and Undercut Anchors in High-Strength Concrete," ACI Structural Journal, v. 94, n. 5, September-October 1997, pp. 583-594.

Priestley, M. J. Nigel ; Sritharan, S. Sri; Conley, James R.; Pampanin, Stefano , "Preliminary results and conclusions from the PRESSS five-story precast concrete test building", PCI Journal, v 44, n 6, 42-67, November/December 1999.

Priestley, M. J. Nigel ; Sritharan, S. Sri; Conley, James R.; Pampanin, Stefano , "Preliminary results and conclusions from the PRESSS five-story precast concrete test building", PCI Journal, v 44, n 6, 42-67, November/December 1999.

Rao SS "Engineering Optimization: theory and practice" John Wiley and Sons, New Jersy, 1996.

Reid J.D., Hiser N.R., "Friction modeling between solid elements" International Journal of Crashworthiness Vol. 9 (1), 65–72, 2004.

Rozvany GIN, Hampson AJK "Optimum design of prestressed plates" Journal of American Concrete Institute, 60(8), 1065–1082, 1963.

Sahab MG, Ashour AF, Toropov VV "A hybrid genetic algorithm for reinforced concrete flat slab buildings" Computers and Structures, 83(8-9), 551–559, 2005 (a).

Sahab MG, Ashour AF, Toropov VV "Cost optimisation of reinforced concrete flat slab buildings" Engineering Structures, 27(3), 313–322, 2005 (b).

Santiago, S.D. and Hilsdorf. H.K. "Fracture Mechanics of Concrete under Compressive Loads" Cement and Concrete Research, Vol 3 (4), 363-388, 1973.

Schultz A.E. and Magana R. A., "Seismic Behavior of Connections in Precast Concrete Walls", Mete A. Sozen Symposium, ACI Special Publication Vol.162, 273-312, August 1996.

Schultz A.E. and Magana R. A., "Seismic Behavior of Connections in Precast Concrete Walls", Mete A. Sozen Symposium, ACI Special Publication Vol.162, 273-312, August 1996.

Schultz, A. E., and R. A. Magana. "Seismic Behavior of Connections in Precast Concrete Walls" Mete A.Sozen Symposium, Paper SP 162-12, American Concrete Institute (ACI), 273–311, 1996.

Schwer, Leonard E. and Malvar, L. Javier. "Simplified Concrete Modeling with MAT_CONCRETE_DAMAGE_REL3" JRI LS-DYNA USER WEEK August 2005.

Soudki K. A. "Behavior of horizontal connections for precast concrete loadbearing shear wall panels subjected to large reversed cyclic deformation" Ph.D. Thesis, University of Manitoba, Winnipeg, Manitoba, 1994.

Soudki, K. A., Rizkalla, S. H., LeBlanc B. "Horizontal connections for precast concrete shear walls subjected to cyclic deformations part 1: mild steel connections" PCI Journal, v 40, n 4, 78-96, Jul-Aug 1995.

Soudki, K., J. West, S., Rizkalla S., and Blackett, B. "Horizontal Connections for Precast concrete Shear Wall Panels under Cyclic Shear Loading" PCI Journal, V. 41, No. 3 (May–June 1996): 64–81.

Templeman A "Optimization methods in structural design practice" ASCE Journal of Structural Engineering, 109(10), 2420–2432, 1983.

Tu Zhenguo and Lu Yong "Evaluation of typical concrete material models used in hydrocodes for high dynamic response simulations" International Journal of Impact Engineering, v 36, n 1, 132-146, January 2009.

West J. "Behaviour of Horizontal Connections for Precast Concrete Load-bearing Shear Wall Panels Subjected to Reversed Cyclic Shear Loading" M.A.Sc thesis, University of Manitoba, Winnipeg, Manitoba, 1993.

Wyllie, L. A. JR. and Filson, J. R. "Armenia earthquake reconnaissance report" Earthquake Spectra Publication No. 89.01, Special Supplement.

Yonten, K., Manzari MT., Marzougui D., Eskandarian A. "An assessment of constitutive models of concrete in the crashworthiness simulation of roadside safety structures" International Journal of Crashworthiness, Volume 10 No.1, 5-19, 2005.

Zitzler E and Thiele L "Multiobjective evolutionary algorithms a comparative case study and the strength pareto approach" IEEE Transact on Evolutionary Computation 3(4), 257–271, 1999.

Appendix I

(Photos of the experimental program)

Specimen fabrication

Reinforcement and formwork of the precast concrete panel

Close up to reinforcement

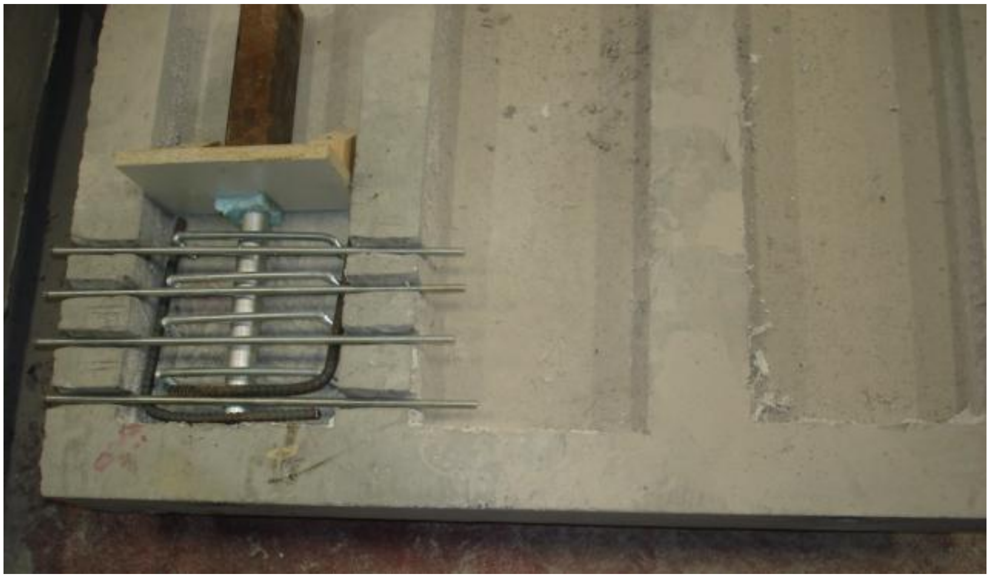

Strengthening panel against concrete breakout failure (increasing anchor block size)

Reinforcement of the upper loading beam

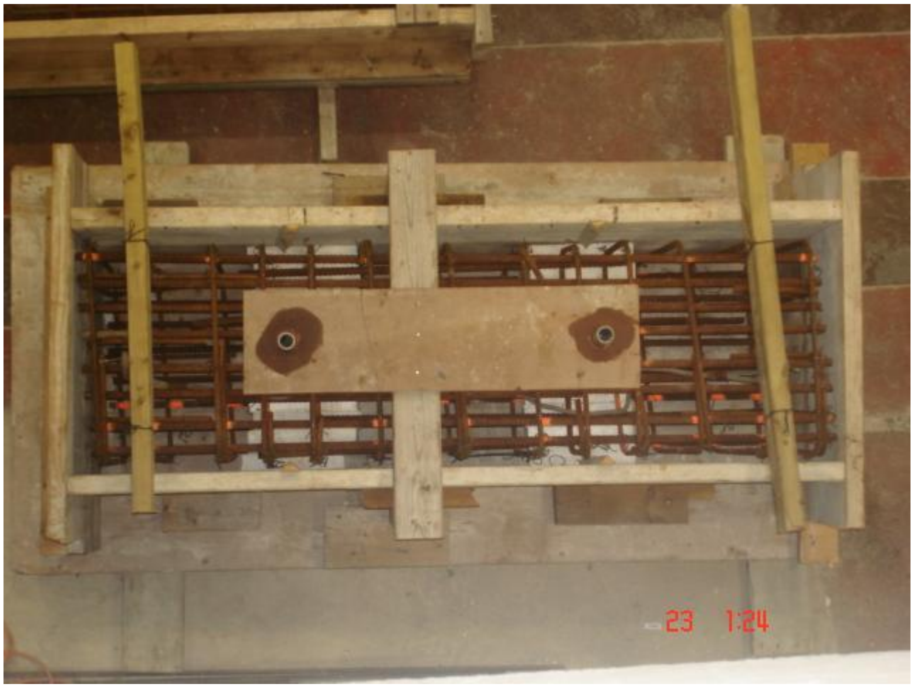

Reinforcement and formwork of the base block

Slump flow test for the self-compacting concrete

Placing concrete

Panel curing

Specimen Assembly

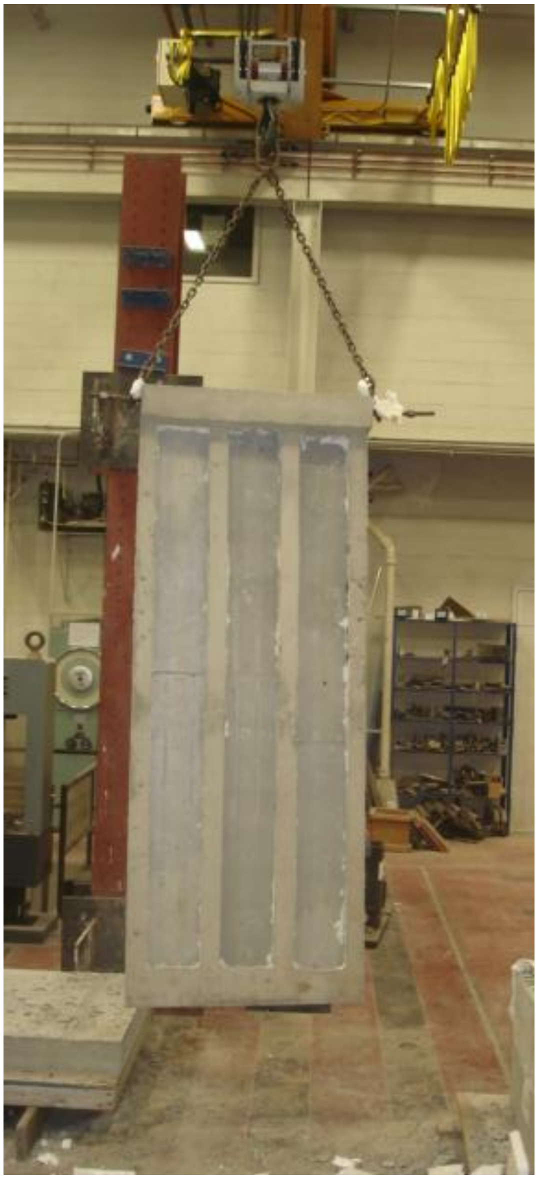

Panel handling with laboratory crane

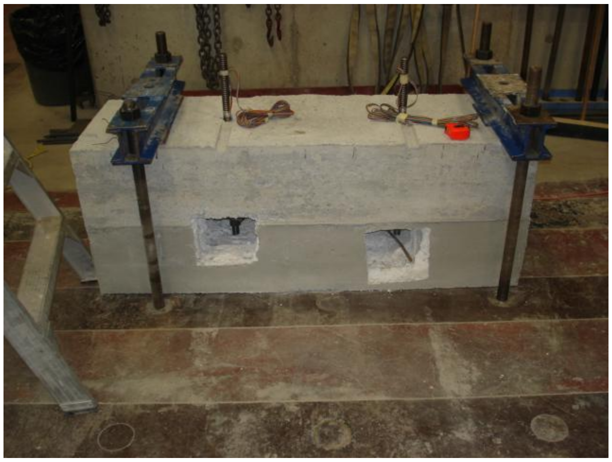

Concrete base block with anchors in place and protruding out

Beams supporting base block

Elevation and side view of test set-up

Over all view of test set-up

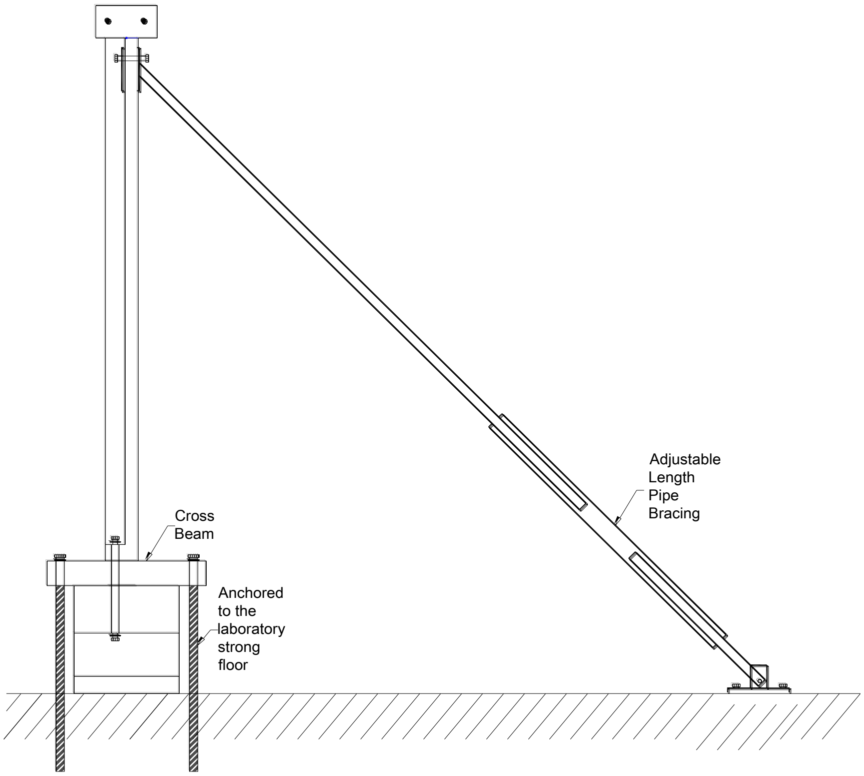

Out-of-plane bracing system

Pin connection at the end of the out-of-plane bracing

Direct tensile test for Grade-75 bar

Testing Grade70 – 1'' anchor bolt under direct tension test

Failure of Grade70 – 1 '' anchor bolt under direct tension

Failure of Grade70 – 1'' anchor bolt under direct tension (close up)

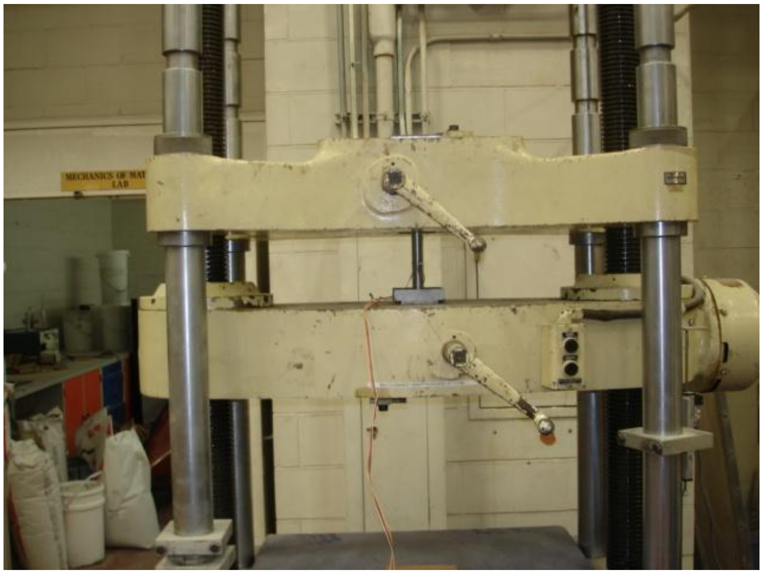

Testing 3/4'' threaded anchor bolt under direct tension test

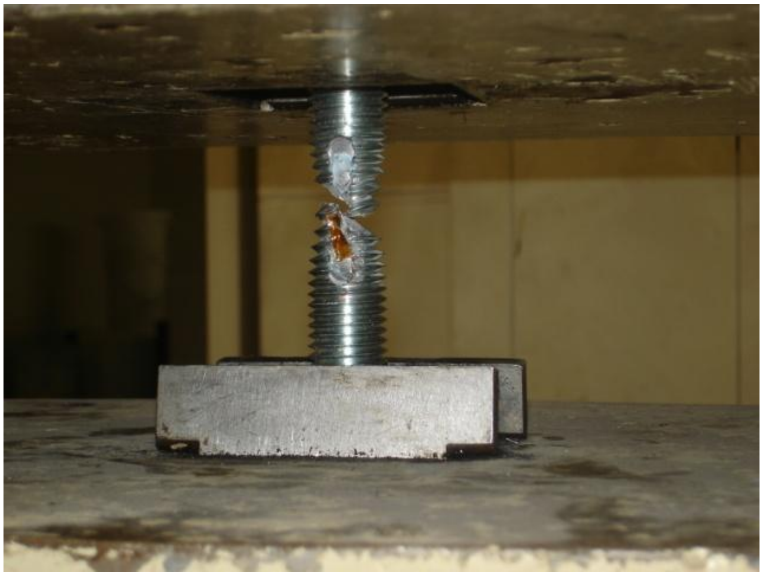

Failure of 3/4'' threaded anchor bolt anchor bolt under direct tension (notice necking and elongation in the bar)

Failure of 3/4'' threaded anchor bolt under direct tension (close up)

Data acquisition system

Appendix II

(Steel anchor data sheet)

Reinforcing Bar

Grade 75 All-Thread Rebar

Threads

Williams Grade 75 All-Thread Rebar has a cold rolled, continuous, rounded course thread form. Because of the full 360º concentric thread form, Williams All-Thread Rebar should only be bent under special provisions. Williams special thread (deformation) pattern projects ultra high relative rib area at 3 times that of conventional rebar. This provides for superior bond performance in concrete. Threads are available in both right and left hand.

Sizes

All-Thread Rebar is available in 11 diameters from #6 (20 mm) through #28 (89 mm). Most diameters are available in continuous lengths up to 50' (15.2 m).

Welding

Welding of All-Thread Rebar should be approached with caution since no specific provisions have been included to enhance its weldability. Refer to ANSI/AWS D1.4 for proper selections and procedures.

R61 Grade 75 All-Thread Rebar - ASTM A615

Bar Designation Nominal Diameter & Pitch	Minimum Net Area Thru Threads	Minimum Ultimate Strength	Minimum Yield Strength	Nominal Weight	Approx. Thread Major Dia.	Part Number
#6 - 3/4" - 5 (20 mm)	0.44 in^2 (284 mm^2)	44 kips (196 kN)	33 kips (147 kN)	1.5 lbs./ft. (2.36 Kg/M)	7/8" (22 mm)	R61-06
#7 - 7/8" - 5 (22 mm)	0.60 in^2 (387 mm^2)	60 kips (267 kN)	45 kips (200 kN)	2.0 lbs./ft. (3.04 Kg/M)	1" (25 mm)	R61-07
#8 - 1" - 3-1/2 (25 mm)	0.79 in^2 (510 mm^2)	79 kips (351 kN)	59.3 kips (264 kN)	2.7 lbs./ft. (3.94 Kg/M)	1-1/8" (29 mm)	R61-08
#9 - 1-1/8" - 3-1/2 (28 mm)	1.00 in^2 (645 mm^2)	100 kips (445 kN)	75 kips (334 kN)	3.4 lbs./ft. (5.06 Kg/M)	1-1/4" (32 mm)	R61-09
#10 - 1-1/4" - 3 (32 mm)	1.27 in^2 (819 mm^2)	127 kips (565 kN)	95.3 kips (424 kN)	4.3 lbs./ft. (5.50 Kg/M)	1-3/8" (35 mm)	R61-10
#11 - 1-3/8" - 3 (35 mm)	1.56 in^2 (1006 mm^2)	156 kips (694 kN)	117 kips (521 kN)	5.3 lbs./ft. (7.85 Kg/M)	1-1/2" (38 mm)	R61-11
#14 - 1-3/4" - 3 (45 mm)	2.25 in^2 (1452 mm^2)	225 kips (1001 kN)	169 kips (750 kN)	7.65 lbs./ft. (11.8 Kg/M)	1-7/8" (48 mm)	R61-14
#18 - 2-1/4" - 2-3/4 (55 mm)	4.00 in^2 (2581 mm^2)	400 kips (1780 kN)	300 kips (1335 kN)	13.6 lbs./ft. (19.6 Kg/M)	2-7/16" (62 mm)	R61-18
#20 - 2-1/2" - 2-3/4 (64 mm)	4.91 in^2 (3168 mm^2)	491 kips (2184 kN)	368 kips (1637 kN)	16.7 lbs./ft. (24.8 Kg/M)	2-3/4" (70 mm)	R61-20
#24 - 3" - 2-3/4 (76 mm)	6.82 in^2 (4400 mm^2)	682 kips (3034 kN)	511 kips (2273 kN)	24.0 lbs./ft. (35.8 Kg/M)	3-3/16" (81 mm)	R61-24
#28 - 3-1/2" - 2-3/4 (89 mm)	9.61 in^2 (6200 mm^2)	960 kips (4274 kN)	720 kips (3206 kN)	32.7 lbs./ft. (48.6 Kg/M)	3-3/4" (95 mm)	R61-28

All Couplings and Hex Nuts exceed 100% of the bar's published ultimate strength and meet ACI 318 Section 12.14.3.2 for mechanical rebar connections.

Hex

Collar

R62 Stop-Type Coupling - ASTM A108

Bar Desig. & Nominal Dia.	Outside Diameter	Overall Length	Part Number
#6 - 3/4" (20 mm)	1-1/4" (31.8 mm)	3-1/2" (88.9 mm)	R62-06
#7 - 7/8" (22 mm)	1-3/8" (35.1 mm)	4" (101.6 mm)	R62-07
#8 - 1" (25 mm)	1-5/8" (41.4 mm)	4-1/2" (114.3 mm)	R62-08
#9 - 1-1/8" (28 mm)	1-7/8" (47.7 mm)	5" (127.0 mm)	R62-09
#10 - 1-1/4" (32 mm)	2" (50.8 mm)	5-1/2" (139.7 mm)	R62-10
#11 - 1-3/8" (35 mm)	2-1/4" (57.2 mm)	6" (152.4 mm)	R62-11
#14 - 1-3/4" (45 mm)	2-7/8" (73.0 mm)	7-7/8" (200 mm)	R62-14
#18 - 2-1/4" (55 mm)	3-1/2" (88.9 mm)	9-1/8" (233.0 mm)	R62-18
#20 - 2-1/2" (64 mm)	4" (101.6 mm)	9-1/2" (241.3 mm)	R62-20
#24 - 3" (76 mm)	5" (127 mm)	11-1/4" (286 mm)	R62-24
#28 - 3-1/2" (89 mm)	5-1/2" (140.0 mm)	12" (305 mm)	R62-28

R63 Hex Nut - ASTM A108

Bar Desig. & Nominal Dia.	Across Flats	Across Corners	Thickness	Part Number
#6 - 3/4" (20 mm)	1-1/4" (31.8 mm)	1.444" (36.7 mm)	1-5/8" (41.4 mm)	R63-06
#7 - 7/8" (22 mm)	1-7/16" (36.5 mm)	1.66" (42.2 mm)	1-3/4" (44.5 mm)	R63-07
#8 - 1" (25 mm)	1-5/8" (41.3 mm)	1.877" (47.7 mm)	2" (50.8 mm)	R63-08
#9 - 1-1/8" (28 mm)	1-7/8" (47.8 mm)	2.166" (55.0 mm)	2" (51 mm)	R63-09
#10 - 1-1/4" (32 mm)	2" (50.8 mm)	2.309" (58.6 mm)	2-3/16" (55.6 mm)	R63-10
#11 - 1-3/8" (35 mm)	2-1/4" (57.2 mm)	2.526" (64.2 mm)	2-13/32" (61.1 mm)	R63-11
#14 - 1-3/4" (45 mm)	2-3/4" (73.0 mm)	3.175" (80.6 mm)	3-1/4" (82.6 mm)	R63-14
#18 - 2-1/4" (55 mm)	3-1/2" (88.9 mm)	4.039" (102.6 mm)	3-1/2" (88.9 mm)	R63-18
#20 - 2-1/2" (64 mm)	4" (101.6 mm)	4.62" (117.3 mm)	4" (101.6 mm)	R63-20
*#24 - 3" (76 mm)	4-1/2" (114 mm)	O.D. 5" (127 mm)	5" (127 mm)	R64-24*
*#28 - 3-1/2" (89 mm)	5-1/2" (140 mm)	O.D. 6" (152 mm)	6" (142 mm)	R64-28*

* Round Collar Nut

WILLIAMS FORM ENGINEERING CORP.

42

Appendix III

(Concrete Cylinder tests)

Compression test

Failure of cylinder under compression test

Compression Tests Results

	Cylinder	Failure load [lb]	concrete strength [MPa]
28 Days moist cured	1	134000	73.55
	2	125000	68.61
	3	128000	70.26
	average	129000	70.81
108 Days	1	135000	74.07
	2	125500	68.86
	average	130250	71.46

Splitting tensile test

$$Splitting\ Strength = \frac{2\,P}{\pi\ D\,L}$$

where P is the failure load, D is the diameter of the cylinder, and L is the length of the cylinder

Splitting Tests Results

	Cylinder	Failure load [lb]	concrete strength [MPa]
28 Days moist cured	1	49500	6.79
	2	41500	5.69
	3	40500	5.56
	average	43833	6.01

Appendix IV

Formulation of the constraint functions

$$G_1 = \begin{cases} \dfrac{|S_{conc}|}{0.6f'_c}, & S_{conc} \le 0 \\ \dfrac{S_{conc.}}{0.5\sqrt{f'_c}}, & \text{else} \end{cases}$$, S_{conc} is the concrete stress under initial loading stage

$$G_2 = \begin{cases} \dfrac{|S_{conc}|}{0.6f'_c}, & S_{conc} \le 0 \\ \dfrac{S_{conc.}}{0.5\sqrt{f'_c}}, & \text{else} \end{cases}$$, S_{conc} is the concrete stress under final loading stage

$$G_3 = \frac{S_{tendon}}{0.7\ f_{pu}}$$

$$G_4 = \frac{M_r}{M_f}$$

$$G_5 = \frac{M_r}{1.2\ M_{cr}}$$

$$G_6 = \frac{v_r}{v_f}$$

Note that G_4 and G_5 are applied in both directions, X and Y independently.

Appendix V

Formulation and Transformation of tendon element stiffness matrix and force vector into the shell element degrees of freedom

It should be noted that in the current element formulation, full compatibility in deformations is assumed between tendon elements nodes and their corresponding nodes in their "parent" shell element, i.e. full bond is assumed. However, adding contact elements to model unbounded tendons is possible.

$$\left[\mathrm{D}_{\mathrm{tendon}}\right]_{12\mathrm{x}12} = \int_{\mathrm{Vol.}} \left[\mathrm{B}_{\mathrm{tendon}}\right]^{\mathrm{T}}_{1\mathrm{x}12}\ \mathrm{E}\ \left[\mathrm{B}_{\mathrm{tendon}}\right]_{1\mathrm{x}12}\ \mathrm{A}_{\mathrm{r}} \sqrt{\left(\frac{\mathrm{dx}}{\mathrm{d}\zeta}\right)^2 + \left(\frac{\mathrm{dy}}{\mathrm{d}\zeta}\right)^2 + \left(\frac{\mathrm{dz}}{\mathrm{d}\zeta}\right)^2}\ \mathrm{d}\zeta$$

$$\left[\mathrm{D}_{\mathrm{tendon}}\right]_{91\mathrm{x}91} = \left[\mathrm{T}\right]^{\mathrm{T}}_{12\mathrm{x}91}\ \left[\mathrm{D}_{\mathrm{tendon}}\right]_{12\mathrm{x}12} \left[\mathrm{T}\right]_{12\mathrm{x}91}$$

$$\left[\mathrm{D}\right]_{91\mathrm{x}91} = \left[\mathrm{D}_{\mathrm{shell}}\right]_{91\mathrm{x}91} + \left[\mathrm{D}_{\mathrm{tendon}}\right]_{91\mathrm{x}91}$$

$$\left[F_{tendon}\right]_{91x1} = \left[T\right]^{T}_{12x91} \left[D_{tendon}\right]_{12x1}$$

$$\left[F\right]_{91x1} = \left[F_{shell}\right]_{91x1} + \left[F_{tendon}\right]_{91x1}$$

where

[D] = the stiffness matrix of the relevant element

[B] = the strain matrix of the tendon element, relating displacement DOFs to the strains

[T] = Transformation matrix relating the DOFs of both shell and tendon elements

E = Modulus of Elasticity of the tendon element
[F] = Force vector of the relevant element
ζ = curvilinear co-ordinate tangent to the tendon element

Displacement field of the shell element

$$\begin{Bmatrix} u \\ v \\ w \end{Bmatrix} = \sum_{i=1}^{13} \overline{N_i} \begin{Bmatrix} u_i \\ v_i \\ w_i \end{Bmatrix} + \sum_{i=1}^{13} N_i M_1 \begin{bmatrix} V_i \end{bmatrix} \begin{Bmatrix} \alpha_i \\ \beta_i \end{Bmatrix} + \sum_{i=1}^{13} N_i M_2 \begin{bmatrix} V_i \end{bmatrix} \begin{Bmatrix} \phi_i \\ \psi_i \end{Bmatrix}$$

where

u,v,w = global displacement of any point inside the shell element

u_i,v_i,w_i = global displacement of a node of the 13 nodes of the shell element

N_i = quadratic interpolation functions

$\overline{N_i}$ = cubic interpolation functions

$\begin{bmatrix} V_i \end{bmatrix}$ = unit vector along x′,y′ axis

M_1,M_2 = shape functions to approximate the displacement field through the depth

Transformation matrix

$$T_{12X91} = \begin{bmatrix} \overline{N}_1 & 0 & 0 & N_1M_1l_1 & -N_1M_1l_2 & N_1M_2l_1 & -N_1M_2l_2 & \\ 0 & \overline{N}_1 & 0 & N_1M_1m_1 & -N_1M_1m_2 & N_1M_2m_1 & -N_1M_2m_2 & \vdots\vdots \\ 0 & 0 & \overline{N}_1 & N_1M_1n_1 & -N_1M_1n_2 & N_1M_2n_1 & -N_1M_2n_2 & \\ \vdots & \vdots & \vdots & \vdots & \vdots & \vdots & \vdots & \ddots \end{bmatrix}$$

where

l_i,m_i,n_i = Directional cosines at a point

For further details on the formulation of the stiffness matrix and load vector for both shell and tendon elements, refer to Koziey (1993).

Appendix VI

Design of base block:

A simplified finite element model is developed to predict the maximum anticipated internal forces within the base block. In that model, the base is modelled using beam elements while the panel is modelled using shell elements. The base is assumed to be connected to the panel for simplicity as this also would be construed as the maximum anticipated internal forces. Strong springs are used to model floor reaction, and hinged support to model the upper beam.

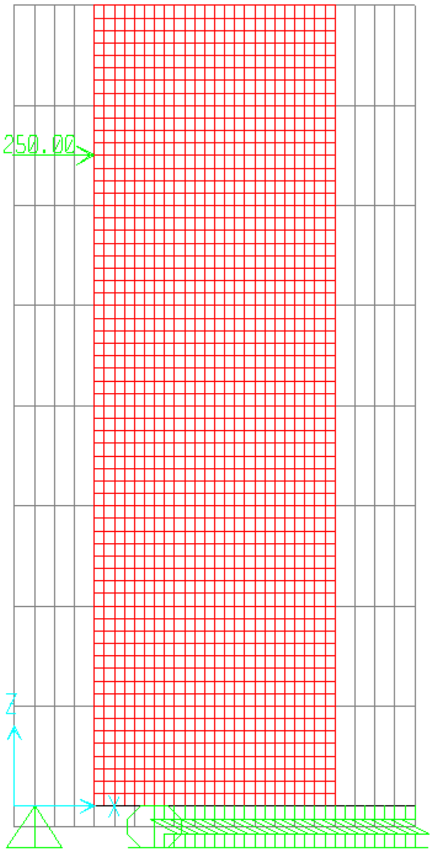

SAP model for base block design

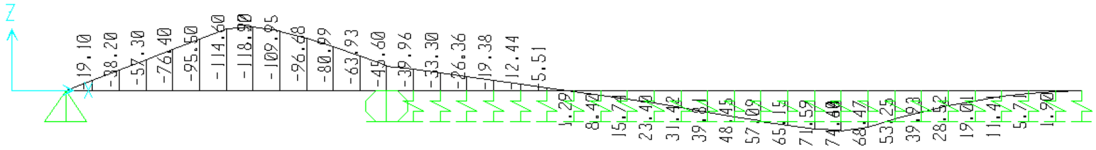

Bending moment diagram

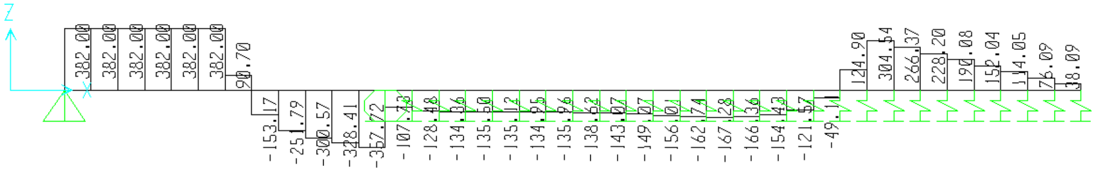

Shear force diagram

The ultimate strength of the strongest bar is equal to 319 kN, the base is resisting this load by concrete breakout resistance.

$$N_{u,c} = \frac{A_{c,N}}{A^{o}_{c,N}}.\psi_{s,N}.N^{o}_{u,C}$$

$where:$

$$N^{o}_{u,C} = 10.\sqrt{f'_c}.h_{ef}^{1.5}$$

$$\psi_{s,N} = 0.7 + 0.3\frac{c}{c_{cr,N}}$$

$$c = 1.5h_{ef}$$

$c_{cr,N}$ = Distance to the base edge

$A_{c,N}$ = Projected concrete failure area of one anchor, not limited by edge distance or spacing

$A^{o}_{c,N}$ = Projected concrete failure area of one anchor limited by edge distance

$$N_{u,c} = \frac{326400}{462400}.\left(0.7 + 0.3\left(\frac{190}{290}\right)\right).\left(10.\sqrt{70}.290^{1.5}\right) = 261.5 \text{ kN} < 319 \text{ kN}$$

The concrete depth can not sustain the maximum anchor load by concrete breakout resistance, thus the two longitudinal beams shown in Figure 2.6 and 2.8 are used to change the load path to be resisted by a compression field in concrete as shown below

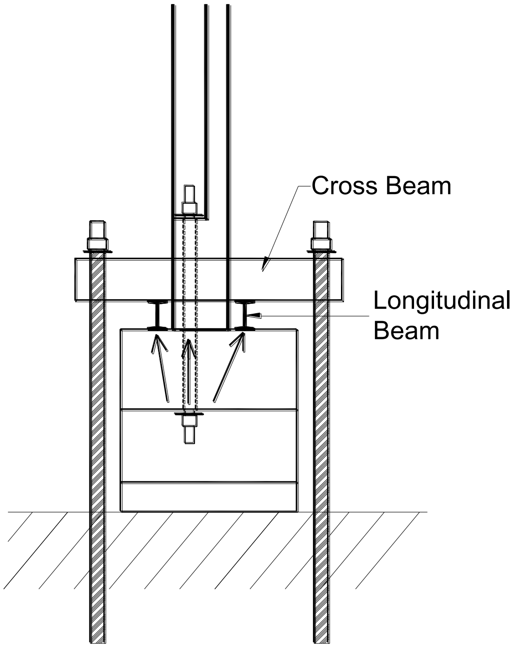

Force transfer

Appendix VII

Experimental data: Sliding between the concrete panel and the base block is defined as the difference between the two horizontal LVDT's at the bottom.

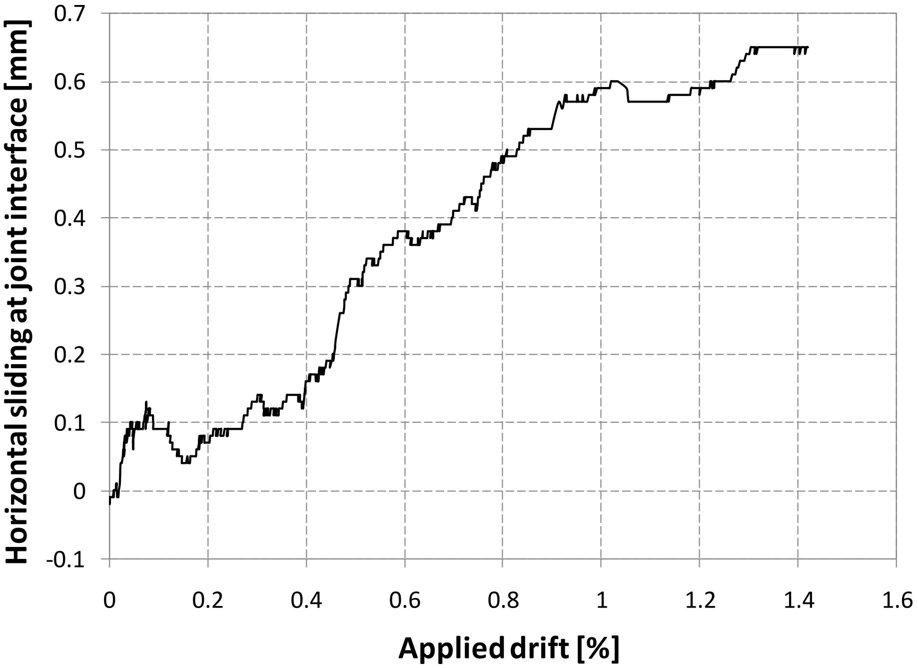

Horizontal sliding at joint interface (Test 1)

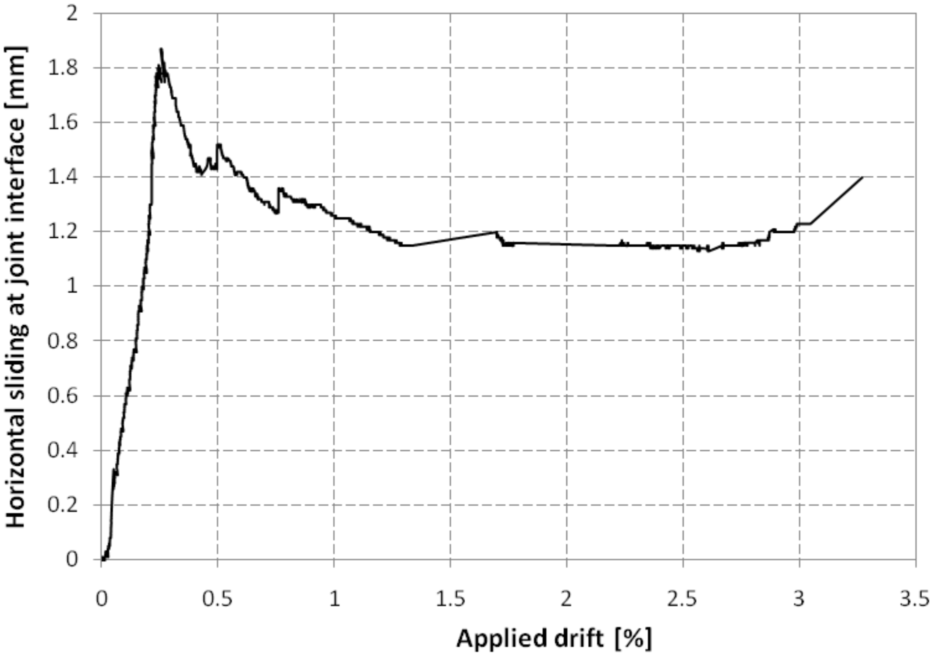

Horizontal sliding at joint interface (Test 2)

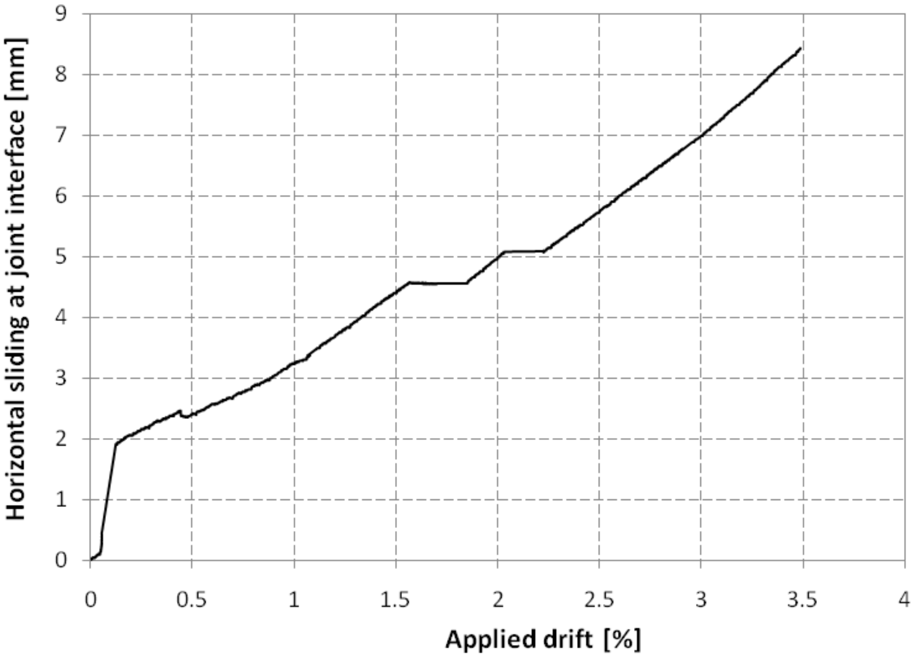

Horizontal sliding at joint interface (Test 3)

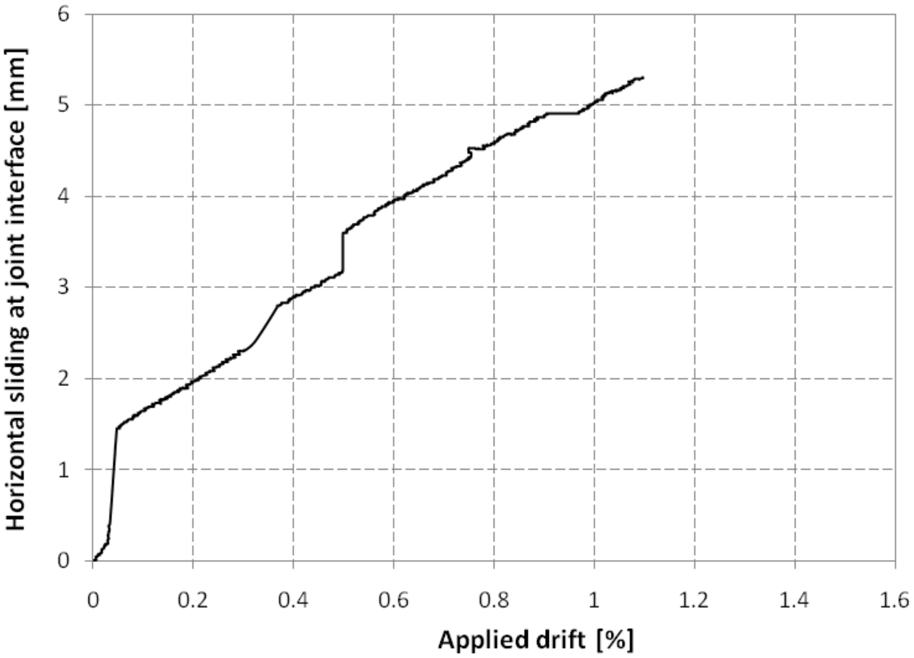

Horizontal sliding at joint interface (Test 4)

RESUME
MOHAMED EL SEMELAWY

ACADEMIC CREDENTIALS

Ph.D. Engineering Science, Civil Engineering, University of Western Ontario, London, Ontario **(May 07 – June 11)**

M.A.Sc., Civil Engineering, University of Toronto, Toronto, Ontario. **(Sep. 04 – Dec. 06)**

BSc., Civil Engineering, Structural Section, Ain-Shams University, Cairo, Egypt **(Sep. 97– June 02)**

Cumulative Grade: Distinction with Honor (85 % - 6th out of 385 Successful students)

Graduate courses:

University of Western Ontario: Prestressed Concrete, Engineering Optimization, Finite Element Analysis for Solids, and Response of Structures to Lateral Loads (Average Grade: 98/100).
University of Toronto: Solid Mechanics, Mechanics of Reinforced Concrete, Bridge Engineering, Structural Dynamics and Earthquake Engineering, and Bridge Engineering (GPA: 3.72/4.00).
Ain-Shams University: Advanced Testing of Products and Structures and Soil Dynamics.

WORK EXPERIENCE

Structural Engineer (Part – time) **(Mar. 08 – Aug. 09)**
Engineering Analysis and Dynamics Ltd., London, Ontario, Canada

During this period I was part of the design team for the following projects:

- Carmen Hampton Inn Hotel (65 story building), Niagara Falls, Ontario:
- South Tower building, Niagara Falls, Ontario:
- Technia Factor (Precast Concrete), Jedda, Saudi Arabia:
- The Mansions of Forest Glen, Niagara Falls, Ontario:
- Le Monaco condominium, Georgetown, Ontario:

My responsibilities ranged from modeling, analysis, and design of flooring system, columns, shear walls, and shear wall pile cap; design included consideration of lateral wind and earthquake loads.

Structural Engineer (Part – time) **(June 02 – Sep. 04)**
Hany El Zayat Engineering Consulting Office, Cairo, Egypt:

Carried out structural design for several commercial-and-residential RC skeleton type buildings ranging from single story to twenty-story medium-rise buildings

Structural Engineer (Part – time) **(Mar. /Apr. 03)**
RC Research Centre, Ain-Shams University, Cairo, Egypt:

Field tested bridges located in Greater Cairo ring road.

PROFESSIONAL ORGANIZATION AND AFFILIATION

- The Canadian Society for Civil Engineering
- The American Society of Civil Engineers
- Precast/Prestressed Concrete Institute (ID # 102807)
- Registered Engineer at "The Egyptian Syndicate of Engineers" (2002–Present)

EXTRACURRICULAR ACTIVITIES

- Big Beam Competition 2008 (design, build and test a precast concrete beam to meet certain criteria) – First place zone 7 – 6th place international (1000$ prize).
- Elected Councilor, Society of Graduate Students – University of Western Ontario

MERITS & AWARDS

- **Western Graduate Research Scholarship:**
  University of Western Ontario (2007 **–** 2011)
- **University of Toronto Graduate Research Scholarship:**
  University of Toronto (2004 **–** 2006).
- **Honors, Ain-Shams University, Cairo, Egypt:**
  The Government Award of Excellence in Undergraduate Studies (1997 **–** 2002).